Geochemical investigations of Corchia speleothems: Implications for past climate change

PETRA BAJO
(ORCID: 0000-0002-0395-8113)

Thesis submitted in total fulfilment of
the requirements of the degree of

DOCTOR OF PHILOSOPHY

February 2016

School of Geography
Faculty of Science
The University of Melbourne

"Produced on archival quality paper"

Abstract

This PhD thesis addresses three research questions using speleothems from Corchia Cave (Italy). An outline of the major findings follows.

The first question concerns glacial-interglacial cycles. The greatest obstacle in resolving the question of which orbital parameter (or combination thereof) forces Earth's climate to switch between glacial and interglacial states is a lack of radiometrically dated records of glacial terminations. In this study, three stalagmites (CC8, CC119 and CC122) were precisely and accurately dated using the U-Pb dating method, and a composite age-depth model developed. The speleothem chronology was then transposed to a series of deep-sea sediment records, allowing three glacial terminations during the Middle Pleistocene Transition (MPT) to be radiometrically dated. The results reveal that Terminations XII and X are separated by two obliquity cycles, and that Marine Isotope Stages 25 to 22 are not part of a 100-kyr cycle as previously thought. Both terminations started at the same phase of obliquity but show an inconsistent relationship with precession-driven maxima in summer insolation intensity. This implicates obliquity as the major forcing parameter, while the role of precession is less conclusive.

The second question concerns the integrity of speleothems for radiometric dating. Speleothems are considered as one of the most suitable materials for U-series dating. High-resolution U-Th dating of Corchia Cave stalagmite CC26, however, revealed a number of age outliers, which was unexpected due to the otherwise pristine appearance of the speleothem. The aim was to explore the potential causes for these outliers. By using a multi-aliquot approach, analytical problems were eliminated. Micro-CT analyses revealed a limited number of micro-voids, and it is proposed that these were pathways for small (localised), but significant (in terms of dating implications) U loss. Uranium-loss modeling constrains the possible timing of the diagenetic

processes. These results show that such “invisible” diagenesis has implications for the accuracy of U-Th based chronologies for speleothems and suggests a need for a more careful approach, particularly in studies which are based on low-resolution dating.

The third and final question relates to the drivers of stable carbon isotope ($\delta^{13}C$) changes in Corchia Cave speleothems at the onset of interglacials. The ‘dead carbon proportion’ (DCP) record from stalagmite CC26 was used to develop a more robust interpretation of the factors driving carbon isotope variation. High DCP (44.8 to 68.8%) was interpreted as a result of two processes: closed-system dissolution and sulphuric-acid dissolution. A ~parallel decrease in $\delta^{13}C$ and DCP during the Holocene provides support for the previous interpretation of $\delta^{13}C$ as reflecting long-term post-glacial soil recovery. Additionally, short-term changes in DCP are compared to the Mean Anomaly Index based on the trace element and stable isotope record from the same specimen (Regattieri et al., 2014), which reveals that DCP is also sensitive to millennial-scale changes in recharge hydrology.

Declaration

This is to certify that:

I. the thesis comprises only my original work towards the PhD except where indicated in the Acknowledgment of collaboration,
II. due acknowledgement has been made in the text to all other material used,
III. the thesis is less than 100 000 words in length, exclusive of tables, maps, bibliographies and appendices.

Publications arising from this PhD thesis

Chapter 4.

Bajo, P., Drysdale, R., Woodhead, J. Hellstrom, J., Zanchetta, G., 2012. High-resolution U-Pb dating of an Early Pleistocene stalagmite from Corchia Cave (central Italy). *Quaternary Geochronology* 14, 5-17.

Chapter 5.

Bajo, P., Drysdale, R., Woodhead, J., Hellstrom, J., Ferretti, P., Wolff, E., Zanchetta, G., Frisia, S., Spötl, C., Fallick, A.E., *in preparation for resubmission*. Obliquity pacing of ice-age terminations at the Middle Pleistocene Transition. *Science*

Chapter 6.

Bajo, P., Hellstrom, J., Frisia, S., Drysdale, R., Black, J., Woodhead, J., Borsato, A., Zanchetta, G., Wallace, M.W., Regattieri, E., Haese, R., *in preparation*. "Invisible" diagenesis and its implications for speleothem geochronologies. *Quaternary Science Reviews*

Chapter 7.

Bajo, P. et al., *in preparation*. Interpreting carbon isotopes in a Corchia Cave speleothems by combining $\delta^{13}C$ and dead carbon proportion (DCP). *Geochimica et Cosmochimica Acta*

Acknowledgement of Collaboration

I hereby certify that some of the work embodied in this Thesis has been performed in collaboration with other researchers, or carried out in other institutions. Below I have outlined the extent of collaboration, with whom and under what auspices.

Patrizia Ferretti (IDPA-CNR Venice- Italy) helped with tuning of the Corchia $\delta^{18}O$ time series and marine records presented in the Chapter 5. Eric Wollf (University of Cambridge- UK) critically commented on the content of the Chapter 5. Giovanni Zanchetta (University of Pisa- Italy), Christoph Spötl (University of Innsbruck - Austria) and Anthony Fallick (SUERC- Scotland, UK) performed stable isotope measurements on speleothems CC8 and CD3 presented in Chapter 5. Silvia Frisia (University of Newcastle) and Malcolm Wallace (University of Melbourne) helped to carry out petrographic analysis of thin sections presented in Chapters 5 and 6. Jay Black (University of Melbourne) and Ralf Haese (University of Melbourne) carried out micro-CT scanning of the stalagmite CC26 presented in Chapter 6. Andrea Borsato (University of Newcastle) and Silvia Frisia (University of Newcastle) performed synchrotron analyses presented in Chapter 6. Quan Hua (Australian Nuclear Science and Technology Organisation - ANSTO) performed radiocarbon analysis presented in Chapter 7. All the co-authors listed in the Publications arising from this PhD thesis list commented on the corresponding manuscripts.

Acknowledgement of Authorship

I hereby certify that the work embodied in this Thesis contains a published paper/s/scholarly work of which I am a joint author. I have included as part of the Thesis a written statement, endorsed by my Principal Supervisor, attesting to my contribution to the joint publication/s/scholarly work.

I, Petra Bajo, was the primary investigator and lead author of a published manuscript and manuscripts in preparation presented in this Thesis.

Russell Drysdale

Petra Bajo

Acknowledgments

My sincerest thanks to:

- My supervisors ***Russell Drysdale, Jon Woodhead and John Hellstrom***

for being great supervisors throughout my PhD candidature. I would never have reached this stage without your help, guidance and support. Special thanks to my principal supervisor Russell Drysdale for making it possible for me to work on the exciting Corchia project.

- ***Quan Hua and Henri Wong***

for supporting my AINSE PGRA application; for hosting me at ANSTO and for the opportunity to learn so much from you both.

- ***Silvia Frisia and Andrea Borsato***

for many fruitful scientific discussions and encouragement; for hosting me at your home while visiting Newcastle; for your help with petrographic and synchrotron analyses and contributions to writing up the "invisible" diagenesis chapter.

- ***Patrizia Ferretti***

for your contribution to aligning the Corchia and marine records and your critical review of the background chapter on the MPT. Also for your messages of support and encouragement.

- ***Eric Wolff***

for your critical review of chapter 6.

- ***Giovanni Zanchetta, Christoph Spötl and Anthony Fallick***

for performing stable isotope analyses on the speleothems CC8 and CD3; for your helpful comments on the manuscripts as co-authors. Additional thanks to Giovanni Zanchetta and Christoph Spötl for being great hosts during my visits to Pisa and Innsbruck, thank-you.

- ***Jay Black and Ralf Haese***

for carrying out micro-CT scanning analyses; and also for your feedback on the "invisible" diagenesis manuscript.

- ***Malcolm Wallace***

for an opportunity to do petrographic analyses at the Melbourne University and for sharing your expertise; for your support and insightful comments on the "invisible" diagenesis manuscript.

- ***Colleagues and friends from the School of Geography and the School of Earth Sciences (Andrea C., Roland, Alan, Bence, Helen, Robyn, Haslina, Fahmida, Nurruzaman, Carlo, Tony, Angeliki...)***

for help whenever it was needed and for fruitful discussions not only of scientific matters; for friendly environment in the office.

- ***Family and friends in Croatia (mama, tata, families Ujević, Bajo, Bošnjak, Misilo, Pavičić and Vranković, Nike, Tomo, Alan, Helena, Ines, Mate, Ana...) and Australia (family Tarle and Popovic, Zdenka, Tephy, Dragana, Tanja, Dario, Sandra, Maria, Matej, Senka, Lobel...)***

To those in Croatia for reminding me constantly where my heart and home are and for those in Australia for making Melbourne truly feel like my second home. I also thank you for your encouragement and all the special moments that enriched our lives in Australia.

- ***Mušura family***

for providing us with security when it was most needed: at the beginning of our Aussie adventure (John, Ivana, Kristofer, Lora and Patrik) and when Jure was about to arrive (hvala ujac i ujna!).
Hvala vam od srca!

- ***Tomo, Jure and the little one to arrive***

za vašu bezuvjetnu podršku i razumijevanje, za svaki osmjeh i poljubac koji su me osnažili kad bih posumnjala da će ovaj dan ikada doći. Vi ste ti koji ste me nosili do ovdje i ovaj rad posvećujem vama.

"Leti ko lišće što vir ga vije,
za let si, dušo stvorena.
Za zemlju nije, za pokoj nije
cvijet što nema korijena."

(*Igračka vjetrova- Tin Ujević*)

I am also very grateful for the financial support provided for this PhD research project by the following organisations:

- ***Australian Research Council***
(Discovery Projects DP110102185 and DP0664621)

- ***Australian Institute of Nuclear Science and Engineering***
(PGRA- Post Graduate Research Award)

- ***University of Melbourne***
(MIRS and MIFRS scholarships)

TABLE OF CONTENTS

LIST OF FIGURES

LIST OF TABLES

Chapter 1

1 INTRODUCTION

1.1 THESIS AIMS

Speleothems (secondary cave carbonates, such as stalagmites, stalactites and flowstones) are considered important palaeoclimate archives due to their amenability to robust radiometric dating and sensitivity to climate-driven environmental changes (Henderson, 2006). This research focuses on a number of speleothems from Corchia Cave in Italy. The thesis has three major components (themes), each of them dealing with a unique geochemical problem but with a common subject centred on new geochronological methodologies, or newly recognised problems with existing techniques.

Theme 1 is in the domain of the recently developed U-Pb dating method for speleothems, and investigates glacial-interglacial transitions during the Middle Pleistocene Transition (MPT). The second theme concerns a previously unrecognised diagenetic problem which may affect the reliability of the U-Th dating method. In theme 3, both U-Th and radiocarbon dating are employed to develop a more robust interpretation of post-glacial carbon isotope systematics in Corchia speleothems, using as an example a Holocene stalagmite. Three themes are discussed in detail in the following section.

Theme 1: Developing of a precise and accurate radiometric chronology for glacial-interglacial climate transitions during the part of the Middle Pleistocene Transition (0.98 to 0.86 Ma)

Glacial-interglacial cycles are the primary feature of Quaternary climate. A wealth of information on Quaternary glacial-interglacial climate transitions (called 'glacial terminations') has been derived from marine and ice-core records. However, a consensus explanation for these transitions has yet to emerge due to the difficulty of dating these records precisely. Previous studies have shown the great potential of using speleothems to absolutely date deep-sea and/or ice-core records and to use them in testing orbital theories responsible for Late Pleistocene terminations (Cheng et al., 2009; Drysdale et al., 2009; Winograd et al., 1992). However, no study has explored this potential for older speleothems. Recent advances in the U-Pb dating method now make this task possible (Woodhead et al., 2006; 2012).

The thesis aims in this respect are:

- To determine whether robust U-Pb chronologies for Corchia Cave speleothems can be assembled through glacial-interglacial transitions (terminations) of the Middle Pleistocene Transition at a sufficiently high precision (a few thousand years) to probe the likely orbital forcing mechanisms responsible.
- To develop precisely dated climate-proxy time series from stable isotopes of Corchia stalagmites, which have already proven to be sensitive to glacial-interglacial climate change (Drysdale et al., 2009).
- To produce replicate U-Pb chronologies and stable isotope proxy time series in three different stalagmites in order to develop a more precise master chronology and to confirm (through replication) the palaeoclimate significance of the record.
- To synchronise the speleothem time series to nearby North Atlantic deep-sea sediment records and transfer the Corchia radiometric chronology to the benthic $\delta^{18}O$ record of ice-volume change.

- To test competing theories for the orbital forcing of terminations using these speleothem-tuned benthic time-series, which are independent of the usual orbital tuning methods used for benthic records.

The significance of this objective is threefold.

- ✓ Firstly, dating speleothems by the U-Pb technique is challenging in its own right. Further improvement of U-Pb protocols and the development of time series for older speleothems are recognized as one of the main future scientific goals in speleothem palaeoclimate science (Fairchild and Baker, 2012). The U-Pb dating of Corchia speleothems in this study would contribute to an improved understanding of U-Pb dating of speleothems. This is the first study where robust age-depth models for speleothems of this age will be produced.
- ✓ Radiometrically based ages for terminations are highly sought after in palaeoclimate research. Without precise and direct age control of these events from marine cores, it is impossible to determine the leads and lags in the climate system, and thus impossible to assess levels of inter-hemispherical phasing. Most importantly, without accurate and precise chronologies, it is impossible to determine the orbital factors that lead to these changes.
- ✓ The outcomes of this objective will improve our knowledge about the timing and duration of glacial-interglacial transitions during the Middle Pleistocene Transition, regarded as "one of the greatest mysteries in the palaeoclimatology" (Raymo and Huybers, 2008).

Theme 2: To explore "invisible" diagenesis and its effects on the accuracy of the U-Th chronometer for speleothems

Theme 2 is retrospective and it was possible thanks to the results obtained under theme 3, where high-resolution U-Th dating was

performed in order to produce precise U-Th chronologies crucial for robust DCP calculations. While conducting this study, it was discovered that a number of U-Th analyses resulted in reversed ages and it was decided to probe this problem further in order to understand the reasons for the observed outliers. Because multi-aliquot U-Th analyses were performed, analytical problems could not be held responsible for these outliers. The hypothesis was that the sample must have experienced localised diagenesis.

An increasing number of studies have reported cases where speleothems have undergone diagenesis (Lachniet et al., 2012; Scholz et al., 2014). This affects the U-series chronometer because it breaches the closed-system behaviour rule, leading to U loss from the system and finally resulting in inaccurate (typically older than true) ages (Richards and Dorale, 2003). Consequently, in most cases altered samples cannot be used in palaeoclimate research. While all previous studies dealing with diagenesis in speleothems report cases where the alterations are visible to the naked eye or by microscopy, here a case of an apparently pristine stalagmite which undergone very localized “invisible” diagenesis is reported. Furthermore, previous low-resolution U-Th dating did not show any evidence of diagenesis in this specimen (Zanchetta et al., 2007). In order to find an explanation for these outliers, the following steps were performed:

- High-resolution Laser Ablation Inductively Coupled Plasma Mass Spectrometry (LA-ICP-MS) and synchrotron analyses were employed to explore U distribution in the key areas of the stalagmite.
- Detail petrographic analyses of thin sections were used to investigate if speleothem fabric displayed features characteristic of diagenesis.
- High-resolution micro-computer tomography (micro-CT) was employed to determine the 3D porosity distribution in the affected part of the stalagmite and to find possible explanations for the observed U loss.

- A U-loss model was produced and the possible timing of diagenesis was modelled.

The significance of these results are as follows:

- ✓ A better understanding of the processes that may affect U-series systematics in speleothems is needed in order to secure more reliable speleothem-based palaeoclimate reconstructions.
- ✓ Invisible diagenesis may be a very localised process but with a significant influence on U-series age profiles. The localised nature may be hard to detect using classical low-resolution dating approaches.
- ✓ Micro-CT is a relatively new method in the field of speleothem science and still underutilised. This study illustrates how the micro-CT method may be used in the targeting of sample locations for U-Th dating.

Theme 3: Using the Holocene as a case study, to decipher the mechanisms driving post-glacial stable carbon isotope ($\delta^{13}C$) changes in Corchia speleothems by combining ^{14}C dating, U-Th dating and $\delta^{13}C$ data.

Speleothem $\delta^{13}C$ is much less understood compared to oxygen (Fairchild and Baker, 2012), and has thus received less attention in published studies. This is mainly due to the diversity of C sources and the complex processes that affect their incorporation into speleothems. $\delta^{13}C$ data for the last twelve glacial-interglacial transitions from Corchia Cave show that each glacial-interglacial transition is characterised by a gradual decrease in $\delta^{13}C$ (Drysdale et al., 2004; 2009; 2011; Zanchetta et al., 2007). This sluggish rate of decrease was interpreted as indicative of the slow rate of soil development above the cave as a result of amelioration of climate conditions characteristic of glacial-interglacial transitions (Drysdale et al., 2004; 2009; Zanchetta et al., 2007).

Gradual soil and vegetation development following glacial conditions would cause a long-term increase in soil air pCO_2 due to plant respiration, leading to an increase in the availability of isotopically light biogenic carbon for dissolution by infiltration waters, leading to decreased speleothem $\delta^{13}C$ (Drysdale et al., 2004; 2009; Zanchetta et al., 2007).

The aim of theme 3 is to test this interpretation by studying changes in the dead carbon proportion (DCP) data from a stalagmite which grew during the last ~12 ka. If the post-glacial $\delta^{13}C$ decrease is caused by sluggish rates of soil development above the cave it should also be reflected in DCP. Namely, soil development and increased soil air pCO_2 would generate an increased proportion of contemporaneous ^{14}C into the DIC of infiltration waters, decreasing the proportion of dead carbon sourced from the host rock. This would decrease the DCP in the speleothem (Genty et al., 2001). In order to test this hypothesis the following steps were performed:

- To employ paired radiocarbon and U-Th analyses to determine the dead carbon proportion (DCP) using the atmospheric ^{14}C data from the IntCal13 calibration curve (Reimer et al., 2013).
- To compare the DCP record with stable isotope and trace element results from the same specimen (Regattieri et al., 2014; Zanchetta et al., 2007) to explore possible common climatic forcing mechanisms.

The significance of this theme is:

- ✓ Independent support for the previous interpretation of $\delta^{13}C$ in Corchia speleothems is required and this study will provide a test of the proposed hypothesis.
- ✓ The DCP results from Corchia Cave will bring a new perspective on the interpretation of carbon isotopes in geologically complex settings characterised by sulphuric acid dissolution which acts in concert with classical carbonic acid dissolution processes.

- ✓ A previous study proposed that DCP is more sensitive to wet than to dry climate events (Noronha et al., 2014). Our results will enable the testing of this hypothesis.

1.2 ORGANISATION OF THE THESIS

The thesis is organised in accordance with its themes.

The *second* chapter constitutes a literature review on the current knowledge surrounding the Middle Pleistocene Transition and key aspects of speleothem science. The *third* chapter introduces the study site and provides an overview of previous palaeoclimate studies from Corchia Cave. In the *fourth* and *fifth* chapters, the results of theme 1 are presented. The contents of the fourth chapter were published in *Quaternary Geochronology* in 2012; chapter five is a manuscript under revision and planned for resubmission to *Science*. Chapter *six* addresses the question of invisible diagenesis. These results are planned to be submitted for publication to *Quaternary Science Reviews*. Chapter *seven* concerns the origin of carbon isotope variations in Corchia speleothems and this represents a manuscript in preparation, planned to be submitted to *Geochimica et Cosmochimica Acta.* In the final, *eighth* chapter, the conclusions of the thesis and suggestions for future work are provided.

Chapter 2

2 BACKGROUND

2.1 PALAEOCLIMATOLOGY- THE STUDY OF PAST CLIMATES

Palaeoclimatology is the scientific discipline that considers the (predominantly natural) past climate and environmental changes spanning different time scales (e.g. tectonic, orbital, millennial) and spatial domains (global through to local). It uses a variety of climate archives (e.g. deep-sea sediments, ice cores, lake sediments, peat bogs, loess, coral terraces, speleothems) which, in their physical, chemical and organic properties, capture different aspects of climate change, producing so-called 'proxy' records. The properties that the climate archives are required to posses can be proxies - a 'surrogate' for quantitative estimates of given parameters (chemical, physical or biological) of past environment and climate - but also 'real' measurements (e.g. CO_2 and CH_4 in ice cores) related to environmental conditions or processes that may provide quantitative or qualitative insights into such conditions or processes. Apart from the requirement that climate archives need to posses one or more properties that can be used to infer palaeoclimate conditions, they ultimately have to be datable (directly or indirectly) in order to be used in palaeoclimate research. The utility of each archive in deciphering palaeoclimate changes will strongly depend not only on its ability to be precisely dated

but also on the level of understanding of the palaeoclimate signal captured in its proxies and "real" measurements. For this reason, a multiproxy approach is commonly employed in modern palaeoclimate research where two or more proxies are combined to secure a reliable interpretation of its climate significance. Furthermore, the climate system is characterized by a complex interplay between its different components (atmosphere, hydrosphere, lithosphere and biosphere) and each of these can modify the recorded signal in often complicated ways. Combining different archives from different environments and areas of the globe can thus greatly assist in the exploration of leads, lags and teleconnections in the complex climate system.

In cases where archives can be dated directly to give absolute ages, they can serve as valuable tools in deciphering spatial and temporal climate variability, the phasing of different components of the climate system, and in the determination of the causes of these changes. Developing a better understanding of past climate variations is of great importance, particularly now that the Earth's climate is experiencing rapid changes with unpredictable outcomes. Climate models are based largely on instrumental data obtained from the last ~150 years. In order to test models of past climates, as well as those aimed for predictions of future changes, palaeoclimate records extending deeper into Earth history are urgently needed (McDermott, 2004).

2.2 SPELEOTHEMS

Speleothems are secondary carbonate cave deposits formed mostly in a vadose karst environment - karst being a specific geologic setting comprised of (usually) carbonate rocks, which are soluble in slightly acidic waters (Ford and Williams, 2007). Speleothem formation requires the availability of rainwater which equilibrates with CO_2 from the air and becomes slightly acidic. Percolating through the soil zone the water

is further exposed to soil CO_2, originating from the decomposition of organic matter and microbial and root respiration, forming carbonic acid. This water can percolate through the transition zone between soil and bedrock (called the epikarst) where the majority of carbonate dissolution takes place. The water, now enriched in carbonate, then percolates through the fissures and joints in the bedrock and possibly further dissolves bedrock (although deposition is also possible). Once the water reaches an underground cavity, different partial pressures of CO_2 in the cave air and the percolation water cause degassing of CO_2 from the latter, driving the solution to supersaturation with respect to calcite, which is then deposited in the form of speleothem (**Figure 2-1**). A significant role in speleothem formation is cave ventilation, which removes CO_2 released during speleothem formation and maintains a pCO_2 gradient between drip water and cave air which is crucial for furthering calcite formation. The simplified chemical reaction of speleothem formation can be represented by the **Equation 2-1** (Ford and Williams, 2007):

Equation 2-1. $Ca^{2+}{}_{(aq)} + 2HCO_{3\,(aq)}^{-} \leftrightarrow CaCO_{3\,(s)} + CO_{2(g)} + H_2O_{(l)}$

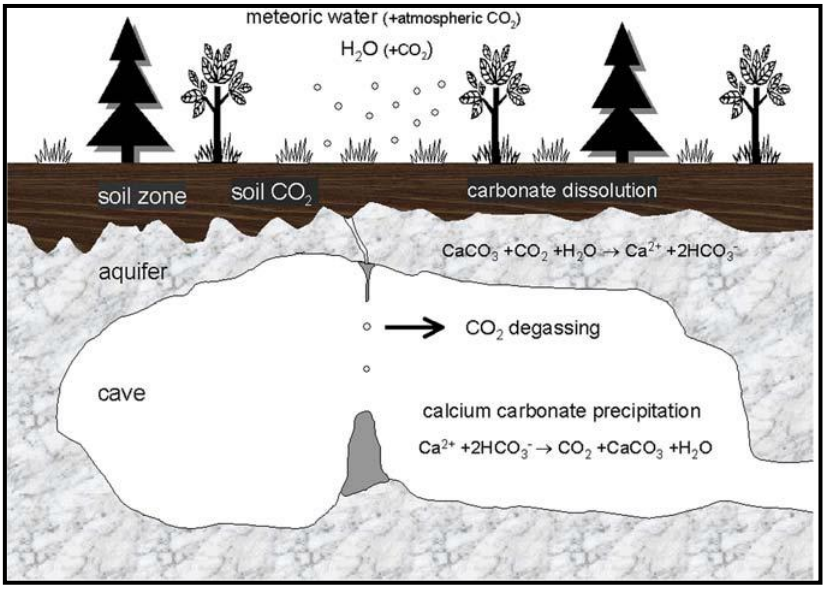

Figure 2-1. Process of speleothem formation, from Frisia and Borsato (2010)

Climate signals are transported to and captured in speleothems in multiple ways. The water from which speleothems are formed is the major link, since its geochemical composition is dependent on the composition of rainfall and its later modification in the interaction with soil and bedrock (Fairchild and Baker, 2012). Water also has a crucial role in the transport of solid particles and colloids, as well as trace elements, from the atmosphere, soil zone and bedrock. Many or all of these processes may be climate and environmentally dependant (Fairchild et al., 2006). Furthermore, there is a link between cave microclimate conditions and climate on the surface, e.g. it is well known that cave temperatures reflect the mean annual temperature on the surface (Fairchild and Baker, 2012; Li et al., 2014).

Speleothems occur in many different forms (Ford and Williams, 2007) and can be constructed from different minerals (Hill and Forti, 1997), calcite and aragonite being the most common. In palaeoclimate research, stalagmites are predominantly used due to their simple growth geometry, although flowstones are used occasionally (Hellstrom et al., 1998) and stalactites (Bar-Matthews et al., 2003) and soda-straw stalactites (Desmarchelier et al., 2006) very sporadically.

Speleothems are found in almost all climate zones of the world, and often remain protected from erosion and diagenesis in stable cave environments for long periods of time. Furthermore, they are characterised by multiple climate-sensitive properties, and are precisely datable via U-series dating methods (Hellstrom, 2003; Zhao et al., 2009), thus playing an increasingly important role in shaping our knowledge about past climate and environmental change (Fairchild et al., 2006; McDermott, 2004). Additionally, they can be studied at high-resolution (sometimes sub annual) thanks to advances in sampling protocols (Drysdale et al., 2012) and analytical (Orland et al., 2012) techniques.

Despite the explosion of new proxies and techniques, as well as improvements to existing ones, speleothems have their limitations like

every other climate archive. For speleothems, these are primarily related to the complex nature of the processes that force changes in speleothem properties and the relative lack of fully developed quantitative interpretations of proxy data. To overcome these complexities, it is the norm nowadays to use a multi-proxy approach combining several different proxies in order to provide a robust environmental and climate interpretation.

Despite these limitations, compared to other sources of palaeoclimate information, speleothems have been shown to be excellent archives for determining the precise and accurate timing of global and regional climate variability, and have improved our knowledge of, for example, monsoonal systems as well as opening up exciting possibilities to test orbital theories of global glacial-interglacial transitions (Cheng et al., 2009; Drysdale et al., 2009; Wang et al., 2001).

2.3 SPELEOTHEM PROXIES

2.3.1 PETROGRAPHY

Petrographic studies are recommended to be performed prior to analyses for other proxies because petrography may reveal characteristics of speleothem growth not visible to the naked eye that can significantly influence the palaeoclimate interpretation (Frisia and Borsato, 2010). For example, petrographic studies on speleothems may help to determine whether or not a sample has been recrystallised. Recrystallisation (e.g. transformation of aragonite to calcite) breaches the “closed-system assumption” of U-series dating and thus may result in inaccurate ages, rendering the samples useless for palaeoclimate research. Furthermore, depositional breaks or hiatuses, shifts of growth axis or areas in speleothems containing the highest incidence of fluid inclusions can be easily recognised petrographically.

Mineralogy (e.g. calcite or aragonite) and fabric (i.e. the nature and arrangement of the rock components) can serve as palaeoclimate proxies in their own right. For example, aragonite precipitation is often linked to higher Mg/Ca ratios in the drip water, higher cave temperatures and lower drip-water supply when compared to calcite (Frisia et al., 2002). In some samples, calcite and aragonite laminae interchange regularly which may point to regular changes in one or more environmental variables (Wassenburg et al., 2012). Some samples also exhibit changes in fabric pattern. For example, open and closed columnar fabric can occur interchangeably potentially indicating seasonal changes in recharge. A closed columnar fabric is more indicative of stable drip discharge while an open fabric indicates more variable recharge conditions (Belli et al., 2013). Fabric can also reflect changes in supersaturation. For example, large crystals indicate slightly supersaturated and stable conditions while small crystals are usually an indicator of highly supersaturated deposition conditions (Frisia et al., 2000).

2.3.2 OXYGEN ISOTOPES

The first-developed and most often used geochemical proxies in palaeoclimate research are the stable isotopes of oxygen (^{18}O and ^{16}O). Since the time of Emiliani (Emiliani, 1966) they have been used in palaeoceanographic studies. The use of oxygen isotopes in speleothem research has a similarly long history going back almost 50 years (Hendy, 1971; Hendy and Wilson, 1968) with a large number of experimental, modelling and case studies (Day and Henderson, 2011; Deininger et al., 2012; Griffiths et al., 2010a).

Variations in oxygen isotope abundances are well understood in the global hydrological cycle where, during phase changes equilibrium or kinetic processes lead to fractionation between ^{18}O and ^{16}O due to their mass difference. Fractionation causes one isotope to be favoured

over the other and this effect is expressed as the fractionation factor (α_{A-B}) (**Equation 2-2**) where R_A and R_B are isotopic ratios (i.e.$^{18}O/\ ^{16}O$) of different phases (e.g. water and vapour) (Lachniet, 2009 and references therein).

Equation 2-2. $$\alpha_{A-B} = \frac{R_A}{R_B}$$

In practice, the ratio ($\delta^{18}O$) of two stable isotopes of oxygen, ^{18}O and ^{16}O, is measured on a mass spectrometer relative to a standard. Although internal standards differ between laboratories, all results are reported in respect to VSMOW (Vienna Standard Mean Ocean Water) for water and carbonates or VPDB (Vienna Pee Dee Belemnite) for carbonates. Their $\delta^{18}O$ (and $\delta^{13}C$) are arbitrarily equal to 0.0‰ and the variation of the $\delta^{18}O$ and $\delta^{13}C$ measured in a sample is expressed as difference in respect to this value (Sharp, 2007). The results are reported in δ notation in per mil (‰) (**Equation 2-3**) where:

Equation 2-3. $$\delta^{18}O = \left(\frac{\left(\frac{O^{18}}{O^{16}}\right)_{\text{sample}} - \left(\frac{O^{18}}{O^{16}}\right)_{\text{standard}}}{\left(\frac{O^{18}}{O^{16}}\right)_{\text{standard}}} \right) * 1000$$

Fractionation also occurs during formation of speleothems between the water and calcite phase and it can be accompanied by equilibrium and kinetic processes. Equilibrium processes are dominant during speleothem formation due to slow degassing of CO_2 combined with an absence of evaporation. This will lead to fractionation between ^{18}O and ^{16}O in drip water and calcite driven only by the isotopic composition of drip water and cave temperature (McDermott, 2004).

In cases where degassing of CO_2 occurs due to, for example, decreased humidity or/and increased air ventilation in a cave chamber, kinetic fractionation effects may dominate and $\delta^{18}O$ values of the

speleothem are modified (Mickler et al., 2004a), making their use in palaeoclimate research challenging. For this reason, samples which grew close to cave entrances are rarely used in palaeoclimate research while samples from deeper chambers characterised by stable climate conditions with high humidity are usually preferred.

The traditional practice is to conduct a series of so-called “Hendy tests” (Hendy, 1971) to check for equilibrium deposition. The following criteria must be met for equilibrium deposition: 1) $\delta^{18}O$ is stable along the growth layer while $\delta^{13}C$ changes irregularly; and 2) there is no correlation between $\delta^{18}O$ and $\delta^{13}C$ along the growth axis (Hendy, 1971). However, an increasing number of studies point out that the Hendy test may ‘fail’ for multiple reasons (Dorale and Liu, 2009; Spötl and Mangini, 2002). For example, $\delta^{18}O$ and $\delta^{13}C$ may covary along a growth axis for climatic reasons (Hellstrom et al., 1998). Furthermore, sampling of single growth layers has been proven to be extremely difficult despite improvement in microsampling techniques (Drysdale et al., 2012). Another way to confirm equilibrium deposition is to collect recent calcite and compare its $\delta^{18}O$ to the drip water $\delta^{18}O$ using one of several possible equilibrium fractionation equations e.g. (Kim and O'Neil, 1997). However, this approach assumes the same conditions were valid in the past and, furthermore, there are sites where recent calcite cannot be collected. The most reliable way to check for equilibrium deposition is to replicate the record using another speleothem from the same or a neighbouring cave site. If the $\delta^{18}O$ records are similar in more than one sample, kinetic fractionation can be presumed unlikely and the record reliably used in palaeoclimate research.

Table 2-1. Environmental and climatic influences on $\delta^{18}O$ in rainwater and speleothems (Lachniet et al., 2009; McDermott, 2004)

EFFECT	***LINK TO $\delta^{18}O$***
ATMOSPHERE	
Temperature	Positive correlation between rainfall $\delta^{18}O$ and mean annual temperature
Altitude	Negative correlation between rainfall $\delta^{18}O$ and altitude of studied site (-2 to -3 ‰ $\delta^{18}O$ km^{-1})
Latitude	Decrease in $\delta^{18}O$ with distance from tropical moisture sources
Continentality	Decrease in rainfall $\delta^{18}O$ with site's distance from oceanic sources of rainfall (related to Rayleigh distillation but possibly masked by recycling of continental waters)
Amount	Negative correlation between rainfall $\delta^{18}O$ and the amount of rainfall at the studied site
Source	Changes in rainfall $\delta^{18}O$ depending on the changes in source of air masses (for example North Atlantic sourced precipitation has lower $\delta^{18}O$ than precipitation originating in the Mediterranean Sea)
Seasonality	Changes in relative proportions of summer vs winter precipitation
Ice volume	Long-term changes in ocean $\delta^{18}O$ with respect to changes in ice volume
SOIL ZONE AND EPIKARST	
Evaporation	Increase in evaporation leads to an increase in $\delta^{18}O$
Transit time and mixing	Increase in percolation time increases groundwater mixing which can lead to attenuation of climate signal
The saturation state	Only water supersaturated in $CaCO_3$ can precipitate calcite, otherwise dissolution of previously deposited calcite may occur
Prior calcite precipitation (PCP)	$\delta^{18}O$ (and $\delta^{13}C$) can increase due to precipitation of calcite before it reaches the speleothem if the speleothem is formed under kinetic fractionation conditions. The PCP can happen in the aquifer above the cave or on the cave ceiling (Fairchild et al., 2000)
CAVE CHAMBER	
High evaporation	High evaporation can be caused by low humidity and/or high air circulation. Increased evaporation will lead to increased $\delta^{18}O$ of drip water
pCO_2 gradient between drip water and cave air	
Temperature dependent fractionation	Equilibrium isotopic fractionation between drip water and calcite is temperature dependent with -0.19 to -0.24‰/°C for temperature range of 35 to 5°C (Lachniet, 2009)

Even in cases of replicated records, the interpretation of $\delta^{18}O$ in speleothems is far from straightforward. This is because the $\delta^{18}O$ of percolation water is significantly modified before being incorporated into the stalagmite via a plethora of environmental and climatic effects (

Table 2-1). Each of these modifies the $\delta^{18}O$ signal, sometimes in complex ways, and imposes significant challenges in extracting a reliable explanation. To overcome this issue there is an increasing number of cave sites worldwide where speleothem palaeoclimate studies are accompanied by studies of climate conditions above the cave, the hydrology and hydrochemistry of the aquifer, as well as cave monitoring (McDonald and Drysdale, 2007; Riechelmann et al., 2011; Tremaine et al., 2011). These studies are of paramount importance in deciphering specific local conditions, which affect the speleothem record, and in providing confidence that modern mechanisms are in some way applicable to the past.

Since drip-water - calcite fractionation is temperature-dependent, it was held that speleothem $\delta^{18}O$ could provide valuable information on mean air temperature in the past. Indeed, extracting data on the variability of past temperatures was one of the main goals at the beginning of speleothem research (Hendy, 1971). With the known water-calcite fractionation equation (Kim and O'Neil, 1997) it should be possible to calculate the cave temperature, thought to correspond to the mean annual temperature above the site. However, this has been proven difficult because of the complexities that affect $\delta^{18}O$ (Lachniet, 2009). Also, there is still debate as to which of several fractionation equations is correct since each results in different predicted temperature estimates (Coplen, 2007; Kim and O'Neil, 1997).

2.3.3 CARBON ISOTOPES

Stable carbon (C) isotope ratios ($\delta^{13}C$) are less widely used in palaeoclimate studies because of their dependence on more complex factors compared to $\delta^{18}O$. The main source of C in speleothems is soil CO_2 where the C originating from the atmosphere is significantly fractionated by photosysnthesis, and then transported to the percolation water via plant root respiration and decomposition of soil

organic matter. Another source is the host rock (limestone, dolomite). The majority of studies show that the proportion of host-rock-derived CO_2 in speleothems is 10-20% (Genty et al., 1999; Hoffmann et al., 2010; Noronha et al., 2014; Southon et al., 2012). However, the ratio of soil-sourced versus host-rock-sourced CO_2 is variable and depends on whether closed- or open-system conditions are experienced along the percolation path (McDermott et al., 2005). In an open-system, there is a constant equilibration between percolation water and an infinite reservoir of soil CO_2, and the $\delta^{13}C$ in the speleothem will reflect the carbon isotopic ratio of the soil CO_2, with a small contribution from the carbon isotope signal of the carbonate host rock. The situation is the opposite for closed-system conditions. However, in nature a mixture of closed- and open-system deposition usually occurs (McDermott et al., 2005).

Due to all the parameters involved (**Table 2-2**), $\delta^{13}C$ will be very site specific, and for reliable palaeoclimate and palaeoenvironmental interpretation of the results independent proxies have to be used in concert with $\delta^{13}C$.

Changes in the $\delta^{13}C$ of speleothems are often interpreted as a result of climate-driven changes in the type of vegetation (C3 or C4)[1] as well as the intensity of vegetation activity above the cave (Drysdale et al., 2004, 2007; Genty et al., 2001; Genty et al., 2003; Zanchetta et al., 2007). The interpretation of carbon isotopes in regions where there are switches in the proportions of C3 and C4 plants can be independently verified (e.g. from pollen data) and is relatively straightforward. However, in temperate regions where natural C4 vegetation is lacking, the interpretation remains difficult, and support from other speleothem proxies is needed (e.g. Mg/Ca ratio) (McDermott, 2004; McDermott et al., 2005).

[1] C3 and C4 types of vegetation have different photosyntetic pathways and the C4 type is more adapted to warmer and arid conditions while the C3 type prefers cool and moist climates.

Table 2-2. Environmental and climatic influences on $\delta^{13}C$ in speleothems

EFFECT	*LINK TO $\delta^{13}C$*
VEGETATION, SOIL ZONE, EPIKARST AND BADROCK	
Type of vegetation	Speleothem $\delta^{13}C$ will depend on changes in the proportion of vegetation types above the cave, where C3 (most of the Earth's plant biomass) have lower $\delta^{13}C$ than the C4 vegetation type (mostly represented by grasses) and their distribution is climate dependent (limited by temperature and precipitation) (McDermott, 2004)
Biogenic activity	Higher biogenic activity, independent of vegetation type, will lead to more negative $\delta^{13}C$
Changes in soil pCO_2	Related to changes in vegetation (C3 vs C4) but also depends on the proportion of atmospheric vs soil-derived CO_2. Increase in atmospheric proportion of CO_2 relative to soil-dervied CO_2 leads to increased $\delta^{13}C$
Changes in open vs closed system	During open-system conditions percolation water is constantly in contact with soil CO_2, while in a closed system it is isolated from it. In open-system conditions lower soil $\delta^{13}C$ will prevail, while in a closed system bedrock $\delta^{13}C$ will become more dominant. In nature, however, mixed conditions are most often encountered (Hendy, 1971)
Prior calcite precipitation	$\delta^{13}C$ can increase due to precipitation of calcite before the dripwater reaches a speleothem. This can happen in the aquifer above the cave or on the cave ceiling (Fairchild et al., 2000)
Incongruent dissolution	This effect may occur in cases where bedrock is of mixed limestone and dolomite composition. Dolomite is characterised by slower dissolution rates comparing to calcite, so changes in proportion of these two components will affect $\delta^{13}C$
CAVE CHAMBER	
Kinetic fractionation	High evaporation can be caused by low humidity and/or high air circulation. Increase in evaporation will promote kinetic fractionation and lead to increase in $\delta^{13}C$ (Mattey et al., 2010; Spötl et al., 2005)

2.3.4 TRACE ELEMENTS

Many trace elements are incorporated into speleothems during their formation. The major source of calcium and most trace elements in speleothems is the bedrock and overlying regolith, including bedrock fragments in the soil and epikarst (Fairchild and Treble, 2009). There may also be contributions from aerosols and aeolian particles as well as from anthropogenic changes in the elemental composition of the atmosphere and soil above the cave in younger samples (Borsato et al., 2007; Dredge et al., 2013). Processes involved in the transport of trace

elements from these sources and their incorporation into speleothems are diverse and complex (Fairchild et al., 2006).

Divalent trace elements (Mg^{2+}, Sr^{2+}, Ba^{2+}) are mostly transported as solutes in drip waters and they substitute for Ca^{2+} in the calcite crystal. The relation between their composition in drip water and mineral phase is defined via a *partition coefficient* **Equation 2-4**:

Equation 2-4. $$\left(\frac{Tr}{Ca}\right)_{CaCO_3} = K_{Tr} * \left(\frac{Tr}{Ca}\right)_{solution};$$

where Tr is the trace element and K_{Tr} is partition coefficient for the same trace element. Partition coefficients have been experimentally determined (Day and Henderson, 2013; Huang and Fairchild, 2001) and, for a single trace element, they tend to be dependent on a different suite of factors: temperature, growth rate, crystal morphology, mineral phase (K_{Tr} for the same Tr in aragonite and calcite differs), and water residence time (Fairchild and Treble, 2009). For example, it is believed that the Mg partition coefficient (Mg_{Tr}) is mostly hydrologically dependent and that Sr_{Tr} is more related to growth rate (Treble et al., 2005). The latest laboratory experiments, however, indicate there is no correlation between Sr_{Tr} and growth rate (Day and Henderson, 2013).

Divalent trace elements may be also incorporated into speleothems as solids or in the colloidal phase, although these mechanisms are more common for less mobile elements such as Pb, Al, Fe, Zn, and Y (Hartland et al., 2012). Colloidal and particulate transport can be enhanced during wetter periods when weathering of overlying soil and regolith is pronounced and water infiltration increased. The majority of analytical techniques, however, measure bulk trace element compositions (Borsato et al., 2007) and thus to distinguish between different modes of transport and origin special separation techniques must be employed (Hartland et al., 2012).

Despite these complexities, trace elements may be linked to many climate and environmental variables and their use for this purpose has rapidly increased in recent years (Griffiths et al., 2010a; Wassenburg et al., 2012). They are used as a proxy in palaeohydrology but they can also be used to determine atmospheric circulation patterns (Ayalon et al., 1999; Goede et al., 1998). Although initial studies argued that Mg could be used as a proxy for temperature because of its temperature dependent partition (Gascoyne, 1992), subsequent studies on drip water as well as on spelethems (Fairchild et al., 2001; McDonald et al., 2004; Treble et al., 2003; 2005) indicate that Mg in speleothems is driven more by palaeohydrology and reflects water residence time- where an increase in Mg usually corresponds to a decrease in rainfall which consequently causes longer residence time. Simultaneous increases in Mg, Sr and/or $\delta^{13}C$ are interpreted as a sign of prior calcite precipitation (PCP). This means that degassing of CO_2 and precipitation of calcite from percolation water has occurred 'upstream' in the aquifer before reaching the cave chamber due to a longer residence time caused by lower rainfall (Fairchild et al., 2000). Cave monitoring studies of drip water and farmed calcite however suggest that in order to interpret speleothem Mg/Ca and Sr/Ca in terms of wet versus dry periods, Sr/Ca and Mg/Ca variations must be coherent and in phase over all time periods i.e. Sr/Mg ratio must be constant at all times (Tremaine and Froelich, 2013).

Most speleothem trace-element studies have focused on recent climatic periods e.g. (Borsato et al., 2007; McMillan et al., 2005; Treble et al., 2003). Often, such studies have been conducted in parallel with drip-water monitoring studies, the results of which are compared with instrumental climate data to determine the nature of the climate-cave response at a particular site (e.g. McDonald et al., 2004). Parallel trace element studies of overlying soil and bedrock are also advisable to distinguish between local and regional effects on trace element composition in speleothems.

2.4 RADIOMETRIC DATING OF SPELEOTHEMS

The greatest strength of speleothems, compared to other palaeoclimate archives, is their ability to be precisely and accurately dated by radiometric methods (Richards and Dorale, 2003). The first dating of speleothems was accomplished using radiocarbonmin the 1960s (Broecker et al., 1960) but later development of alpha spectrometry, thermal ionisation mass spectrometry (TIMS) (Li et al., 1989) and multi-collector inductively coupled plasma mass spectrometry (MC-ICPMS) (Hellstrom, 2003) put the U-Th method at the forefront of speleothem research.

Relatively recently it has been shown that the U-Pb method, usually applied to resistant minerals such as zircons, can also be used for dating speleothems (Richards et al., 1998; Woodhead et al., 2006). This method has been greatly improved in recent years, particularly in regards to screening procedures for sample selection, chemical separation, and sample-size requirements due to the advent of the multi-collector inductively coupled mass spectrometry (MC-ICP-MS) method for performing the isotopic measurements (Woodhead et al., 2006; 2012).

2.4.1 RADIOCARBON (^{14}C) DATING METHOD

^{14}C was the first method used to date speleothems (Broecker, 1960) but after the development of the more flexible U-Th dating method it became less attractive. Radiocarbon (^{14}C) is produced in the upper atmosphere by the bombardment of nitrogen nuclei by cosmic-ray neutrons. It is then incorporated into the biosphere through the process of photosynthesis and, after the death of an organism, ^{14}C concentrations decrease exponentially following the law of radioactive decay. From the ^{14}C concentrations at the time of measurement and the known half-life one can calculate the age of the sample. Due to the relatively short half-

life of ^{14}C (5730 years) the dating range of this method is limited to the last ~50 kyr (Bard et al., 2004).

During its growth, speleothem calcite captures ^{14}C derived from the atmosphere (usually via the soil) which enables speleothems to be dated. However, there are two general problems with this method, namely the difference between atmospheric radiocarbon and radiocarbon present in speleothems due to the incorporation of dead carbon from ancient limestone bedrock (specific to most secondary carbonates), and uncertainty over the history of atmospheric radiocarbon variations (which affects all ^{14}C recorders):Noronha et al., 2014. Conversion of radiocarbon chronologies to calendar ages can be made using calibration curves that describe changes in atmospheric ^{14}C activity based on independently derived data, especially tree rings (Hua et al., 2009; Reimer et al., 2013).

Speleothems are recognized as a potentially useful tool in the determination of atmospheric ^{14}C activity variations through time and thus in improving ^{14}C calibration curves. This is because they can be dated independently by U-series methods (Hoffmann et al., 2010; Noronha et al., 2014). Using this approach on submerged speleothems from the Bahamas, a ^{14}C calibration curve was proposed for the period spanning 28-44 ka BP (Beck et al., 2001). The results showed extremely large oscillations in atmospheric ^{14}C concentrations, but this has since been attributed to a previously unrecognized ^{14}C blank effect. A new study of speleothems from the same cave (Hoffmann et al., 2010) provided a revised comparison curve that fits much better with existing calibrations (Reimer et al., 2013).

The biggest problem of using speleothems as ^{14}C calibration curves is the dead carbon proportion (DCP) that is incorporated into speleothems from the overlying bedrock and, to a lesser extent, soil organic matter. DCP can be estimated successfully in young speleothems using the immediate pre-bomb atmospheric ^{14}C activity, enabling a relatively precise radiocarbon chronology to be obtained

(Genty and Massault, 1999; Hodge et al., 2011; Hua et al., 2012). There are also examples where $^{87}Sr/^{86}Sr$ was used together with DCP to distinguish the contributions of soil and bedrock (Oster et al., 2010) or where DCP has been used as a hydrological proxy (Griffiths et al., 2012; Noronha et al., 2014).

2.4.2 U-Th DATING METHOD

U-Th dating is the most often used method for dating speleothems and is a generally reliable chronometer for samples old up to ~800 000 yr (Cheng et al., 2013). Parent isotopes of U (^{238}U, ^{235}U) are fractionated in groundwater from their long-lived daughter isotopes of ^{230}Th and ^{231}Pa due to their different chemical properties (low solubility of Th in natural waters) and this fractionation forms the basis of the U-Th technique (Richards and Dorale, 2003). When speleothems form the U-Th decay scheme is thus in a state of isotopic disequilibrium. As soon as the system becomes closed, radioactive decay of U to Th (and ultimately to stable Pb) changes the parent/daughter nuclide ratios and thus, as long as the system remains closed with respect to the migration of these nuclides, dating will be possible up to the point where a state of secular equilibrium between U and Th is re-established. Secular equilibrium means that the activity of the daughter is the same as the activity of the parent, and this occurs after ~7 half-lives of ^{230}Th. At this point, the upper limit of the dating method will be reached. In ideal cases where the stalagmite is free of initial Th contamination, the age of the sample can be calculated from known decay constants for ^{234}U and ^{230}Th (Cheng et al., 2013) and from measured $^{230}Th/^{238}U$ and $^{234}U/^{238}U$ ratios (Hellstrom, 2003).

Knowledge of the initial $^{234}U/^{238}U$ ratio is required because these two nuclides are also prone to fractionation. This is mostly as a result of preferential leaching of ^{234}U from the crystal lattice compared to ^{238}U, which will lead to the initial $^{234}U/^{238}U$ being higher than 1 in many

groundwaters (Richards and Dorale, 2003). Initial $^{234}U/^{238}U$ ratios fractionated in the opposite sense are also known (e.g. Corchia Cave speleothems).

For the majority of speleothems the contribution of non-radiogenic Th is significant, and additional corrections must be made to the age calculations to incorporate this effect (Hellstrom, 2006): this represents the most significant limitation of the method. Usually, during isotopic measurements, the $^{230}Th/^{232}Th$ ratio is determined as a means of screening the purity of the sample. ^{232}Th is not a part of the ^{238}U-^{234}U-^{230}Th decay scheme used in U-Th dating, and its presence, quantified by the $^{230}Th/^{232}Th$ ratio, provides an indication of the degree to which a sample is contaminated by detrital Th. Corrections for initial Th composition are usually performed using an isochron method, *a priori* assumptions about the composition of the contaminating phase, or using stratigraphic constraint approach (Hellstrom, 2006).

2.4.3 U-PB DATING METHOD

The U-Pb dating method is an extension of the U-series decay chain and it uses the ingrowth of stable ^{206}Pb and ^{207}Pb that are the ultimate daughter isotopes formed by decay of their parent isotopes ^{238}U and ^{235}U via a number of intermediate radioisotopes. Because of the very long half-life of the parent isotope, this method offers the possibility to date the oldest rocks on Earth but, at the same time, it is challenging to date young rocks since they possess very low amounts of radiogenic Pb.

Certain conditions must be fulfilled for the successful dating of speleothems by U-Pb (Woodhead and Pickering, 2012). First, samples should possess sufficient U (i.e. concentrations >1 ppm are preferred) and a low content of initial/common Pb (in the low ppb range). Furthermore, the initial Pb composition should be homogeneous throughout the dated layers and, furthermore, there should be a spread in U-Pb ratios along the single growth layers to be dated. Preliminary

information about U and/or Pb content is usually obtained by using phosphor imaging (Pickering et al., 2010) or by laser ablation trace element analyses (Woodhead et al., 2012). Phosphor imaging gives relative information on U concentration in the sample only, while the LA method is superior in providing information not only on concentrations of U and Pb but also those of many other trace elements. This has been shown to be a useful tool in deciphering whether speleothems have single or multiple sources and/or transport mechanisms of common Pb, based on the correlation between Pb and other elements, with Y being particularly useful (Woodhead et al, 2012). This is an important consideration because multiple sources of common Pb will result in poor chronology constraints. Additionally, knowing the amount of U and Pb in the speleothem prior to dating facilitates optimal spiking.

Speleothems usually contain ppm levels of U and low ppb levels of Pb. This is because U is highly soluble in natural waters and it is relatively easily incorporated into the crystal lattice of calcite. In contrast, Pb is almost insoluble in natural waters, and in ideal cases all Pb measured in speleothems should originate from the radioactive decay of U (Woodhead et al., 2006). However, Pb is adsorbed on and transported in detrital phases that accumulate in speleothems (clays, airborn dust...) or complexed with Fe and Mg oxides (Borsato et al., 2007) as well as in colloidal phases (Fairchild and Treble, 2009; Hartland et al., 2012).

For successful dating it is crucial to distinguish between radiogenic Pb (originated by *in situ* radioactive decay of U) and common Pb (incorporated into the speleothem at the moment of its formation). This is achieved by constructing U-Pb isochrons. Here, several coeval samples (usually 6-10 subsamples) are collected from the stalagmite and are analysed separately. Isotopic data are usually presented graphically using concordia plots. The most useful of these for young samples, or those with a substantial common Pb component, is the so-called Tera-Waserburg isochron diagram which plots $^{238}U/^{206}Pb$ vs

$^{207}Pb/^{206}Pb$ ratio (Tera and Waserburg, 1972). U and Pb measured from coeval samples will have different $^{238}U/^{206}Pb$ ratios and should lie on a straight line defining radiogenic and common Pb components. The initial Pb component can be calculated from the intercept of the regression line and the *y*-axis ($^{207}Pb/^{206}Pb_i$) while the age of the sample is calculated mathematically from the intersection of the isochron with the Concordia curve, the locus of all purely radiogenic Pbs (Woodhead et al., 2006).

Furthermore, to successfully date speleothems it is critical that the calcite has not undergone recrystallization since formation as this would breach the prerequisite condition of closed-system behaviour (Richards and Dorale, 2003). If recrystalization was isochemical or occurred soon after formation of the speleothem then the U-Pb systematics would not be adversely affected and dating might still be possible.

If the initial Pb was homogeneous and the system has remained closed, all the scatter of measured values around the regression line in the Tera-Waserburg plot will only depend on the analytical uncertainties. This scatter is reflected in the so-called mean-squared weighted deviates (MSWD), with values of 1 or lower. In cases when the MSWD is significantly higher than 1 it could indicate that one or more of the preconditions have been breached (i.e. heterogeneous initial Pb or/and recrystalization).

An additional important issue in the U-Pb dating of speleothems younger than a few million years is related to the fact that speleothems precipitate out of secular equilibrium with respect to uranium isotopes (Richards and Dorale, 2003). This means that the $^{234}U/^{238}U$ activity ratio is not equal to 1 and indeed in the majority of cases the ratio is higher than 1 due to alpha recoil and preferential leaching of ^{234}U compared to ^{238}U, as stated above. In this case, there is also an unknown amount of the intermediate radioisotope ^{234}U in the percolation water, which, after incorporation into the speleothem

calcite, also decays to ^{206}Pb and hence influences the final result producing an apparent age that is older than the true age of the sample. In contrast, initial $^{234}U/^{238}U$ ratios lower than 1 will result in younger ages. For this reason, it is essential to measure or assume $^{234}U/^{238}U$ values and then to apply a correction for each U-Pb age determination (Richards et al., 1998; Woodhead et al., 2006).

Woodhead et al. (2006; 2012) suggested that in the case of uniform common Pb compositions in a whole speleothem, it should be possible to use single-aliquot ages instead of the more laborious and time-consuming isochron method. In principle, several isochron measurements determined in one or more speleothems from the same site are used to estimate an overall common Pb composition. If this value is homogeneous then it can be used to constrain the ages of more numerous single-point analyses along the growth axis. The method is very powerful for developing precise age-depth models due to the potential for a high density of ages, and indeed this PhD thesis is the first study where this approach will be applied and tested.

2.4.4 AGE-DEPTH MODELS

One particularly important approach in dating of speleothems concerns the derivation of reliable age models. An age model mathematically describes the relationship between the distance and age along a stalagmite (Scholz and Hoffmann, 2011). This is an important issue: in palaeoclimatology, in combination with isotope measurement accuracy, age-model precision governs the specific palaeoclimate questions that speleothem studies can address. One possible solution for constructing an age-model from U-Pb data is to use a Monte-Carlo finite positive growth-rate model (Drysdale et al., 2005; Hendy et al., 2012; Scholz et al., 2012). In this model, for each iteration of the Monte-Carlo simulation all dates are randomised with respect to their uncertainties and a least-square fit is obtained for a series of line segments for which

growth rate is always finite and positive. An additional weighting to minimise the variation between segments is also performed. Finally, the median value and its 2σ and 1σ uncertainty are determined.

2.5 QUATERNARY GLACIAL-INTERGLACIAL CYCLES AND THE LINK TO ORBITAL FORCING

The climate of the Quaternary (the last ~2.6 Ma of Earth history) is characterized by regular climate shifts from glacial (cold) to interglacial (warm) states and back again, also known as terminations and glacial inceptions respectively. These are spatially and temporally the largest climate cycles currently observed on Earth. Terminations, the principal focus of this thesis, are the most-pronounced and most-often-studied large-scale climate shifts, and are recognised in a restricted range of geological archives: deep-sea sediments, Antarctic and Greenland ice cores, lake sediments and speleothems (Drysdale et al., 2009; Elderfield et al., 2012; Huber et al., 2010; Jouzel et al., 2007). However, the major source of data recording glacial-interglacial cycles lies in benthic foraminifer $\delta^{18}O$ values from deep-sea cores (Lisiecki and Raymo, 2005). Glacial states are characterized by an increased ratio of ^{18}O to ^{16}O in seawater and the foraminifera growing therein because during glacial/cold conditions more of the lighter ^{16}O isotope evaporates preferentially and it is locked up in large continental ice sheets. During deglaciation, when melting of ice sheets is promoted, this excess ^{16}O is returned to seawater, causing the ^{18}O to ^{16}O ratio in benthic foraminifera to decrease. The $\delta^{18}O$ values of these single-celled protists therefore act as a reliable proxy for global ice-volume changes. There is also a deep-ocean temperature component to $\delta^{18}O$ variations (Siddall et al., 2010a), which has been recently successfully deconvolved (Elderfield et al., 2012). Glacial terminations may also be recorded indirectly in isotope data from other archives, e.g. speleothems (Cheng et al., 2009; Drysdale et al., 2009).

Long-term glacial-interglacial variability is currently best represented by a globally distributed benthic $\delta^{18}O$ record extending back to 5.3 Ma called the *LR04 stack* (**Figure 2-2**) (Lisiecki and Raymo, 2005). The LR04 stack is based on benthic foraminifer $\delta^{18}O$ records from 57 deep-sea cores from all the major ocean basins and is used as a reference record of global ice-volume changes. This stack clearly displays some characteristics of palaeoclimate changes on orbital time scales. For example, one can see:

- The onset of North Hemisphere glaciations and the overall cooling trend from ~2.8 Ma to the present;
- Rapid shifts from extreme glacial to extreme interglacial conditions (terminations), and less dramatic changes from interglacials to glacial periods. The asymmetry of glacial-interglacial cycles is more pronounced during the last ~600 ka when glaciations lasted on average ~90,000 and deglaciation events just ~10,000 years.
- Glacial-interglacial cycles from 2.8-~1.2 Ma have a periodicity of around 41,000 years, then after ~700 ka the frequency shifted to ~100,000 years. The transition period between these two states lasted from ~1.2 Ma to ~0.7 Ma and is called the *Middle Pleistocene Transition (MPT).*
- The amplitude of glaciations/deglaciations has increased during the last ~600ka

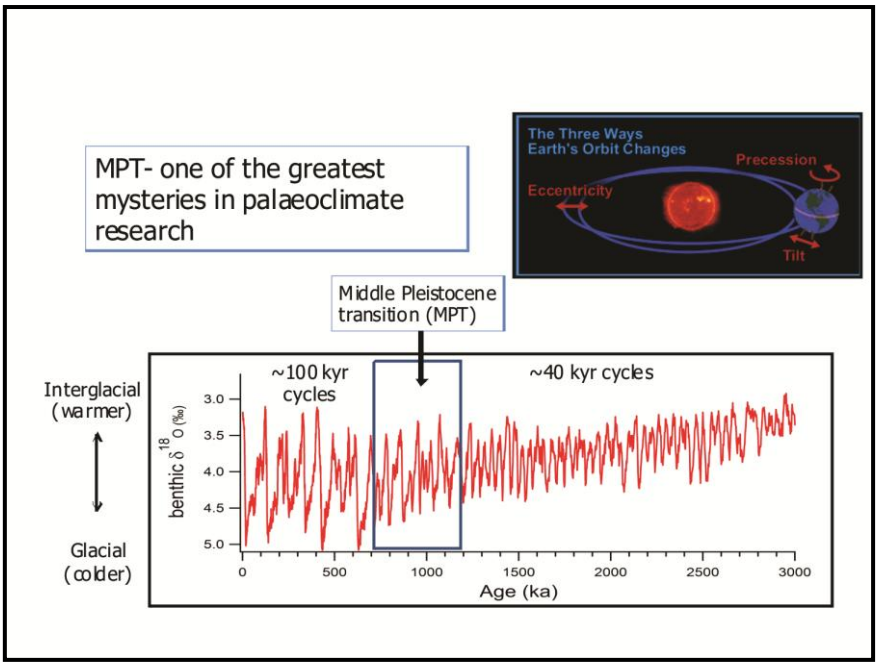

Figure 2-2. Orbital parameters discussed in the text and climate changes recorded in benthic $\delta^{18}O$ data for global LR04 stack during the last 3 Ma.

The majority of scientists today agree that long-term variations in climate occur due to changes in insolation, which are in turn caused by quasi-periodic oscillations of the Earth's three main orbital parameters: precession, obliquity and eccentricity (Cronin, 2010 and references therein).

Precession is a measure of changes in the timing of perihelion, i.e. the time in a year when the Earth is closest to the Sun. It is divided into two parts: precession of the equinoxes (axial) and elliptical precession, and is characterized by ~21,000 year cycles. Precession influences the intensity of summer insolation, and has its strongest climatic effect in the low latitudes. For this reason, its influence is most easily recognized in tropical and subtropical palaeoclimate records (Cronin, 2010 and references therein).

Obliquity is the tilt of Earth's rotational axis with respect to the ecliptic plane. One obliquity cycle lasts 41,000 years. This tilt is responsible for the seasons observed on Earth and its influence is more remarkable in higher latitudes. Obliquity-forced insolation changes are

symmetric but anti-phased in Northern and Southern Hemispheres (Cronin, 2010 and references therein).

Eccentricity is the extent to which the Earth's orbit around the Sun deviates from a circle. It oscillates at periods of 100,000 and 405,000 years and it is the only orbital parameter that causes changes in the total amount of insolation that reaches the Earth. However, the changes are so minor that it is generally agreed that it cannot directly cause glacial-interglacial transitions (Cronin, 2010 and references therein). However, eccentricity modulates the variations in insolation caused by precession and obliquity, and thus may significantly affect climate (Lisiecki, 2010; Raymo et al., 1997).

Retrospective changes in orbital parameters and thus insolation can be calculated using analytical and trigonometrical solutions based on the gravitational attractions of the Earth, the Moon and other planets in Solar system (Berger and Loutre, 1991). Because all three parameters occur simultaneously and modulate each other, the insolation response is not a simple sinusoidal curve.

Although variations in past insolation can be determined from astronomical calculations, there is no unique explanation for which of the orbital parameters or combination of them is responsible for all characteristics of climate changes recorded in palaeoclimate proxies (**Figure 2-2**). The ability to answer this question is further complicated by complex positive and negative feedbacks internal to the climate system (e.g. CO_2, albedo, vegetation, thermohaline circulation). Currently there are many (more than 30) competing theories that have been proposed to explain different aspects of the orbital forcing of glacial-interglacial transitions (Huybers and Wunsch, 2005). Generally, most of these theories can be divided in two groups which hold that glacial-interglacial transitions are caused by:

- precession or eccentricity modulation of precession;
- obliquity or some combination of obliquity and precession

Glacial-interglacial cycles were recognised in marine sediments for the first time in 1970s (Hays et al., 1976) but Louis Agassiz had already described evidence of multiple episodes of continental ice-sheet growth in Europe in the first half of 19th century. Soon after, Adhemar (1842) proposed that changes in the Earth's orbital parameters were responsible for these climate shifts whilst Croll was the first to point to the role of eccentricity and precession of the equinoxes in leading to these climate changes (Imbrie and Imbrie, 1979). In the middle of the 20th century Milankovitch was the first to mathematically describe insolation changes for different latitudes and months in a year and their influence on climate and ice sheets. He proposed that glaciations occur when the tilt is small and when aphelion coincides with Northern Hemisphere summer. He argued that Northern Hemisphere low summer insolation intensities (resulting from precession) are crucial for the onset of glaciations because snow from the previous season does not have the chance to melt. This in turn increases albedo for the next season and causes further cooling (Cronin, 2010 and references therein). Hence, higher summer insolation intensities will have an opposite effect, i.e. a termination will occur. Milankovitch theory, however, does not explain the existence of 41 000 years cycles from the Early and Middle Pleistocene nor the transition from the 41-kyr to 100-kyr world.

Raymo et al. (2006) offered support for Milankovitch theory, arguing that precession is the main orbital parameter in controlling Northern Hemisphere ice ages. They explain that the absence of a strong precession signal in the benthic $\delta^{18}O$ of marine records prior to the MPT (when the obliquity frequency of 41,000 years is dominant) is the result of the "cancelling-out" of the precession signal in global proxies because precession is out of phase in the Northern and Southern Hemispheres i.e., Northern Hemisphere summer insolation maximum occurs simultaneously with Southern Hemisphere summer minimum insolation (Raymo et al., 2006).

An opposing set of hypotheses (Huybers, 2006; Huybers and Wunsch, 2005) finds its support in the fact that summers with the greatest insolation intensity (at perihelion) are also about a week shorter than the average duration of summer because, for the hemisphere at perihelion, the Earth passes through its summer part of the annual cycle more quickly. Huybers (2006) argues that ice-sheet growth and decay are better gauged by total summer energy which varies at the obliquity frequency, which is consistent with glacial-interglacial cycles prior to the MPT. He showed that terminations occurred every obliquity cycle prior to the MPT then every 2 or 3 cycles in the Late Pleistocene. Regarding the latter, he argues that the ~100-kyr cycles of the Late Pleistocene are actually of either ~80-kyr or 120-kyr duration, and that the 100,000 period is the average length of Late Pleistocene cycles.

More recently, however, Huybers has suggested that a combination of obliquity and precession is responsible for Late Pleistocene terminations where precession tends to influence the precise timing of a termination within an obliquity cycle, but that obliquity will more fundamentally govern the interval between terminations (Huybers, 2011). Although this new perspective supports Milankovitch theory, Huybers holds that there is no exclusive influence of one Hemisphere on terminations.

The problem with this and other proposed hypotheses is that none of them is entirely capable of explaining the complete pattern of glacial-interglacial transitions. For example, a recent modelling study offers an explanation for 100-kyr cycles but it does not explain the Middle Pleistocene Transition (Abe-Ouchi et al., 2013). This study suggests that the interplay of insolation, atmosphere and lithosphere are drivers of glacial-interglacial cycles and emphasize the role of the unique geographical and climatological setting of the North American continent.

Although terminations are best recorded in benthic $\delta^{18}O$ records, the problem of using this proxy to test orbital theories of the timing of terminations is in difficulties in producing high resolution and accurate chronologies for them. One approach used by palaeoceanographers to circumvent this problem is orbital tuning, which is based on the assumption that cyclic variations in benthic $\delta^{18}O$ match with changes in insolation (Imbrie et al., 1984; Shackleton et al., 1990; Lisiecki and Raymo, 2005). Unfortunately this then adds an element of circularity into the proxy record and is known as the "circular tuning problem" because the record is not free from the assumptions about the orbital theory that it is trying to test (Crucifix, 2008).

Another precious source of climate proxy records is ice cores. However, these are largely limited to polar areas. A problem directly related to this PhD project is that currently there is no ice-core record older than 800,000 years although there are plans to drill new 1 Ma+ cores from Antarctica in the coming years (Fischer et al., 2013; Jouzel and Masson-Delmotte, 2010).

2.6 THE MIDDLE PLEISTOCENE TRANSITION (MPT)

2.6.1 DEFINITION AND DURATION

The *Middle Pleistocene Transition (MPT)* (Pisias and Moore Jr, 1981) *or Middle Pleistocene Revolution (MPR)* (Maslin and Ridgwell, 2005) is one of the major climate transitions in the Quaternary and represents a shift from 41-kyr to quasi-100-kyr glacial-interglacial cycles. Together with the change in periodicity, the amplitude of these cycles also changed with post-MPT glacial-interglacial cycles being more pronounced than those before the MPT, mostly due to the increased severity of post-MPT glaciations. While glacial-interglacial cycles before the MPT are symmetric with no significant difference in the duration of glacial and interglacial periods, the 100-kyr cycles are asymmetric with

a longer build up of larger ice masses during glacials and sudden, rapid melting during glacial-interglacial transitions (Head et al., 2008). The MPT is a time period characterised by pronounced global climate reorganization which was reflected in great changes in ocean and atmospheric circulation, ice-sheet distribution as well as evolution of biota coinciding with one of the largest extinctions of deep sea foraminifera species (Hayward et al., 2007; Head and Gibbard, 2005; Kawagata et al., 2005).

Despite being investigated for more than thirty years there is still no consensus on the duration of the MPT. For example, the MPT onset and duration has been suggested as from 1.1-0.4 Ma (Ruddiman et al., 1986); 1.25 to 0.7 Ma (Clark et al., 2006) or 1.2-0.5 Ma (Head and Gibbard, 2005). Mudelsee and Schulz (1997) even distinguished two phases in the MPT; the first one related to an increase in ice volume at ~922 kyr, and the second one marked by the switch to 100-kyr cycles which is delayed and started only at ~641 kyr.

Uncertainties concerning the onset and duration of the MPT are not surprising since these studies are based on different marine records and each of them registers this climate transition in a different way. Any global signal in benthic records on which the timing is based can be obscured by regional and local changes in deep water temperature and/or hydrographic effects due to changes in the T- $\delta^{18}O$ signature of deep-water bathing the core sites (Clark et al., 2006). The stacked LR04 record is usually used to overcome this issue (Lisiecki and Raymo, 2005) although some newer studies question its global significance because the deep- water temperature component of this record (which is a local rather than a global signal) may approach as much as 50% of the range in $\delta^{18}O$ of calcite (Elderfield et al., 2012). These authors also claim that the LR04 is biased towards North Atlantic conditions.

2.6.2 RECORDS OF THE MPT

Marine cores covering the time period of the MPT have been studied intensively in order to unravel the timing, causes, and climate conditions prevalent at this time at different sites around the globe. However, the number of records from this time period is significantly smaller than is the case for late Quaternary ice ages (i.e. last ~400 kyr). This especially holds for terrestrial records where the MPT is recorded only in few low resolution records, mostly loess and pollen sequences (Sun et al., 2006; Tzedakis et al., 2006). The challenges of exploring climate changes in this time interval are not only related to the availability of records but also to their lower resolution and relatively poor age control which together leads to significant shortcomings concerning their use in testing orbital theories.

Undoubtedly, records of the MPT from all around the world point to large environmental and climate changes during this time period. Sea-surface temperature (SST) records from 16 sites worldwide (McClymont et al., 2013) reveal long-term cooling in the early Pleistocene which intensifies from 1.2-0.9 Ma. The most extensive cooling happened from Marine Isotope Stages (MIS) 24-22 and it is often called as “900-ka event” (Clark et al., 2006). At this time period, both glacial and interglacial SSTs were decreasing. The study of McClaymont et al. (2013) also notes that cooling in SSTs predates the decrease in the benthic $\delta^{18}O$ ice-volume proxy, although the trend is the opposite in the North Atlantic.

MIS 24 and 22 are also related to the first major expansion of polar ice sheets (Elderfield et al., 2012; Head and Gibbard, 2005) and are associated with a strong reduction in the North Atlantic glacial thermohaline circulation (Venz et al., 1999). The expansion of sea ice in the Arctic Ocean during this time period has also been suggested based on the gradual decrease in foraminiferal assemblages and changes in lithological proxies (Polyak et al., 2013).

Expansion of the Southern Ocean Polar Frontal Zone was recorded at the onset of the MPT (Diekmann and Kuhn, 2002; Kemp et al., 2010; Marino et al., 2009; Rodríguez-Sanz et al., 2012) when polar cooling caused strengthening of meridional SST gradients (McClymont et al., 2013).

Data from the loess plateau in China during the MPT revealed intensification of winter monsoon variations and weakening of the summer monsoon (Sun et al., 2006). Strengthening of the winter monsoon has been recorded in marine cores from the South China Sea as well (Jin and Jian, 2013). During the MPT global aridity had increased, especially at ~0.9 Ma, during MIS 22 (Raymo et al., 1997). For example, aridity over the African continent increased (Malaizé et al., 2012) during MIS 22 and has been directly linked to the increase in dust supply to the South Atlantic Ocean (Martínez-Garcia et al., 2011). Increased aridity was followed by an increase in loess deposition in Europe (Dodonov, 2005), pointing to the severity of the climate at this time, an observation additionally supported by pollen records from Greece (Tzedakis et al., 2006). Furthermore, one the largest IRD events in the North Atlantic in the last 1Ma at site ODP 982 happened at 920 kyr during MIS 22 (Venz et al., 1999). The pollen record from the Western Mediterranean (ODP site 976) revealed precession and obliquity cycles in climatically mediated vegetation successions at this site (Joannin et al., 2011). This record also implies warmer and wetter interglacials and colder/drier glacials at the time of deposition (MIS 31-MIS 23) compared to today's climate conditions.

2.6.3 WHY DID IT HAPPEN?

The MPT is one of the most puzzling climate transitions in Earth's recent climate history and the causes for its occurrence are still debated (Raymo and Huybers, 2008). There are two schools of thought. The first is based on the observation that during the MPT no change in orbital

forcing parameters occurred (Berger and Loutre, 1992; Pisias and Moore Jr, 1981), which suggests a role for internal climate feedbacks. The range of possible feedbacks, as well as the proposed hypotheses to explain them, is wide:

- A drop in atmospheric CO_2 (Paillard, 1998; Raymo et al., 2006; Raymo et al., 1997);
- erosion of regolith which led to an increase in ice-sheet stability and duration (Clark et al., 2006; Clark and Pollard, 1998);
- a drop in sea-surface (McClymont et al., 2013) and deep-ocean temperatures (Sosdian and Rosenthal, 2009);
- an increase in sea-ice cover and changes in ice-sheet dynamics (Gildor and Tziperman, 2001; Raymo et al., 2006; Tziperman and Gildor, 2003);
- increase in Antarctic ice volume (Elderfield et al., 2012);
- changes in ocean thermohaline circulation (THC) based on benthic $\delta^{13}C$ (Raymo et al., 1990; 2004). This hypothesis is furthermore supported by Nd isotopes which identify a weakening in THC during the post-MPT glacials (Pena and Goldstein, 2014).

The second group of hypotheses holds that the reason for the MPT lies purely in orbital forcing and that no internal feedbacks are required to explain it (Huybers, 2007, 2009; Lisiecki, 2010b). For example, recent modelling study reports orbitally caused switch from 40-kyr to 100-kyr cycles at around 1 Ma without any change in model parameters implying that feedback mechanisms are not needed to explain the MPT (Imbrie et al., 2011).

While the majority of proxy studies link the MPT to increased severity of Northern Hemisphere glaciations (Clark et al., 2006), a new study from the Southern Hemisphere points to the increase of Antarctic ice volume as a cause for decreased $\delta^{18}O$ in global benthic record (Elderfield et al., 2012) and sheds new light on an inter-hemispheric role for this transition. Raymo et al. (2006) offered an explanation for

the MPT, proposing that long-term cooling, through changes from a land-based to a marine-based East Antarctic ice sheet at ~1 Ma, was responsible. Ice volumes thus increased in both hemispheres because of the establishment of positive globally synchronous feedbacks (albedo and CO_2) at the precession frequency (Raymo et al., 2006). However, Hönisch et al. (2009) concluded that a slight decrease in atmospheric pCO_2 occurred only during glacials (~30 µatm) but interglacial values remained unchanged before and after the MPT. This led them to conclude that a fall in CO_2 cannot be used as a main driver of the MPT (Hönisch et al., 2009).

2.6.4 WAS IT AN ABRUPT OR GRADUAL SHIFT?

The Elderfield et al. (2012) study of a marine core from the SW Pacific shows that the MPT was an abrupt reorganisation of the climate system. This is opposite to the majority of earlier studies that invoke a long-term trend towards increased ice volume and colder temperatures (Clark et al., 2006). This is one of the rare studies where the deep-ocean temperature effect on the benthic $\delta^{18}O$ signal has been decoupled from the ice-volume effect by measuring the Mg/Ca on the same benthic foraminifera. This study also points to MIS 22 as a major event during the MPT. Before MIS 22, sea-level low stands during glaciations were ~70 m below present but during MIS 22 sea level dropped to ~-120 m for the first time (equivalent to levels during the Last Glacial Maximum), which caused exposure of the shelf break and upper slope deposits. On the other hand, studies from other sites suggest that the MPT was a gradual change (Huybers, 2007). For example, SST studies of marine cores from all major ocean basins show that the MPT was a gradual change (McClymont et al., 2013) as well as results from a study in the South China sea (Jin and Jian, 2013).

2.6.5 MILLENNIAL-SCALE CLIMATE OSCILLATIONS AND SAPROPELS DURING THE MPT

Studies of millennial-scale climate oscillations during the MPT suggest that these climate changes are not only limited to the Late Quaternary (Siddall et al., 2010b).

Hernández-Almeida et al. (2012) document millennial-scale climate oscillations in marine sediments sampled from the Gardar Drift in the North Atlantic. Their results support the occurrence of precession harmonics in this record before the MPT, marked by several IRD events, the largest of which happened during the MIS 26-25 transition. This time interval signals the transition from the 40-kyr to the 100-kyr world (Hernández-Almeida et al., 2012). Millennial-scale instabilities during the MPT are also recorded in the subtropical Atlantic (Weirauch et al., 2008), as well as in changes in deep-water ventilation in the North Atlantic based on $\delta^{13}C$ data (Kleiven et al., 2003). Interpretation for millennial-scale climate oscillations during the MPT involves insolation forcing at low-latitudes, which is then transported to high latitudes by ocean-atmospheric circulation processes (Ferretti et al., 2010; Hernández-Almeida et al., 2012; Weirauch et al., 2008).

Similar to findings of millennial-scale climate variations, previous studies have revealed that sapropel events in the Mediterranean basin also occurred during the MPT (Rossignol-Strick, 1985; Rossignol-Strick and Paterne, 1999). Sapropels are organic-rich, sediment layers deposited as a consequence of marine anoxic conditions. They are well known and described in many marine cores in the eastern Mediterranean (Capozzi et al., 2006; Emeis et al., 1998; Kroon et al., 1998; Mangini and Schlosser, 1986) and 'sapropel events' are recorded in speleothems from cave sites surrounding the Mediterranean (Bar-Matthews et al., 2000; Zanchetta et al., 2007). There are only a few cores covering the time period of the MPT in the Mediterranean and they indicate that sapropels occurred during the MPT as well. For

example, a sapropel event linked to the insolation maxima at ~955 ka was registered during MIS 25 in the Mediterranean (Lourens, 2004). Additionally, Incarbona et al. (2013), in a core from the Ionian Sea, recorded a peak in the foraminifer species *G. quadrilobatus* at ~940 ka which implies warm surface waters with relatively low salinity conditions, and indicates sapropel deposition at this time in the Mediterranean.

Chapter 3

3 STUDY SITE

3.1 LOCATION

Corchia Cave is located on Monte Corchia, which is part of the Alpi Apuane (Apuan Alps) in northern Tuscany (Italy) (**Figure 3-1**). The cave has been explored intensively since its discovery in the middle 19th century and yet, despite this, new passages are still awaiting exploration. At the time of writing, 14 natural entrances have been discovered, and a few artificial ones created, and together they lead to a ~1200 m deep and more than 60 km long cave system. A ~2 km long tourist path was opened to the public in 2001. Although palaeoclimate research in the cave had started already in 1998, the tourist path facilitated accessibility and reinforced scientific research. A huge amount of effort has been expended in exploration of this site since then has resulted in a number of publications, and the recognition of Corchia as a site of great potential in environmental and palaeoclimate studies with global significance.

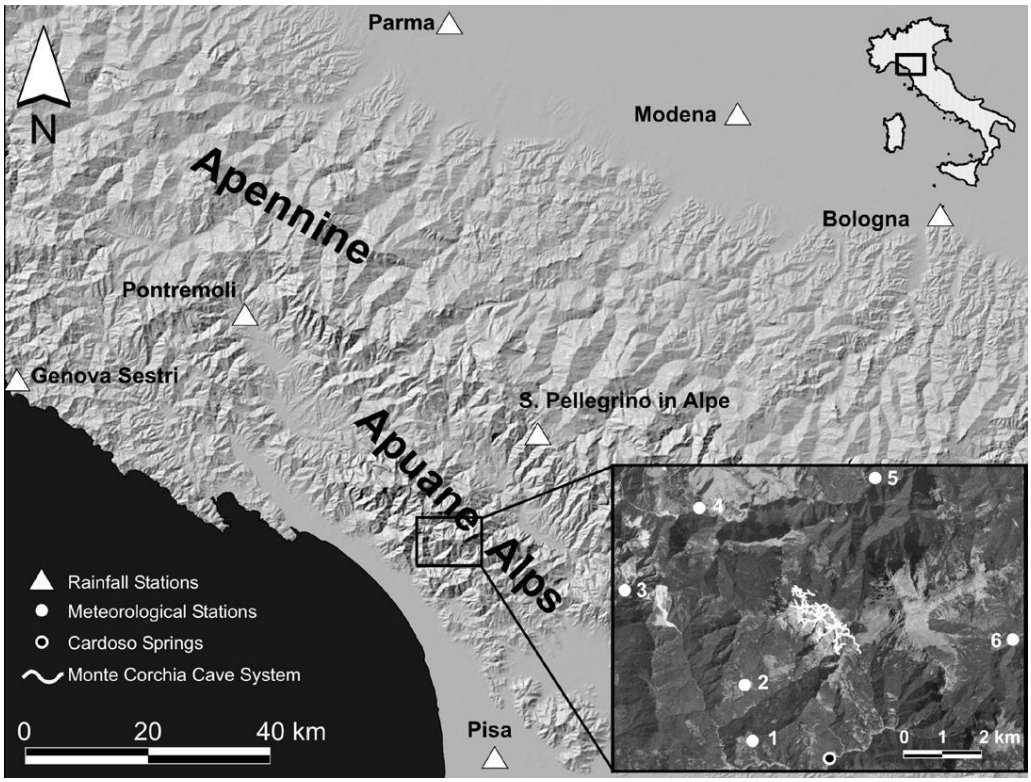

Figure 3-1. Location of Corchia Cave (from Piccini et al., 2008)

3.2 GEOMORPHOLOGY AND GEOLOGY

The Alpi Apuane is characterized by an alpine-like landscape as a result of differential erosion of rocks (Piccini et al., 2008). The highest peaks are more than 1800 m high, with steep slopes almost without any soil and covered by very sparse vegetation. The geology of the Monte Corchia is complex, with carbonate rocks forming the core of the large west-orientated overthrusted syncline, surrounded by low-permeabilty, non-carbonate basement rocks (mainly phyllites and metavolcanics) (Piccini et al., 2008). The area is free of large karst surface landforms but has a well-developed system of cave passages, the biggest of which is the Antro del Corchia (Corchia Cave) system. The majority of the cave is developed in dolostones ("Grezzoni") and marble (part of the famous Carrara marble, which has been exploited in the area for millennia) and only a small portion of the cave is formed in cherty meta-limestone,

"Brecce di Seravezza" or dolomitic marble units (Piccini et al., 2008). Corchia is a classical multilevel cave system composed of a complex maze of numerous interconnected, relict and active, phreatic and vadose passages (**Figure 3-2**).

The part of the cave of greatest interest is the Galleria delle Stalattiti (GdS), from where most of the Corchia speleothems have been collected and where monitoring has been conducted for more than ten years (Drysdale et al., 2004). The GdS is located deep inside the cave at ~840 m a.s.l., 2 km away from the closest natural entrance and ~400 m below the surface. This is the gallery from where the samples used in this study were collected.

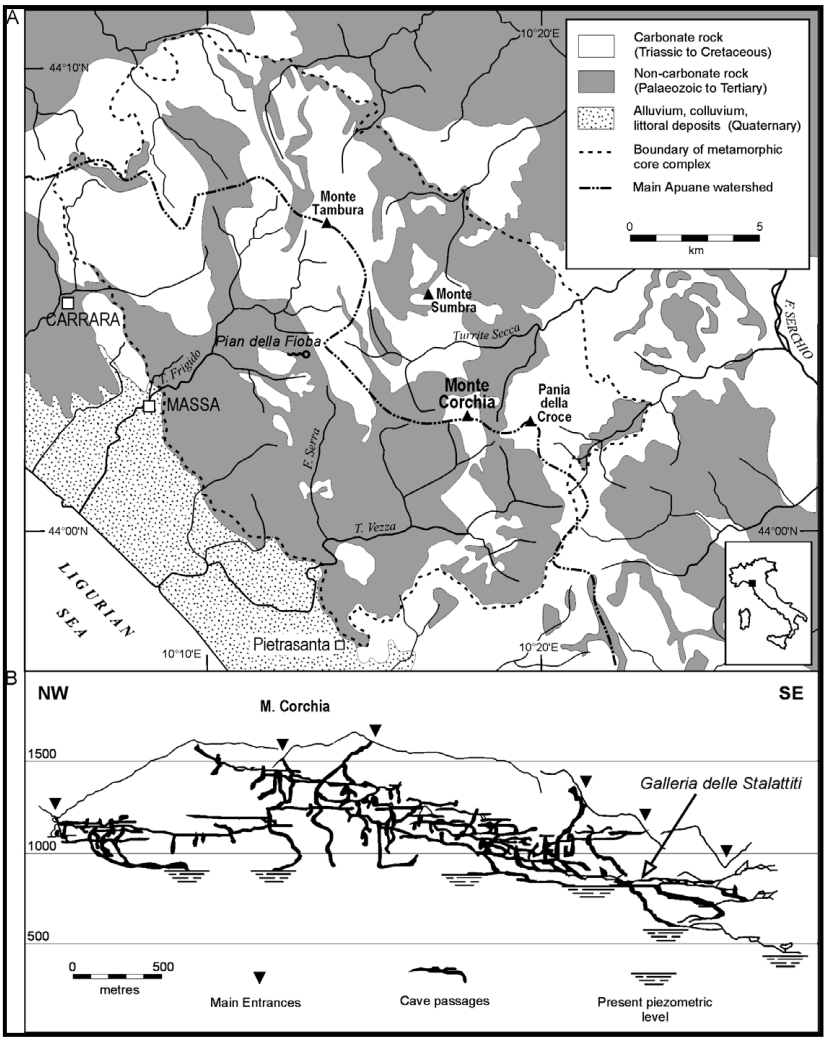

Figure 3-2. (A) Geological map of the area surrounding the study site. (B) Cross-profile of Corchia Cave with the position of Galleria delle Stalattiti marked (from Drysdale et al., 2004 and references therein).

3.3 CLIMATE

The Alpi Apuane comes under the strong influence of air masses moving generally eastwards from the western Mediterranean and the North Atlantic (Drysdale et al., 2004). Today, about 60% of the precipitation originates from the North Atlantic and the rest is derived from the Mediterranean (Bard et al., 2002a). The Alpi Apuane extends in a northwest-southeast direction and it presents an imposing orographic barrier to westerly air masses. This makes it one of the rainiest areas in Europe, with a mean annual precipitation reaching around 3000 mm at the highest parts of Monte Corchia, from where the GdS is supplied with percolation water. The majority of rain falls in autumn and spring, and there is no pronounced dry season (Piccini et al., 2008). The effective infiltration is also high, with amounts estimated to be 1500-1600 mm/year. The highest infiltration is concentrated in early spring, when the snow melts, and in autumn, which is the rainiest season (Piccini et al, 2008).

3.4 CAVE CLIMATE AND WATER CHEMISTRY

Microclimate monitoring and physical and chemical analyses of drip water have been performed intermittently from 1998 (Baneschi et al., 2011; Piccini et al., 2008). In addition, two meteorological stations were installed above/outside the cave. Additonal monitoring stations are located in different parts of the cave interior and, of particular interest for this research, are the results collected from the stations located inside or close to the GdS. Monitoring results from these stations show that GdS is characterised by very stable microclimatic conditions. Maximum annual temperature oscillations are less than 0.8°C and humidity is close to 100% (Piccini et al., 2008). The elemental composition of drip water is also stable, reflecting the long travel times and the significant buffering of short-term variations afforded by the

thickness of overlying rock. This is additionally supported by results of $\delta^{18}O$ analyses of drip water samples, which are characterised by low variability (mean -7.4 +/- 0.1‰: Piccini et al., 2008).

There are no seasonal oscillations in drip rate. The results of tritium analyses for two water samples from the CNR2 station reveal a relatively long residence time of around 50 years, implying a well-mixed plumbing system above the GdS chamber (Piccini et al., 2008).

Drip and pool waters in GdS are enriched in Mg^{2+} and SO_4^{2-}. High Mg^{2+} reflects the dolomitic composition of the bedrock above the chamber ("Grezzoni") while SO_4^{2-} originates from oxidation of the mineral pyrite present in the same lithostratigraphic unit (Piccini et al., 2008).

Drip waters are also characterized by very low Ca concentrations (0.7-1.1mmol/l), which reflect the thin soils on the surface and the low input of soil CO_2, which in turn limits the amount of bedrock dissolution. This is regarded to be the reason for low deposition rates of speleothems at this site in general and a plausible explanation for the lack of yield in calcite farming experiments (Drysdale et al., 2004).

Stable cave microclimate conditions are one of the prerequisites for the successful use of speleothems in palaeoclimate research. It is assumed that the climatic stability of the GdS is caused by the position of the chamber well removed from the entrance, its deep location inside the massif and the cover of overturned basement rocks of low-permeability directly above the chamber. Long percolation times together with extremely slow growth rates of GdS speleothems mean that these speleothems can record only long-term (multi-centennial or longer) climate changes, with a high signal-to-noise ratio, but without any ability to record short-term (seasonal-annual-decadal) climate variability (Baneschi et al, 2011).

3.5 PREVIOUS PALAEOCLIMATE STUDIES

Previous research on Corchia speleothems has demonstrated that geochemical proxies in these samples record regional climate and environmental changes, sometimes with global implications (Drysdale et al., 2004; 2005; 2007; 2009; Regattieri et al., 2014; Zanchetta et al., 2007; 2014). The speleothem results published by so far cover intermittently the time period from MIS10? to the Holocene (~380 000 to 300 years before present). During the extreme late Quaternary glaciations, breaks in deposition are registered (Drysdale et al., 2004).

$\delta^{18}O$ time series of Corchia speleothems show very similar trends to coeval records from other archives from different parts of the world (the Vostok and Greenland ice cores; marine cores in the North Atlantic; and other speleothem records) during glacials, interglacials and terminations, which supports the notion that the Corchia site is responsive to climate variability during all climate states (Drysdale et al., 2004; 2005; 2007; 2009; Zanchetta et al., 2007).

Mechanisms responsible for $\delta^{18}O$ variability in rainfall and hence in cave drip-water and finally speleothems, are various (temperature, composition and source of water vapour, altitude, latitude, amount of rainfall, seasonality, continentality), and determination of the most responsible parameter for a particular cave site is sometimes difficult to disentangle. Previous research at Corchia site suggests that the most likely mechanism driving the $\delta^{18}O$ in these speleothems is "rainfall amount" (Drysdale et al., 2004; 2005; 2007; 2009; Regattieri et al., 2014; Zanchetta et al., 2007). The periods when $\delta^{18}O$ in Corchia speleothems is high correspond to drier and colder climate conditions while periods of low $\delta^{18}O$ are related to wetter and warmer climate conditions registered in other palaeoclimate archives (ice cores, marine records) (Drysdale et al., 2004). This coupling is explained by the greater evaporation from a warmer versus a colder sea surface in the North Atlantic and Western Mediterranean, increasing the amount of

rainfall reaching the Corchia Cave site (Drysdale et al., 2004). The "amount effect", although usually presumed to be important only in tropics, is argued to be additionally emphasized by the orographic role of the Alpi Apuane, which is the first high-relief barrier for westerly air masses crossing the western Mediterranean. The rainfall amount effect has been supported by other geochemical properties in Corchia speleothems, i.e. trace element data (Drysdale et al., 2009), initial uranium isotope ratios (Drysdale et al., 2005) and $\delta^{13}C$ (Zanchetta et al., 2007).

In contrast to speleothems from other middle latitude sites, Corchia speleothems are characterized by relatively high $\delta^{13}C$ values (Drysdale et al, 2004; Zanchetta et al., 2007). This peculiarity has been attributed to the very thin soil and almost no vegetation above the cave as a consequence of the very steep terrain. This is additionally supported by the low Ca content of percolation waters collected from the cave, as Ca content is directly linked to the amount of dissolved bedrock, which in turn is largely dependent upon soil pCO_2 (Drysdale et al, 2004; Zanchetta et al., 2007).

Corchia Cave speleothems are specifically well suited for obtaining precise and accurate U-Th and U-Pb chronologies due to their relatively high U content and very low contamination by detrital thorium (Drysdale et al., 2009). These characteristics have helped in development of precise chronologies which anchor palaeoclimate interpretations. One of the benchmark findings was published by Drysdale et al. (2009), who determined the timing of glacial Termination II based upon stable isotope time series from two coeval Corchia stalagmites. These results supported the hypotheses that obliquity played an important role in driving late Quaternary terminations, in contrast to the widely accepted interpretations of "Milankovitch theory". Comparing these results with the already well-constrained chronology for TI, and exploring the timing of both Terminations (I and II) in respect to orbital configurations, they suggested that the obliquity hypotheses

(Huybers and Wunsch, 2006), with a Southern Hemisphere lead, could be invoked to explain the timing and pacing of such climate transitions (Drysdale et al, 2009).

Other publications on palaeoclimate research of stalagmites from Corchia Cave include: a study on intermittent $\delta^{18}O$ and $\delta^{13}C$ record covering the ~380 to ~43 ka time period (Drysdale et al., 2004); studies of Sapropel 1 (Zanchetta et al., 2007) and Holocene hydrological variability, as recorded in a stalagmite CC26 (Regattieri et al., 2014; Zanchetta et al., 2014); precise chronologies for the onset of the last interglacial (Drysdale et al., 2005) and two cold events during the early last glacial (Drysdale et al., 2007).

Since the beginning of palaeoclimate research in Corchia Cave, many samples from this site have been dated using U-series methods. From this work it was realised that many samples were in secular equilibrium meaning that they exceed the upper limit of the U-Th dating method (~600 000 years)- Woodhead et al., (2006). This discovery coincided with development of the U-Pb dating method at the University of Melbourne, with the first U-Pb age estimate from Corchia published in 2006 (Woodhead et al., 2006). Since then, many more samples have been dated by U-Pb and one of the aims in this PhD is to explore how precise U-Pb based age-depth models can be in order to explore the full palaeoclimate potential of these stalagmites.

Chapter 4

4 HIGH-RESOLUTION U-Pb DATING OF AN EARLY PLEISTOCENE STALAGMITE FROM CORCHIA CAVE (CENTRAL ITALY)[2]

Recent developments in the uranium-lead (U-Pb) dating of speleothems have opened up new opportunities in palaeoclimate research. An important goal in this new frontier is to produce palaeoclimate records underpinned by precise and accurate age models, which together will increase the range of palaeoclimate questions that can be addressed by the speleothem research community. In this paper, the level of age-model precision that is achievable by applying high-resolution U-Pb dating of a stalagmite (CC8) from Corchia Cave (Italy) was investigated. The growth period of investigated speleothem spans part of the Middle Pleistocene Transition (~970 – ~810 ka). Focusing largely on the periods encompassing three glacial terminations, age sampling of CC8 at a density similar to that performed in many studies of younger (i.e. U-Th-dated) speleothems was carried out. Using a combination of Tera-Wasserburg isochron and model age approaches, coupled with age-depth modelling, the results show that age-model uncertainties of ~4 kyr are

[2] This chapter is an adapted version of the manuscript published in *Quaternary Geochronology* (Bajo et al., 2012).

possible, equivalent to a precision of about 0.4%. At this level of precision palaeoclimate time series derived from speleothems of this age can be used to test hypotheses of orbital forcing.

4.1 INTRODUCTION

Speleothems are well-established archives of palaeoenvironmental change (Fairchild et al., 2006; McDermott, 2004). The proxy data that underpin their utility in this regard are derived from the study of the physical and chemical properties of speleothem calcite, including the stable isotopes of oxygen and carbon (McDermott, 2004; Lachniet, 2009); trace elements (e.g. Mg, Sr and Ba — Borsato et al., 2007; Fairchild and Treble, 2009; Griffiths et al., 2010a; Hellstrom and McCulloch, 2000); growth rates and growth intervals (Baker et al., 1998; Baldini, 2010; Drysdale et al., 2005); strontium isotopes (Frumkin and Stein, 2004; Goede et al., 1998; Zhou et al., 2009); and fluid inclusions (Griffiths et al., 2010b; van Breukelen et al., 2008). The major strength of speleothems when compared to other palaeoclimate archives (e.g. deep-sea and ice cores), however, is that they can be accurately and precisely dated using the U-series decay scheme (Richards and Dorale, 2003), allowing palaeoclimate series to be fixed in absolute time.

Virtually all speleothem-based palaeoclimate studies up until now have been confined to the Middle to Late Pleistocene period because of the time constraints imposed by the practical upper limit of the U-Th dating method, i.e.~500 ka (Richards and Dorale, 2003). Although advances in U-series isotopic measurements continue to push this boundary (Stirling et al., 2001; Cheng et al., 2009), the age of many speleothems clearly exceeds the U-Th limit (Walker et al., 2006; Woodhead et al., 2006, 2010). The possibility of probing the many important but unanswered questions in palaeoclimatology (and other fields, such as palaeoanthropology) using such older speleothems has traditionally been considered remote. However, recent refinement of the

U-Pb dating method for speleothems has opened up new research opportunities in this field.

Since the publication of the first substantial paper on U-Pb dating of speleothems (Richards et al., 1998), the method has been improved, particularly in regards to screening procedures for sample selection, chemical separation, and sample-size requirements in response to the advent of multi-collector inductively coupled mass spectrometry (MC-ICP-MS) e.g., Woodhead et al., (2006, 2012). This has led to a rapid increase in the number of speleothem papers based around U-Pb dating. For example, U-Pb dating of flowstones has been used to bracket the age of early hominin fossil-bearing sediments (de Ruiter et al., 2009; Pickering and Kramers, 2010; Pickering et al., 2010, 2011a, 2011b; Walker et al., 2006) and to determine rates of landscape evolution (Meyer et al., 2009, 2011; Polyak et al., 2008). Results of parallel dating of speleothems younger than 500 ka by U-Th and U-Pb methods have also been reported (Cliff et al., 2010), and a recent study has demonstrated that speleothems as old as the Permian can be successfully dated by U-Pb (Woodhead et al., 2010). Notwithstanding this recent upsurge of interest in speleothem U-Pb chronologies, so far no study has tested the limits of the method in terms of the age-model precision that might be accurately achieved. This is an important issue: in palaeoclimatology, in combination with isotope measurement accuracy, age-model precision and accuracy govern the specific palaeoclimate questions that speleothem studies are able to address.

Here is presented the first high-resolution U-Pb chronology study of a single speleothem. The principal aim is to explore the limiting precision achievable by applying a high density of age sampling comparable to that performed in studies of younger (U-Th dated) speleothems (Drysdale et al., 2009; Fleitmann et al., 2009). The stalagmite comes from Corchia Cave (central Italy) and grew during the Middle Pleistocene Transition, an interval during which the period of glacial-interglacial cycles apparently shifted from 40,000 yr to 100,000

yr (Raymo and Huybers, 2008). The results demonstrate that levels of age-model uncertainty as low as 0.4 to 1.3%, equivalent to a few thousand years (95% confidence) are achievable after all sources of random and correlated uncertainty are considered, enabling the assembly of speleothem palaeoclimate records capable of testing competing hypotheses of climate forcing.

4.2 STUDY SITE AND SAMPLE DESCRIPTION

Corchia Cave is a ~60-km-long and ~1250-m-deep system located in the Alpi Apuane massif in central Italy (**Figure 4-1**). The massif is composed mainly of steeply dipping and complexly folded Mesozoic calcareous rocks (marbles and metadolostones). Large-scale structural features within the massif and a wet climate have permitted the development of one of the longest and deepest cave systems in Europe.

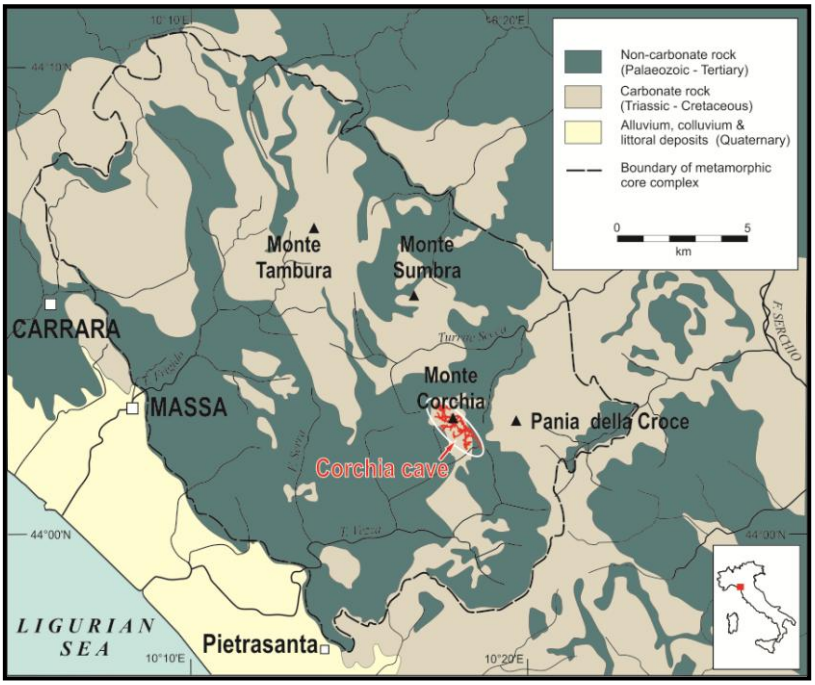

Figure 4-1. Location of Corchia Cave (modified from Drysdale et al., 2004)

The object of this study is stalagmite CC8, which was recovered in three broken pieces from the upper part of the Galleria delle Stalattiti

(GdS), situated 800 m from the nearest entrance and 400 m below the surface. The GdS is well decorated and is part of a 2 km-long tourist path. It experiences a very stable climate (Baneschi et al., 2011), and its speleothems have previously yielded important information on long- and short-term palaeoclimate events during the late Quaternary (Drysdale et al., 2004, 2005, 2007, 2009; Zanchetta et al., 2007). A key feature of these speleothems is the tendency for their stable isotope and trace element patterns to respond to changes in regional rainfall, which in turn are thought to be driven by changes in North Atlantic sea-surface temperatures (Drysdale et al., 2009).

The three pieces of CC8 have a combined length of 825 mm. The stalagmite is composed of translucent to opaque calcite, and is white to grey in colour (**Figure 4-2**).

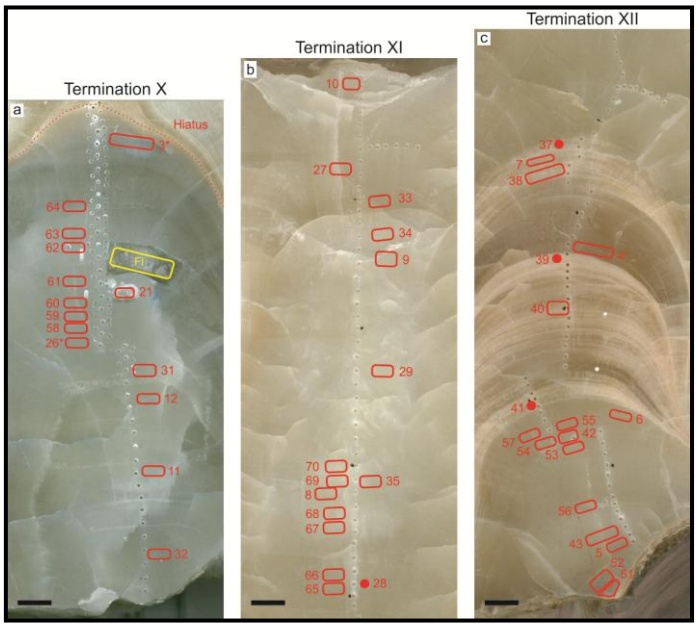

Figure 4-2. Photograph of stalagmite CC8. Each plot (**a**, **b**, **c**) contains Terminations X, XI or XII as indicated on the figure. Red boxes are U-Pb dating samples positions; red dots are samples taken only for [$^{234}U/^{238}U$] measurements, the yellow box is the position of a fluid-inclusion sample (not discussed in the text). Black scale bars are 1cm in length.

Laminations are generally faint to absent to the naked eye, although one section towards the base displays a well-developed lamination pattern (**Figure 4-2c**). There are no visible signs of

diagenesis. However, along the stalagmite growth axis several potential growth hiatuses can be observed, as well as obvious changes in growth-axis direction. Although climate changes may be responsible for both, the effects of past earthquakes on the disruption of water flow paths in this seismically active region cannot be ruled out.

Exploratory U-Pb dating revealed that CC8 grew between ~810 ka and ~970 ka, and confirmed the presence of one significant hiatus that divides the speleothem into two main growth phases: 813 to 824 ka, and 873 to 968 ka. In this paper, the focus was on the lower, older phase of stalagmite growth, which, based on a comparison with the deep-sea benthic oxygen isotope record, encapsulates three Middle Pleistocene glacial terminations. A stable-isotope profile, which, together with other proxy measurements, is the subject of work in preparation, was used to determine the position of these glacial terminations and thus target the appropriate sections for intensive U-Pb dating.

4.3 METHODS

4.3.1 SAMPLING

The three pieces of stalagmite CC8 were individually embedded in resin to prevent breakage during sample preparation then sectioned into slabs of 1-2 cm thickness for polishing. A total of 56 samples were extracted from the older 873 to 968 ka growth phase. For each sample $^{234}U/^{238}U$ analysis and U-Pb dating were performed. Of the total 56 samples, five were run as U-Pb isochron analyses, in which six to twelve prisms of calcite were extracted from a single growth segment as identified from the faint lamination patterns. Two isochron analyses were also carried out on the upper section of CC8.

For the U-Pb analyses, samples of between 50 and 200 mg were extracted either manually using a dental air drill or, after an upgrade of our speleothem sampling facility, by using a dental air drill fixed to a

manually operated, video-guided X-Y-Z milling machine. In the former case, the samples were removed from the main slabs. For the video-guided sampling, smaller sections were cut from the main slabs and attached to the lathe's fixing plate. Two video cameras positioned along the X and Y stage axes of the lathe allowed for a high level of sampling precision to be achieved. Precise tracing of the laminations in the Z (vertical) axis was achieved using a tilting sub-stage fitted to the fixing plate. Due to the high-intensity sampling and limited availability of speleothem, some samples were taken from the opposite side of the slabs. Lamination pattern-matching was used to place these samples on to a common depth scale. The sampling-depth uncertainties (which are used in the final age-depth model construction) for these samples were less than 0.5 mm.

For the $^{234}U/^{238}U$ measurements powdered samples were used. The powders were taken from the same depth position as corresponding U-Pb sample using a separate computer-guided micromilling machine (Drysdale et al., 2012).

4.3.2 U-Pb DATING AND $^{234}U/^{238}U$ ANALYSIS

U and Pb were chemically separated and analysed according to a slightly modified version of the method described in Woodhead et al. (2006). Briefly, aliquots were cleaned by two, short (~1 minute) immersions in very dilute (~0.1M) HCl and washed in ultrapure water. The dried samples were dissolved in 6M HCl, and a mixed $^{233}U/^{205}Pb$ spike was added. After refluxing to ensure spike-sample equilibration and dry down, Pb and U were separated by conventional ion-exchange procedures. Full details of the method are contained in Woodhead et al. (2006) and Woodhead et al. (2012).

Isotope ratio analyses were performed on a Nu Plasma MC-ICPMS equipped with a DSN desolvation unit and employing a Glass Expansion Opal Mist nebuliser uptaking at ~50 microlitres/minute. The NIST SRM

981 reference material for Pb and an internal $^{238}U/^{235}U$ ratio of 137.88 for U were used to monitor and correct for mass fractionation effects. Total Pb blanks were typically in the range 5-10 pg and appropriate blank corrections, coupled with isotope-dilution calculations, were made using the Schmitz and Schoene (2007) algorithm.

Isochrons were constructed from five sample positions in the older section and two sample positions in the younger section of CC8, and were used to assess the composition and variability of the common Pb component present. Thereafter, ages were determined from single-sample aliquots using the common-Pb corrected model age methods outlined in Woodhead et al. (2012).

For $^{234}U/^{238}U$ analysis, samples of ca. 5 mg were prepared and analysed following the U-Th method described by Hellstrom (2003). Powder samples dissolved in concentrated HNO_3 to which a mixed ^{236}U-^{233}U-^{229}Th isotopic spike was added. After overnight refluxing, ion-exchange chemistry was employed for U and Th separation.

The samples were analysed on a Nu Plasma MC-ICP-MS, with frequent repeat measurements of the uranium isotopic standard NBL-112A used to determine external $^{234}U/^{238}U$ variability, then propagated into the reported uncertainties.

4.3.3 AGE-DEPTH MODEL CALCULATION

U-Pb data were interpolated versus depth using a Monte-Carlo simulation of a finite positive growth-rate model (Drysdale et al., 2004, 2005; Hendy et al., 2012; Scholz et al., 2012). For each iteration of the Monte-Carlo simulation all dates were randomised with respect to their uncertainties, and a least-squares fit obtained of a series of line segments such that growth rate is always finite and positive with an additional weighting to minimise its variation between segments. After 10,000 iterations all model outputs were ranked at each of 500 depths

to construct curves for the 97th, 50th and 3rd percentiles of the model. All age model outputs are reported and discussed in terms of (typically asymmetric) 95% confidence intervals.

4.3.4 AGE MODEL ACCURACY AND PRECISION

Until recently (Scholz et al., 2012) there has been little discussion of how speleothem age models should be produced, and the question of accuracy versus precision remains largely unaddressed. Existing age models treat all uncertainty as random as is expected from measurement uncertainty, however there may also be correlated, systematic sources of uncertainty present such as in decay constants, tracer calibration, isotopic compositions etc. Although these sources of uncertainty are usually included in the calculation of individual ages, overlapping densely sampled ages can lead to overly precise age model uncertainties. Because of this, it might sometimes be necessary to quarantine the effects of known, correlated uncertainties during age model generation and add them to the resulting uncertainty envelope afterwards.

4.4 RESULTS

4.4.1 U AND Pb CONCENTRATIONS

The U-Pb dating results are presented in **Table 4-1** and **Table 4-2**. As with earlier studies on younger Corchia speleothems (e.g. Drysdale et al., 2005, 2009; Zanchetta et al., 2007), the radiometric analyses revealed high U concentrations: ~3.8 to ~11.3 ppm. The Pb concentrations are very low, ranging from ~0.8 to ~6.1 ppb. Again, this mirrors previous observations regarding the relatively clean nature of Corchia speleothems, as determined from low Th concentrations

recorded in U-Th-dated samples. Additional evidence for the purity of stalagmite CC8 is recorded in extremely high $^{230}Th/^{232}Th$ activity ratios measured for all of 56 samples with the minimum value greater than 10,000 (**Table 4-1**). As noted by Woodhead et al. (2006), who reported the U-Pb age of another Corchia speleothem (CC16), the combination of high U and low Pb presents significant advantages for U-Pb chronologies and confines the major source of final age uncertainty to the initial uranium disequilibrium correction. This limitation is minimised by measuring $^{234}U/^{238}U$ activity ratios for each U-Pb sample position.

Table 4-1. U-Pb and $^{234}U/^{238}U$ data from the lower portion of stalagmite CC8. Five samples with an asterisk are the most radiogenic single-aliquot samples of the five isochron analyses from this portion of CC8.

Sample ID	Depth from the top (mm)	± 100% error (mm)	Total Pb (ppb)	U (ppb)	$^{238}U/^{206}Pb$	$^{238}U/^{206}Pb$ 2σ error (%)	$^{207}Pb/^{206}Pb$	$^{207}Pb/^{206}Pb$ 2σ error (%)	$(^{230}U/^{232}U)$ measured	$(^{234}U/^{238}U)$ measured	$(^{234}U/^{238}U)$ measured 2σ error	Age Ma corr. for $(^{234}U/^{238}U)i$	Age 2σ error (Myr)
CC8-3	367	4	3.69	7935	4677	1.0	0.441	1.0	27280	0.9771	0.0015	0.877	0.016
CC8-64	383.5	2.5	1.92	5372	5685	4.8	0.351	7.6	85500	0.9799	0.0014	0.879	0.014
CC8-63	393	2.5	0.89	6321	8592	2.9	0.117	20.0	60060	0.9790	0.0016	0.877	0.009
CC8-62	398	2.5	1.57	7202	7110	2.6	0.227	8.0	64180	0.9822	0.0018	0.878	0.010
CC8-61	406	2.5	1.55	6709	7026	3.4	0.240	9.6	154900	0.9816	0.0014	0.872	0.009
CC8-21	410	2	3.05	9329	5676	0.5	0.351	0.7	36660	0.9816	0.0018	0.873	0.012
CC8-95*	410	2	1.44	7292	7787	7.0	0.174	30.0	58080	0.9825	0.0011	0.871	0.012
CC8-60	413	2.5	2.06	7084	6139	1.4	0.313	2.6	31900	0.9810	0.0013	0.875	0.010
CC8-59	417	2.5	2.70	6881	5187	1.5	0.389	2.0	91920	0.9832	0.0012	0.869	0.011
CC8-58	419	2.5	1.17	6235	7578	2.1	0.191	7.9	69450	0.9803	0.0021	0.882	0.012
CC8-26*	421	3	1.19	5881	7377	3.1	0.204	11.0	30700	0.9821	0.0011	0.879	0.008
CC8-86	426	1	2.14	4899	5208	8.9	0.386	12.0	21050	0.9820	0.0020	0.877	0.021
CC8-31	428	2.5	1.43	5956	6520	2.2	0.273	5.0	69220	0.9830	0.0018	0.878	0.010
CC8-85	434	1.5	1.98	5877	5860	6.6	0.312	13.0	39480	0.9853	0.0012	0.897	0.015
CC8-12	437.5	2	1.85	5934	5735	0.7	0.330	1.2	138000	0.9841	0.0019	0.890	0.011
CC8-11	459.5	2	2.97	6912	4750	0.4	0.406	0.4	117600	0.9850	0.0015	0.902	0.013
CC8-32	479	2	2.53	7631	5528	0.9	0.342	1.5	38000	0.9849	0.0012	0.896	0.010
CC8-10	503	2	3.42	7343	4494	0.3	0.423	0.3	92660	0.9869	0.0024	0.905	0.017
CC8-27	519.5	3.5	1.10	6124	7328	1.2	0.180	4.9	18130	0.9850	0.0014	0.904	0.008
CC8-83*	531	2	1.49	6597	6991	5.0	0.207	17.0	51060	0.9845	0.0017	0.911	0.012
CC8-33	537	2	2.33	5101	4576	0.7	0.425	0.8	40330	0.9844	0.0019	0.895	0.016
CC8-91	542.5	2	2.80	7769	5460	3.4	0.346	5.5	81380	0.9821	0.0010	0.914	0.012
CC8-34	546.5	2	3.37	7726	4732	0.4	0.415	0.5	105500	0.9803	0.0018	0.911	0.015
CC8-9	556	2	2.07	6653	5711	0.3	0.325	0.3	48240	0.9831	0.0020	0.907	0.013
CC8-29	586.5	2	5.88	8061	3343	0.4	0.527	0.3	133500	0.9837	0.0010	0.914	0.021
CC8-70	613.5	2.5	1.82	6908	6355	2.0	0.270	4.8	78690	0.9824	0.0014	0.910	0.011
CC8-90	616	1.5	1.36	7045	7664	7.4	0.150	37.0	39760	0.9825	0.0011	0.920	0.013

CC8-69	617.5	2.5	1.83	6723	6230	1.7	0.280	3.8	29150	0.9815	0.0017	0.917	0.012
CC8-35	619	2	1.55	5412	5934	1.4	0.304	2.8	54100	0.9832	0.0013	0.910	0.010
CC8-8	622	2	0.80	5972	8131	0.6	0.112	3.8	54560	0.9813	0.0022	0.923	0.014
CC8-68	627.5	2.5	1.38	5270	6440	3.8	0.256	9.6	55850	0.9829	0.0014	0.919	0.012
CC8-67	631.5	2.5	2.19	4989	4779	2.2	0.398	2.8	26390	0.9824	0.0017	0.929	0.016
CC8-81*	637	2	1.35	5034	6754	10.0	0.224	31.0	114500	0.9842	0.0016	0.917	0.020
CC8-66	645	2.5	2.04	5229	5106	2.7	0.357	4.2	52320	0.9854	0.0014	0.936	0.013
CC8-65	649	2.5	1.14	4600	6538	3.7	0.233	11.0	25370	0.9836	0.0018	0.938	0.014
CC8-79	668	1.5	1.38	5129	6354	6.2	0.232	18.0	79380	0.9874	0.0014	0.945	0.014
CC8-89	689	1.5	1.51	5743	6463	7.2	0.218	23.0	79510	0.9858	0.0021	0.962	0.018
CC8-7	696	2	4.46	5547	3093	2.0	0.535	1.4	12000	0.9878	0.0013	0.937	0.023
CC8-38	701	2.5	2.49	5651	4677	2.7	0.382	3.8	25360	0.9889	0.0021	0.947	0.017
CC8-4*	720.5	3.5	2.28	4470	4286	3.1	0.420	3.6	21690	0.9879	0.0021	0.950	0.018
CC8-40	741	2.5	4.63	4595	3651	1.6	0.485	1.0	53270	0.9844	0.0017	0.957	0.021
CC8-75	756	1.5	2.93	4922	3954	4.8	0.453	4.8	63140	0.9870	0.0019	0.951	0.021
CC8-74	767	2	4.98	4815	2567	1.7	0.580	1.0	43820	0.9863	0.0022	0.961	0.033
CC8-6	773	2	1.38	4454	5472	0.9	0.298	1.8	58760	0.9887	0.0011	0.966	0.010
CC8-57	775.5	2.5	1.55	5677	5984	2.3	0.253	5.8	32970	0.9896	0.0019	0.953	0.013
CC8-54	780	2.5	1.61	5652	5400	1.7	0.307	3.3	39110	0.9884	0.0022	0.964	0.016
CC8-42	781	2	2.19	5708	4881	1.0	0.356	1.5	16450	0.9885	0.0017	0.965	0.013
CC8-73	782.5	2	2.77	6072	4648	5.2	0.375	7.4	79030	0.9875	0.0016	0.977	0.019
CC8-53	784	2.5	1.34	5473	6278	1.9	0.227	5.7	39960	0.9891	0.0021	0.954	0.014
CC8-72	793	1.5	2.27	6022	5236	6.5	0.313	12.0	21630	0.9906	0.0017	0.969	0.018
CC8-71	799	1.5	2.67	5046	4166	3.3	0.421	3.9	93900	0.9879	0.0019	0.977	0.019
CC8-56	802.5	2.5	2.17	4705	4488	2.5	0.387	3.4	10010	0.9892	0.0010	0.975	0.013
CC8-43	807.5	2.5	4.05	6109	6137	1.8	0.230	4.5	23030	0.9912	0.0014	0.959	0.009
CC8-5	813.5	2	1.76	5427	5534	4.0	0.285	8.8	30160	0.9908	0.0012	0.965	0.011
CC8-52	818	2.5	1.46	6094	6353	3.4	0.206	12.0	14170	0.9900	0.0016	0.970	0.012
CC8-51	821.5	2.5	1.27	5983	6617	2.4	0.184	9.3	35080	0.9899	0.0012	0.966	0.009

Table 4-2. U and Pb data for seven isochrons measured along the whole section of stalagmite CC8. The common Pb composition has been used to calculate single-point isochron ages following the method of Woodhead et al. (2012). The underlined samples correspond to the most radiogenic samples for each isochron: these have been used as the input ages in the age-depth modelling.

Sample ID	Depth from the top (mm)	± 100% error (mm)	Total Pb (ppb)	U (ppb)	$^{238}U/^{206}Pb$	$^{238}U/^{206}Pb$ 2σ error (%)	$^{207}Pb/^{206}Pb$	$^{207}Pb/^{206}Pb$ 2σ error (%)	MSWD *	$(^{234}U/^{238}U)$ measured	$(^{234}U/^{238}U)$ measured 2σ error	Age Ma corr. for $(^{234}U/^{238}U)i$	Age error 2σ (Myr)
CC8-1	**5.0**	**2.0**							54				
CC8-1-1			2.54	9974	6767	0.4	0.309	0.7					
CC8-1-2			1.69	7706	7296	0.7	0.272	1.6					
CC8-1-3			2.30	8396	6514	0.5	0.327	0.8					
CC8-1-4			1.10	6524	8161	1.0	0.200	3.4		0.9762	0.0020	0.822	0.011
CC8-1-5			2.40	8022	6192	0.5	0.349	0.8					
Isochron												**0.820**	**0.060**
CC8-2	**187.5**	**2.5**							7.5				
CC8-2-1			1.0	9237	9134	1.1	0.105	8.1		0.9800	0.0020	0.833	0.009
CC8-2-2			1.3	9349	8407	0.9	0.161	4.2					
CC8-2-3			2.0	1126	7802	0.8	0.211	2.5					
CC8-2-4			2.1	1125	7609	0.8	0.224	2.6					
CC8-2-5			2.0	1032	7411	0.7	0.240	1.9					
Isochron												**0.833**	**0.024**
CC8-95	**410.0**	**2.0**							13				
CC8-95-1			2.38	8206	6285	3.5	0.300	7.2					
CC8-95-2			2.14	7873	6619	5.8	0.269	14.0					
CC9-95-3			2.13	8005	6685	6.2	0.255	16.0					
CC8-95-4			2.91	8225	5555	1.9	0.358	3.0					
CC8-95-5			1.83	7698	7029	4.9	0.237	14.0					
CC8-95-6			3.26	8198	5212	1.9	0.394	2.4					
CC8-95-7*			1.44	7292	7787	7.0	0.174	30.0		0.9825	0.0011	0.871	0.011
CC8-95-8			2.35	7488	6037	3.6	0.325	6.4					
CC8-95-9			2.40	8150	6095	1.9	0.310	3.7					
CC8-95-10			3.43	7964	4868	1.1	0.413	1.3					
CC8-95-11			3.14	8109	5217	1.6	0.383	2.2					
CC8-95-12			2.56	7949	5928	3.4	0.331	6.0					
Isochron												**0.876**	**0.014**
CC8-26	**421.0**	**3.0**							65				

CC8-26-1			1.76	5626	5792	0.5	0.336	0.8				
CC8-26-2			1.14	5793	7262	0.6	0.217	1.9				
CC8-26-3			1.10	5531	7216	0.5	0.218	1.6				
CC8-26-4			1.24	5441	6816	0.4	0.255	1.1				
CC8-26-5*			1.19	5881	7377	3.1	0.204	11.0		0.9821	0.0011	0.879	0.008
CC8-26-6			1.30	5951	7204	3.9	0.217	13.0				
Isochron												**0.877**	**0.016**
CC8-83	531.0	2.0							5.5				
CC8-83-1			2.37	6691	5504	4.3	0.331	7.5				
CC8-83-2			2.58	6641	5193	3.8	0.357	5.9				
CC8-83-3			2.49	6786	5449	5.0	0.338	8.5				
CC8-83-5			2.13	6926	5898	3.2	0.300	6.4				
CC8-83-6			2.27	6896	5707	2.7	0.327	4.8				
CC8-83-7			1.41	6261	7537	13.0	0.158	60.0				
CC8-83-8*			1.49	6597	6991	5.0	0.207	17.0		0.9845	0.0017	0.911	0.012
CC8-83-9			2.05	6943	5979	2.6	0.293	5.4				
CC8-83-10			2.33	6851	5626	4.2	0.321	7.6				
Isochron												**0.908**	**0.019**
CC8-81	637.0	2.0							6.9				
CC8-81-1			4.35	5446	3218	2.9	0.541	2.0				
CC8-81-2			4.99	5476	2904	3.0	0.562	1.9				
CC8-81-3			2.51	5268	4677	5.2	0.408	6.4				
CC8-81-4			4.04	5432	3373	3.1	0.519	2.3				
CC8-81-5			2.53	5164	4620	4.9	0.425	5.6				
CC8-81-6*			1.35	5034	6754	10.0	0.224	30.0		0.9842	0.0016	0.917	0.020
CC8-81-7			5.23	5060	2622	3.1	0.580	1.8				
CC8-81-8			6.11	5042	2299	2.8	0.608	1.4				
CC8-81-9			5.82	5107	2424	3.0	0.597	1.6				
Isochron												**0.915**	**0.041**
CC8-4	**720.5**	**3.5**							18				
CC8-4-1			2.23	4216	4053	0.4	0.437	0.4				
CC8-4-2			2.47	4187	3764	0.4	0.462	0.3				
CC8-4-3			2.37	4087	3806	0.3	0.459	0.3				
CC8-4-4			2.20	4076	3993	0.4	0.442	0.4				
CC8-4-5			2.07	3961	4085	0.4	0.435	0.4				
CC8-4-6			2.44	3779	3541	0.5	0.484	0.4				
CC8-4-7			2.62	3823	3472	1.6	0.494	1.3				

CC8-4-8	2.45	4416	4012	2.2	0.441	2.3				
CC8-4-9*	2.28	4470	4286	3.1	0.420	3.6	0.9879	0.0021	0.950	0.018
Isochron									**0.947**	**0.045**

4.4.2 RAW U-Pb DATA AND DISEQUILIBRIUM-CORRECTED AGES

4.4.2.1 ISOCHRON AGE RESULTS

The seven isochron age results are shown in **Table 4-2** and **Figure 4-3**. As reported in Woodhead et al. (2012), single-aliquot U-Pb ages are a possible alternative to the more labour-intensive isochron ages in cases where the speleothem is highly radiogenic (i.e. with high $^{238}U/^{206}Pb$, where measured samples occupy a position relatively close to concordia) and where the isotopic composition ($^{207}Pb/^{206}Pb$ ratio) of the common-Pb end member is well constrained. If these two criteria are met, the individual aliquot ages should be statistically indistinguishable from the isochron age. $^{207}Pb/^{206}Pb$ intercept values for all seven isochrons are within error of each other (**Figure 4-4**), which is indicative of a consistent net source of common Pb throughout the growth of the stalagmite. The robust median of all seven isochron *y*-intercepts and their uncertainties gives an estimate of the common Pb composition of 0.818 +0.006/-0.011 (98.4% confidence).

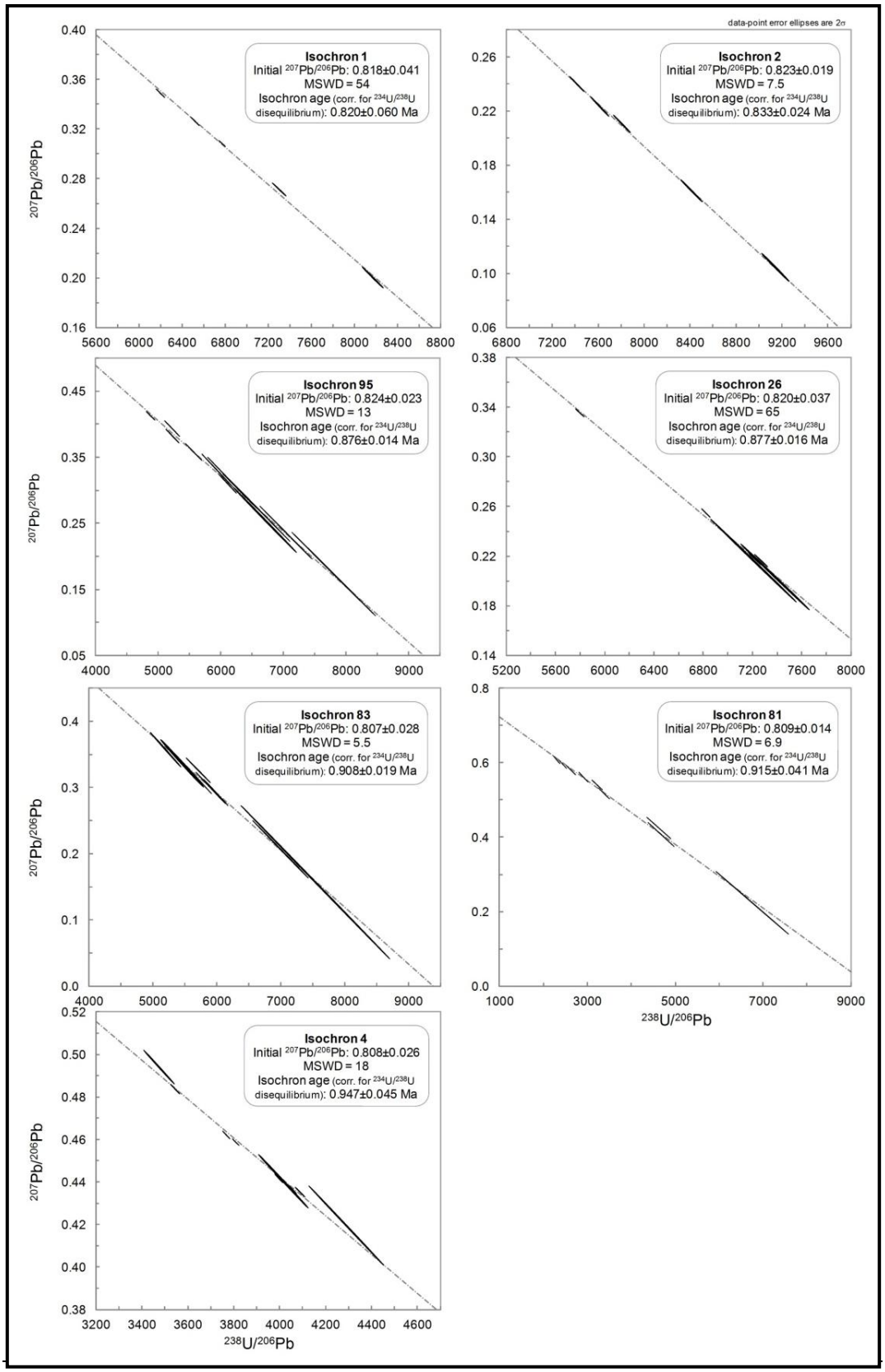

Figure 4-3. Plots for seven full isochrons determined for CC8 and constructed using Isoplot (Ludwig, 2001). NB: the *x*- and *y*-axis ranges are different for each plot.

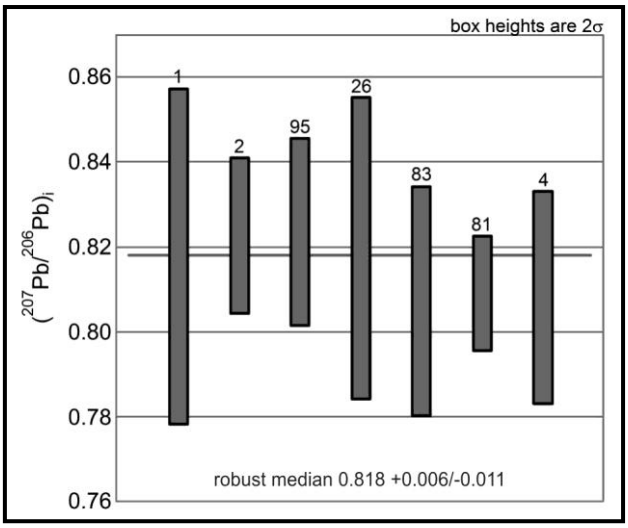

Figure 4-4. $^{207}Pb/^{206}Pb$ intercept values for all seven isochrons are within error of each other, suggesting a consistent source of common Pb. The robust median for this common Pb composition is 0.818 +0.006/-0.011 (98.4% confidence), indicated by the thick horizontal line.

4.4.2.2 $^{234}U/^{238}U$ RESULTS AND SECULAR DISEQUILIBRIUM CORRECTION

Due largely to weathering and hydrological processes, speleothems are always deposited out of secular isotopic equilibrium with respect to the initial $^{234}U/^{238}U$ activity, i.e. $(^{234}U/^{238}U)_i \neq 1$ (Richards & Dorale, 2003). The age effect of this disequilibrium (when compared to the more traditional U-Pb assumption of U-series equilibrium at the time of deposition) can amount to more than 100 ka and thus its accurate quantification is very important for samples of a few Ma or less in age (Ludwig, 1977; Richards et al., 1998; Woodhead et al., 2006). For a given U-Pb sample, such a correction is based on an estimate of the $(^{234}U/^{238}U)_i$, which for relatively young samples can be quantitatively derived from direct measurement of $(^{234}U/^{238}U)$ within the calcite. For the latter, $(^{234}U/^{238}U)$ measurements were performed on all U-Pb samples from the older portion of CC8 (**Table 4-1**, **Figure 4-5**).

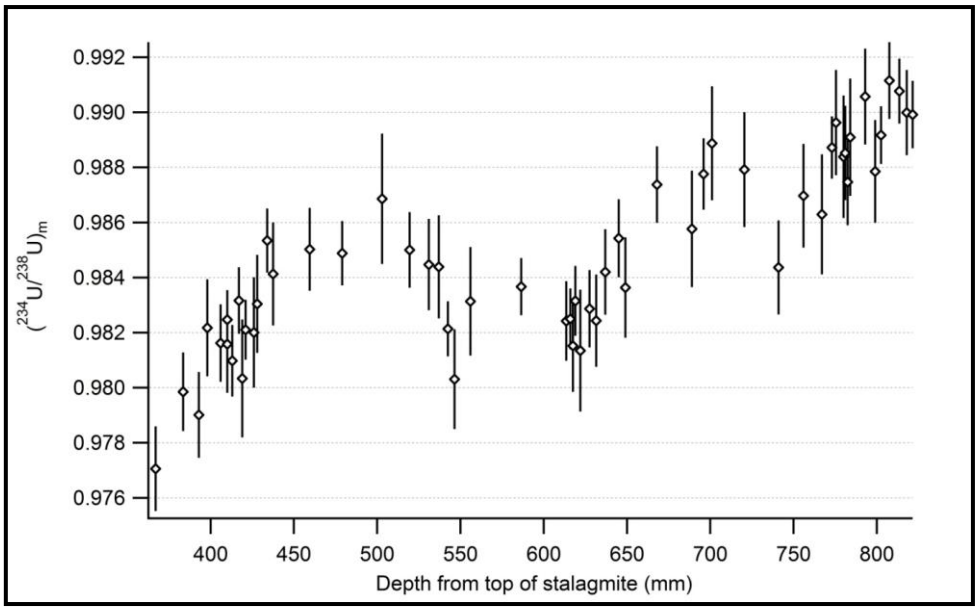

Figure 4-5. ($^{234}U/^{238}U$) measurements were performed along the lower part of the CC8. ($^{234}U/^{238}U$) sample depth positions correspond to U-Pb sample positions. Although ($^{234}U/^{238}U$) is decreasing with time, the trend is not monotonic. This observed variability likely reflects changing hydrological conditions during different climate states, a subject of ongoing study at Corchia.

($^{234}U/^{238}U$) values varied from 0.9771 ± 0.0015 to 0.9912 ± 0.0013 during the ~100 kyr-long growth period of this section of CC8. These values are low compared to those of speleothems from most other cave systems (Richards and Dorale, 2003), but consistent with previous U-Th studies at Corchia (Drysdale et al., 2009).

Although the overall trend of ($^{234}U/^{238}U$) is decreasing with time, high density of sampling reveals that this is not monotonic: there is significant variability in ($^{234}U/^{238}U$) that likely reflects changing hydrological conditions during different climate states. This is currently the subject of ongoing study.

4.4.2.3 U-Pb AGE CALCULATION

Disequilibrium-corrected, single-aliquot U-Pb ages were determined by projecting an assumed initial $^{207}Pb/^{206}Pb$ through the measured $^{207}Pb/^{206}Pb$-$^{238}U/^{206}Pb$ point onto a disequilibrium concordia corresponding to measured $^{234}U/^{238}U$, and assuming complete initial exclusion of all other daughter products (Woodhead et al, 2006). All inputs are randomised with respect to their uncertainties, taking account of measured $^{207}Pb/^{206}Pb$-$^{238}U/^{206}Pb$ error correlation, during a 1000-point Monte-Carlo simulation from which age and its 95% uncertainty are determined.

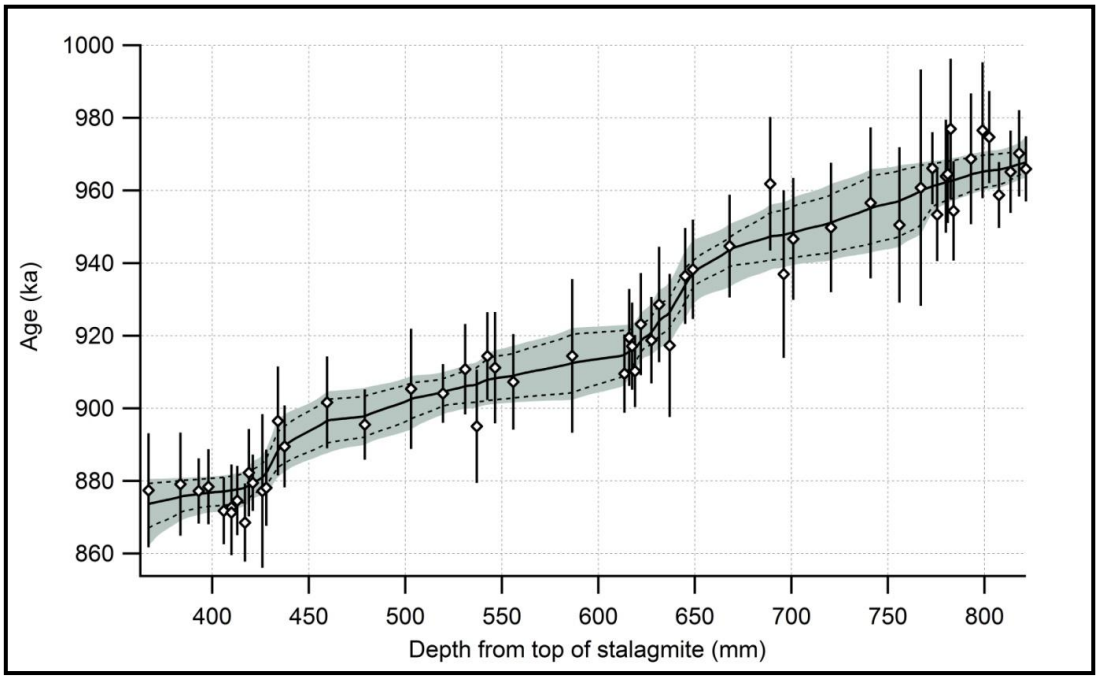

Figure 4-6. Age-depth model for the older portion of CC8 based on 56 U-Pb dates and their associated uncertainties. The grey shaded area represents the 95% confidence age-model uncertainty envelope. Black dashed lines are age-depth models calculated using common Pb values of 0.8125 ± 0.0070 and 0.8265 ± 0.0070 and they are presented here to emphasize the effect of common Pb variability on final model ages. All U-Pb analyses returned ages in correct stratigraphic order when the age uncertainties of stratigraphically successive sample pairs are considered. The MSWD of 0.62 indicates that analytical uncertainties more than explain the observed scatter.

The final U-Pb ages for the lower part of CC8 are plotted versus depth in **Figure 4-6**. Although this plot shows some degree of age

scatter with depth, all U-Pb analyses returned ages in stratigraphic order when viewed within the constraints of the combined age uncertainties of stratigraphically successive sample pairs. A finite positive-growth-rate age-depth model determined through these data gave an MSWD of 0.62 indicating that, if anything, their uncertainties had been overstated. Removing the assigned uncertainty of the common Pb $^{207}Pb/^{206}Pb$ from the ages gives an age-model MSWD of 1.05. Varying the assigned $^{207}Pb/^{206}Pb$ yields a minimum MSWD of 1.03 at 0.8195, giving a stratigraphically-constrained (Hellstrom, 2006), best-fit initial $^{207}Pb/^{206}Pb$ well within the range determined by isochron analyses. A conservative uncertainty of ±0.010 was assigned on the basis of both approaches.

4.4.3 AGE UNCERTAINTIES AND AGE-DEPTH MODELLING

A finite, positive-growth-rate age-depth model was determined through the entire population of single-aliquot U-Pb ages. A feature of this and other commonly used speleothem age-depth models (Scholz et al, 2012) is that all age uncertainty is treated as independent, and as such increasing age measurement density leads to increasingly higher-precision models, with no limit. Here, the isochron-dependent initial common $^{207}Pb/^{206}Pb$ value assigned to the single-aliquot ages is taken to be invariant between samples, and any error in the determination of it will affect all of them in a systematic manner. To address this, a component of the assigned $^{207}Pb/^{206}Pb$ uncertainty (of ±0.007) was removed from the U-Pb ages prior to age-model calculation using $^{207}Pb/^{206}Pb = 0.8195 \pm 0.0070$. Two additional age models were determined for ages calculated with $^{207}Pb/^{206}Pb$ of 0.8125 ± 0.0070 and 0.8265 ± 0.0070, and their differences from the original model were calculated along their lengths. The offsets to these two additional age-depth models were then combined with the uncertainty envelope

originally derived for the first model to give a composite uncertainty reflective of the impacts of both random and correlated uncertainty.

The resulting age model for the entire lower part of CC8 is shown in **Figure 4-6** together with the 95% confidence interval. Although individual U-Pb 2σ age uncertainties ranged between values of 7.7 to 32.5 kyr (on average, about 1.5% of the determined age), the age-model uncertainties are in the range 3.9 to 12.2 kyr if the values before and after the two extreme age points are excluded (NB: lack of radiometric ages beyond the limits of the section results in an end-effect amplification of the age uncertainties). This equates to uncertainties between 0.4 and 1.3% of the modelled age. The age uncertainties through each of the three glacial terminations represented in the lower section of CC8 will be now considered in detail.

4.4.3.1 AGE UNCERTAINTIES THROUGH TERMINATION X

Details of the age-depth model spanning Termination X, as well as the corresponding age uncertainty plot, are shown in **Figure 4-7a-b**. According to the age-model results, this 88.5 mm long section grew continuously over a ~22 kyr period. Of the 15 U-Pb ages determined along this section, only one raw age deviates appreciably from the age model curve (CC8-59: 417 mm) but this still lies well within the overlapping 2σ age error bars of the neighbouring samples. The model age uncertainties range from 3.9 to 11.0 kyr, with highest values occurring at the youngest end of the section due to the end effect noted above: this is the youngest end of the age-depth model for the lower part of stalagmite CC8.

The section defining the start of Termination X is of greatest interest and is located around 877 ka. From the age uncertainty plot (**Figure 4-7b**) it can be seen that model age uncertainties here are in the range 4.1 to 4.9 kyr, or 0.5 to 0.6% of modelled age.

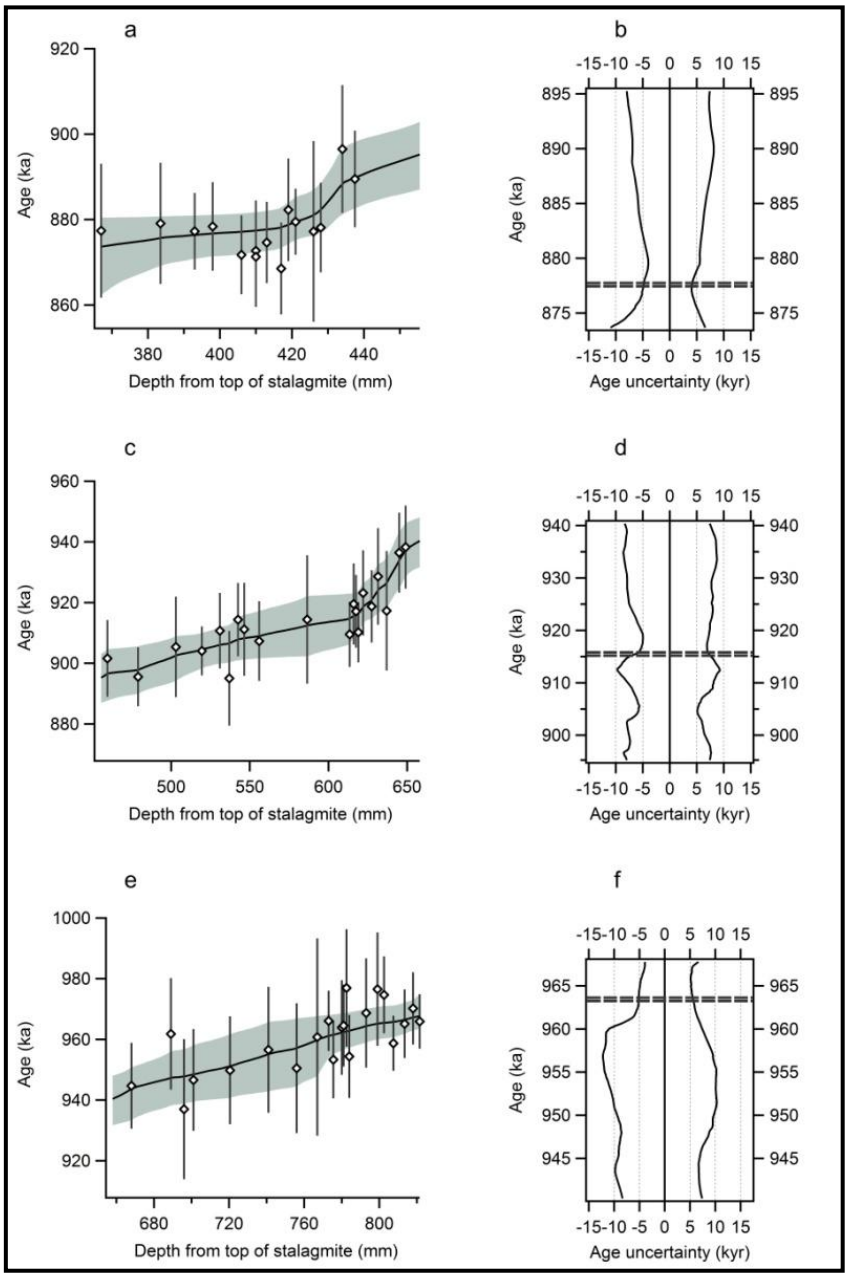

Figure 4-7. (**a, c, e**) Details of the age-depth model through portions of CC8 where Terminations X, XI and XII are recorded, and the corresponding age-model uncertainty plots (**b, d, f**). Thick dashed lines on the uncertainty plots show the periods when terminations started according to stable isotope data from this specimen.

4.4.3.2 AGE UNCERTAINTIES THROUGH TERMINATION XI

The age model and age uncertainty plot for Termination XI is presented in **Figure 4-7c-d**. With a length of 202.5 mm, this is the longest of all three sections and according to the mean modelled ages it spans ~45 kyr of time. Twenty samples were dated along this section. As with the T-X section, there is one clear outlying age-depth point but this overlaps with neighbouring samples within their respective uncertainties. Model age uncertainties along this section are in range from 4.9 to 9.7kyr, or 0.5 to 1.1% of the corresponding model ages.

As can be seen in **Figure 4-7d**, the model age uncertainties through the region where Termination XI commences are in the range of 7.3 to 7.5 kyr (i.e. 0.8% of the modelled age).

4.4.3.3 AGE UNCERTAINTIES THROUGH TERMINATION XII

The lowest part of the stalagmite captures palaeoclimate information about Termination XII, the oldest termination preserved in CC8. Detail of the age-depth model for this 163.5 mm long section, as well as the age uncertainty plot, are shown in **Figure 4-7e-f**. In **Figure 4-7e** we can see that the U-Pb ages for this part of stalagmite are characterized by the highest U-Pb age uncertainties, particularly in the area from ~700 to 790 mm of depth. The age model is relatively poorly constrained in this part of the stalagmite, with uncertainties greater than 10 kyr. This reflects greater scatter in the ages determined at this depth.

According to stable isotope data the onset of Termination XII occurred at ~963 ka, where the model age uncertainty is in the range of 5.2 to 5.9 kyr (i.e. ~0.6% of the corresponding modelled ages).

4.5 DISCUSSION

4.5.1 FACTORS INFLUENCING AGE-MODEL PRECISION AND ACCURACY IN CC8

Accurate, robust age models and minimised age uncertainties are crucial for the successful application of speleothem time-series to palaeoclimate problems. Total age uncertainties of 1% or less for speleothems in the range of the U-Th dating method are now commonly reported. However, the results show that accurate ages with a precision as low as 0.4% are possible for older speleothems dated by the U-Pb method. Achieving high precision and accuracy provides an opportunity to date some of the most prominent but as yet insufficiently explored palaeoclimate events of the Early Pleistocene, such as the shift from 40-kyr to 100-kyr glacial-interglacial cycles.

The low magnitude of the age uncertainties in CC8 can be attributed to a combination of the high U content, low common Pb, and readily quantifiable residual $^{234}U/^{238}U$ disequilibrium. Careful sample selection and thorough pre-screening procedures play a large role in satisfying the first two of these factors. Even in cases where U concentrations are lower than those at Corchia (see Woodhead et al., 2012, for a summary of typical U and Pb contents in speleothems), satisfactory ages and age models with reduced age uncertainties should be achievable provided common Pb concentrations are in the low ppb range.

Regardless of the raw uncertainties, densely dated records such as the one presented here (i.e. where the uncertainties of many age determinations overlap) can lead to final age-depth model uncertainties significantly smaller than those of their best individual uncertainties (e.g. Scholz et al., 2012). An important consideration in improving age-model precision by this means is to correctly identify and quantify all sources of random and correlated uncertainties. Here the biggest source of uncertainty is a common component of the assigned initial

$^{207}Pb/^{206}Pb$ of the single-aliquot ages and so this source of correlated uncertainty was propagated into the age model after completion of the age-depth modelling process. An earlier version of the CC8 age-depth model depicted by Woodhead et al. (2012) did not consider the effect of correlated common uncertainty, which was exacerbated by the use of sparsely-constrained $^{234}U/^{238}U$ data rather than the per-sample measurement approach used here. This serves to illustrate the importance of per-sample measurement of $^{234}U/^{238}U$ where samples are sufficiently young that resolvable disequilibrium remains. Final sources of correlated age-model uncertainty to consider are spike calibration, decay constant and $\lambda^{238}U$ uncertainties. These are small compared to analytical and common Pb uncertainties and do not significantly affect the age uncertainties reported here for CC8. They do, however, limit the age model uncertainties that could be theoretically achieved, to a little over 0.1%. Correlated uncertainties seem to be an important consideration in age-depth modelling in general and their impact is also likely to be of significance to U–Th chronologies in some cases, particularly where a non-trivial initial Th component is present.

Although U-Pb age uncertainties as low as 1-2% are readily achievable (Cliff et al., 2010; Meyer et al., 2009; Woodhead et al., 2006; 2010), another factor that controls the absolute magnitude of the age uncertainties is the time interval under consideration. Once age-model uncertainties move significantly beyond ~10 kyr (about half a precession cycle) the ability to make a first-order discrimination between the different orbital parameters disappears.

4.5.2 AGE DENSITY VERSUS AGE UNCERTAINTY

The final issue discussed here is the point at which the addition of further ages does not measurably improve the age model. On first viewing of the age-depth model (**Figure 4-6**), it is obvious that the distribution of dated samples is unevenly spread throughout the section

of the stalagmite. This was by design: the rationale here was to derive precise age-model solutions through specific palaeoclimate events. Hence, the sections of highest age density and thus in most cases lowest modelled age uncertainties correspond to these events. An important consideration in U-Pb dating of speleothems is estimating the density of ages that are required to achieve a certain level of age-model uncertainty. To address this, a simple age-density function was derived and compared this to age uncertainty. The model age and maximum model age uncertainty at the depth of each age determination were first derived by interpolation of the raw age-depth model; raw U-Pb ages were not used because of the scatter of mean ages along the depth profile. The age-density function was calculated as the inverse of the difference in kyr between each successive model-interpolated age, expressed as "dating samples per kyr". When plotted against the maximum model age uncertainty achieved within each successive pair of age positions (**Figure 4-8**), there is, overall, a negative correlation that is best described by a power function.

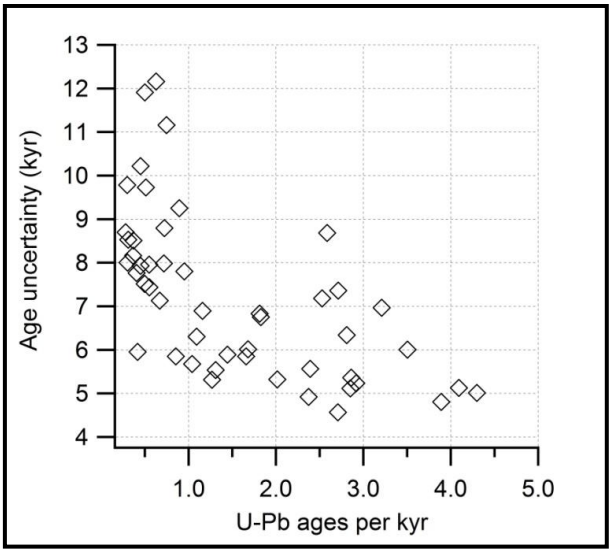

Figure 4-8. Plot of age-model uncertainty versus age density. Here, density is expressed as the number of U-Pb modelled ages per kyr. Once a density of one age per kyr is achieved there is no significant improvement in age-model uncertainties.

From this plot, it can be seen that uncertainties of <10 kyr can be achieved consistently once the sampling density reaches 0.8 (i.e. eight age determinations every 10 kyr), and that once a density of 2.0 is reached (i.e. two age determination per kyr) uncertainties of ~5 kyr are possible, although not consistently so. Thus, to establish the timing of a glacial termination during the late Early Pleistocene to a precision of 5 to 10 kyr, a minimum of eight U-Pb determinations are necessary, assuming that a typical termination spans a 10-kyr interval and that the speleothem has similar characteristics to CC8, i.e. high U, low common Pb, and well-constrained $^{234}U/^{238}U$ and initial $^{207}Pb/^{206}Pb$. This represents considerable analytical effort, particularly if isochron ages are required. Ultimately, this approach is limited by the impact of correlated uncertainty of the $^{207}Pb/^{206}Pb$ determination, and further progress can only be made by refinement of this parameter.

4.6 CONCLUSION

Although speleothems from the late Quaternary have been increasingly used in palaeoclimate research during the last few decades, exploration of the palaeoclimate potential of individual speleothems older than 500 ka has been hampered by an inability to produce accurate and precise age models within a single sample. Further improvement of the U-Pb method and development of time series for older speleothems is recognized as one of the main scientific goals in speleothem palaeoclimate science (Fairchild and Baker, 2012). The study on stalagmite CC8 from Corchia Cave shows that this is well within the realms of possibility.

The palaeoclimate significance of stalagmite CC8 lies in the three Middle Pleistocene glacial terminations recognized from its stable isotope profile (not presented here). The main goal in this study was to explore how precisely the timing of these events can be established. To achieve this, 56 samples unevenly distributed along the lower portion of

CC8 were dated by the U-Pb method (Woodhead et al., 2006). Five of these were isochron ages and the remaining 51 samples were single-aliquot ages determined using the common-Pb procedure of Woodhead et al. (2012) based on a common Pb composition calculated from the five isochrons plus a further two from the upper part of the stalagmite. For disequilibrium corrections $^{234}U/^{238}U$ ratios for each age point were measured.

With carefully selected samples from the key parts of the speleothem an age-depth model was developed. This model produced age uncertainties to just below 4 kyr (i.e. 0.4% of the accompanying modelled age, at a position through Termination XII). Although the dataset may still be refined, this analysis suggests age uncertainties of 4.1 to 4.9 kyr, 7.3 to 7.5 kyr and 5.2 to 5.9 kyr have been achieved for the onset of Terminations X to XII respectively. Coupled with ongoing refinements in the age model, this level of accuracy shows that CC8 can be used to test orbital theories responsible for these terminations. The results demonstrate the necessity for intensive U-Pb sampling to date late Early Pleistocene terminations. In spite of the large time and analytical effort involved in producing precise and accurate age models, a palette of significant palaeoclimate questions can now be addressed with this method.

Chapter 5

5 OBLIQUITY PACING OF ICE-AGE TERMINATIONS AT THE MIDDLE PLEISTOCENE TRANSITION

The question of which orbital parameters force Earth's climate to switch between glacial and interglacial states is a persistent one in palaeoclimatogy. The lack of radiometrically dated records of glacial terminations is the greatest obstacle to resolving this issue. A speleothem-based U-Pb chronology was applied to the deep-sea sediment record to anchor in radiometric time three terminations coincident with the Middle Pleistocene Transition (MPT), an interval when the pacing of glacial-interglacial cycles shifted from ~40-kyr to ~100-kyr. The results reveal Terminations XII and X are separated by two obliquity cycles, and that Marine Isotope Stages 25 to 22 are not part of a 100-kyr cycle as previously thought. Both terminations started at the same phase of obliquity but show an inconsistent relationship with precession-driven maxima in summer insolation intensity. This implicates obliquity as the major forcing parameter, whereas the role of precession is less conclusive.

5.1 MAIN TEXT

It is almost 40 years since stable oxygen isotope ratios measured from foraminifera in deep-sea sediments provided the first substantive evidence linking changes in solar radiation to the pacing of Pleistocene glacial-interglacial (G-IG) cycles (Hays et al., 1976). These changes, in response to systematic variations in Earth's orbit and axial tilt, affect the amount, intensity and seasonality of insolation received across the Earth's surface, ultimately driving the growth and decay of large continental ice sheets.

The most intriguing feature of Pleistocene G-IG cycles is the change in the period of ice-age 'terminations' – the relatively rapid switches from full glacial to full interglacial conditions – during the Middle Pleistocene Transition (MPT) (1.25-0.7 Ma) (Clark et al., 2006; Head and Gibbard, 2005; Pisias and Moore Jr, 1981). Evidence from deep-sea sediment cores shows that terminations occurred, on average, every ~40 kyr prior to the MPT, but every ~100 kyr in the post-MPT interval (Lisiecki and Raymo, 2005). This shift in period occurred in the absence of any significant change in orbital parameters (Berger and Loutre, 1991), implying that processes internal to the Earth system caused the climate to cross a threshold, leading to longer and more intense glaciations (Mudelsee and Schulz, 1997; Shackleton and Opdyke, 1976).

The marine record suggests that pre-MPT G-IG cycles were paced by changes in Earth's axial tilt, or obliquity (Raymo and Nisancioglu, 2003; Shackleton and Opdyke, 1976), which affects the degree of seasonality in a given year. During obliquity maxima (period: ~41 kyr) the higher latitudes receive more insolation during both Northern and Southern Hemisphere summers, potentially inducing significant ice-sheet ablation in both hemispheres (Berger and Loutre, 1991; Crucifix, 2008). On the other hand, the longer period of post-MPT terminations implies a reduced influence of obliquity and a greater sensitivity of the

cryosphere to changes in eccentricity (period: ~100 kyr) and precession (period: ~21 kyr) (Hays et al., 1976; Paillard, 1998). Whilst eccentricity *per se* has a negligible effect on insolation (Berger and Loutre, 1991), periods of high eccentricity may amplify the effects of precession sufficiently to trigger terminations (Lisiecki, 2010), although, notably, the large deglaciations of Terminations I (TI) and V (TV) occurred at low eccentricity.

Recently, Elderfield et al. (2012) provided compelling evidence that the MPT was abrupt, rather than gradual as previously thought (Clark et al., 2006). They suggest that a sudden increase in global ice volume during Marine Isotope Stage 22 (MIS 22, ~ 900 ka), inferred from a significant increase in the $\delta^{18}O$ of deep ocean water $\delta^{18}O_w$), marks the transition to the '100-kyr world', with MIS 22 - 25 forming part of the first 100-kyr cycle. However, while this work clarifies the onset of the MPT and offers a plausible explanation of its causes, a consensus has yet to be reached regarding which orbital parameter, or combination of parameters, triggered terminations immediately before and after this refined MPT boundary, reinforcing the importance of the MPT itself as a key for resolving the enigma of G-IG cycles (Head and Gibbard, 2005; Clark et al., 2006).

Testing theories of G-IG cycles ultimately requires global ice-volume time series firmly anchored in absolute time. Given the inability to directly date marine sediments beyond the limit of radiocarbon dating, other archives must be utilized. Accordingly, a radiometrically dated $\delta^{18}O$ time series from speleothems that can be used to independently determine the age of terminations at the MPT was compiled. Palaeoclimate proxy records from speleothems spanning the period covered by the uranium-thorium (U-Th) dating method (about the last ~500-600 ka) have already yielded exceptional (Fairchild et al., 2006) absolute radiometric chronologies for past climate events (Wang et al., 2001), including terminations (Cheng et al., 2009; Drysdale et al., 2009). The recent breakthrough in the dating of speleothems via the U-

Pb chronometer (Woodhead et al., 2006, 2012) is explored in this study, which extends this potential into the deep past.

The speleothem record comes from Corchia Cave (Apuane Alps, NW Italy; **Chapter 5.2.1** and **Figure 5-4**) and encompasses three consecutive deglaciations labeled as terminations (TXII to TX). The cave site has strong climate teleconnections with the North Atlantic, from where some of the best-resolved marine-sediment records of the MPT have emerged (Hernández-Almeida et al., 2012; Ruddiman et al., 1989). Previous research at Corchia has revealed that speleothem $\delta^{18}O$ correlates with sea-surface temperature (SST) changes reconstructed from North Atlantic and Western Mediterranean marine sediments during glacial, interglacial and termination states (Drysdale et al., 2004, 2009) through the effect of changes in SST on moisture advection and rainfall amount above the cave site. The validity of this relationship around the MPT is difficult to test, but the relatively large and abrupt changes in environmental conditions through a termination should impart coeval, unambiguous responses in speleothem $\delta^{18}O$ and marine proxies (for further explanation see **Chapter 5.2**). The ability to link continental and marine archives in this way enables the anchoring of the marine-sediment record in absolute time, establishing an accurate and precise radiometric chronology for glacial terminations. This allows comparison of these records with orbital parameters and the testing of orbital hypotheses, independent of any astronomically tuned time scale.

A series of $\delta^{18}O$ measurements (n = 1610; **Chapter 5.2.2**) was made on three stalagmites (CC8, CC119 and CC122) and a subaqueous speleothem (CD3), which were collected from Galleria delle Stalattiti, a chamber located deep inside Corchia Cave. The stalagmites were dated using the U-Pb method (Woodhead et al., 2006, 2012; **Chapter** 4), producing a chronology based on 17 U-Pb isochrons and 59 single-aliquot ages (**Chapter 5.2.3**). Together with the undated isotopic profile of CD3, which grew too slowly to give meaningful U-Pb ages but whose stable isotope patterns unequivocally match those of the three

stalagmites, these yielded a completely replicated $\delta^{18}O$ time series spanning the interval ~970 to ~870 ka. Concordance between each overlapping stable-isotope profile allowed all speleothem ages to be positioned onto a common depth scale relative to stalagmite CC8 (**Chapter 5.2.4**), producing the age-depth model shown in **Figure 5-1**. Almost the entire record is dated with a precision better than 7 kyr (95% confidence interval), after all sources of random and correlated uncertainties have been included (**Chapter** 4), with precision at the start of each of the three terminations better than +/- 4.1 kyr.

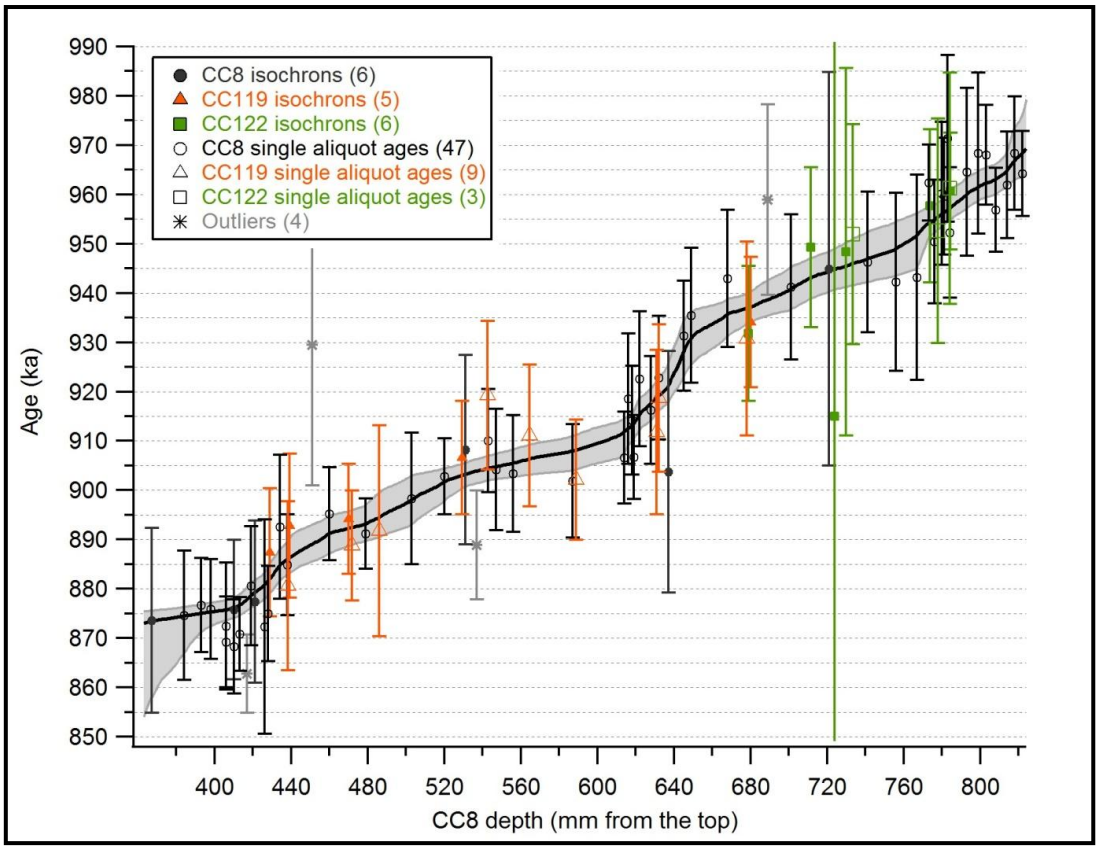

Figure 5-1. The composite age-depth model for Corchia speleothems CC8, CC119 and CC122. The age sampling positions of CC119 and CC122 were transposed to the CC8 depth scale based on the cross-tuning of their $\delta^{18}O$ profiles. The age-depth model was produced using information from 17 isochron and 59 single-aliquot U-Pb ages. The four outliers shown are single-aliquot ages and are not included in the age-depth model. The median model age is represented by the full black line. Age values for each depth position in the isotopic profiles of the three stalagmites were derived from this line (see **Chapter 5.2)**; the grey shaded area represents the 95% confidence interval.

The Corchia speleothem chronology was tied to the SST record from North Atlantic Integrated Ocean Drilling Program (IODP) Sites U1313 (Naafs et al., 2012) and U1314 (Hernández-Almeida et al., 2012), the benthic $\delta^{18}O$ data from Sites U1314 (Hernández-Almeida et al., 2012) and Ocean Drilling Program (ODP) Site 1123 (Elderfield et al., 2012) (SW Pacific), and the LR04 benthic $\delta^{18}O$ stack (Lisiecki and Raymo, 2005) (**Figure 5-2** and **Figure 5-4**) using a tuning procedure explained in the **Chapter 5.2.5**.

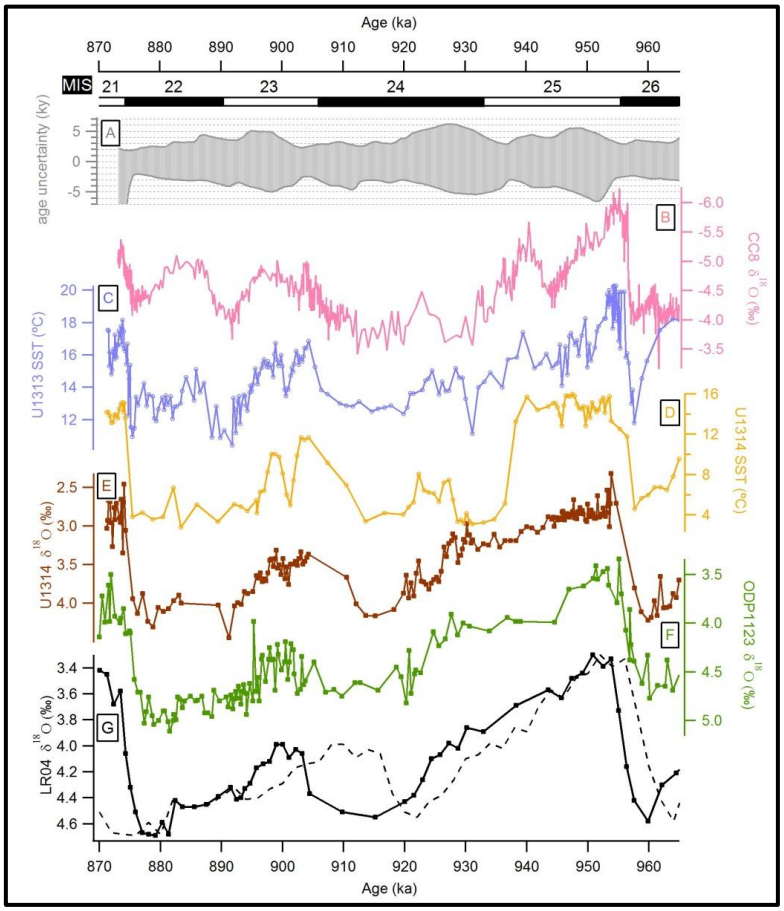

Figure 5-2. Deep-sea sediment data used in this study and placed on the Corchia U-Pb time scale using the procedure described in the SOM. (**A**) Corchia speleothem age-for-age-uncertainty envelope (95%; grey shading), showing age uncertainty variability through the interval of speleothem growth. (**B**) Corchia CC8 speleothem $\delta^{18}O$ time series (pink) based on the composite age-depth model shown in Figure 1. (**C**) $U^{K'}_{37}$ alkenone-based SST record from Site U1313 (blue) (Naafs et al., 2012). (**D**) SST from IODP Site U1314 (orange) estimated by counting foraminifera species *Neogloboquadrina pachyderma* sinistral, *Neogloboquadrina pachyderma* dextral, *Globigerina bulloides*, *Globorotalia inflata* and *Turborotalita quinqueloba* by using a transfer function

based on a back-propagation, artificial neural network (ANN) method (Hernández-Almeida et al., 2012). The link between Corchia $\delta^{18}O$ and SST from marine cores is used to date terminations in benthic $\delta^{18}O$ records from sites (**E**) U1314 (brown) (Hernández-Almeida et al., 2012), (**F**) ODP1123 (green) (Elderfield et al., 2012) and (G) LR04 $\delta^{18}O$ stack (solid black) (Lisiecki and Raymo, 2005). The dashed black line in (**G**) is the LR04 $\delta^{18}O$ stack on the original LR04 chronology, showing the offset with radiometric-based chronology from this study. Marine Isotope Stages (MIS) are shown at the top.

Applying the Corchia chronology to the LR04 stack shows that the commencement of each termination, taken as the point where the benthic $\delta^{18}O$ begins to monotonically decrease above the measurement uncertainty, is dated with a precision of better than 0.5%, with termination XII (TXII) starting at 959.9 +3.4/-2.7 ka, TXI at 909.8 +3.2/-4.1 ka and TX at 877.0 +2.3/-2.1 ka (**Figure 5-2** and **Figure 5-3**). Although there is some imprecision in tying the speleothem and marine records through TXI, this is clearly not the case for TXII and TX. The original LR04 ages for these two latter terminations lie beyond the 95% age uncertainties of speleothem-based LR04 chronology (**Figure 5-2**, panel G), and the age difference across the TXII-to-TX interval based on the data from this study is almost 10 kyr shorter than the original LR04 age model (92 kyr compared to 83 kyr for the speleothem-anchored radiometric chronology). This refines previous assessments that the interval encompassing MIS 25 to 22 constitutes part of the first ~100-kyr cycle (Elderfield et al., 2012; Hernández-Almeida et al., 2012; Pena and Goldstein, 2014) by suggesting that 40-kyr cycles persisted right up to the abrupt MPT, as proposed by (Elderfield et al., 2012), and that the interval between TXII and TX is part of a single G-IG spanning two obliquity cycles. It therefore seems that not only was the MPT abrupt, but also that obliquity pacing of G-IG cycles occurred up to *at least* the transition point identified by (Elderfield et al., 2012).

It has long been recognized that the benthic $\delta^{18}O$ signal contains a significant temperature component (Clark et al., 2006; Shackleton, 1967) and, further, that the isotopic signal is diachronous across

terminations (Skinner and Shackleton, 2005), detracting from its ability to act as a global ice-volume proxy. This implies that the approach of anchoring the benthic $\delta^{18}O$ to a U-Pb speleothem chronology used here may therefore not provide a robust estimate of termination spacing. A recent attempt to remove the temperature component produced a more accurate estimate of long-term global ice volume based on changes in bottom-water composition ($\delta^{18}O_w$) (Elderfield et al., 2012). Consequently, the U-Pb chronology was applied to this $\delta^{18}O_w$ series to determine the presence (if any) of phasing between the benthic $\delta^{18}O$ and $\delta^{18}O_w$ for the two larger terminations, TXII and TX. The results reinforce the findings noted above that two obliquity cycles (79 kyr if $\delta^{18}O_w$ is used as a tuning target versus 80 kyr in the case of benthic $\delta^{18}O$) separate these terminations, strengthening the argument against a 100-kyr cycle (**Figure 5-15**).

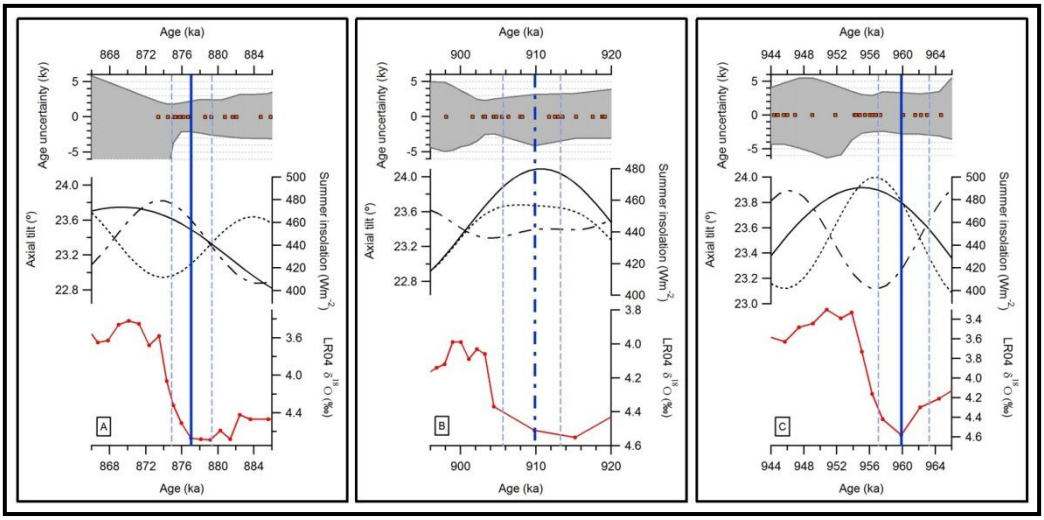

Figure 5-3. The LR04 benthic δ18O for the three terminations investigated here (red; TX- panel A, TXI- panel B and TXII-panel C) anchored to the Corchia U-Pb chronology and compared to orbital parameters (Berger and Loutre,1991) (obliquity: solid line; summer insolation for 65°N: fine dashed line; summer insolation for 65°S: coarse dashed line. NB: the range of summer insolation and LR04 benthic δ18O y-axis values is different for each plot.) The upper portion of each panel shows the age-for-age uncertainty (95%) plot with positions of model U-Pb ages (orange rectangles) to illustrate the density of age determinations. Blue vertical lines mark the onset time for each termination recorded in the LR04 stack based on the point where the monotonic decrease above measurement uncertainty in δ18O commences. The 95% age

uncertainties are shown by blue dashed lines. The onset of TXI is presented with a coarse dashed line to emphasize ambiguity in determination of the timing of this termination.

Finally, the results provide an opportunity to test the recent modeling by (Huybers, 2011) suggesting that a combination of obliquity and precession drove terminations over the last million years. Under this model, 100-kyr G-IG cycles actually comprise clusters of two (80 kyr) or three (~120 kyr) obliquity cycles (Huybers and Wunsch, 2005), and terminations are triggered during periods of strong insolation forcing, with the spacing between terminations paced by obliquity but the exact timing within a given obliquity cycle occurring when the Earth is at perihelion during the Northern Hemisphere summer solstice (Huybers, 2011). Whilst results of this study show that terminations TXII and TX both started at points of relatively high tilt angle, the phasing with respect to precession is the opposite (**Figure 5-3**). TXII started when Northern Hemisphere summer insolation was approaching maximum intensities, whereas TX started when Southern Hemisphere summer insolation was approaching maximum intensities. This implicates obliquity as the principal driver of both terminations, leaving a more ambiguous role for precession.

The results highlight that the climate system was still characterized by 40-kyr cycles right up to the MPT, and raises the tantalizing question: to what extent were terminations after the MPT also paced by obliquity? Speleothems have the potential to offer critical perspectives in this next frontier, given their unique combination of both amenability to precise radiometric dating, and preservation of multiple climate proxies.

5.2 SUPPLEMENTARY TEXT

5.2.1 DESCRIPTION OF SAMPLES

Three stalagmites (CC8, CC119 and CC122) were collected as broken pieces from Galleria delle Stalattiti, located ~1 km from the nearest entrance of the Corchia Cave system, and 400 m below the surface) (**Figure 5-4**).

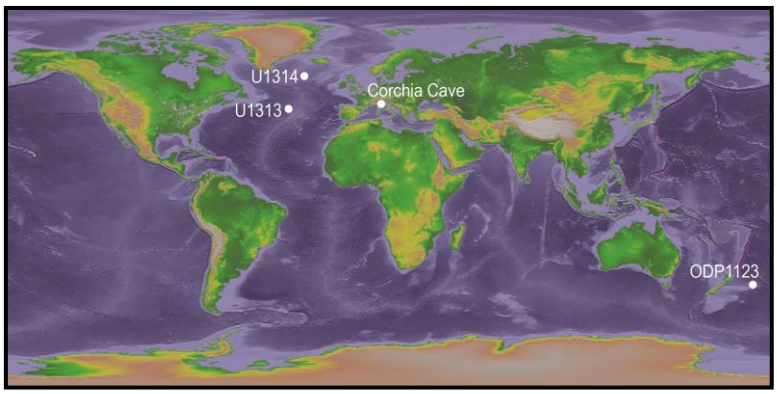

Figure 5-4. Map indicating positions of Corchia Cave in Italy and IODP Sites U1313, U1314 in North Atlantic and ODP Site 1123 in South West Pacific.

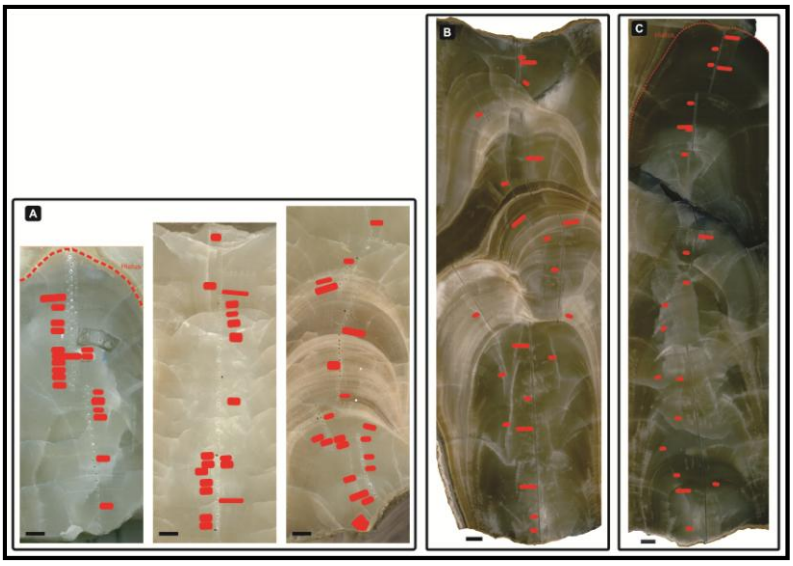

Figure 5-5. Photos of sample slabs with U-Pb dating positions indicated (red rectangles) and showing stable isotope sampling tracks along growth axes. Only portions below hiatuses in CC8 and CC119 were used in this study.

The cave gallery where the samples were collected is characterized by a relatively stable microclimate, with seasonal temperature oscillations within 1°C and relative humidity close to 100% (Baneschi et al., 2011). After their removal from the cave, the stalagmites were halved along their vertical growth axis, polished and mounted into resin to prevent breaks during further sampling.

The stalagmites are composed of translucent to opaque calcite, white to grey in colour (**Figure 5-5**). Petrographic examination of polished slabs was undertaken at the University of Newcastle (Australia) using a Zeiss optical microscope. The results indicate changes between a compact and open acicular fabric (Frisia et al., 2000). The acicular fabric is consistent with X-ray diffraction (XRD) analyses of eight samples performed at La Trobe University (Melbourne, Australia), using a Siemens D5000 diffractometer equipped with a Cu Kα source, operating at 40kV and 30mA in continual scan mode and with a speed of 1°/min from 4° to 70° 2Θ. Eva software was used for qualitative mineralogical analysis and quantitative analysis was based on the reference-intensity-ratio (RIR) method (Bruker, 2010). The results reveal that the speleothems are composed of, on average, 86% of low Mg-calcite and ~14% of high-Mg calcite, excluding one sample being composed exclusively of high-Mg calcite. This high-Mg calcite corresponds to the beginning of the MIS 22, possibly testifying prolonged water-rock interaction caused by lower recharge to the cave during this glacial. Furthermore, the system did not reach the threshold in Mg/Ca ratio in drip water and supersaturation needed to form aragonite, as confirmed by XRD analyses. There are no obvious signs of diagenetic alteration. Two pronounced hiatuses were recorded, one in CC8 and another in CC119, separating each stalagmite into two growth phases. For the purpose of this study, only data from the lower part of both of these speleothems are discussed. There were no discernible changes in petrography during the time period corresponding to the glacial terminations.

The hiatus in stalagmite CC8 likely occurred at the end of Termination X and the beginning of interglacial MIS21. Stable isotope data (see below) from a core (CD3) taken from a subaqueous speleothem in the same cave chamber were used to verify this hypothesis. It is clear from this continuously growing subaqueous speleothem that the hiatus in CC8 post-dates Termination X. Although the CD3 core cannot be dated reliably by the U-Pb dating method owing to its very slow growth rate (26 cm in ~1 Ma, based on preliminary $^{234}U/^{238}U$ ages), it is clear that, in its deepest part, it replicates the isotopic signal from the three stalagmites, including that observed through Termination X (**Figure 5-9**).

5.2.2 STABLE ISOTOPE ANALYSES

Powder samples for stable isotope analysis were drilled at 1 mm resolution along the growth axis of each stalagmite using a tungsten carbide dental drill attached to either a Taig CNC micromilling lathe or a Dremel hand drill. Through the oldest and youngest parts of CC8, micromilling at a resolution of 250 microns perpendicular to the growth axis was performed. Stable isotope analyses were conducted at the Scottish Universities Environmental Research Centre (East Kilbride, UK), The University of Newcastle (Australia) and The University of Melbourne (Australia) on the same model (AP2003/GV2003) mass spectrometer, operated in continuous-flow mode. The results are expressed in delta notation relative to the VPDB standard. Long-term analytical precision of in-house reference materials of Carrara marble, previously calibrated to international reference materials NBS-18 and NBS-19, was better than 0.05 and 0.1‰ (1σ) for $\delta^{13}C$ and $\delta^{18}O$ respectively. Analyses were repeated where $\delta^{18}O$ differed by more than 0.4‰ between adjacent samples.

The CD3 core was microsampled at 200-µm increments using a New Wave Micromill and analysed by continuous-flow IRMS at the Institut für Geologie at the Universität Innsbruck using a Thermo Fisher Delta^{plus}XL (Spötl and Vennemann, 2003). The long-term analytical uncertainty for $\delta^{18}O$ and $\delta^{13}C$ is 0.08‰ and 0.06‰ respectively (Spötl, 2011).

5.2.3 U-Pb DATING, $^{234}U/^{238}U$ INITIAL DISEQUILIBRIUM AND AGE-DEPTH MODELLING

Samples for U-Pb dating (red rectangles on **Figure 5-5**) were extracted using a dental air drill fixed to a manually navigated milling machine with a tiltable stage, housed at the University of Melbourne. Despite the high U and low common Pb content of these samples (**Table 5-1** and **Table 5-2**), their relatively young age required the use of subsamples between 50 and 200 mg to allow for accurate measurement of the radiogenic Pb component. U and Pb were chemically separated following the method described in (Woodhead et al., 2006). Isotopic ratios were measured on a Nu Instruments Nu Plasma multicollector-inductively coupled plasma mass spectrometer (MC-ICPMS) at The University of Melbourne. The NIST SRM981 reference material for Pb and an internal $^{238}U/^{235}U$ ratio of 137.88 for U were used for mass-fractionation corrections, employing software developed in-house for this purpose. Blank corrections for Pb (5-10 pg), together with isotope-dilution calculations, were performed using the algorithm published in (Schmitz and Schoene, 2007). U blanks were negligible.

The majority of previous studies where the U-Pb dating method for speleothems has been employed have used a variety of isochron approaches to calculate sample ages (Richards et al., 1998; Woodhead et al., 2006). Although it is undoubtedly the most robust, this approach is difficult to employ in high-resolution palaeoclimate studies involving

numerous age determinations because it uses large amounts of sample, and is very time intensive. Following successful determination of many isochrons, a single-aliquot approach was instead adopted to increase the resolution of the age model. This methodology has been discussed elsewhere (e.g. Woodhead et al., 2012; **Chapter** 4) but, in brief, where very stringent conditions can be met (i.e. where common Pb compositions either in one speleothem or in the same cave site are well constrained and when the speleothems are relatively radiogenic) the mean estimate of common Pb based on previously determined isochron data, and its uncertainty, can be used in the calculation of model ages based upon single-aliquot analyses (Woodhead et al., 2012; **Chapter** 4). The U-Pb dating of CC8 was the first documented example of using this method and the data presented in **Chapter** 4 have since been updated taking into account an improved estimate of the common-Pb composition for these stalagmites by inclusion of an additional isochron for CC8 and 13 isochrons for stalagmites CC119 and CC122 into the previous dataset (**Figure 5-6**).

Table 5-1. U-Pb dating results for isochrons analyses performed on CC8, CC119 and CC122 stalagmites.

Sample ID	Depth of sample centre from the top (mm)	Depth error ± 100% (mm)	Total Pb (ppb)	U (ppb)	$^{238}U/^{206}Pb$	$^{238}U/^{206}$ Pb 2σ error (%)	$^{207}Pb/^{206}Pb$	$^{207}Pb/^{206}$ Pb 2σ error (%)	MSWD	$(^{234}U/^{238}U)$ (measured)	$(^{234}U/^{238}U)$ (measured) 2σ error	Age Ma corr. for $(^{234}U/^{238}U)i$	Age error 2σ (Myr)
CC8-3	367.0	4.0							227.00	0.9788	0.0015	**0.874**	**0.01**
CC8-3-1			2.29	7857	6060.97	0.53	0.323	0.931					
CC8-3-2			2.35	7489	5836.35	0.29	0.343	0.424					
CC8-3-3			1.54	7103	7011.64	0.54	0.247	1.400					
CC8-3-4			1.60	6965	6827.80	0.57	0.260	1.350					
CC8-3-5			2.14	7653	6203.86	0.41	0.314	0.739					
CC8-3-6			2.69	7469	5385.32	0.36	0.375	0.482					
CC119-1	428.8	5.0							0.94	0.9722	0.0018	**0.887**	**0.01**
CC119-1-1			2.68	4698	4196.47	3.07	0.484	2.701					
CC119-1-3			4.62	4870	2819.72	1.12	0.592	0.597					
CC119-1-5			5.37	4969	2541.47	1.10	0.614	0.526					
CC119-1-6			7.79	5110	1899.71	0.73	0.665	0.268					
CC119-1-9			9.66	5016	1547.79	0.61	0.692	0.190					
CC119-1-12			0.87	4590	7946.35	5.16	0.186	20.032					
CC119-2	439.2	5.0							0.48	0.9708	0.0017	**0.893**	**0.01**
CC119-2-2			5.17	4800	2569.91	2.07	0.610	1.010					
CC119-2-4			5.05	5017	2695.93	1.37	0.601	0.702					
CC119-2-7			5.47	5285	2635.16	1.31	0.607	0.652					
CC119-2-10			4.06	5419	3391.08	1.45	0.547	0.958					
CC119-2-12			2.90	5465	4397.10	2.65	0.468	2.490					
CC119-2-14			2.02	5055	5327.28	3.73	0.395	4.849					
CC119-3	470.0	5.0							0.15	0.9743	0.0016	**0.894**	**0.01**
CC119-3-2			2.12	8442	6758.46	2.72	0.270	6.427					
CC119-3-4			4.23	8724	4581.01	1.60	0.446	1.663					
CC119-3-6			5.80	7538	3300.15	1.32	0.549	0.866					
CC119-3-8			5.06	7338	3580.97	1.26	0.526	0.918					
CC119-3-11			3.09	8801	5618.58	2.20	0.363	3.306					
CC119-4	529.2	5.0							0.66	0.9741	0.0016	**0.907**	**0.01**
CC119-4-1			0.80	5477	8776.15	6.39	0.100	51.873					
CC119-4-3			1.10	6025	7845.43	3.88	0.176	16.178					

CC119-4-5			3.93	6475	3931.95	1.86	0.494	1.562				
CC119-4-8			8.38	6153	2089.66	1.37	0.642	0.567				
CC119-4-12			10.19	5605	1622.55	0.85	0.680	0.285				
CC119-6	680.1	5.0							3.60	0.9756	0.0016	**0.934**	**0.01**
CC119-6-2			2.41	5361	4781.96	2.74	0.412	3.300				
CC119-6-4			32.67	4554	449.91	0.28	0.775	0.057				
CC119-6-6			47.81	4099	281.01	0.21	0.790	0.027				
CC119-6-8			42.49	4158	319.80	0.24	0.786	0.033				
CC119-6-10			19.69	4830	775.56	0.71	0.748	0.152				
CC119-6-12			5.79	5286	2489.53	1.58	0.602	0.801				
CC122-1	679.0	5.0							1.40	0.9773	0.0019	**0.932**	**0.01**
CC122-1-2			1.78	4511	5165.31	3.35	0.376	4.685				
CC122-1-4			1.82	5083	5472.11	2.85	0.351	4.530				
CC122-1-5			2.56	5246	4517.17	2.51	0.431	2.770				
CC122-1-6			2.59	5205	4512.01	3.42	0.432	3.780				
CC122-1-8			1.59	5261	5988.35	2.68	0.308	5.241				
CC122-1-10			1.44	5395	6446.17	3.67	0.268	8.777				
CC122-1-12			1.48	5161	6243.92	3.74	0.289	8.016				
CC122-1-14			5.04	4337	2380.72	1.61	0.616	0.763				
CC122-4	711.5	5.0							0.43	0.9756	0.0019	**0.949**	**0.01**
CC122-4-1			1.74	6120	6147.11	2.50	0.289	5.347				
CC122-4-3			9.29	7798	2299.84	0.66	0.617	0.312				
CC122-4-6			9.85	7484	2125.97	1.04	0.632	0.458				
CC122-4-8			10.02	7466	2089.48	0.90	0.635	0.387				
CC122-4-10			3.61	7290	4441.63	1.96	0.435	2.137				
CC122-4-12			2.13	5619	5308.06	3.56	0.360	5.430				
CC122-2	724.1	5.0							10.00	0.9775	0.0014	**0.915**	**0.09**
CC122-2-2			16.15	5391	1028.52	0.57	0.724	0.147				
CC122-2-4			19.58	5298	845.46	0.43	0.740	0.096				
CC122-2-6			16.62	5180	964.40	0.47	0.730	0.112				
CC122-2-8			16.00	4924	954.46	0.60	0.730	0.145				
CC122-2-10			13.88	4817	1063.97	0.53	0.720	0.141				
CC122-2-12			15.04	4782	983.80	0.65	0.728	0.158				
CC122-2-14			18.39	4724	804.31	0.43	0.741	0.095				
CC122-2-16			15.28	4723	958.14	0.51	0.731	0.124				
CC122-5	730.0	5.0							5.00	0.9785	0.0016	**0.948**	**0.03**
CC122-5-2			4.50	6720	3625.62	2.62	0.498	2.159				

CC122-5-3			5.98	6554	2873.07	1.82	0.567	1.098					
CC122-5-5			4.18	6790	3814.85	1.78	0.483	1.573					
CC122-5-6			6.38	6890	2799.26	0.94	0.569	0.556					
CC122-5-7			6.40	7106	2862.17	0.86	0.565	0.519					
CC122-5-9			7.49	7307	2602.10	1.38	0.587	0.753					
CC122-6	773.6	5.0							0.37	0.9780	0.0019	**0.958**	**0.01**
CC122-6-2			2.74	7589	5354.55	2.78	0.344	4.570					
CC122-6-5			4.22	8515	4352.59	1.10	0.432	1.208					
CC122-6-9			20.94	8309	1196.49	0.39	0.706	0.110					
CC122-6-11			11.96	8783	2044.34	0.54	0.633	0.230					
CC122-6-14			2.87	7526	5164.95	2.10	0.362	3.182					
CC122-7	784.5	5.0							1.30	0.9784	0.0015	**0.961**	**0.01**
CC122-7-2			2.60	7559	5459.44	2.01	0.334	3.452					
CC122-7-4			2.50	7544	5540.20	1.67	0.326	2.989					
CC122-7-7			1.38	8693	7746.63	2.19	0.133	12.709					
CC122-7-10			1.25	8007	7781.12	1.91	0.131	11.364					
CC122-7-13			1.91	6786	6102.31	2.65	0.280	5.958					
CC122-3	n.a.	n.a.							1.50	0.9777	0.0011	**0.978**	**0.01**
CC122-3-2			0.88	5185	7766.37	5.24	0.122	33.763					
CC122-3-4			1.38	6358	6910.68	3.28	0.202	11.491					
CC122-3-5			1.84	7474	6442.05	2.07	0.243	5.655					
CC122-3-6			1.85	7459	6426.64	2.17	0.245	5.896					
CC122-3-8			1.89	6912	6103.51	2.01	0.271	4.719					
CC122-3-9			1.71	6282	6165.42	2.31	0.269	5.512					
CC122-3-10			1.55	5991	6315.85	2.66	0.253	6.897					
CC122-3-11			1.33	5656	6663.19	3.67	0.221	11.431					

* Note: the MSWDs are calculated by Isoplot (Ludwig, 2001) based upon the assumptions of a model 1 or 2 fit.

Table 5-2. U-Pb results for single aliquot ages. Outliers are marked with ^{O}. Samples with $^{238}U/^{206}Pb$ ratio lower than 2500 are rejected from the age-depth model and marked with ^{R}.

Sample ID	Depth from the top (mm)	± 100% depth error (mm)	Total Pb (ppb)	U (ppb)	$^{238}U/^{206}Pb$	$^{238}U/^{206}Pb$ 2σ error (%)	$^{207}Pb/^{206}Pb$	$^{207}Pb/^{206}Pb$ 2σ error (%)	($^{230}Th/^{232}Th$) (measured)	($^{234}U/^{238}U$) (measured)	($^{234}U/^{238}U$) (measured) 2σ error (%)	**Age Ma corr. for ($^{234}U/^{238}U$)i**	**Age 2σ error (Myr)**
CC8-64	383.5	2.5	1.92	5372	5684.76	4.81	0.351	7.637	85499	0.9799	0.0014	**0.875**	**0.013**
CC8-63	393.0	2.5	0.89	6321	8591.53	2.86	0.116	19.461	60064	0.9790	0.0016	**0.877**	**0.010**
CC8-62	398.0	2.5	1.57	7202	7109.84	2.64	0.227	7.950	64182	0.9822	0.0018	**0.876**	**0.010**
CC8-87	406.0	2.5	1.55	6709	7026.30	3.44	0.239	9.605	154902	0.9816	0.0014	**0.869**	**0.009**
CC8-61	406.0	1.0	7.02	3495	4575.96	3.70	0.440	3.957	69119	0.9807	0.0013	**0.872**	**0.013**
CC8-21	410.0	2.0	3.05	9329	5676.34	0.45	0.351	0.688	36661	0.9816	0.0018	**0.868**	**0.010**
CC8-60	413.0	2.5	2.06	7084	6139.49	1.35	0.313	2.565	31898	0.9810	0.0013	**0.871**	**0.007**
CC8-59 ^{O}	417.0	2.5	2.70	6881	5187.30	1.47	0.389	1.963	91919	0.9832	0.0012	**0.863**	**0.008**
CC8-58	419.0	2.5	1.17	6235	7578.41	2.09	0.191	7.855	69454	0.9803	0.0021	**0.881**	**0.012**
CC8-86	426.0	1.0	2.14	4899	5207.73	8.89	0.386	12.059	21046	0.9820	0.0020	**0.872**	**0.022**
CC8-31	428.0	2.5	1.43	5956	6520.20	2.24	0.273	4.960	69223	0.9830	0.0018	**0.875**	**0.010**
CC119-15 ^{R}	433.1	5.0	10.0	5993	1753.90	0.81	0.677	0.277	62424	0.9714	0.0016	**0.884**	**0.033**
CC8-85	434.0	1.5	1.98	5877	5859.68	6.58	0.312	12.625	39479	0.9853	0.0012	**0.893**	**0.015**
CC8-12	437.5	2.0	1.85	5934	5734.93	0.70	0.330	1.200	138000	0.9841	0.0019	**0.885**	**0.010**
CC119-16	438.3	5.0	4.80	6159	3309.01	1.67	0.556	1.059	34937	0.9712	0.0016	**0.881**	**0.017**
CC119-9 ^{O}	451.0	5.0	2.51	3239	3304.94	2.34	0.542	1.580	36739	0.9727	0.0030	**0.929**	**0.028**
CC8-11	459.5	2.0	2.97	6912	4750.37	0.35	0.406	0.402	117579	0.9850	0.0015	**0.895**	**0.009**
CC119-17	471.7	5.0	2.13	7785	6450.20	2.09	0.299	4.258	46769	0.9741	0.0016	**0.889**	**0.011**
CC8-32	479.0	2.0	2.53	7631	5527.61	0.89	0.342	1.460	37996	0.9849	0.0012	**0.891**	**0.007**
CC119-18	485.9	5.0	8.46	8242	2633.94	0.94	0.603	0.475	365416	0.9739	0.0017	**0.892**	**0.021**
CC8-10	503.0	2.0	3.42	7343	4493.98	0.31	0.423	0.330	92661	0.9869	0.0024	**0.898**	**0.013**
CC8-27	519.5	3.5	1.10	6124	7328.15	1.21	0.180	4.860	18131	0.9850	0.0014	**0.903**	**0.008**
CC119-19 ^{R}	534.4	5.0	10.1	5729	1654.79	0.67	0.678	0.228	42219	0.9766	0.0019	**0.898**	**0.032**
CC8-33 ^{O}	537.0	2.0	2.33	5101	4575.82	0.73	0.425	0.821	40329	0.9844	0.0019	**0.889**	**0.011**
CC8-91	542.5	2.0	2.80	7769	5460.20	3.40	0.346	5.529	81382	0.9821	0.0010	**0.910**	**0.010**
CC119-20	542.7	5.0	0.96	4776	7514.34	3.77	0.200	13.390	142232	0.9734	0.0018	**0.919**	**0.015**

Sample ID	Depth from the top (mm)	± 100% depth error (mm)	Total Pb (ppb)	U (ppb)	$^{238}U/^{206}Pb$	$^{238}U/^{206}Pb$ 2σ error (%)	$^{207}Pb/^{206}Pb$	$^{207}Pb/^{206}Pb$ 2σ error (%)	($^{230}Th/^{232}Th$) (measured)	($^{234}U/^{238}U$) (measured)	($^{234}U/^{238}U$) (measured) 2σ error (%)	**Age Ma corr. for ($^{234}U/^{238}U$)i**	**Age 2σ error (Myr)**
CC8-34	546.5	2.0	3.37	7726	4732.16	0.44	0.415	0.512	105476	0.9803	0.0018	**0.904**	**0.012**
CC8-9	556.0	2.0	2.07	6653	5711.02	0.34	0.325	0.344	48241	0.9831	0.0020	**0.903**	**0.012**
CC119-11	564.6	5.0	2.15	6222	5661.74	3.02	0.348	4.860	188804	0.9754	0.0018	**0.911**	**0.014**
CC8-29	586.5	2.0	5.88	8061	3342.69	0.44	0.527	0.327	133538	0.9837	0.0010	**0.902**	**0.012**
CC119-21	588.7	5.0	2.68	7236	5388.43	1.64	0.376	2.327	503023	0.9749	0.0016	**0.902**	**0.012**
CC8-70	613.5	2.5	1.82	6908	6354.81	2.02	0.270	4.763	78685	0.9824	0.0014	**0.907**	**0.009**
CC8-90	616.0	1.5	1.36	7045	7664.03	7.38	0.150	37.392	39758	0.9825	0.0011	**0.919**	**0.013**
CC8-69	617.5	2.5	1.83	6723	6230.14	1.69	0.280	3.802	29147	0.9815	0.0017	**0.914**	**0.011**
CC8-35	619.0	2.0	1.55	5412	5934.37	1.40	0.304	2.790	54097	0.9832	0.0013	**0.907**	**0.009**
CC8-8	622.0	2.0	0.80	5972	8130.74	0.55	0.112	3.780	54558	0.9813	0.0022	**0.923**	**0.014**
CC8-68	627.5	2.5	1.38	5270	6439.73	3.77	0.256	9.625	55850	0.9829	0.0014	**0.916**	**0.011**
CC119-22	630.8	7.0	5.05	7862	3727.57	0.92	0.508	0.726	250654	0.9748	0.0020	**0.912**	**0.017**
CC8-67	631.5	2.5	2.19	4989	4778.54	2.21	0.398	2.838	26392	0.9824	0.0017	**0.923**	**0.013**
CC119-5	632.0	7.0	1.52	6775	7064.90	3.11	0.230	9.143	101463	0.9749	0.0019	**0.919**	**0.015**
CC8-66	645.0	2.5	2.04	5229	5106.22	2.72	0.357	4.202	52320	0.9854	0.0014	**0.931**	**0.011**
CC119-12 R	645.0	7.0	29.1	5527	605.69	0.30	0.763	0.054	69409	0.9738	0.0020	**0.938**	**0.108**
CC8-65	649.0	2.5	1.14	4600	6538.01	3.69	0.233	10.698	25374	0.9836	0.0018	**0.936**	**0.014**
CC119-23 R	655.3	7.0	11.9	7135	1729.74	0.56	0.671	0.197	300353	0.9748	0.0016	**0.920**	**0.031**
CC8-79	668.0	1.5	1.38	5129	6353.80	6.24	0.232	18.218	79381	0.9874	0.0014	**0.943**	**0.014**
CC119-24 R	668.6	5.0	17.4	5819	1027.67	0.38	0.727	0.094	181297	0.9757	0.0014	**0.930**	**0.057**
CC122-15 R	677.3	5.0	18.4	6762	1123.09	0.40	0.719	0.106	227910	0.9760	0.0015	**0.935**	**0.052**
CC119-25	678.1	5.0	4.18	5768	3421.23	1.50	0.527	1.082	180919	0.9754	0.0019	**0.931**	**0.020**
CC122-16 R	685.5	5.0	10.2	6410	1818.96	1.51	0.659	0.571	41147	0.9753	0.0019	**0.947**	**0.033**
CC119-13 R	687.7	5.0	25.4	6412	791.91	0.41	0.746	0.088	243510	0.9746	0.0019	**0.950**	**0.082**
CC8-89 O	689.0	1.5	1.51	5743	6463.31	7.21	0.218	22.851	79510	0.9858	0.0021	**0.959**	**0.019**
CC122-8 R	699.0	5.0	11.5	7201	1794.34	0.73	0.661	0.274	44502	0.9755	0.0017	**0.946**	**0.034**
CC8-38	701.0	2.5	2.49	5651	4676.79	2.72	0.382	3.752	25360	0.9889	0.0021	**0.941**	**0.015**
CC122-17 R	715.6	5.0	11.6	5147	1335.02	0.80	0.699	0.239	151687	0.9763	0.0016	**0.951**	**0.043**
CC122-18	733.3	5.0	7.30	7032	2565.03	0.78	0.592	0.414	340828	0.9770	0.0016	**0.952**	**0.022**

Sample ID	Depth from the top (mm)	± 100% depth error (mm)	Total Pb (ppb)	U (ppb)	$^{238}U/^{206}Pb$	$^{238}U/^{206}Pb$ 2σ error (%)	$^{207}Pb/^{206}Pb$	$^{207}Pb/^{206}Pb$ 2σ error (%)	($^{230}Th/^{232}Th$) (measured)	($^{234}U/^{238}U$) (measured)	($^{234}U/^{238}U$) (measured) 2σ error (%)	**Age Ma corr. for ($^{234}U/^{238}U$)i**	**Age 2σ error (Myr)**
CC8-40	741.0	2.5	4.63	4595	3651.10	1.58	0.485	0.992	53272	0.9844	0.0017	**0.946**	**0.014**
CC122-9 R	741.7	5.0	22.3	7157	986.09	0.40	0.727	0.097	219311	0.9763	0.0025	**0.979**	**0.068**
CC122-19 R	752.3	5.0	9.04	7390	2242.67	0.70	0.619	0.326	84778	0.9766	0.0016	**0.964**	**0.027**
CC8-75	756.0	1.5	2.93	4922	3953.69	4.80	0.453	4.839	63139	0.9870	0.0019	**0.942**	**0.018**
CC8-74	767.0	2.0	4.98	4815	2567.49	1.69	0.580	0.961	43823	0.9863	0.0022	**0.943**	**0.021**
CC122-10 R	767.5	5.0	9.99	7764	2145.99	0.58	0.625	0.263	52189	0.9770	0.0017	**0.975**	**0.029**
CC8-6	773.0	2.0	1.38	4454	5471.66	0.87	0.298	1.770	58759	0.9887	0.0011	**0.962**	**0.008**
CC122-20 R	775.4	5.0	12.5	7109	1643.56	0.64	0.667	0.228	319641	0.9751	0.0016	**1.015**	**0.042**
CC8-57	775.5	2.5	1.55	5677	5983.79	2.25	0.253	5.820	32966	0.9896	0.0019	**0.950**	**0.013**
CC122-21	777.8	5.0	3.00	7592	5055.91	2.23	0.371	3.233	159506	0.9792	0.0029	**0.953**	**0.023**
CC8-54	780.0	2.5	1.61	5652	5400.31	1.66	0.307	3.251	39108	0.9884	0.0022	**0.960**	**0.014**
CC8-42	781.0	2.0	2.19	5708	4880.67	0.96	0.355	1.490	16445	0.9885	0.0017	**0.960**	**0.012**
CC122-12 R	781.5	5.0	14.8	8091	1586.74	0.47	0.671	0.162	287802	0.9757	0.0018	**1.018**	**0.044**
CC8-73	782.5	2.0	2.77	6072	4648.23	5.22	0.375	7.428	79031	0.9875	0.0016	**0.971**	**0.017**
CC8-53	784.0	2.5	1.34	5473	6277.53	1.90	0.227	5.708	39955	0.9891	0.0021	**0.952**	**0.013**
CC122-22	784.0	5.0	1.79	8035	6793.83	2.24	0.218	7.061	142317	0.9781	0.0028	**0.961**	**0.024**
CC8-72	793.0	1.5	2.27	6022	5235.76	6.51	0.313	12.425	21628	0.9906	0.0017	**0.965**	**0.017**
CC8-71	799.0	1.5	2.67	5046	4165.55	3.33	0.421	3.859	93897	0.9879	0.0019	**0.968**	**0.016**
CC8-56	802.5	2.5	2.17	4705	4487.73	2.53	0.387	3.424	10013	0.9892	0.0010	**0.968**	**0.010**
CC8-43	807.5	2.5	4.05	6109	6137.32	1.79	0.230	4.500	23030	0.9912	0.0014	**0.957**	**0.009**
CC8-5	813.5	2.0	1.76	5427	5534.28	4.02	0.285	8.790	30158	0.9908	0.0012	**0.962**	**0.011**
CC8-52	818.0	2.5	1.46	6094	6353.26	3.41	0.206	11.650	14166	0.9900	0.0016	**0.968**	**0.011**
CC8-51	821.5	2.5	1.27	5983	6617.00	2.36	0.184	9.333	35076	0.9899	0.0012	**0.964**	**0.009**
CC122-24 R	n.a.	n.a.	12.6	8155	1835.31	0.90	0.647	0.360	200552	0.9775	0.0016	**1.007**	**0.034**
CC122-14 R	n.a.	n.a.	10.1	8246	2216.07	0.97	0.613	0.466	326379	0.9784	0.0019	**0.994**	**0.028**

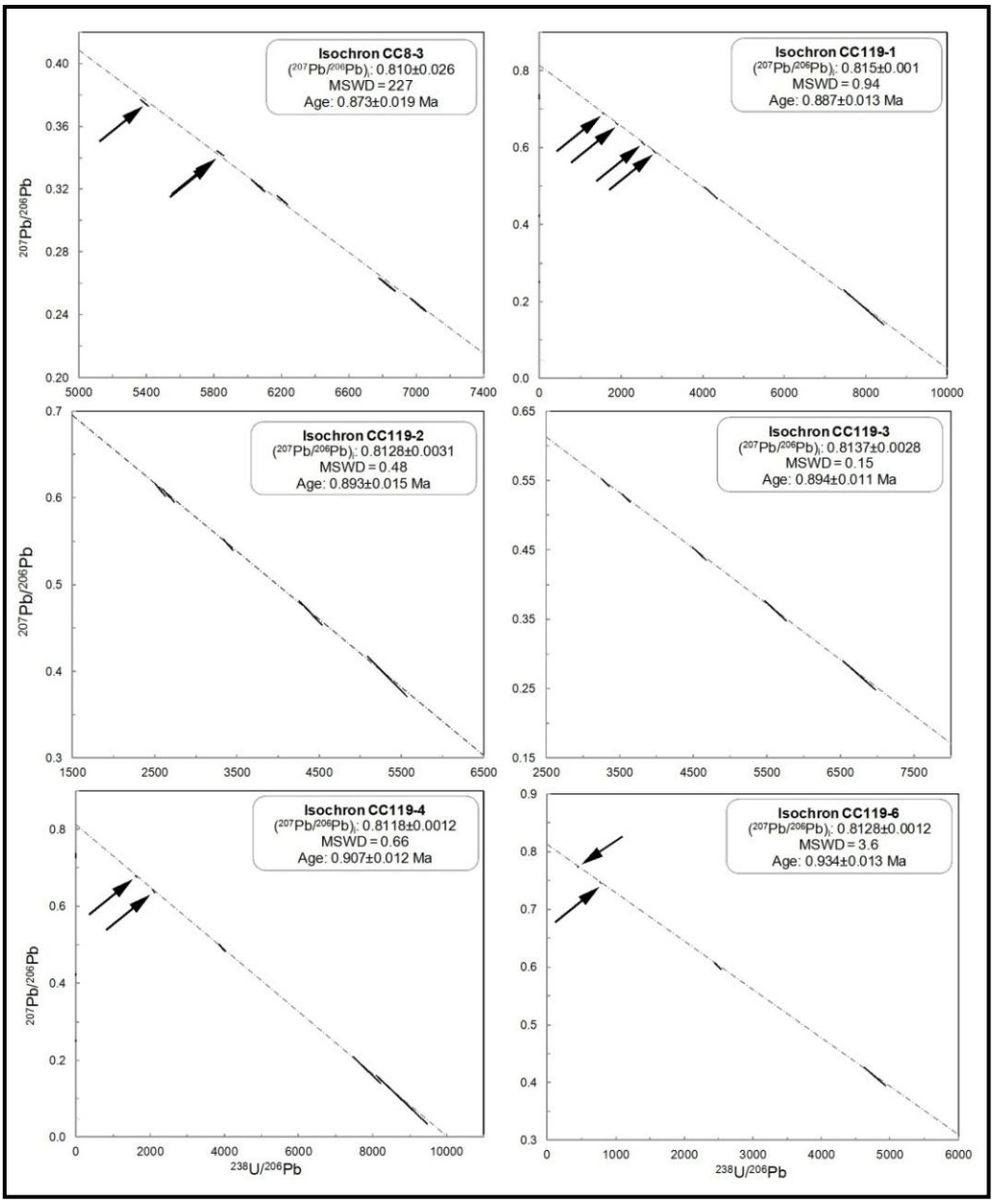

Figure 5-6. Plots of CC8-3 and all CC119 isochrons. All ages are corrected for initial disequilibrium in the U-Pb decay chain.

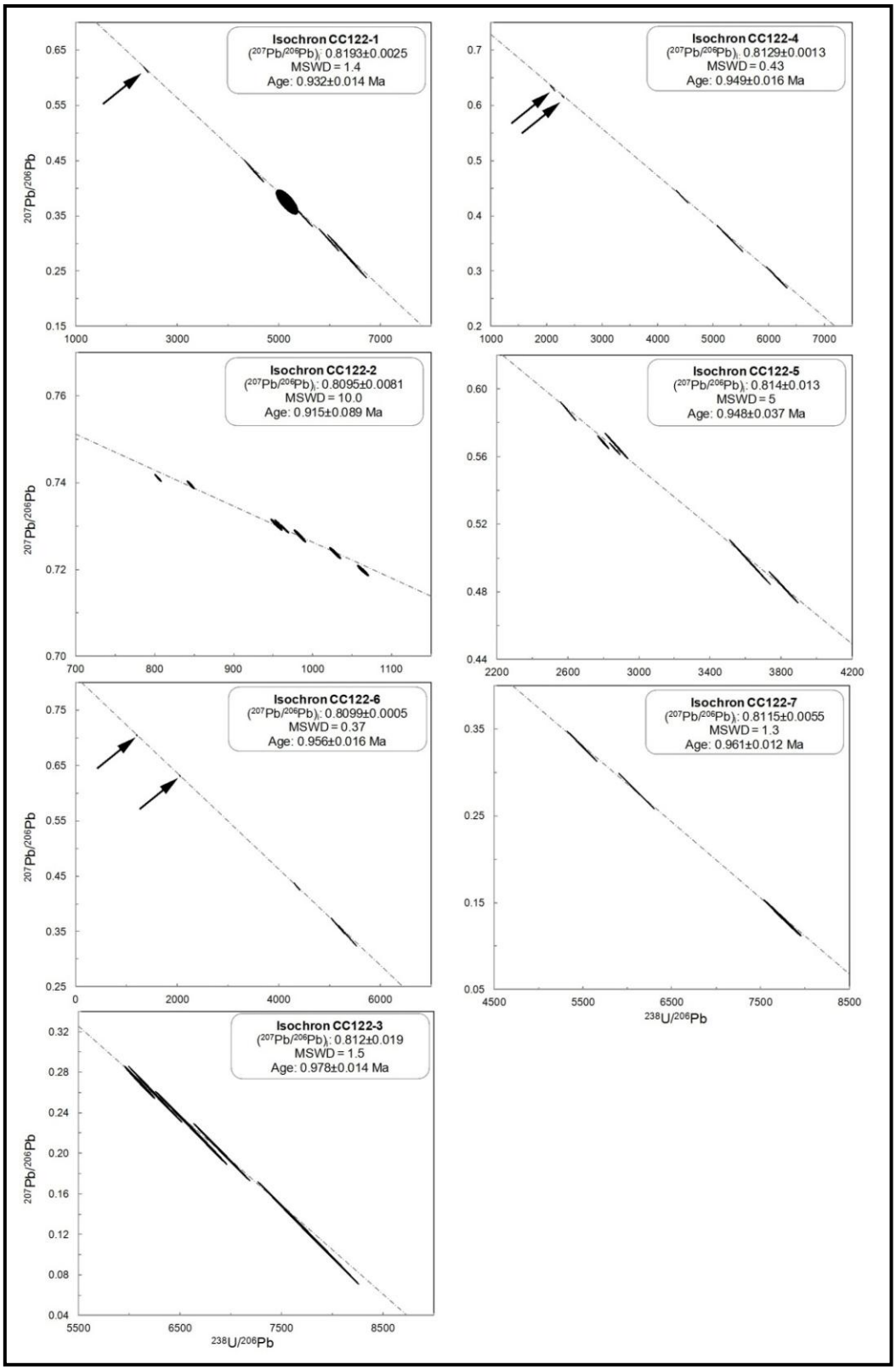

Figure 5-6. (Cont.) Plots for CC122 isochrons. Based on these measurements an initial $^{207}Pb/^{206}Pb$ ratio was estimated and used to calculate single aliquot ages.

Data from these new isochrons refined the previously published common Pb estimate from 0.818 +0.006/-0.011 to 0.81341 +/-0.005 (**Figure 5-7**) although it should be stressed that the new mean value is within the previously estimated uncertainty.

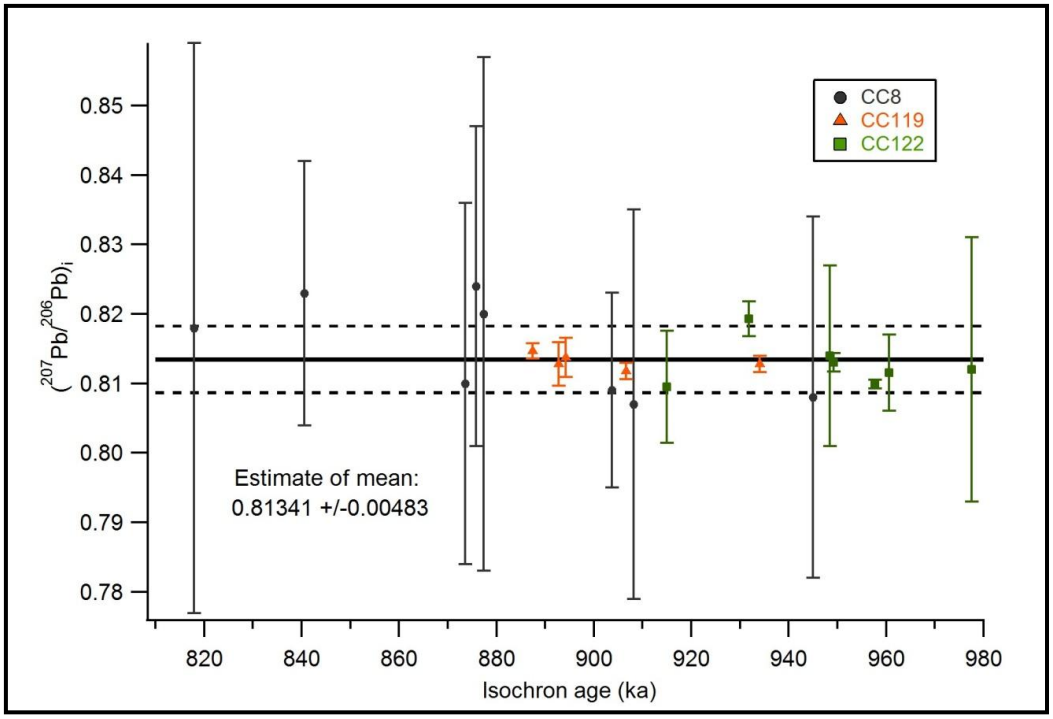

Figure 5-7. Initial 207Pb/206Pb ratio for all 20 full isochrons determined in this study suggests a stable and consistent source of common Pb. The estimated mean is indicated with a thick horizontal black line while dashed lines present its 95% uncertainty.

In general, isochrons for stalagmites CC112 and CC119 have a better fit (lower MSWD) than the previously published CC8 isochrons (**Figure 5-6** and **Chapter** 4). This is the result of a larger spread in isotopic ratios in these isochrons as well as their higher Pb content, which enabled improved precision in isotopic measurements for individual aliquots. However, due to their generally less radiogenic nature, some single-aliquot ages had to be rejected from the age-depth modeling (Woodhead et al., 2012). For this reason, all samples with $^{238}U/^{206}Pb$ ratios lower than 2500 were rejected. However, their

inclusion in the age-depth modeling affects neither the mean model age nor its uncertainty due to their large age uncertainties, which are, in almost all cases, over 25 kyr.

Since speleothems are often deposited out of secular isotopic equilibrium with respect to initial $^{234}U/^{238}U$ activity (Richards and Dorale, 2003), every sample has to be corrected for this effect. To achieve this, $^{234}U/^{238}U$ isotope ratios were measured for each sample aliquot separately following the procedure of Hellstrom (2003). The analyses were performed on the Nu Instruments Nu Plasma MC-ICPMS at The University of Melbourne. Uranium isotopic reference materials NBL-112A and HU-1 were used to correct for external $^{234}U/^{238}U$ variability. To calculate disequilibrium-corrected U-Pb ages and their uncertainties, an in-house macro was developed (see **Chapter** 4 for further details). All isotope ratios and ages corrected for initial disequilibrium effects are provided in **Table 5-1** and **Table 5-2**

The age-depth modeling followed the procedure documented in **Chapter** 4 and (Hendy et al., 2012). The only difference to the approach used in **Chapter** 4 is that here the original isochron ages were used instead of choosing the most radiogenic single-aliquot age from an individual isochron set, as was the case in **Chapter** 4. This modification was introduced to acknowledge that the results based on the isochron method are more robust since they do not rely on the estimated common Pb composition.

Sample aliquots rejected based on their less radiogenic nature, together with two isochrons from the upper part of CC8, were excluded from age-depth modeling. The oldest isochron and two single-aliquot ages from CC122 were also excluded because they predate CC8. For completeness, the age-depth model inclusive of the less-radiogenic, rejected samples is presented in **Figure 5-8**.

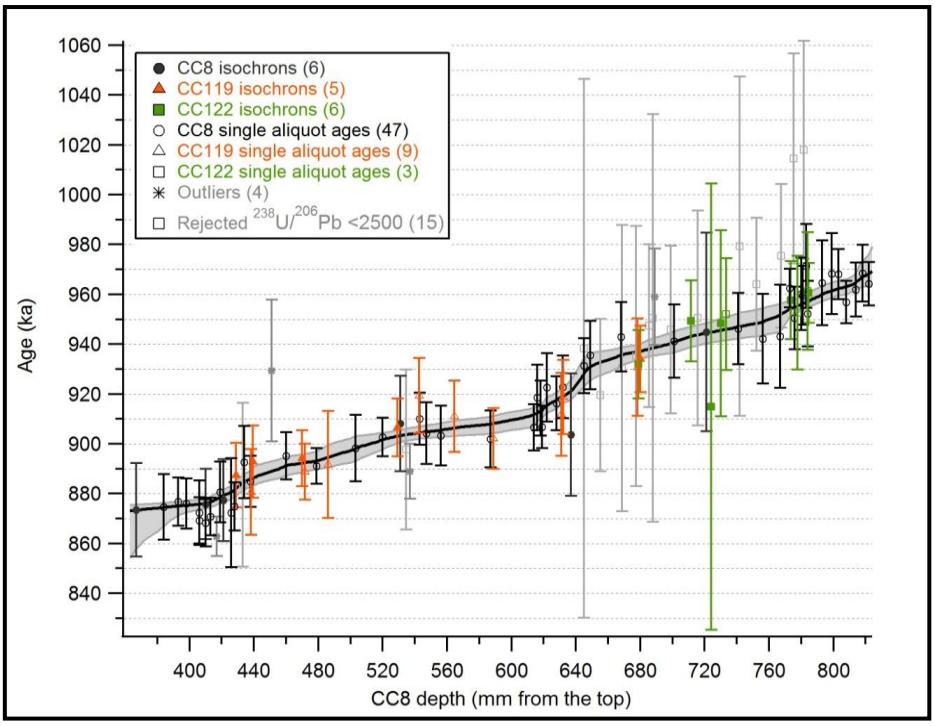

Figure 5-8. Composite age depth model with rejected unradiogenic samples for which 238U/206Pb ratio is lower than 2500. These were rejected because the single aliquot approach becomes less reliable for unradiogenic samples (Woodhead et al., 2012).

5.2.4 CROSS TUNING OF CORCHIA SPELEOTHEM $\delta^{18}O$ PROFILES

The stable isotope profiles of all speleothems were transferred onto the depth scale of stalagmite CC8, which has the longest record of the three stalagmites used in this study (**Figure 5-9**).

The cross tuning of the speleothems was based on correlating their $\delta^{18}O$ profiles, while $\delta^{13}C$ data (more susceptible to variation between speleothems of the same age due to the sensitivity of $\delta^{13}C$ to differences in the hydrogeochemical evolution of percolation waters) were used to evaluate the goodness of fit. Correlation coefficients between CC8, CC122 and CD3 are higher than 0.8 ($p<0.001$) for both O and C, while correlation between CC119 with CC8 and CD3 is slightly

lower but still above 0.5 ($p<0.001$) (**Table 5-3**). Further support for the match between the stalagmites comes from their individual age-depth models. The three age-depth models all overlap with respect to their uncertainties, indicating that all speleothems grew during the same time period and reflect the same climatic conditions (**Figure 5-10**).

The range of values of $\delta^{18}O$ for different stalagmites are mostly within analytical uncertainties except for the part of the record between 564 and 650 mm of the composite depth profile, where CC8 shows enrichment of up to 0.8‰ compared to CC119 and CD3 (**Figure 5-9**). The reason for this offset is not entirely clear but, given the close match between the two stalagmite carbon profiles during this interval, as well as the structural similarities between their oxygen profiles, this offset does not prevent reliable cross tuning.

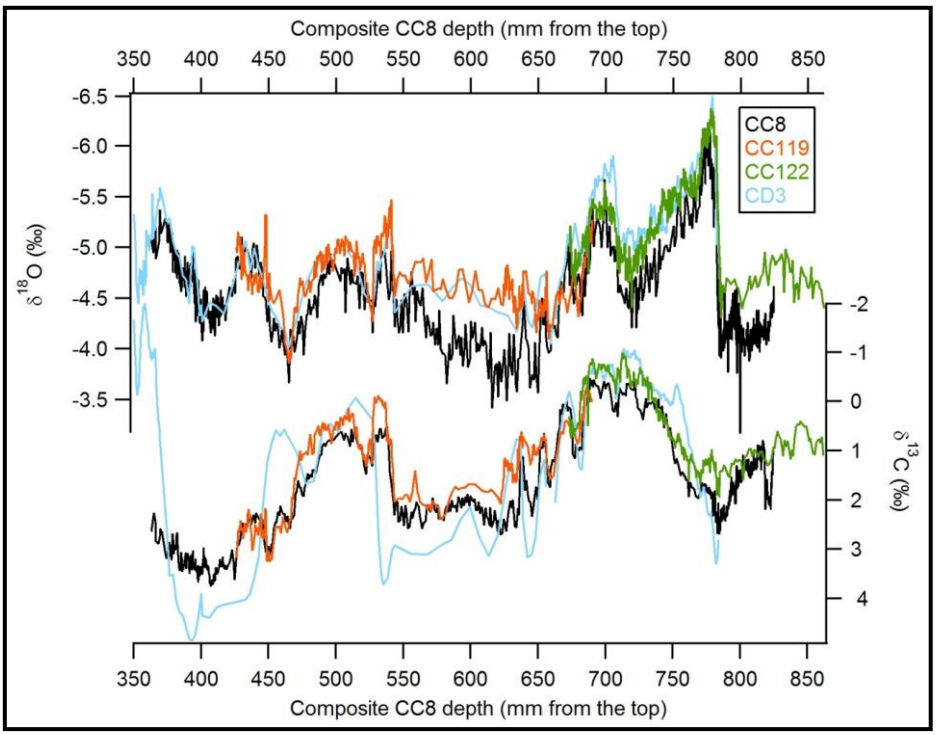

Figure 5-9. Stable isotopes series for all speleothems (CC8 in black; CC119 in orange; CC122 in green and CD3 in light blue) translated onto the CC8 depth scale using δ18O as a major proxy for cross tuning. δ13C was used to evaluate goodness of fit.

Table 5-3. Correlation coefficients for $\delta^{18}O$ and $\delta^{13}C$ for all speleothems is in most cases higher than 0.6 indicating a good correlation between the four different speleothems ($p<0.0001$).

Correlation coefficient for $\delta^{18}O$ (r)			
	CC119	CC122	CD3
CC8	**0.60**	**0.92**	**0.86**
CD3	**0.69**	**0.82**	***I***
Correlation coefficient for $\delta^{13}C$ (r)			
	CC119	CC122	CD3
CC8	**0.89**	**0.93**	**0.79**
CD3	**0.51**	**0.82**	***I***

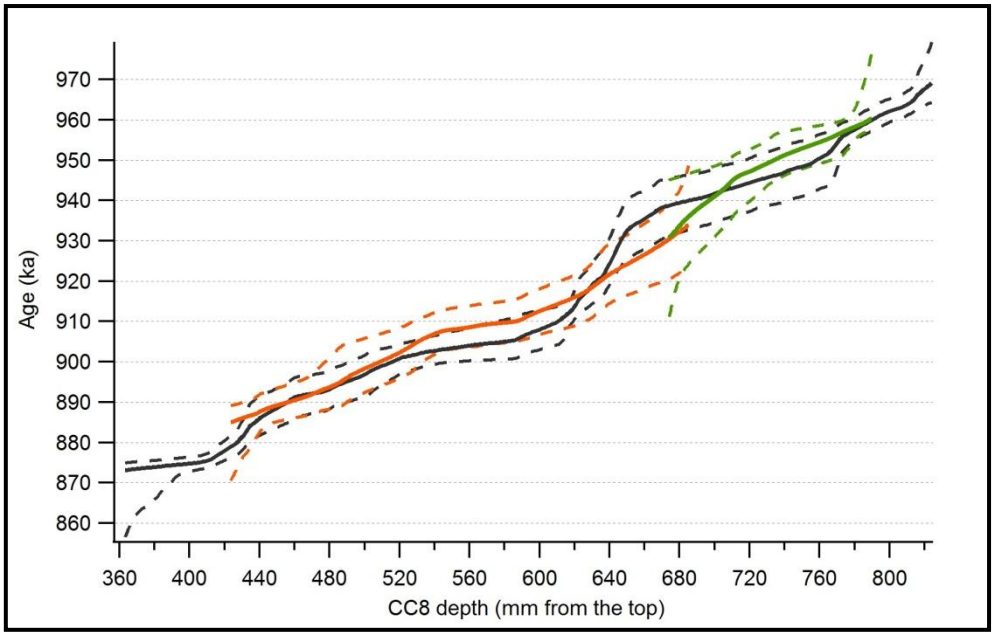

Figure 5-10. Individual age depth models for CC119 (orange), CC122 (green) and CC8 (grey) show these samples grew during the same time period implying that they reflect the same climate conditions.

5.2.5 TUNING OF THE MARINE RECORD TO THE CORCHIA TIME SCALE

To tie the Corchia $\delta^{18}O$ time series to marine records from the North Atlantic the approach of (Drysdale et al., 2009) was used. In that study it was demonstrated that Corchia $\delta^{18}O$ followed changes in sea-surface temperature (SST) from the North Atlantic and Western Mediterranean during the penultimate deglaciation. In doing so, the same relationship was assumed to be valid for the time period under investigation here (see below). There are a limited number of high-resolution (better than 0.5 kyr in this case) marine records in the North Atlantic encompassing the time period of this study and no records of sufficient resolution from the western Mediterranean. The most detailed North Atlantic records come from Sites U1313 and U1314 (**Figure 5-4**) - these were utilized in this study. Site U1313 is chosen as the key record because it has a higher-resolution SST series than Site U1314 and consequently shows a more robust correlation with the much higher resolution Corchia $\delta^{18}O$.

All tuning in this study was achieved based on visual correlation using tie points between which linear interpolation was employed. The U1313 SST record tuned to the CC8 stable isotope profile is shown in **Figure 5-11**. Although the primary signal used for tuning was the SST from Site U1313, four additional datasets from Site U1313 used in parallel assisted the tuning exercise. These records were: the relative abundance of $C_{37:4}$ alkenones, indicative of high-latitude waters; the abundance of dolomite, indicative for the input of ice-rafted detritus from the Hudson Bay area; the abundance of quartz, reflecting input from different circum-Atlantic ice sheets (Naafs et al., 2011); and the lightness record, which reflects the carbonate content at the site (Expedition 306 Scientists, 2006). The four records allowed identification of climate events during which more than one proxy showed a consistent and rapid response, and successively to assign to them the ages of the postulated equivalent in the target. From the

perspective of this study, it is necessary to emphasize that the match is not compromised during any of the terminations. Indeed, mismatches occur mostly during glacials, possibly as a result of local (in-cave) effects on speleothem $\delta^{18}O$ or due to episodes of sea-surface disruption related to enhanced iceberg discharges into the North Atlantic as a consequence of instability of the Northern Hemisphere ice sheets.

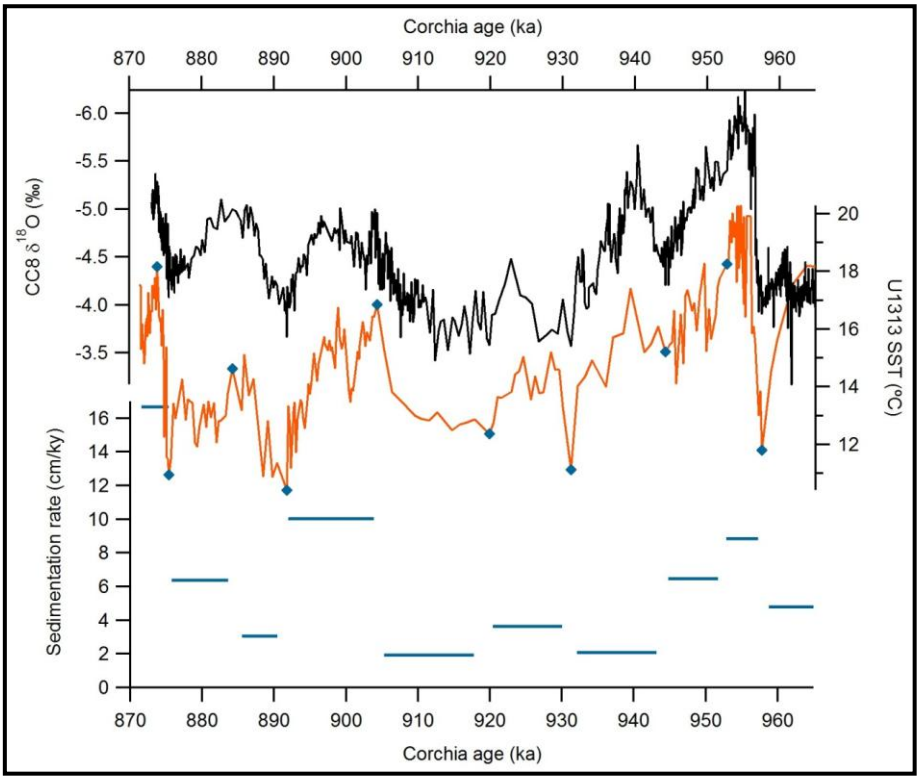

Figure 5-11. CC8 $\delta^{18}O$ time series (black) vs SST record from the IODP Site U1313 (orange) with tie points used to tune these records (blue diamonds). Sedimentation rate for Site U1313 calculated using the Corchia chronology is provided on the lower plot. Unusually high sedimentation rate at the top of sedimentary sequence is probably a result of the higher age uncertainties of the Corchia chronology at this time.

Benthic $\delta^{18}O$ data from Site U1313 currently cover only part of the time period under investigation (up to 910 ka) (Ferretti et al., 2010) preventing the use of this site to date two of the glacial terminations investigated in this study. For this reason, once tuning the Site U1313 SST to the radiometric Corchia time scale was completed, the SST record from Sites U1313 and U1314 were cross tuned (**Figure 5-12**)

and the Site U1314 benthic $\delta^{18}O$ record (Hernández-Almeida et al., 2012) was used to determine the onset of terminations in the LR04 stack (**Figure 5-13**). The latter represents a global mean of benthic $\delta^{18}O$ records (Lisiecki and Raymo, 2005) and has been used as the principal tuning target for the majority of benthic data published after 2006.

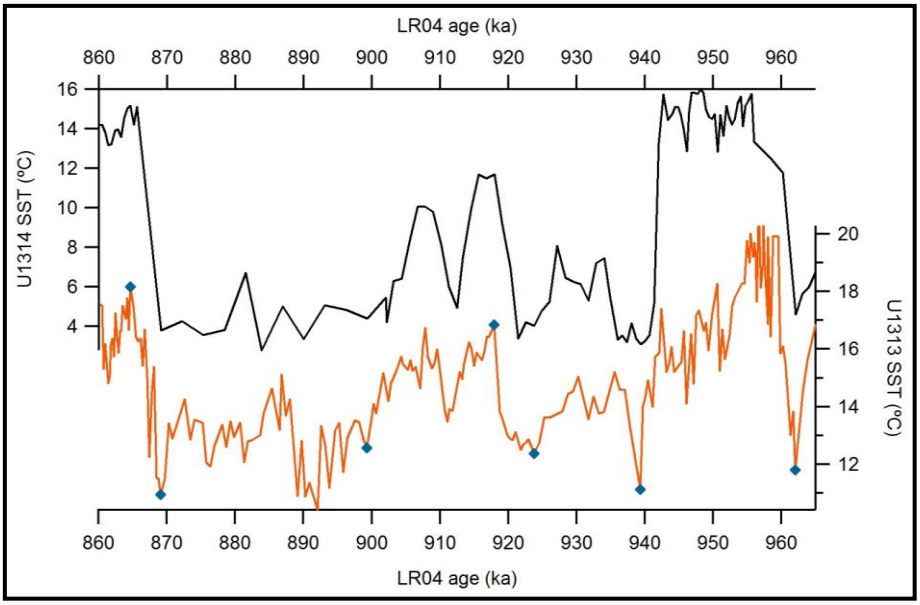

Figure 5-12. Matching of SST record from IODP Sites U1313 (black) and U1314 (orange) with tie points (blue diamonds). The overall match between these two records is compromised in some parts, possibly due to the lower resolution of the U1314 record and due to the fact the two records are based on different SST calculation methods.

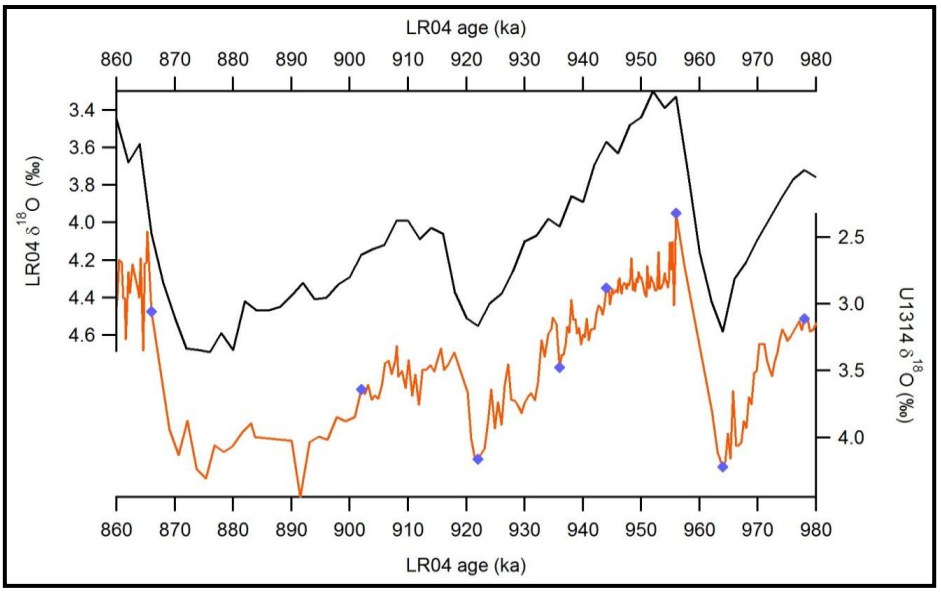

Figure 5-13. Benthic $\delta^{18}O$ record from the IODP site U1314 (orange) retuned to LR04 (black) chronology using tie points marked with blue diamonds. Employment of additional tie points compared to the original age model (Hernández-Almeida et al., 2012) was required to improve the fit between these two records.

A slight tuning adjustment to the original Site U1314 benthic chronology with respect to LR04 (Hernández-Almeida et al., 2012) was performed, including additional tie points, to improve the match without affecting sedimentation rates significantly (**Figure 5-13**). The slight offset between the Site U1314 benthic oxygen isotopes and the LR04 stack published in (Hernández-Almeida et al., 2012) is of no great significance for their long-term focus but, from the perspective of this work, it is important to optimally tune the record to LR04 to be able to transfer radiometric Corchia chronology onto the LR04 stack and evaluate precisely the length of glacial-interglacial cycles (**Figure 5-14**). The link between the benthic record from the Site U1314 and the LR04 stack is then used to determine chronology for the record from ODP Site 1123 (Lisiecki and Raymo, 2005).

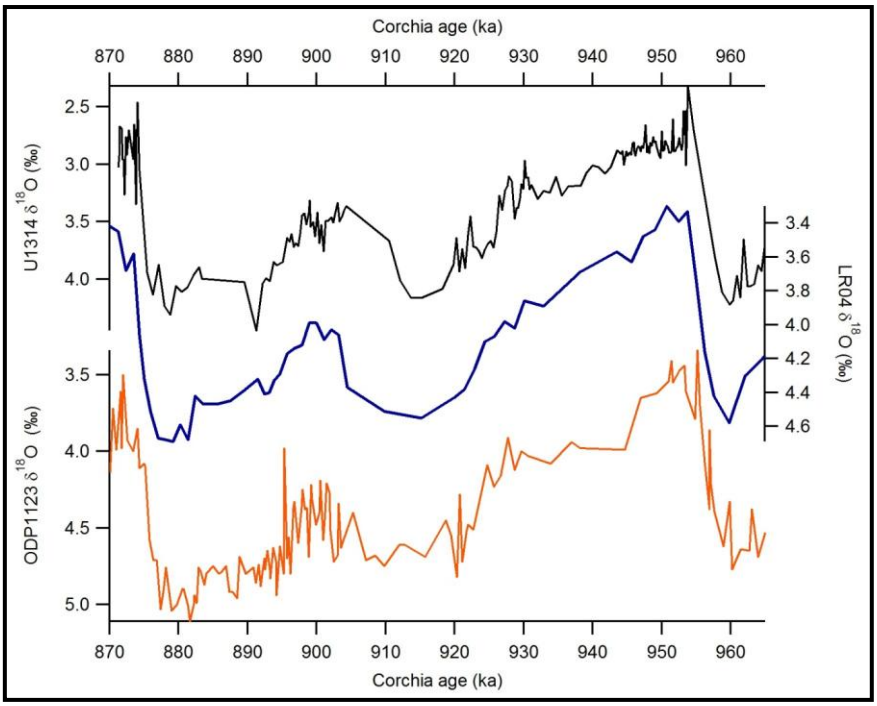

Figure 5-14. Transposition of the Corchia chronology for IODP Site U1314 (black) onto LR04 (blue) and ODP Site 1123 (orange) benthic records.

5.2.6 TIMING OF TERMINATIONS

Based on marine data from Site ODP1123 it was recently proposed that changes in bottom-water $\delta^{18}O$ composition ($\delta^{18}O_w$) are a better gauge of global ice-volume changes than benthic foraminifera $\delta^{18}O$ values due to the deep-ocean temperature effect on the latter (Elderfield et al., 2012). It has also been shown (Elderfield et al., 2012) that during the last 1.5 Ma there was a phase lag between these three components, which would have implications for the timing of the three terminations under investigation here. To explore if there is a time-lag present in the ODP Site 1123 data during the time period under study here the Corchia chronology was transposed onto both the $\delta^{18}O_w$ and benthic $\delta^{18}O$ record from ODP Site 1123. The higher frequency component of both $\delta^{18}O_w$ and benthic $\delta^{18}O$ records was smoothed by using a 3-point running average in order to focus on the low frequency components of these proxy records (**Figure 5-15**). This comparison reveals that there is neither a

systematic nor a large offset between these two records for TXII and TX, which lends support for use of the benthic LR04 in estimating the timing of terminations during this period.

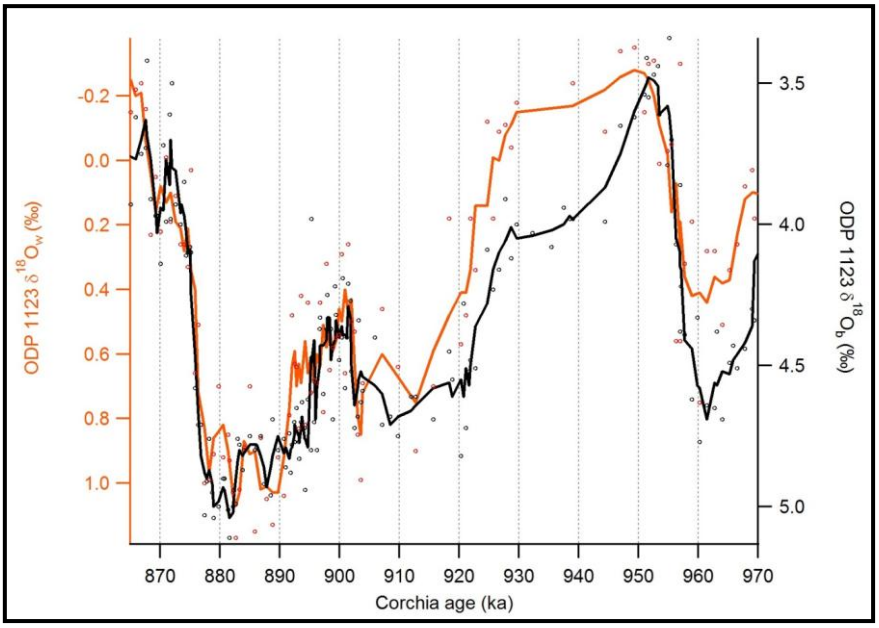

Figure 5-15. Phase lag between benthic $\delta^{18}O$ (black dots, black line is a three point running average) and $\delta^{18}O_w$ (in orange, same scheme as for benthic) at site ODP Site 1123 is negligible at the onset of TXII and TX which demonstrates that the LR04 benthic $\delta^{18}O$ record can be used to determine timing of these terminations.

Additionally, criteria for the onset of terminations vary (Drysdale et al., 2009; Huybers, 2011; Lisiecki and Raymo, 2005). The approach of Drysdale et al. (2009) was slightly adjusted here: the onset of terminations was determined by using the point where benthic $\delta^{18}O$ starts to monotonically decrease above the measurement uncertainty. On the other hand, Huybers uses a point where the rate of change in $\delta^{18}O$ crosses a threshold of 0.095 ‰/kyr (Huybers, 2011). To check whether the choice of method affects the spacing of terminations these two approaches were compared by using the LR04 stack (**Figure 5-16**).

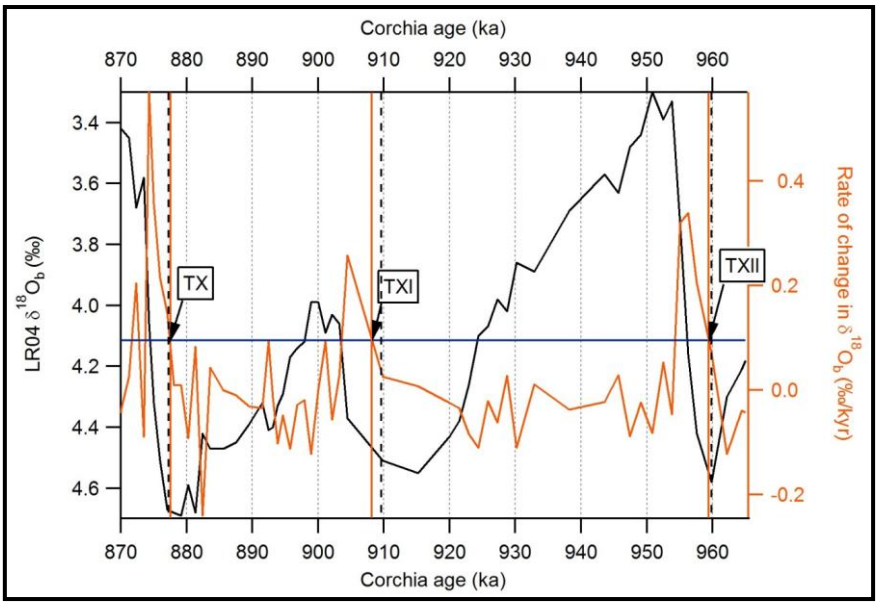

Figure 5-16. Determination of the onset of terminations using the monotonic decrease in benthic $\delta^{18}O$ above the measurement uncertainty (black) and rate of change approaches of (Huybers, 2011) (orange) for the same parameter in the LR04 stack. Vertical lines indicate the position when terminations started using the first (black line) and second (orange dashed line) approaches. Both methods yield an ~80 kyr cycle between TXII and TX and demonstrate that the choice of the method does not affect the final conclusions of this work.

The comparison reveals that each approach results in a similar timing and spacing of terminations TXII and TX, while it produces a difference of 1.6 kyr in the position of TXI. As alluded to in the main text, this termination is the least pronounced of all three and the mismatch, as well as its structure (less abrupt when compared to TXII and TX), implies that it represents an aborted termination. Despite a slight offset in the timing of TXII and TX, it is convincing to see that the period between these terminations corresponds to two obliquity cycles in both cases. Since the choice of method does not affect the major conclusion of this study, the criterion of a monotonic decrease above measurement uncertainty in LR04 benthic $\delta^{18}O$ was adopted to determine the timing of terminations.

5.2.7 POSSIBLE NON-PERSISTENCE OF THE LINK BETWEEN SST AND CORCHIA $\delta^{18}O$

Previous work on Corchia speleothems has highlighted the close correspondence between regional SSTs and speleothem $\delta^{18}O$ through the influence of SSTs on rainfall amount at the cave site (Drysdale et al., 2009; Drysdale et al., 2007; Drysdale et al., 2004). It is this association that forms the basis for transferring the speleothem chronology to the marine record in this study. However, the possibility that this SST-speleothem $\delta^{18}O$ link may not have persisted at the time of the MPT must be considered, as it was assumed to have prevailed at the time of TII (Drysdale et al., 2009). While it has been acknowledged that other factors can contribute to changes in Corchia $\delta^{18}O$ (see discussion in Drysdale et al., 2004 and 2009), the most important of these – namely changes in the temperature of speleothem mineralisation, which equates to the cave temperature (the 'cave temperature effect'), and changes in the condensation temperature of moisture reaching the cave (the so-called 'air temperature effect'), cancel one-another out for this part of the Mediterranean, as shown in modelling by (Bard et al., 2002b) under glacial, interglacial and intermediate climate modes. The most likely alternative factor forcing much of the change in speleothem $\delta^{18}O$ through a termination is changes in the composition of North Atlantic surface ocean waters, the source of most local rainfall. This is plausible because terminations produce large amounts of isotopically-depleted meltwater relatively quickly in the rainfall source region, potentially leading to depletion in local rainfall $\delta^{18}O$ that is significant enough to override other effects, such as reduced rainfall amount. Given that relative changes in regional air temperatures at the cave site (for which cave mineralization temperature is a proxy) would closely track relative changes in ocean surface temperatures, the best proxy for surface ocean water changes is planktic $\delta^{18}O$. Tuning the marine record to the Corchia chronology

using the planktic δ ^{18}O rather than SSTs was evaluated previously for TII (Drysdale et al., 2009) and rejected on the grounds that the inferred palaeoclimate changes through the termination from the marine record were inconsistent with the palaeoclimate changes inferred from the full suite of speleothem proxies measured. Tuning to the SSTs in the case of TII was much more consistent with the suite of speleothem proxies. Nevertheless, for this MPT study, the marine record to the Corchia chronology was also tuned by using the planktic δ ^{18}O from IODP Site U1314 as the tuning target (**Figure 5-17A**). The results show that the differences in termination ages between the Corchia-SST-tuned LR04 stack and the Corchia-planktic-tuned LR04 are statistically indistinguishable (**Figure 5-17B**) and that the conclusions from this study thus remain entirely intact.

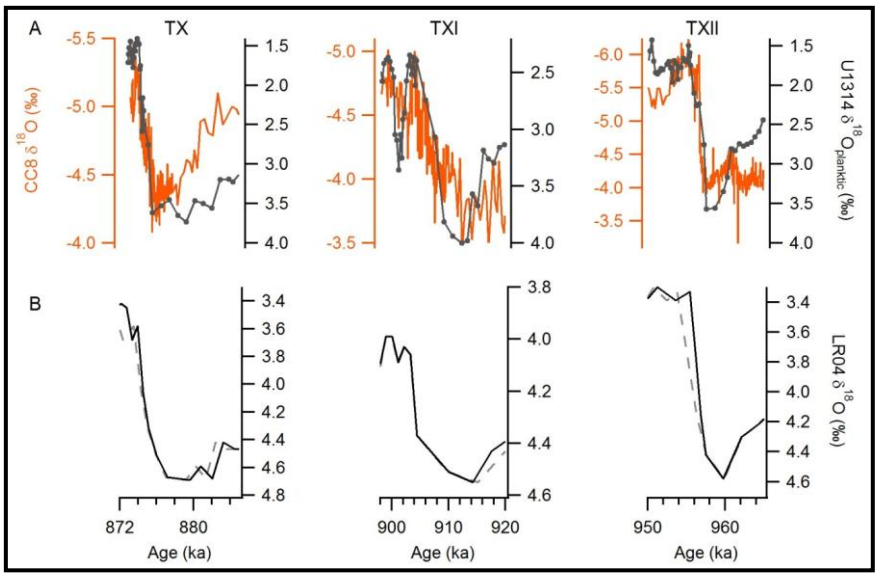

Figure 5-17. Tuning of the planktic δ^{18}O record from IODP Site U1314 (grey) to the Corchia δ^{18}O time series (orange) (Panel **A**) reveals there is no statistically distinguishable differences in termination ages between the Corchia-SST-tuned LR04 stack (dashed grey line) and the Corchia-planktic-tuned LR04 stack (full black line) (Panel **B**).

Chapter 6

6 "INVISIBLE" DIAGENESIS AND ITS IMPLICATIONS FOR SPELEOTHEM GEOCHRONOLOGIES

Speleothems are usually considered as one of the most amenable palaeoclimate archives for U-series dating. A number of studies in recent years, however, report cases of diagenetic alteration which compromises the use of U-series systematics in speleothems, resulting in inaccurate U-Th ages. Here are presented the results of a high-resolution U-Th dating study of a stalagmite (CC26) from Corchia Cave in Italy where a number of departures from an otherwise well-defined age-depth model are documented, and where potential causes for these outliers are explored. Unlike examples illustrated in previous studies, CC26 contains no visible evidence of neomorphism, and appears, at least superficially, ideally suited to dating. Good reproducibility obtained between multi-aliquot U-Th analyses removes any possibility of analytical issues contributing to these outliers. Furthermore, replicate analyses of samples from the same stratigraphic layer yielded ages in stratigraphic sequence, implying very localized open-system behavior. Uranium loss is suggested as a causative mechanism on account of the fact that all the outliers are older than their assumed true age. A limited number of micro-voids were observed under micro-CT analyses, and it is proposed that these were

pathways for U loss. Uranium-loss modelling allows constraining of the possible timing of diagenetic alteration and indicates that the precursor for the outlier with the largest age discrepancy (309%) must have been aragonite.

This study indicates that visibly unaltered speleothems may still contain small domains that have experienced post-depositional alteration. Such "invisible" diagenesis, as recorded in this stalagmite, has implications for the constancy of accuracy of the U-series dating technique, and suggests a need for careful examination of speleothems prior to dating, particularly in low-resolution U-Th studies.

6.1 INTRODUCTION

The ability to generate robust, high-precision radiometric age profiles is arguably the principal advantage of using speleothems in studies of past climate and environmental change (Fairchild et al., 2006; Hellstrom, 2003; Henderson, 2006). For accurate radiometric dating, however, the speleothem carbonate must have remained completely closed with respect to post-depositional loss or gain of uranium (U) and thorium (Th) isotopes from non-radiogenic (i.e. diagenetic) processes (Richards and Dorale, 2003). This assumption is often axiomatic in most speleothem studies because they are typically composed of a thermodynamically stable polymorph of calcium carbonate (low-Mg calcite) arranged in stacked, compact layers of columnar crystals.

In recent years, however, there has been increasing evidence for diagenetic alteration, or neomorphism, reported in speleothems (Frisia et al., 2002; Hoffmann et al., 2009; Lachniet et al., 2012; Martín-García et al., 2009; Ortega et al., 2005; Perrin et al., 2014; Railsback et al., 1994; Scholz et al., 2014; Zhang et al., 2014). Neomorphism is the process of *in-situ* transformation of a mineral into a polymorph (Folk, 1965). In speleothems, it includes aragonite-to-calcite transformation and calcite-to-calcite recrystallization (e.g. Frisia et al., 2002). In many

cases, the chemical properties are re-set to the extent that they no longer represent the original depositional conditions (Frisia et al., 2002; Zhang et al., 2014). For speleothems, U is commonly mobilised from the site of diagenesis, leading to an increase in the $^{230}Th/^{238}U$ isotopic ratio, which results in older-than-true U-Th ages (Lachniet et al., 2012; Ortega et al., 2005). This can severely compromise the accuracy of the U-Th chronology.

Neomorphism in speleothems is diagnosed by observation of petrological details on polished cut surfaces, on thin sections of the internal microstratigraphy and/or from trace element analysis (Frisia, 1996, 2002; Railsback et al., 2002; Ortega et al., 2005). Textural changes are typical of neomorphism (Frisia et al., 2002; Lachniet et al., 2012; Zhang et al., 2014), where a mosaic of equant calcite crystals shows relicts of the original aragonite needles and replaces the original fabric. However, primary features inherited from aragonite can be preserved in the secondary calcite (Lachniet et al., 2012; Zhang et al., 2014). In the case of calcite-to-calcite alteration, evidence of chemical re-setting is dependent upon micro-analytical techniques such as laser ablation inductively coupled plasma mass spectrometry (LA-ICP-MS) and synchrotron radiation–based micro XRF microscopy (Scholz et al., 2014; Zhang et al., 2014). In spite of the recent interest in speleothem neomorphism, most speleothem studies assume no alteration has occurred based on a lack of visible evidence in hand specimen.

Here, the results of a high-resolution geochronological study of a speleothem (CC26) from Corchia Cave (Italy) are presented. The study demonstrates how an apparently pristine stalagmite can undergo localized diagenesis, not visible to the naked eye, yet significant in terms of its impact on the sequence of U-Th ages. The study was initially conceived to explore Holocene variations in the dead-carbon proportion in the speleothem and its relationship to $\delta^{13}C$ (and potentially post-glacial vegetation recovery) by combining high-resolution, multi-aliquot uranium-thorium (U-Th) analyses with high-

resolution radiocarbon dating. The speleothem had been the subject of previous studies of Holocene climate variability (Regattieri et al., 2014; Zanchetta et al., 2007, 2014).

The results of the high-resolution U-Th dating campaign revealed several previously unrecognized age inversions for which an explanation was sought. Unlike the recent study of Scholz et al. (2014), the Holocene portion of CC26 contained no visible or microscopic evidence of neomorphism, with the specimen appearing ideally suited to dating. Fabric characterization via optical microscopy, high-resolution (LA-ICP-MS) trace-element mapping and synchrotron radiation–based micro XRF microscopy were used to investigate the regions affected by age inversion. Additionally, high-resolution micro X-ray computed tomography scanning (micro-CT) was used to explore micro-porosity and thus possible U-loss pathways. Finally, a model for significant but localized U loss is presented with the constraints on its timing.

The X-ray CT method has been used previously in studies of speleothems, beginning with the pioneering work of Mickler et al. (2004b), who explored its potential in determining the growth axis in speleothems as well as its utility in the selection of material suitable for palaeoclimate research, particularly in terms of porosity. Zisu et al. (2012) combined CT and magnetic resonance imaging (MRI) to distinguish between water and air-filled macro holes in a suite of 21 speleothems and explored the potential of these methods for targeting specimens for fluid-inclusion analyses. This study revealed the existence of both axial holes formed penecontemporaneously with growth in discrete layers, and post-depositional off-axis holes which suggests that water escaped post-depositionally through micro fissures, crystal boundaries, connected hole systems and crystal defects. The latest study by Walczak et al. (2015) for the first time used density data based on CT scanning as a palaeoclimate proxy in a speleothem from southern Iberia. They linked changes in sample density to shifts in palaeohydrological and climate conditions above the cave.

Despite its potential, the CT method is still underutilized. A new approach is presented here that extends the potential of the CT method for exploring evidence for diagenesis in speleothems. Speleothems used in previous studies were characterized by significantly higher porosities than is the case for CC26. All previous speleothems were analysed at a much lower resolution (with CT slice spacing between 0.21 and 2 mm), which would not be sufficient to address the aims of this study. High-resolution micro-CT scanning, as used in this study, has the potential to provide additional support to confirm U-loss hypotheses proposed to explain the U-Th outliers.

6.2 SAMPLE DESCRIPTION AND METHODS

6.2.1 SITE AND SAMPLE DESCRIPTION

The CC26 stalagmite was recovered from Antro del Corchia (Corchia Cave), a large, multi-level cave system in the Alpi Apuane massif of central Italy (Piccini et al., 2008). The cave is overlain by metamorphosed Mesozoic shallow marine carbonates and siliciclastics (marbles, dolomitic marbles, dolomites, metabreccias, and calcschists) and Paleozoic basement rock (phyllites). CC26 was removed from the Galleria delle Stalattiti, a chamber located at 840 m a.s.l. The feedwaters for this chamber pass through the Upper Triassic Grezzoni dolomites, metamorphosed carbonates and calcschists (Piccini et al., 2008). The chamber's microclimate is characterized by seasonal temperature oscillations within 1°C (mean 8.4 ± 0.3) and a high relative humidity (100 ± 0.2%) (Piccini et al., 2008). Drip-water analyses from a site within the chamber reveal minimal variability in major ion concentrations, typical of deep-seated caverns (Piccini et al., 2008): Ca^{2+} 0.82±0.02 mmol/L, Mg^{2+} 0.91±0.03, SO_4^{2-} 0.36±0.02 mmol/L, and a Mg/Ca 1.11±0.03 (mol/mol). Drip waters are slightly supersaturated with respect to calcite and have a pH range between 8.1 and 8.4

(Baneschi et al., 2011). High Mg concentrations in CC26 (mean Mg/Ca molar ratio 0.0418; Regattieri et al., 2014), and in older speleothems from the cave (Drysdale et al., 2009), are consistent with the prevalence of dolomite above the cave chamber. The stable isotope (Zanchetta et al., 2007, 2014) and trace element profiles (Regattieri et al., 2014) of CC26 have yielded palaeoclimate information on Holocene climate variability using the original chronology of Zanchetta et al. (2007), from which an age-depth model produced from 17 U-Th determinations was derived. All ages in this chronology were in correct stratigraphic order.

CC26 shows evidence for several growth phases (**Figure 6-1**). In the older phases (unstudied in previous work), there is clear evidence of aragonite-to-calcite neomorphism, with significant negative correlations between Mg/Ca and Sr/Ca, suggesting a partially open system (cf. Pingitore, 1982). In the present study, only the youngest growth phase (the top 157 mm of the stalagmite), which grew continuously over the last ~12 ka (Zanchetta et al., 2007), was investigated.

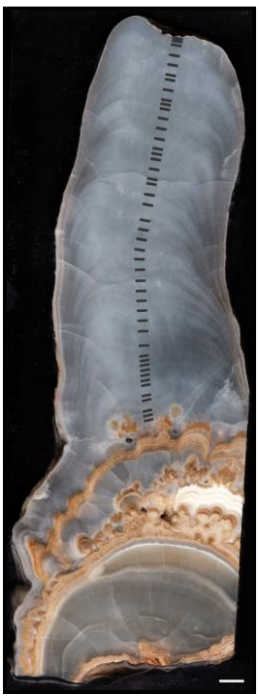

Figure 6-1. Scan of the sectioned stalagmite CC26 with U-Th sampling positions indicated. White scale bar is 1 cm.

6.2.2 SAMPLE PREPARATION AND METHODOLOGY

Half of the stalagmite was sliced into a ~1 cm-thick slab and cut along its growth axis. One section was used for U-Th sampling (and for ^{14}C; not considered here) while another was used for petrographic and trace element analyses. Samples for dating (solid pieces) were extracted along the growth axis using a dental air drill fixed to a manually navigated milling machine. In total, 78 samples were extracted, 47 of which were selected for this study. The samples were chemically processed for U-Th dating and analysed following the methods described in Hellstrom (2003) and Drysdale et al. (2012). In short, 2.5-12.2 mg solid pieces were dissolved in nitric acid, then spiked with a mixed ^{229}Th-^{233}U-^{236}U tracer solution. The U and Th were eluted in Eichrom TRU-spec selective ion-exchange resin. Dried samples were then dissolved in diluted nitric acid. Each sample was typically split into two or three aliquots, which were analysed in different mass spectrometry sessions, usually a week apart. In total, 123 measurements were performed using a Nu Instruments Plasma MC-ICPMS at the University of Melbourne. An equilibrium reference material (HU-1) was used to correct for instrumental drift; an additional in-house speleothem standard of known age (YB-1) was used to check for the reproducibility of results. An initial $^{230}Th/^{232}Th$ ratio of 1.5+/-1.5 was used to calculate corrected ages following (Hellstrom, 2006).

The other half of the sample was used for optical microscopy, synchrotron radiation based micro-XRF spectroscopy and laser ablation (LA) trace element analyses. Four 30-µm-thick, polished and uncovered thin sections were used for petrographic examination, which was conducted using a Leica M16 stereoscope and a Zeiss petrographic microscope at the University of Newcastle, and a Wild M400 Photomacroscope at the University of Melbourne. LA-ICP-MS trace element analyses were performed on the same thin sections after petrographic observations.

Trace element analyses on the upper thin section were performed at the University of Melbourne using a 193-nm ArF excimer laser-ablation system coupled to an Agilent 7700x quadrupole ICP-MS. The data were collected using a 12-µm spot size with a scan rate of 10 µm/sec and laser pulse rate of 10 Hz. Samples were pre-ablated to clean the surface before data acquisition and analyses were calibrated relative to the NIST SRM612 glass Reference Material. Spatially resolved trace element images draped over a reflected light image were produced using the CellSpace (Paul et al., 2012) module within Iolite (Paton et al., 2011) the time-resolved analysis software used to reduce the LA-ICPMS data.

X-ray fluorescence microscopy (XFM) was performed on the XFM beamline at the Australian Synchrotron using the Kirkpatrick-Baez mirror microprobe end-station. The 12-mm thick polished slabs (see Borsato et al., 2007 for sample preparation) were analysed with a monochromatic 2-µm beam spot size at energy of 18.5 keV. The XFM beamline is equipped with a Maia 384 detector array, which can acquire full spectral X-ray data for each detector at step sizes down to 2 µm over areas of several square centimetres (Ryan et al., 2010). The Maia XFM spectral data were analysed using the GeoPIXE™ software suite, which uses a fundamental parameters approach, with spectral deconvolution and imaging using the dynamic analysis method. Spectra were fitted using X-ray line relative intensities that reflect integration of yields and X-ray self-absorption effects for the calcite matrix and the contrasting efficiency characteristics across the detector array (Ryan et al., 2010). The detection limits for Sr and U are between 1 and 2 ppm and the attenuation depths are 250 µm and 370 µm respectively.

Micro-CT analysis was performed on the same slice that was used for U-Th dating and focusing on an upper portion of ~26.5 mm of the speleothem. The analyses were conducted using a GE Phoenix Nanotom M scanner. The sector scan module was used to take 1500 X-ray images of the sample through 226 degrees of rotation with an X-ray

power of 110 kV and 430 µAmp at a magnification of 9.04 (focus-object distance (FOD) = 25 mm; focus-detector distance (FDD) = 225 mm) giving a voxel resolution of 11.058 µm. The scan integrates 5 images over 500 ms with an extra image skipped. A 0.25 mm Cu filter was used to prevent saturation of the detector. Data were reconstructed using the Phoenix Datos reconstruction software and the reconstructed volumes were segmented for porosity analysis using Avizo®.

6.3 RESULTS

6.3.1 U-Th RESULTS AND AGE-DEPTH MODEL

The U-Th data, including isotopic ratios and corrected ages, are provided in the Supplementary Materials **Table 6-1**. Replicate (duplicate or triplicate) analyses of the same sample analysed in different mass spectrometry sessions show good analytical reproducibility, with an average MSWD of 1.3 and an average probability of fit of 46 % for error-weighted-mean corrected ages (**Table 6-2**).

However, the scatter in the $^{230}Th/^{238}U$ ratio, and consequently the calculated ages, amongst the replicates of six samples (CC26-4; CC26-8a; CC26-14; CC26-34; CC26-53; CC26-64) were not reproducible at 5% probability. Four of these samples (CC26-4; CC26-14; CC26-34; CC26-64) were run in triplicate. One of these triplicate measurements was rejected based on its lack of concordance with the results from the other two aliquots of the same sample. However, this criterion could not be applied to the remaining two samples (CC26-8a and CC26-53), which were only run twice. Since the age-depth model was produced based on a relatively dense distribution of ages, one could easily decide which of the two replicate analyses of CC26-8a and CC26-53 was the outlier by comparing each age against the age-depth model output. Although one of the age determinations in both cases precisely aligns with the mean value of the age-depth model, neither of these two age

determinations was used in the final age-depth model due to the difficulty of objectively interpreting the observed scatter.

The age-depth model was produced using the error-weighted-mean corrected U-Th ages from multiple measurements of the same aliquot and employing a finite positive growth-rate model (Drysdale et al., 2005; Scholz et al., 2012). Results showed that ages for five out of 47 dated samples (CC26-8; CC26-14; CC26-24; CC26-49; CC26-66) are older than expected with respect to their neighbours (**Figure 6-2**).

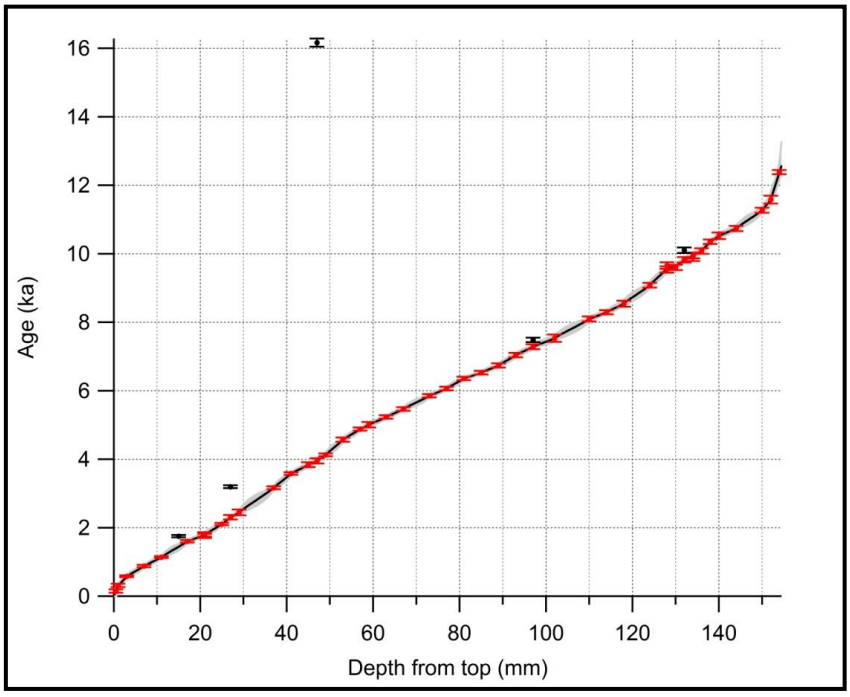

Figure 6-2. Age-depth model for stalagmite CC26. The full black line is the mean model age and the grey shaded area is the 95% uncertainty envelope. The error weighted mean U-Th ages based on replicated analyses of the same aliquot are shown in red. These are used to construct the age depth model while outliers in black are not included in the modelling. For more details please refer to the text.

Sample pieces leftover from these outliers were then chemically re-processed for repeat measurements. The repeat analyses for these samples (CC26-14a; CC26-24a; CC26-49a; CC26-66a) were consistent with those of the neighbouring samples, in line with the uniform growth rate throughout the Holocene for this stalagmite, indicating that if diagenetic alteration is responsible for these outliers, it did not affect

the whole stratigraphic layer. Replication of sample CC26-8 was carried out twice, and although the new results (CC26-8a) are in stratigraphic order, the results are not internally consistent, resulting in a low probability of fit of the error-weighted mean age (**Table 6-2**), as explained above. For this reason, this sample was excluded from the final age-depth model.

Table 6-1. U-Th results for CC26. Isotopic ratios are activity ratios and uncertainties are expressed as 95% confidence intervals (c.i.). N.d. stands for not recorded. Age is corrected for initial $^{230}Th/^{232}Th$ of 1.5 +/-1.5. Samples for which U-Th dating was repeated by analysing another calcite prism from the same stratigraphic layer have a suffix a and/or b. Rejected results are marked with * and the outliers with a suffix °. Sampling ±100% error is 0.5 mm for every sample. Samples CC26-5.2 and CC26-11.2 are selected upon micro-CT analyses.

Sample name	Mass (mg)	U (ppb)	Depth from top (mm)	$[^{230}Th/^{238}U]$	$[^{230}Th/^{238}U]$ ± 95% error	$[^{234}U/^{238}U]$	$[^{234}U/^{238}U]$ ± 95% error	$[^{232}Th/^{238}U]$	$[^{232}Th/^{238}U]$ ± 95% error	$[^{230}Th/^{232}Th]$	Age (ka)	Age ±2σ (ka)	$[^{234}U/^{238}U]_i$	$[^{234}U/^{238}U]_i$ ± 95% error
CC26-1	6.6	9104	0.5	0.0014	0.0001	0.6607	0.0013	0.000319	0.000005	5	0.160	0.081	0.6606	0.0013
CC26-1	6.6	9101	0.5	0.0013	0.0001	0.6605	0.0020	0.000319	0.000006	4	0.134	0.081	0.6603	0.0020
CC26-1	6.6	9086	0.5	0.0015	0.0003	0.6601	0.0025	0.000333	0.000003	4	0.160	0.095	0.6599	0.0025
CC26-1a	7.9	4121	1.0	0.0019	0.0003	0.6610	0.0011	0.000005	0.000002	371	0.313	0.048	0.6607	0.0011
CC26-2	10.4	2528	3.0	0.0036	0.0002	0.6615	0.0019	0.000010	0.000002	370	0.593	0.038	0.6609	0.0019
CC26-2	10.4	2529	3.0	0.0035	0.0002	0.6628	0.0013	0.000011	0.000002	328	0.569	0.035	0.6622	0.0013
CC26-4	5.7	2973	7.0	0.0055	0.0003	0.6651	0.0018	0.000023	0.000002	234	0.898	0.044	0.6642	0.0018
CC26-4	5.7	2976	7.0	0.0052	0.0003	0.6648	0.0033	0.000029	0.000002	184	0.856	0.055	0.6640	0.0034
CC26-4*	5.7	2976	7.0	0.0061	0.0004	0.6639	0.0029	0.000022	0.000003	282	0.996	0.068	0.6630	0.0029
CC26-6	9.7	2911	11.0	0.0067	0.0003	0.6627	0.0017	0.000010	0.000002	658	1.111	0.046	0.6617	0.0017
CC26-6	9.7	2911	11.0	0.0070	0.0002	0.6640	0.0015	0.000009	0.000002	807	1.151	0.030	0.6629	0.0015
CC26-8°	5.6	3443	15.0	0.0106	0.0003	0.6639	0.0025	0.000012	0.000001	899	1.756	0.052	0.6622	0.0025
CC26-8°	5.6	3440	15.0	0.0105	0.0007	0.6624	0.0021	0.000010	0.000002	1025	1.741	0.112	0.6607	0.0021
CC26-8°	5.6	3434	15.0	0.0106	0.0003	0.6633	0.0038	0.000015	0.000004	697	1.750	0.052	0.6616	0.0039
CC26-8a*	9.5	3083	15.0	0.0088	0.0003	0.6620	0.0021	0.000005	0.000002	1771	1.455	0.054	0.6606	0.0021
CC26-8a*	9.5	3084	15.0	0.0082	0.0003	0.6639	0.0011	0.000005	0.000001	1712	1.356	0.049	0.6626	0.0011
CC26-9	9.2	3148	17.0	0.0098	0.0003	0.6630	0.0019	0.000008	0.000002	1149	1.617	0.055	0.6614	0.0020
CC26-9	9.2	3151	17.0	0.0096	0.0003	0.6632	0.0012	0.000008	0.000002	1175	1.591	0.053	0.6616	0.0012

Sample name	Mass (mg)	U (ppb)	Depth from top (mm)	$[^{230}Th/^{238}U]$	$[^{230}Th/^{238}U]$ ± 95% error	$[^{234}U/^{238}U]$	$[^{234}U/^{238}U]$ ± 95% error	$[^{232}Th/^{238}U]$	$[^{232}Th/^{238}U]$ ± 95% error	$[^{230}Th/^{232}Th]$	Age (ka)	Age ±2σ (ka)	$[^{234}U/^{238}U]_i$	$[^{234}U/^{238}U]_i$ ± 95% error
CC26-11	5.7	4841	21.0	0.0109	0.0003	0.6637	0.0027	0.000111	0.000004	98	1.779	0.062	0.6620	0.0027
CC26-11	5.7	4839	21.0	0.0109	0.0003	0.6644	0.0018	0.000108	0.000005	101	1.783	0.064	0.6627	0.0018
CC26-11a	2.5	5093	21.0	0.0108	0.0005	0.6651	0.0015	0.000040	0.000001	272	1.782	0.084	0.6634	0.0015
CC26-13	8.8	4593	25.0	0.0127	0.0002	0.6619	0.0010	0.000010	0.000001	1243	2.107	0.035	0.6599	0.0010
CC26-14[o]*	6	3162	27.0	0.0189	0.0004	0.6629	0.0021	0.000025	0.000002	745	3.156	0.068	0.6599	0.0021
CC26-14[o]	6	3153	27.0	0.0193	0.0003	0.6640	0.0016	0.000026	0.000002	754	3.217	0.052	0.6609	0.0016
CC26-14[o]	6	3149	27.0	0.0199	0.0003	0.6635	0.0024	0.000023	0.000003	848	3.323	0.053	0.6603	0.0025
CC26-14a	5.1	4769	27.0	0.0139	0.0004	0.6636	0.0009	0.000005	0.000001	2753	2.304	0.066	0.6614	0.0010
CC26-15	4.9	4447	29.0	0.0147	0.0005	0.6648	0.0017	0.000018	0.000001	842	2.446	0.084	0.6625	0.0017
CC26-17	7.9	3067	33.0	0.0170	0.0003	0.6646	0.0014	0.000019	0.000001	917	2.827	0.049	0.6619	0.0014
CC26-17	7.9	3078	33.0	0.0169	0.0006	0.6630	0.0029	0.000021	0.000001	816	2.821	0.110	0.6603	0.0029
CC26-17	7.9	3067	33.0	0.0173	0.0003	0.6631	0.0022	0.000023	0.000003	753	2.875	0.057	0.6603	0.0022
CC26-17a	10.3	4611	33.0	0.0166	0.0002	0.6637	0.0009	0.000013	0.000001	1325	2.763	0.027	0.6611	0.0009
CC26-19	10.9	2667	37.0	0.0191	0.0004	0.6649	0.0020	0.000003	0.000002	7409	3.179	0.067	0.6618	0.0020
CC26-19	10.9	2666	37.0	0.0190	0.0003	0.6657	0.0010	0.000005	0.000002	4177	3.159	0.052	0.6627	0.0010
CC26-21	7.0	3404	41.0	0.0215	0.0005	0.6654	0.0018	0.000014	0.000001	1550	3.595	0.091	0.6620	0.0018
CC26-21	7.0	3409	41.0	0.0215	0.0004	0.6672	0.0020	0.000014	0.000001	1530	3.579	0.064	0.6638	0.0021
CC26-21	7.0	3402	41.0	0.0215	0.0004	0.6670	0.0025	0.000015	0.000002	1399	3.581	0.063	0.6636	0.0025
CC26-23	4.6	4804	45.0	0.0230	0.0004	0.6667	0.0009	0.000007	0.000001	3129	3.838	0.072	0.6631	0.0010
CC26-24[o]	6.3	3108	47.0	0.0902	0.0008	0.6648	0.0024	0.000004	0.000002	24217	16.097	0.170	0.6492	0.0026
CC26-24[o]	6.3	3109	47.0	0.0908	0.0009	0.6657	0.0027	0.000005	0.000001	17921	16.186	0.190	0.6501	0.0029
CC26-24[o]	6.3	3107	47.0	0.0916	0.0018	0.6640	0.0024	0.000004	0.000004	24534	16.390	0.364	0.6481	0.0026
CC26-24a	8.2	4564	47.0	0.0236	0.0004	0.6643	0.0010	0.000010	0.000001	2462	3.949	0.076	0.6605	0.0010

Sample name	Mass (mg)	U (ppb)	Depth from top (mm)	$[^{230}Th/^{238}U]$	$[^{230}Th/^{238}U]$ ± 95% error	$[^{234}U/^{238}U]$	$[^{234}U/^{238}U]$ ± 95% error	$[^{232}Th/^{238}U]$	$[^{232}Th/^{238}U]$ ± 95% error	$[^{230}Th/^{232}Th]$	Age (ka)	Age ±2σ (ka)	$[^{234}U/^{238}U]_i$	$[^{234}U/^{238}U]_i$ ± 95% error
CC26-25	8.8	4452	49.0	0.0247	0.0003	0.6682	0.0008	0.000006	0.000000	3864	4.126	0.044	0.6643	0.0009
CC26-27	6.1	4594	53.0	0.0274	0.0005	0.6653	0.0022	0.000020	0.000002	1376	4.589	0.090	0.6609	0.0023
CC26-27	6.1	4583	53.0	0.0275	0.0008	0.6669	0.0018	0.000020	0.000004	1368	4.599	0.145	0.6625	0.0019
CC26-27	6.1	4593	53.0	0.0271	0.0006	0.6669	0.0016	0.000020	0.000001	1359	4.537	0.097	0.6626	0.0017
CC26-29	12.2	2886	57.0	0.0292	0.0004	0.6685	0.0018	0.000003	0.000001	9968	4.887	0.072	0.6638	0.0019
CC26-29	12.2	2887	57.0	0.0291	0.0003	0.6684	0.0015	0.000002	0.000001	12045	4.874	0.058	0.6638	0.0015
CC26-30	5.4	5151	59.0	0.0304	0.0008	0.6668	0.0022	0.000048	0.000004	638	5.104	0.147	0.6620	0.0023
CC26-30	5.4	5163	59.0	0.0302	0.0010	0.6670	0.0028	0.000049	0.000006	610	5.052	0.171	0.6622	0.0029
CC26-30	5.4	5158	59.0	0.0295	0.0007	0.6689	0.0021	0.000049	0.000002	600	4.928	0.115	0.6643	0.0021
CC26-32	10.2	3070	63.0	0.0314	0.0005	0.6666	0.0018	0.000004	0.000002	8612	5.283	0.080	0.6616	0.0018
CC26-32	10.2	3069	63.0	0.0310	0.0004	0.6674	0.0012	0.000003	0.000002	9116	5.197	0.064	0.6625	0.0012
CC26-34	5.3	5392	67.0	0.0326	0.0005	0.6683	0.0022	0.000019	0.000002	1724	5.466	0.081	0.6631	0.0023
CC26-34	5.3	5394	67.0	0.0326	0.0004	0.6688	0.0023	0.000018	0.000002	1798	5.466	0.072	0.6637	0.0024
CC26-34*	5.3	5384	67.0	0.0339	0.0006	0.6665	0.0032	0.000020	0.000005	1715	5.709	0.105	0.6611	0.0033
CC26-37	11.1	3373	73.0	0.0347	0.0005	0.6696	0.0017	0.000002	0.000001	13900	5.827	0.086	0.6641	0.0018
CC26-37	11.1	3375	73.0	0.0349	0.0003	0.6695	0.0013	0.000002	0.000001	15560	5.864	0.061	0.6640	0.0013
CC26-39	6.5	4784	77.0	0.0364	0.0006	0.6707	0.0021	0.000021	0.000003	1747	6.113	0.108	0.6649	0.0022
CC26-39	6.5	4774	77.0	0.0361	0.0010	0.6715	0.0027	0.000022	0.000003	1658	6.046	0.174	0.6659	0.0028
CC26-39	6.5	4773	77.0	0.0361	0.0004	0.6723	0.0018	0.000020	0.000002	1785	6.044	0.069	0.6667	0.0018
CC26-41	10.3	2821	81.0	0.0377	0.0004	0.6719	0.0020	0.000002	0.000002	16290	6.324	0.069	0.6659	0.0021
CC26-41	10.3	2819	81.0	0.0381	0.0004	0.6718	0.0016	0.000004	0.000002	10200	6.390	0.066	0.6658	0.0017
CC26-43	5.9	5087	85.0	0.0388	0.0004	0.6738	0.0018	0.000018	0.000002	2199	6.499	0.079	0.6678	0.0018
CC26-43	5.9	5089	85.0	0.0393	0.0011	0.6725	0.0028	0.000020	0.000004	1949	6.599	0.193	0.6663	0.0029

Sample name	Mass (mg)	U (ppb)	Depth from top (mm)	$[^{230}Th/^{238}U]$	$[^{230}Th/^{238}U]$ ± 95% error	$[^{234}U/^{238}U]$	$[^{234}U/^{238}U]$ ± 95% error	$[^{232}Th/^{238}U]$	$[^{232}Th/^{238}U]$ ± 95% error	$[^{230}Th/^{232}Th]$	Age (ka)	Age ±2σ (ka)	$[^{234}U/^{238}U]_i$	$[^{234}U/^{238}U]_i$ ± 95% error
CC26-43	5.9	5094	85.0	0.0391	0.0004	0.6735	0.0020	0.000020	0.000001	1953	6.544	0.075	0.6674	0.0020
CC26-45	9.6	3222	89.0	0.0400	0.0006	0.6702	0.0018	0.000015	0.000001	2610	6.745	0.098	0.6639	0.0018
CC26-45	9.6	3220	89.0	0.0399	0.0005	0.6699	0.0010	0.000015	0.000001	2577	6.731	0.080	0.6636	0.0010
CC26-47	5.6	5500	93.0	0.0420	0.0007	0.6741	0.0020	0.000025	0.000002	1707	7.047	0.118	0.6675	0.0021
CC26-47	5.6	5508	93.0	0.0420	0.0010	0.6721	0.0032	0.000023	0.000003	1794	7.070	0.187	0.6655	0.0033
CC26-47	5.6	5505	93.0	0.0418	0.0005	0.6728	0.0021	0.000023	0.000002	1824	7.032	0.086	0.6662	0.0022
CC26-49[o]	7.8	2798	97.0	0.0448	0.0005	0.6735	0.0017	0.000008	0.000002	5710	7.538	0.098	0.6665	0.0018
CC26-49[o]	7.8	2797	97.0	0.0443	0.0005	0.6749	0.0016	0.000009	0.000002	4863	7.443	0.087	0.6680	0.0017
CC26-49a	5.9	4579	97.0	0.0432	0.0005	0.6740	0.0016	0.000006	0.000002	7347	7.258	0.088	0.6672	0.0016
CC26-49a	5.9	4584	97.0	0.0437	0.0007	0.6747	0.0024	0.000004	0.000003	10592	7.338	0.123	0.6679	0.0025
CC26-51	5.7	5279	102.0	0.0456	0.0011	0.6757	0.0018	0.000026	0.000001	1739	7.657	0.188	0.6686	0.0019
CC26-51	5.7	5267	102.0	0.0446	0.0007	0.6756	0.0012	0.000029	0.000002	1542	7.477	0.127	0.6687	0.0013
CC26-53*	11.2	2850	106.0	0.0460	0.0006	0.6704	0.0019	0.000001	0.000001	51467	7.795	0.112	0.6630	0.0020
CC26-53*	11.2	2856	106.0	0.0452	0.0005	0.6711	0.0013	0.000004	0.000001	12523	7.638	0.084	0.6639	0.0013
CC26-55	5.7	4968	110.0	0.0479	0.0006	0.6734	0.0031	0.000028	0.000002	1696	8.084	0.115	0.6659	0.0032
CC26-55	5.7	4968	110.0	0.0472	0.0015	0.6757	0.0031	0.000029	0.000005	1656	7.940	0.260	0.6684	0.0032
CC26-55	5.7	4962	110.0	0.0482	0.0005	0.6745	0.0023	0.000030	0.000001	1625	8.128	0.102	0.6669	0.0024
CC26-57	9.3	2751	114.0	0.0492	0.0004	0.6732	0.0018	0.000003	0.000002	16700	8.319	0.075	0.6654	0.0019
CC26-57	9.3	2752	114.0	0.0487	0.0006	0.6723	0.0013	0.000004	0.000002	11663	8.239	0.101	0.6646	0.0014
CC26-59	5.5	4380	118.0	0.0512	0.0011	0.6753	0.0020	0.000039	0.000003	1299	8.647	0.203	0.6673	0.0021
CC26-59	5.5	4385	118.0	0.0512	0.0014	0.6730	0.0022	0.000043	0.000005	1189	8.670	0.246	0.6649	0.0023
CC26-59	5.5	4383	118.0	0.0504	0.0006	0.6756	0.0020	0.000038	0.000003	1323	8.489	0.105	0.6677	0.0021
CC26-62	10.0	2659	124.0	0.0536	0.0005	0.6747	0.0020	0.000006	0.000002	9714	9.083	0.085	0.6663	0.0020

Sample name	Mass (mg)	U (ppb)	Depth from top (mm)	$[^{230}Th/^{238}U]$	$[^{230}Th/^{238}U]$ ± 95% error	$[^{234}U/^{238}U]$	$[^{234}U/^{238}U]$ ± 95% error	$[^{232}Th/^{238}U]$	$[^{232}Th/^{238}U]$ ± 95% error	$[^{230}Th/^{232}Th]$	Age (ka)	Age ±2σ (ka)	$[^{234}U/^{238}U]_i$	$[^{234}U/^{238}U]_i$ ± 95% error
CC26-62	10.0	2662	124.0	0.0535	0.0006	0.6745	0.0012	0.000004	0.000002	12749	9.073	0.109	0.6660	0.0012
CC26-64	5.8	4434	128.0	0.0566	0.0009	0.6740	0.0021	0.000066	0.000002	857	9.608	0.163	0.6651	0.0022
CC26-64	5.8	4444	128.0	0.0568	0.0006	0.6717	0.0030	0.000069	0.000006	824	9.677	0.115	0.6627	0.0031
CC26-64*	5.8	4439	128.0	0.0551	0.0007	0.6730	0.0020	0.000070	0.000002	790	9.352	0.133	0.6642	0.0021
CC26-64a	n.d.	n.d.	128.0	0.0560	0.0005	0.6738	0.0015	0.000005	0.000001	11127	9.538	0.092	0.6649	0.0016
CC26-65	6.5	3896	130.0	0.0565	0.0004	0.6751	0.0012	0.000007	0.000001	7895	9.599	0.077	0.6662	0.0013
CC26-66[o]	9.2	2780	132.0	0.0595	0.0006	0.6759	0.0021	0.000008	0.000002	7744	10.123	0.115	0.6665	0.0022
CC26-66[o]	9.2	2781	132.0	0.0594	0.0006	0.6774	0.0017	0.000007	0.000001	8433	10.081	0.110	0.6681	0.0018
CC26-66a	7.5	3928	132.0	0.0579	0.0004	0.6760	0.0014	0.000013	0.000001	4542	9.824	0.080	0.6669	0.0014
CC26-67a	4.9	5071	134.0	0.0587	0.0009	0.6744	0.0016	0.000002	0.000003	24722	9.999	0.161	0.6651	0.0017
CC26-67a	4.9	5070	134.0	0.0575	0.0009	0.6738	0.0029	0.000006	0.000004	10334	9.800	0.171	0.6646	0.0030
CC26-67	6.5	5037	134.0	0.0588	0.0009	0.6787	0.0025	0.000017	0.000002	3480	9.947	0.166	0.6696	0.0027
CC26-67	6.5	5043	134.0	0.0590	0.0008	0.6752	0.0018	0.000022	0.000003	2664	10.028	0.141	0.6659	0.0019
CC26-67	6.5	5043	134.0	0.0581	0.0008	0.6758	0.0018	0.000019	0.000001	2994	9.873	0.141	0.6666	0.0019
CC26-68	10.4	3861	136.0	0.0593	0.0004	0.6759	0.0013	0.000004	0.000000	15007	10.079	0.080	0.6665	0.0013
CC26-69	11.9	2858	138.0	0.0611	0.0005	0.6766	0.0019	0.000005	0.000001	13256	10.402	0.088	0.6670	0.0020
CC26-69	11.9	2864	138.0	0.0603	0.0005	0.6745	0.0015	0.000004	0.000001	14341	10.283	0.100	0.6650	0.0016
CC26-70	5.2	4724	140.0	0.0616	0.0007	0.6737	0.0029	0.000090	0.000002	682	10.521	0.143	0.6639	0.0030
CC26-70	5.2	4713	140.0	0.0614	0.0014	0.6720	0.0037	0.000091	0.000005	676	10.499	0.262	0.6622	0.0039
CC26-70	5.2	4725	140.0	0.0614	0.0008	0.6705	0.0023	0.000090	0.000004	685	10.530	0.150	0.6606	0.0024
CC26-72	10.8	2933	144.0	0.0625	0.0005	0.6719	0.0020	0.000006	0.000001	9953	10.736	0.095	0.6618	0.0021
CC26-72	10.8	2933	144.0	0.0626	0.0007	0.6716	0.0015	0.000009	0.000002	7002	10.741	0.122	0.6615	0.0015
CC26-73	5.6	4841	146.0	0.0619	0.0009	0.6717	0.0018	0.000023	0.000003	2738	10.626	0.171	0.6617	0.0019

Sample name	Mass (mg)	U (ppb)	Depth from top (mm)	$[^{230}Th/^{238}U]$	$[^{230}Th/^{238}U]$ ± 95% error	$[^{234}U/^{238}U]$	$[^{234}U/^{238}U]$ ± 95% error	$[^{232}Th/^{238}U]$	$[^{232}Th/^{238}U]$ ± 95% error	$[^{230}Th/^{232}Th]$	Age (ka)	Age ±2σ (ka)	$[^{234}U/^{238}U]_i$	$[^{234}U/^{238}U]_i$ ± 95% error
CC26-73	5.6	4824	146.0	0.0632	0.0012	0.6740	0.0029	0.000016	0.000005	3991	10.819	0.226	0.6639	0.0030
CC26-73	5.6	4844	146.0	0.0619	0.0009	0.6725	0.0021	0.000021	0.000002	2949	10.603	0.168	0.6625	0.0022
CC26-73a	6.2	4637	146.0	0.0623	0.0005	0.6708	0.0014	0.000006	0.000001	9718	10.707	0.096	0.6607	0.0015
CC26-73b	7.8	2703	146.0	0.0638	0.0006	0.6710	0.0024	0.000014	0.000002	4634	10.978	0.115	0.6606	0.0025
CC26-73b	7.8	2703	146.0	0.0631	0.0006	0.6711	0.0018	0.000012	0.000002	5179	10.845	0.112	0.6608	0.0019
CC26-75	11.0	2819	150.0	0.0659	0.0005	0.6738	0.0020	0.000019	0.000001	3422	11.313	0.104	0.6633	0.0021
CC26-75	11.0	2823	150.0	0.0654	0.0006	0.6737	0.0012	0.000027	0.000002	2413	11.226	0.103	0.6632	0.0013
CC26-76	6.3	4053	152.0	0.0676	0.0010	0.6722	0.0026	0.000020	0.000002	3387	11.651	0.194	0.6612	0.0027
CC26-76	6.3	4059	152.0	0.0661	0.0018	0.6725	0.0021	0.000018	0.000004	3680	11.372	0.325	0.6618	0.0022
CC26-76	6.3	4061	152.0	0.0673	0.0008	0.6732	0.0019	0.000021	0.000001	3149	11.578	0.154	0.6624	0.0020
CC26-77	10.2	6221	154.0	0.0718	0.0010	0.6740	0.0034	0.000013	0.000002	5437	12.388	0.194	0.6624	0.0035
CC26-77	10.2	6242	154.0	0.0720	0.0006	0.6745	0.0021	0.000015	0.000002	4735	12.410	0.121	0.6629	0.0022
CC26-77	10.2	6230	154.0	0.0720	0.0004	0.6769	0.0013	0.000014	0.000001	5120	12.371	0.076	0.6655	0.0014
CC26-5.2	4.6	4681	9.0	0.0070	0.0004	0.6622	0.0035	0.000034	0.000007	207	1.151	0.068	0.6611	0.0035
CC26-5.2	4.6	4697	9.0	0.0065	0.0008	0.6573	0.0047	0.000078	0.000016	83	1.065	0.136	0.6563	0.0047
CC26-5.2	4.6	4682	9.0	0.0073	0.0005	0.6634	0.0034	0.000038	0.000007	191	1.198	0.084	0.6632	0.0034
CC26-11.2	4.7	4606	22.0	0.0121	0.0006	0.6610	0.0035	0.000045	0.000005	268	2.006	0.102	0.6591	0.0035
CC26-11.2	4.7	4601	22.0	0.0114	0.0008	0.6600	0.0040	0.000067	0.000017	170	1.886	0.137	0.6582	0.0040
CC26-11.2	4.7	4586	22.0	0.0115	0.0006	0.6661	0.0042	0.000045	0.000005	255	1.890	0.101	0.6643	0.0042

Table 6-2. U-Th corrected ages for CC26. The error weighted mean (EWM) age with its corresponding mean square weighted deviation (MSWD) and probability of fit is provided for samples for which multi-aliquot analyses were performed. Samples for which U-Th dating was repeated by analysing another calcite prism from the same stratigraphic layer have a suffix a or/and b. Samples CC26-5.2 and CC26-11.2 were selected upon micro-CT results. Rejected results are marked with * and the outliers have a suffix °. N.d. stands for not analysed.

Sample name	Depth from top (±100% error) mm	Aliquot 1 age (±2σ) ka	Aliquot 2 age (±2σ) ka	Aliquot 3 age (±2σ) ka	EWM age (±2σ) ka	MSWD EWM age	Probability of fit EWM age
CC26-1	0.5 (0.5)	0.160 (0.081)	0.134 (0.081)	0.160 (0.095)	0.150 (0.049)	0.1	0.88
CC26-1.5	1.0 (0.5)	0.313 (0.048)	n.d.	n.d.			
CC26-2	3.0 (0.5)	0.593 (0.038)	0.569 (0.035)	n.d.	0.580 (0.026)	0.9	0.36
CC26-4	7.0 (0.5)	0.898 (0.044)	0.856 (0.055)	0.996 (0.068)*	0.882 (0.034)	1.4	0.23
CC26-6	11.0 (0.5)	1.111 (0.048)	1.151 (0.030)	n.d.	1.139 (0.025)	2.2	0.14
CC26-8°	15.0 (0.5)	1.756 (0.052)	1.741 (0.112)	1.750 (0.052)	1.752 (0.035)	0.0	0.96
CC26-8a*	15.0 (0.5)	1.455 (0.054)	1.356 (0.049)	n.d.	1.400 (0.623)	7.4	0.01
CC26-9	17.0 (0.5)	1.617 (0.055)	1.591 (0.053)	n.d.	1.604 (0.038)	0.5	0.50
CC26-11	21.0 (0.5)	1.779 (0.062)	1.783 (0.064)	n.d.	1.781 (0.044)	0.0	0.93
CC26-11a	21.0 (0.5)	1.782 (0.084)	n.d.	n.d.			
CC26-13	25.0 (0.5)	2.107 (0.035)	n.d.	n.d.			
CC26-14°*	27.0 (0.5)	3.156 (0.068)*	3.217 (0.052)	3.323 (0.053)	3.195 (0.041)	2.1	0.15
CC26-14a	27.0 (0.5)	2.304 (0.066)	n.d.	n.d.			
CC26-15	29.0 (0.5)	2.446 (0.084)	n.d.	n.d.			
CC26-17	33.0 (0.5)	2.827 (0.049)	2.821 (0.110)	2.875 (0.057)	2.845 (0.035)	0.9	0.40
CC26-17a	33.0 (0.5)	2.763 (0.027)	n.d.	n.d.			
CC26-19	37.0 (0.5)	3.179 (0.067)	3.159 (0.052)	n.d.	3.167 (0.041)	0.2	0.63

Sample name	Depth from top (±100% error) mm	Aliquot 1 age (±2σ) ka	Aliquot 2 age (±2σ) ka	Aliquot 3 age (±2σ) ka	EWM age (±2σ) ka	MSWD EWM age	Probability of fit EWM age
CC26-21	41.0 (0.5)	3.595 (0.091)	3.579 (0.064)	3.581 (0.063)	3.583 (0.040)	0.0	0.96
CC26-23	45.0 (0.5)	3.838 (0.072)	n.d.	n.d.			
CC26-24^{o}	47.0 (0.5)	16.097 (0.170)	16.186 (0.190)	16.390 (0.364)	16.164 (0.120)	1.1	0.33
CC26-24a	47.0 (0.5)	3.949 (0.074)	n.d.	n.d.			
CC26-25	49.0 (0.5)	4.126 (0.044)	n.d.	n.d.			
CC26-27	53.0 (0.5)	4.589 (0.090)	4.599 (0.145)	4.537 (0.097)	4.571 (0.060)	0.4	0.67
CC26-29	57.0 (0.5)	4.887 (0.072)	4.874 (0.058)	n.d.	4.879 (0.045)	0.1	0.79
CC26-30	59.0 (0.5)	5.104 (0.147)	5.052 (0.171)	4.928 (0.115)	5.007 (0.080)	1.9	0.14
CC26-32	63.0 (0.5)	5.283 (0.080)	5.197 (0.064)	n.d.	5.231 (0.080)	2.8	0.10
CC26-34	67.0 (0.5)	5.466 (0.081)	5.466 (0.072)	5.709 (0.105)*	5.466 (0.054)	0.0	1.00
CC26-37	73.0 (0.5)	5.827 (0.086)	5.864 (0.061)	n.d.	5.852 (0.050)	0.5	0.48
CC26-39	77.0 (0.5)	6.113 (0.108)	6.046 (0.174)	6.044 (0.069)	6.062 (0.055)	0.6	0.55
CC26-41	81.0 (0.5)	6.324 (0.069)	6.390 (0.066)	n.d.	6.359 (0.048)	1.9	0.17
CC26-43	85.0 (0.5)	6.499 (0.079)	6.599 (0.193)	6.544 (0.075)	6.528 (0.052)	0.6	0.53
CC26-45	89.0 (0.5)	6.745 (0.098)	6.731 (0.080)	n.d.	6.737 (0.062)	0.0	0.83
CC26-47	93.0 (0.5)	7.047 (0.118)	7.070 (0.187)	7.032 (0.086)	7.041 (0.065)	0.1	0.93
CC26-49^{o}	97.0 (0.5)	7.538 (0.098)	7.443 (0.087)	n.d.	7.485 (0.065)	2.1	0.15
CC26-49a	97.0 (0.5)	7.258 (0.088)	7.338 (0.123)	n.d.	7.285 (0.072)	1.1	0.29
CC26-51	102.0 (0.5)	7.657 (0.188)	7.477 (0.127)	n.d.	7.534 (0.106)	2.5	0.11
CC26-53*	106.0 (0.5)	7.795 (0.112)	7.638 (0.084)	n.d.	7.694 (0.956)	5.0	0.02
CC26-55	110.0 (0.5)	8.084 (0.115)	7.940 (0.260)	8.128 (0.102)	8.095 (0.073)	0.9	0.39
CC26-57	114.0 (0.5)	8.319 (0.075)	8.239 (0.101)	n.d.	8.290 (0.060)	1.6	0.20
CC26-59	118.0 (0.5)	8.647 (0.203)	8.670 (0.246)	8.489 (0.105)	8.541 (0.087)	1.6	0.20

Sample name	Depth from top (±100% error) mm	Aliquot 1 age (±2σ) ka	Aliquot 2 age (±2σ) ka	Aliquot 3 age (±2σ) ka	EWM age (±2σ) ka	MSWD EWM age	Probability of fit EWM age
CC26-62	124.0 (0.5)	9.083 (0.085)	9.073 (0.109)	n.d.	9.079 (0.067)	0.0	0.88
CC26-64	128.0 (0.5)	9.608 (0.163)	9.677 (0.115)	9.352 (0.133)*	9.654 (0.094)	0.5	0.49
CC26-64a	128.0 (0.5)	9.538 (0.092)	n.d.	n.d.			
CC26-65	130.0 (0.5)	9.599 (0.077)	n.d.	n.d.			
CC26-66^{o}	132.0 (0.5)	10.123 (0.115)	10.081 (0.110)	n.d.	10.101 (0.080)	0.3	0.60
CC26-66a	132.0 (0.5)	9.824 (0.080)	n.d.	n.d.			
CC26-67	134.0 (0.5)	9.947 (0.166)	10.028 (0.141)	9.873 (0.141)	9.950 (0.085)	1.2	0.30
CC26-67a	134.0 (0.5)	9.999 (0.161)	9.800 (0.171)	n.d.	9.905 (0.117)	2.9	0.09
CC26-68	136.0 (0.5)	10.079 (0.080)	n.d.	n.d.			
CC26-69	138.0 (0.5)	10.402 (0.088)	10.283 (0.100)	n.d.	10.350 (0.066)	3.2	0.07
CC26-70	140.0 (0.5)	10.521 (0.143)	10.499 (0.262)	10.530 (0.150)	10.522 (0.096)	0.0	0.98
CC26-72	144.0 (0.5)	10.736 (0.095)	10.741 (0.122)	n.d.	10.738 (0.075)	0.0	0.95
CC26-73	146.0 (0.5)	10.626 (0.171)	10.819 (0.226)	10.603 (0.168)	10.659 (0.106)	1.3	0.27
CC26-73a	146.0 (0.5)	10.707 (0.096)	n.d.	n.d.			
CC26-73b	146.0 (0.5)	10.978 (0.115)	10.845 (0.112)	n.d.	10.910 (0.080)	2.7	0.10
CC26-75	150.0 (0.5)	11.313 (0.104)	11.226 (0.103)	n.d.	11.269 (0.073)	1.4	0.23
CC26-76	152.0 (0.5)	11.651 (0.194)	11.372 (0.325)	11.578 (0.154)	11.578 (0.113)	1.1	0.34
CC26-77	154.0 (0.5)	12.388 (0.194)	12.410 (0.121)	12.371 (0.076)	12.383 (0.061)	0.1	0.86
CC26-5.2	9.0 (0.5)	1.151 (0.068)	1.065 (0.136)	1.198 (0.084)	1.156 (0.049)	1.4	0.24
CC26-11.2	22.0 (0.5)	2.006 (0.102)	1.886 (0.137)	1.890 (0.101)	1.934 (0.064)	1.6	0.20

Apart from the outliers, four additional samples (CC26-11; CC26-17; CC26-66 and CC26-67) were chemically reprocessed once, and one sample (CC26-73) reprocessed twice. CC26-11 was re-sampled from the stalagmite, while for all others the leftovers from the first sampling session were used. Two of these repeats (CC26-17 and CC26-73) resulted in error-weighted mean ages with a probability of fit lower than 5% (**Table 6-3**). Although multiple analyses of the same aliquot for these samples are internally consistent, and although most of them fit the mean age of the age-depth model, the inconsistency between replicate calcite samples is the reason for the exclusion of these analyses from the age-depth modelling.

Table 6-3. Error weighted mean (EWM) age with mean square weighted deviation (MSWD) and probability of fit for samples where multiple calcite prisms were dated from the same stratigraphic layer.

Sample name	Age (ka)	Age ±2σ(ka)	EWM age (ka)	EWM age ±2σ(ka)	MSWD EWM age	Probability of fit EWM age
CC26-11	1.779	0.062				
CC26-11	1.783	0.064	1.781	0.039	0.0	1.00
CC26-11a	1.782	0.084				
CC26-17	2.827	0.049				
CC26-17	2.821	0.110	2.794	0.078	5.1	0.00
CC26-17	2.875	0.057				
CC26-17a	2.763	0.027				
CC26-64	9.608	0.163				
CC26-64	9.677	0.115	9.595	0.066	1.8	0.17
CC26-64a	9.538	0.092				
CC26-67	9.947	0.166				
CC26-67	10.028	0.141				
CC26-67	9.873	0.141	9.934	0.069	1.4	0.23
CC26-67a	9.999	0.161				
CC26-67a	9.800	0.171				
CC26-73	10.626	0.171				
CC26-73	10.819	0.226				
CC26-73	10.603	0.168	10.784	0.148	4.7	0.00
CC26-73a	10.707	0.096				
CC26-73b	10.978	0.115				
CC26-73b	10.845	0.112				

6.3.2 PETROGRAPHY, TRACE ELEMENT ANALYSES AND MICRO-CT RESULTS

Optical microscopy observations of the thin sections reveal that the Holocene section of CC26 consists predominantly of compact columnar calcite with mean crystal sizes about 2 mm long and 0.5 mm wide (Frisia, 2015) with no visible aragonite relicts (**Figure 6-3a**). Partially neomorphosed aragonite needles arranged in fans that nucleated at the tip of the calcite crystals occur only in the top millimetre (**Figure 6-3b**). Evidence for aragonite is visible only along the outer flanks of past stalagmite surfaces, as seen in the internal stratigraphy. Despite the overall compact appearance of the fabric in thin section, there are regions characterized by higher visible porosity, but there is no clear evidence of dissolution of a precursor mineral.

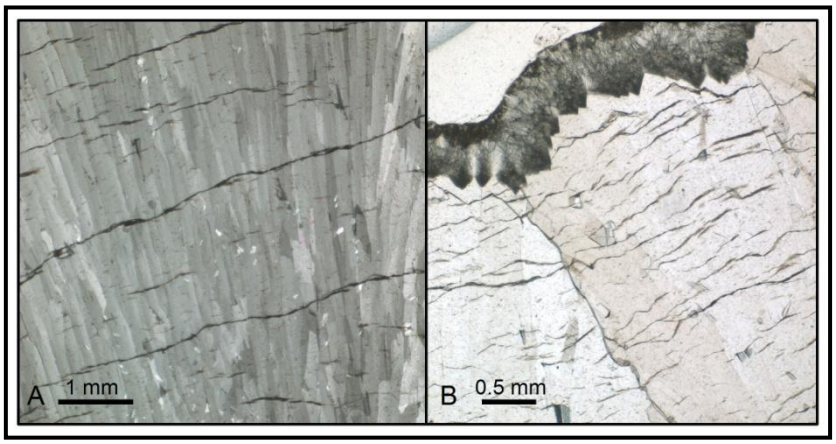

Figure 6-3. Thin sections from stalagmite CC26. Most of the sample consists of compact columnar calcite without any traces of aragonite relicts (**a**) while aragonite needles partially transformed to calcite arranged in fans are observed only in the top millimetre of CC26 (**b**).

LA-ICP-MS results confirm that CC26 is characterised by a relatively high U content, with concentrations in the range 2 to 10 ppm for calcite and more than ten times this (>100 ppm) in the upper aragonite section (**Figure 6-4**). Synchrotron-based micro XRF elemental mapping for the top few millimetres of the stalagmite confirm this distribution and further reveal that U is highly concentrated in small

areas at the nucleus of aragonite fans (**Figure 6-5**). Despite using a small spot size (12 µm) for the LA analyses, these highly enriched zones (~50 µm in diameter) are not clearly distinguishable in the LA maps (**Figure 6-4**).

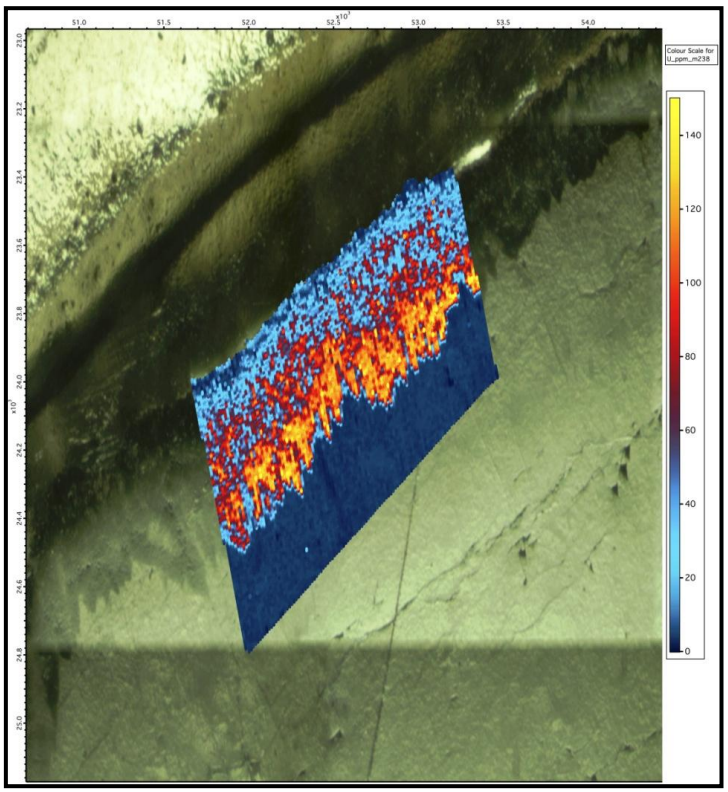

Figure 6-4. Laser ablation (LA) trace element analyses of U in the top section of the CC26. The LA results reveal the U is, in this case, about ten times higher in concentration than the calcite.

Results of micro-CT analysis confirm that the majority of the analysed portion of the stalagmite is characterized by uniform density with no observable large porous sections as seen in speleothems from other studies (Mickler et al., 2004b; Vanghi et al., 2014; Walczak et al., 2015). There are, however, a few regions where the density of the sample is lower, implying an increase in porosity. Two porous zones can be distinguished. The outer porous zone corresponds to a particular growth zone and can be traced regularly from the flanks of the stalagmite towards its centre. The inner porous zone is characterized by over a hundred irregularly distributed porous lenses, i.e. voids

surrounded by compact dense material. These lenses do not correspond to growth layers nor do they correlate to fractures.

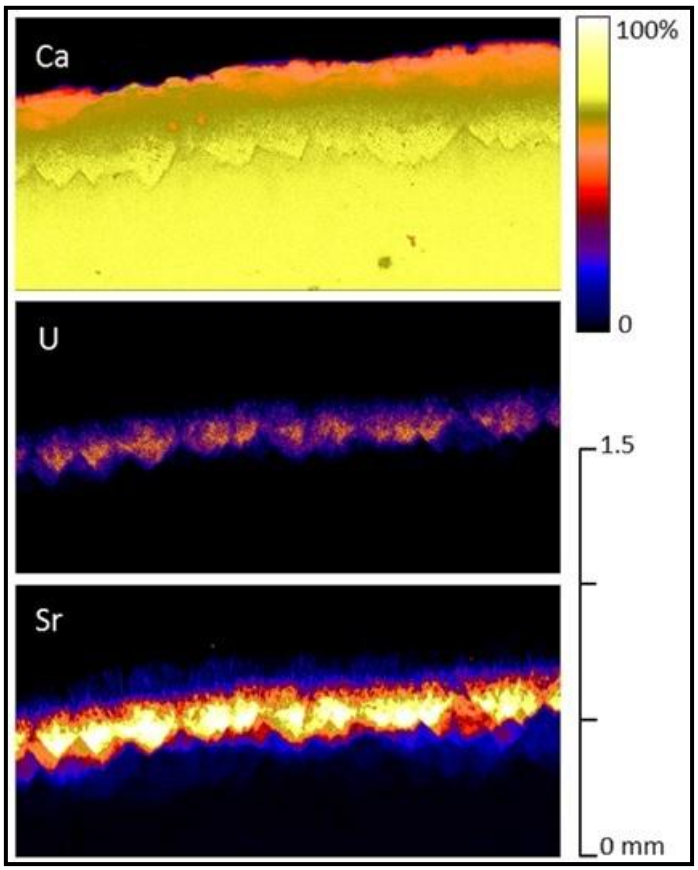

Figure 6-5. Synchrotron results of the upper most portion of CC26. The results reveal that the U is not evenly distributed in the high-U aragonite zone at the top but it is highly concentrated in small "buds" at the nucleus of aragonite fans.

6.4 DISCUSSION

6.4.1 ELIMINATING CONTAMINATION AS AN EXPLANATION FOR THE OBSERVED OUTLIERS IN THE U-Th DATASET

When outliers are encountered in speleothem U-Th datasets their occurrence is anecdotally attributed to analytical problems or initial Th contamination, and these rogue analyses not further discussed (Drysdale et al., 2009; Frisia et al., 2005; Walczak et al., 2015).

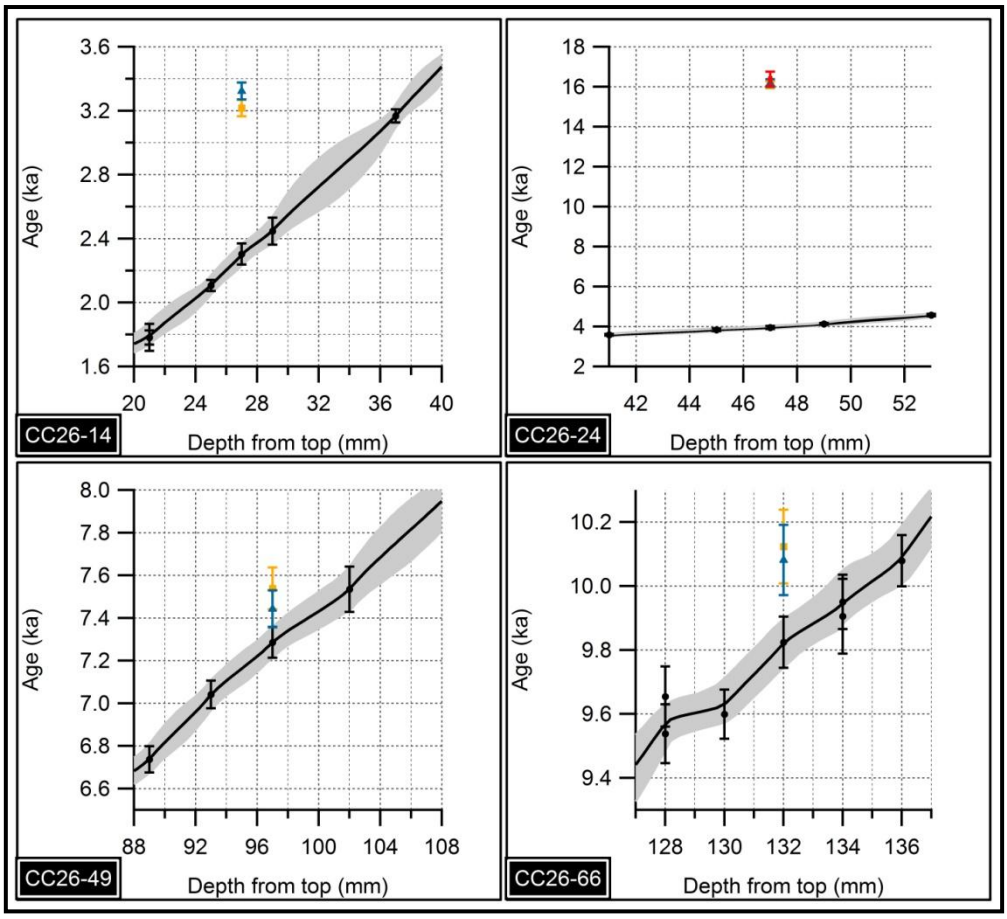

Figure 6-6. Reproducibility in replicated measurements of the same U-Th aliquot. The results preclude analytical issues as an explanation for the observed outliers. The age offset between the analytical and model age ranges between 3 and 309%. The repeat analyses from another calcite prism from the same depth positions are in agreement with the stratigraphic sequence and do not support evidence of large aragonite-to-calcite transformation in CC26.

However, reproducibility in replicated measurements of three (CC26-8; CC26-24) or two (CC26-14; CC26-49; CC26-66) aliquots of the same sample (**Figure 6-6**) preclude analytical issues as an explanation for the outliers reported here. The procedures used during sampling (careful cleaning of sampling equipment and each calcite prism after its sampling) and chemical separation of U and Th under clean laboratory conditions make external contamination extremely unlikely. Contamination can also be ruled out on the basis of U mass balance, with the $^{234}U/^{238}U$ (measured) of the outliers being precisely in sequence with neighbouring samples (**Figure 6-7**). Late Holocene

Corchia stalagmites have a distinctively low $^{234}U/^{238}U$ ratio, ruling out contamination or substitution by older Corchia speleothems or any other material known to have been analysed at the University of Melbourne.

An older apparent age during chemical processing of a sample could only be caused by addition of ^{233}U and ^{236}U in the ratio used in our mixed spike, without adding ^{229}Th, or by incomplete sample-spike equilibration such that proportionately lower $^{229}Th/^{230}Th$ is loaded onto the ion exchange columns. In this case, the former can be ruled out because ^{236}U has never been present in chemical processing clean laboratory except as a component of pre-mixed ^{229}Th-^{233}U-^{236}U isotopic spike and it is found that the $^{233}U/^{236}U$ ratio in these samples is as expected for this spike. Incomplete sample-spike equilibration can never be completely ruled out but is addressed at the University of Melbourne by refluxing overnight in 15 % HNO_3 at 80 to 95°C. All of these lines of evidence point to the potential role of diagenetic alteration as a cause for the observed outliers. All outliers are older than their expected age, providing supporting evidence for U loss.

The offset in outlier age from the corresponding repeated ages is mostly in the range 3-38%, with one extreme outlier of 309% at 47 mm of depth from top of the stalagmite. This sample (CC26-24) is 12.22 ka older than its true age of 3.95 ka (based on the repeated chemistry of coeval calcite, as well as on the age-depth model mean age for this depth position). Since the $^{234}U/^{238}U$ ratio of this sample is almost the same as its replicate and neighbours (**Figure 6-7**), contamination as the cause of this discrepancy can be eliminated. To explain this outlier, one would need a high-U (i.e. aragonite) precursor for which there is no visible petrographic evidence at this particular region in the stalagmite.

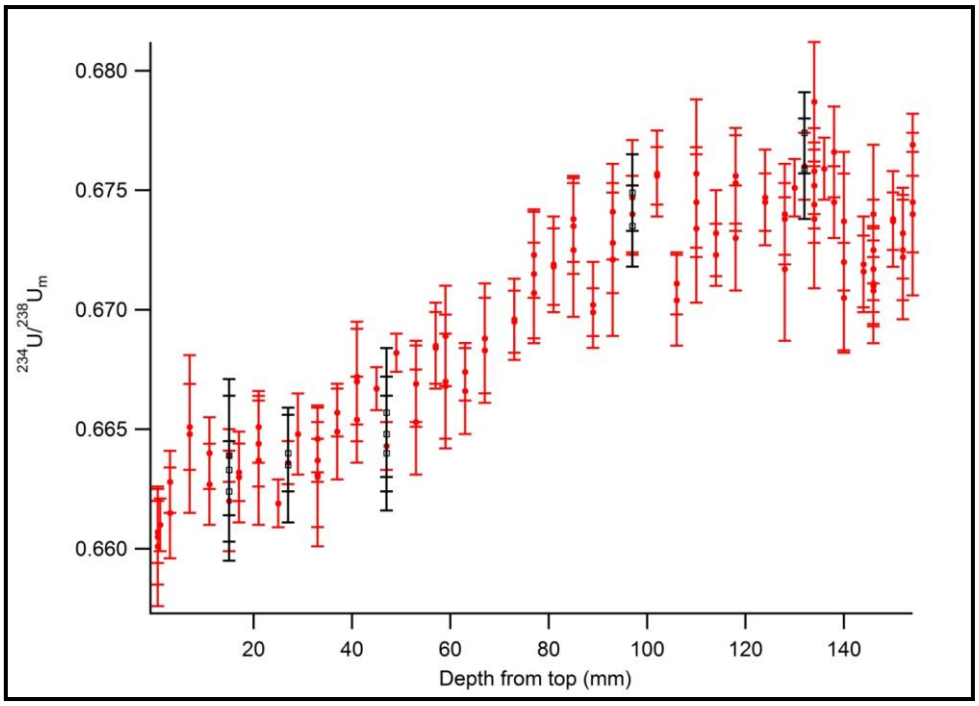

Figure 6-7. $^{234}U/^{238}U$ (measured) of the U-Th samples versus depth from the top of stalagmite. The outliers $^{234}U/^{238}U$ (measured) (in black) are precisely in sequence with neighbouring samples additionally ruling out the problem with contamination of these samples.

6.4.2 MECHANISMS OF ARAGONITE VERSUS CALCITE DEPOSITION AND POSSIBLE PATHWAYS OF U-LOSS IN CC26

Laboratory experiments (Morse et al., 1997; De Choudens-Sánchez and Gonzalez, 2009) and field studies (Frisia et al., 2002) show that the formation of calcite or aragonite is dependent on a combination of factors including: temperature, the drip-water Mg/Ca ratio, the saturation state with respect to calcite and aragonite, and precipitation rate. Although the initial Mg/Ca ratio of the dripwater is determined primarily by the host-rock composition e.g. drip-water Mg/Ca ratios in caves hosted in dolomite bedrock are typically higher (usually above 0.9) than those in limestone (usually below 0.1): Cabrol, (1978); Perrin et al., (2014), Borsato et al., (2016) all of these factors can have a degree of climate dependency. Primary aragonite and primary calcite deposition

may interchange in a single speleothem, and this has been attributed to hydrological variability, where drier conditions cause a decreased drip rate, increased PCP and Mg/Ca of drip-water and consequently promote aragonite deposition (Railsback et al., 1994; Frisia et al., 2002; Wassenburg et al., 2012). Conversely the opposite conditions favour the formation of calcite. As an example, at Grotte de Clamouse, prismatic aragonite is favored over calcite in stalagmites from drips with discharge as low as 0.00035 ml/min (i.e. 1 drop every >3 hours) and a mean Mg/Ca ratio higher than 1.2 (Frisia et al., 2002). In this case aragonite stalagmites form from water with a low Ca content (Ca = 0.95 mmol/L), similar to that of Corchia CNR-2 water, indicating a high degree of PCP.

In CC26, aragonite is present at the very tip and within the pre-Holocene section. The presence of aragonite can be explained by the chemistry of the percolating water nearby in the Galleria delle Stalattiti (Piccini et al., 2008). The saturation indices (SI) calculated using the PHREEQC code (Parkhurst and Appelo, 1999) are slightly supersaturated for both aragonite ($SI_{aragonite}$: 0.11±0.14) and calcite ($SI_{calcite}$: 0.27±0.14), and the Mg/Ca ratio is 1.11±0.03 (mol/mol), close to the aragonite/calcite threshold of 1.2 implying the potential to precipitate (and dissolve) aragonite depending on hydrological processes. Today, the saturation index for Galleria delle Stalattiti dripwater is slightly higher for calcite, which is the most likely phase that would precipitate. However, aragonite precipitation is favored by the combined rise in $SI_{aragonite}$ and Mg/Ca ratio (De Choudez Sanchez and Gonzalez, 2009) and this is usually accomplished when Prior Calcite Precipitation (PCP) removes Ca in the percolating water.

Given the present day long residence time of GdS dripwater which favours a stoichiometric (congruent) dissolution of the dolomitic host rock we should expect that the dripwater Mg/Ca ratio approaches the Mg/Ca ratio of the host-rock (Mg/Ca_{HR}). Thus, a Mg/Ca dripwater ratio > Mg/Ca_{HR} suggests the influence of PCP, and the amount of PCP can be theoretically quantified by the dripwater Mg/Ca ratio excess. By

comparing the mean GdS dripwater Mg/Ca ratio (1.11±0.03 mol/mol) to the mean host rock Mg/Ca ratio composition (0.953 mol/mol : Cortecci et al., 1999) the resulting PCP is 15.3 ±2.7% (i.e. 15.3% Ca loss with respect to the initial Ca composition), and the carbonate phase predicted to precipitate should be calcite. For an increase in PCP over 25-30% the dripwater Mg/Ca ratio should increase to >1.25-1.33 shifting the system to an aragonite or mixed aragonite-calcite mode (Frisia et al., 2002). A significant decrease in the Mg/Ca ratio accompanied by a reduction in the aragonite saturation state, would cause aragonite to be dissolved, but waters should still be supersaturated with respect to calcite causing the reprecipitation of calcite in voids created by the aragonite dissolution.

In CC26, the influence of PCP was documented in a previous study by the positive correlation of Mg/Ca and Sr/Ca ratios, and has been linked to episodes of reduced infiltration (Regattieri et al., 2014). Therefore, it follows that aragonite could have formed in CC26 during episodes of reduced recharge if PCP enough the chemistry of the parent water by rising the Mg/Ca ratio above the aragonite/calcite threshold.

Because the partition coefficient of uranium (D_U) in aragonite is ca. 50 times that of calcite as calculated from speleothem data ($D_{U\text{-calcite}}$ / $D_{U\text{-aragonite}}$ = 52.3±21.3 in Wassenburg et al., 2012 and = 41.8 in Frisia et al., 2002), then whenever aragonite formed at high PCP conditions, it would have been enriched in U.

Synchrotron-radiation based micro XRF in the top layer (**Figure 6-5**), where aragonite is still present, shows that the distribution of U is not homogeneous even in this unstable, U-rich phase. U concentration is at its maximum (~200 ppm) at the nuclei of fans. By contrast, Sr concentration is more equally distributed throughout the aragonite fans (~900 ppm). The elemental map suggests that U in CC26 aragonite is preferentially incorporated onto underlying calcite crystal tips at the onset (nucleation) of aragonite growth. Ortega et al. (2005) observed in a speleothem consisting of aragonite and neomorphic calcite from the

Aranzadi Gallery in Pierre Saint-Martin cave (France) that U (and Sr) is preferentially concentrated in aragonite "buds" about 100 μm in size, which is the same scale of single aragonite fans occurring at the top of CC26. The aragonite-to-calcite transformation in the Aranzadi speleothem resulted in a change in fabric, with neomorphic calcite having an equant mosaic, rather than a columnar fabric. Yet, recrystallization resulted in "abnormally high" U and Sr concentrations in the neomorphic calcite, which is not observed in CC26.

It is therefore reasonable to hypothesize that, if similarly high concentrations of U were present in the zones where the U-Th outliers occur (or elsewhere in the stalagmite), it may have been incorporated in local aragonite "buds", whose transformation into calcite implies the complete dissolution of the bud, and growth of the neomorphic calcite in optical continuity with the surrounding columnar crystals. This phenomenon, however, needs a mechanism by which U can be lost from aragonite and not inherited by the neomorphic calcite (see Ortega et al., 2005), which, in turn, implies post-deposition fluid flow through a stalagmite that otherwise appears to be relatively compact.

Micro-CT results reveal that there are porous areas in the stalagmite, which could explain the U loss from the sample. Detailed inspection of voids observed in the top 26.5 mm of the stalagmite (**Figure 6-8**) reveal cavities more than 2 mm long and oriented in various directions.

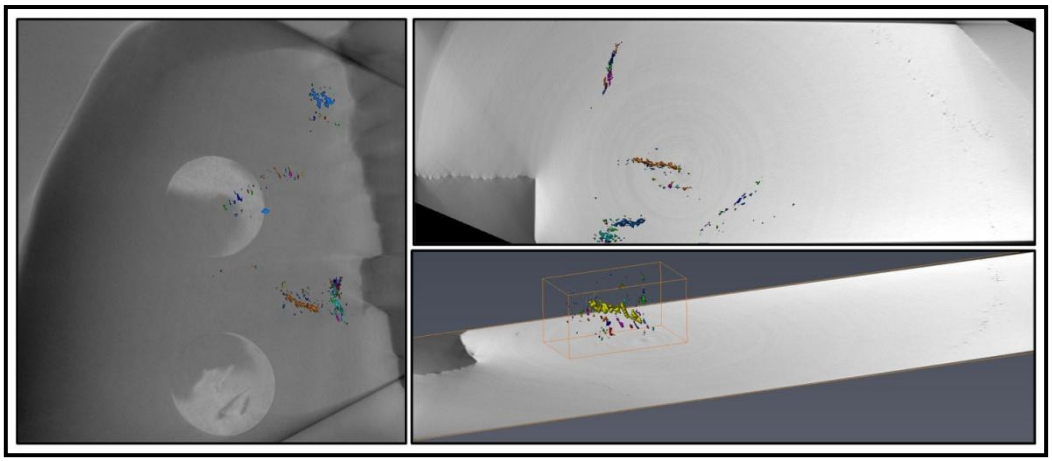

Figure 6-8. Micro-CT results for the upper ~26.5 mm of the stalagmite (three figures present different orientations of the same section) reveal that most of the analysed portion is characterised by uniform density with no observable evidence of large porous sections. There are, however, a few porous areas with cavities more than 2 mm long formed by post-depositional dissolution process. Circular stickers are 6 mm in diameter.

From their positions and directions it is clear that they cross multiple growth layers and do not coincide with fractures in the speleothem. The voids have an irregular shape and rounded surfaces. All of this implies their post-depositional origin by dissolution processes. These are selected as an example although there are further similar-sized voids in the analysed section. At this scanning resolution, these porous areas are not largely interconnected although one cannot exclude the possibility that some of the voids were subsequently filled with calcite that grew in optical continuity with the primary calcite. It is also unclear if these voids are filled with water or air: to answer this question one would need to additionally employ, for example, the MRI method (Zisu et al., 2012). In any case, the observation of voids (water or air filled) in this generally compact stalagmite supports the hypothesis of diagenetic alteration and U loss in very restricted areas of the sample, which resulted in the few observed U-Th age inversions. This might also explain the poor reproducibility of samples CC26-17 and CC26-17a, and CC26-73, CC26-73a and CC26-73b. At the same time, limited distribution of the voids along the growth layer accounts

for the accurate dating of additional calcite prisms from the same stratigraphic position.

To test the role of voids registered after micro-CT scanning two additional samples were dated by targeting the zones with increased porosity at depths of 9 and 22 mm from the top. Two powder samples (CC26-5.2 and CC26-11.2) of less than 5mg in weight were sampled using 1mm wide drill bit and were dated in triplicate. Analyses of both samples were reproducible (**Table 6-1** and **Table 6-2**) and the error weighted ages compared to the ages of surrounding samples together with the age-depth model output are given on the **Figure 6-9**.

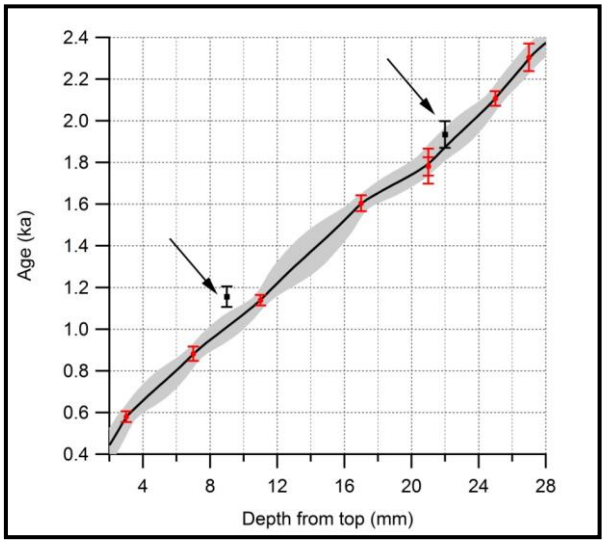

Figure 6-9. The error weighted mean ages of two samples selected from high porous zones based on micro-CT results. The dating results confirm U-loss in the case of the sample CC26-5.2 (9 mm from the top) while the result of the sample CC26-11.2 (22 mm from the top) is in stratigraphic order.

The sample CC26-5.2 resulted in an anomalous old age supporting the interpretation of porous zones as being the pathways for U-loss. Dating of a sample CC26-11.2 however did not result in an outlier. The error weighted mean age of this sample is in stratigraphic order. The reason for this sample to be in stratigraphic order might be in difficulties in targeting this porous zone while sampling this dating sample. Although in stratigraphic order this sample is slightly older than predicted by age-depth model based on surrounding samples

which may also indicate slight U-loss but insufficient to result in an outlier. These results additionally stress out that the stalagmite CC26 experienced very limited diagenetic alterations and that the voids recorded by micro-CT analyses were very likely the pathways of U-loss.

It is proposed that a fluid undersaturated with respect to aragonite percolated through CC26 causing dissolution of any previously formed aragonite buds. This is to be expected if, for example, a short-lived, relatively dry period accompanied by aragonite precipitation was followed by a more humid one during which calcite was deposited. This is discussed further in the next section.

6.4.3 MODELLING OF U-LOSS AND TIMING OF DIAGENESIS

Uranium loss in this case is presumed to be promoted by the dissolution of high-U aragonite and its replacement with (relatively) low-U calcite, whereby all excess U is removed from the system but Th remains adsorbed onto the immediate surrounds of the dissolved material. Because the U loss is by dissolution rather than by leaching there is no reason to suppose that preferential loss of ^{234}U has occurred, and the effect of aragonite dissolution is thus restricted to an increase in $^{230}Th/^{238}U$ in the immediate vicinity of the U loss. Assuming instantaneous U loss (the effect of this assumption is relatively small; Scholz et al., 2014), the effect is an increase in apparent age by an amount dependent on the proportion of U lost, the age of the sample and its average $^{234}U/^{238}U$ at that time. From that time forward (assuming no further U mobility), the sample volume in question will appear to be older than its true age by the same absolute amount, subject to the limits of analytical precision.

The effect of U loss was modelled to give a percentage of aragonite initially present in the sample required to produce the observed offset between true and apparent age, versus time at which the U loss event

occurred. This assumes instantaneous loss of all aragonite in the sample, using the **Equation 6-1**:

Equation 6-1.

$$A = \left(U_c \frac{\left[{}^{230}Th/{}^{238}U \right]_{(t_d+t_x)}}{\left[{}^{230}Th/{}^{238}U \right]_{t_d}} - U_c \right) \Big/ \left(U_a - U_c \right)$$

in which A is the proportion of aragonite originally in the sample volume, U_c is calcite uranium content, U_a is aragonite U content, t_d is age of sample at time of U loss and t_x is the apparent increase of age generated by this loss.

To explore when diagenesis could have occurred at its earliest and how much aragonite would be needed in order to achieve an age offset as large as ~12 ka for sample CC26-24 (**Table 6-2** and **Figure 6-6**), the recrystallization process was modeled assuming U concentrations in aragonite and calcite of 140 ppm and 4 ppm respectively based on LA-ICP-MS results. It was also assumed that all radiogenic Th was preserved in the sample during recrystallization.

Modelling results (**Figure 6-10**) show that, in the case where the whole dated prism consisted of secondary calcite formed by neomorphism of aragonite, such diagenesis likely occurred ~340 years after sample deposition. In the case of 60% initial aragonite composition, aragonite-to-calcite inversion occurred ~570 years after its deposition. The minimum age of ~340 years is for instantaneous inversion from 100% aragonite. Given that the repeat analysis does not support evidence of large-scale aragonite-to-calcite transformation, the occurrence of small, isolated aragonite inclusions seems the most likely explanation, implying relatively recent recrystallization of a smaller proportion of initial aragonite accompanied by U loss. For the case where recrystallization has occurred ~500 years ago, according to the proposed model, only 14% of initial aragonite would be required to explain the U loss from 140 to 4 ppm. Based on the CC26 age-depth

model relationship, the inversion would have been accomplished if the diagenetic fluids had penetrated to a depth of 31 mm beneath the stalagmite tip through an interconnected system of pores. There is no evidence for this connectivity in the micro-CT scans; however, one cannot exclude capillary flow through intercrystalline boundaries, micro fissures and crystal defects (Zisu et al., 2012) as well as the possibility that the voids were subsequently filled with calcite. Modelling results for the other three outliers (CC26-14, CC26-49 and CC26-66) show that an order, or even two orders, of magnitude smaller amount of initial aragonite is required to produce the outliers of this age.

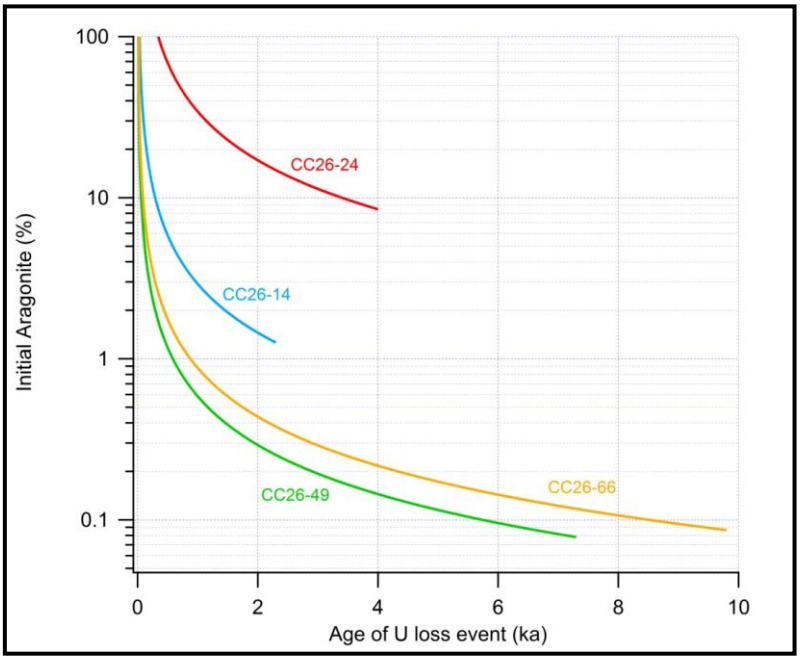

Figure 6-10. U-loss models for outliers from stalagmite CC26. The offset in the age is dependent on the time elapsed since the deposition and the diagenesis event for given amounts of initial aragonite. The four curves present the models for four different outliers. For more details please refer to the discussion.

As mentioned above, replicate U-Th measurements undertaken on another calcite prism from the same depth positions (CC26-14a, CC26-24a, CC26-49a and CC26-66a) resulted in ages that were in stratigraphic order. This result additionally implies that any U loss must be from small, isolated high-U inclusions, not recognisable by visual examination of the polished stalagmite. This is consistent with

evidence from the Galleria delle Stalattiti where irregular and discontinuous patches of aragonite fans occur at the top of some currently dry speleothems, as well as with micro-CT results where only limited voids are registered.

The timing of occurrence of the largest outlier at 47 mm depth correlates to a well-known regional dry event (Drysdale et al., 2006; Regattieri et al., 2014). This correlation provides robustness to the hypothesized occasional formation of aragonite buds. Dry climate conditions promoted PCP (Regattieri et al., 2014) and a higher Mg/Ca ratio in the parent fluid, shifting the system into "mixed aragonite-calcite" mode. Diagenesis is therefore expected once the climate switched to a more humid state, with replacement of the aragonite buds, U loss and partial (to total) occlusion of the porosity due to calcite precipitation driven by degassing in the cave (Boch et al., 2011). Under the proposed model, diagenesis occurred at a relatively early stage, and has significant implications for U, and therefore U-Th dating. The aragonite-to-calcite inversion likely took place in <<1000 years, as already observed for other Holocene stalagmites (Frisia et al., 2002).

Aragonite to calcite conversion in many cases causes alteration of primary chemical properties (Frisia et al., 2002; Zhang et al., 2014). However, the relatively short time necessary to complete the early diagenetic process, as well as very localized diagenesis in CC26, suggest that the geochemistry of the carbonate in this case is largely well preserved. It is therefore suggested that only U experienced "significant recrystallization" (*sensu* Machel 1997); while the geochemical properties dominated by the "water reservoir", including stable isotope ratios of O and C, or those trace elements with similar partition coefficients in aragonite and calcite, are unlikely to be affected.

6.4.4 IMPLICATIONS FOR SPELEOTHEM GEOCHRONOLOGY

The age offset of the largest outlier is larger than any reported in published U-Th datasets, and one which could not remain unrecognized, even in a very low-resolution U-Th age studies. However, the remaining four outliers could be easily interpreted as true ages in low- to medium-resolution studies. These datasets might then ultimately be used to produce misleading interpretations of the timing of palaeoclimate variability.

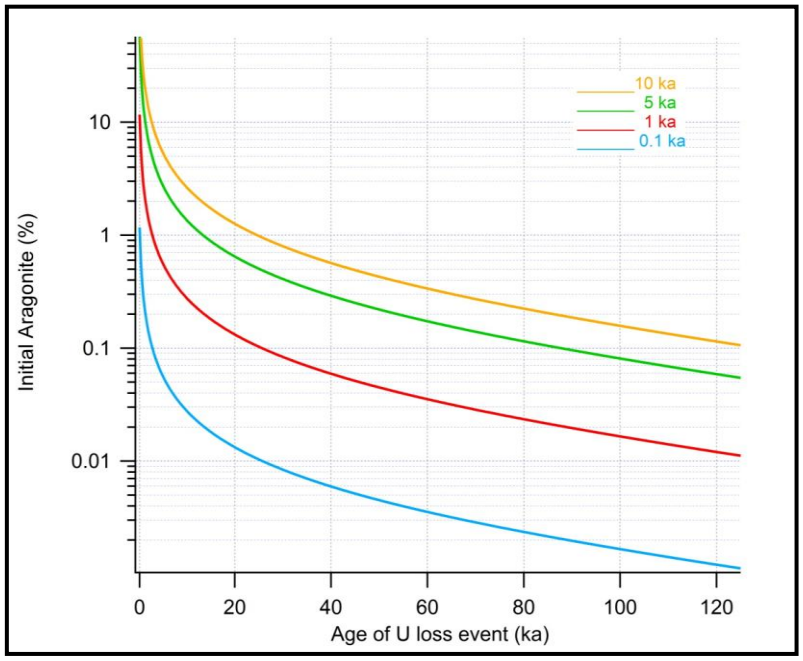

Figure 6-11. U-loss models for a hypothetical last interglacial speleothem with four different offsets of apparent age in the range 0.1 to 10 ka.

To explore the potential of consequences of U loss for older speleothems, U-loss for a last interglacial speleothem was modelled assuming $^{234}U/^{238}U$ of 1.4 and U 35 times more concentrated in aragonite than in calcite. Four different offsets of apparent age in the range 0.1 to 10 ka are given in **Figure 6-11**.

For an age offset of +1 ka in which U loss occurred 5 ka after deposition, only 0.6% of initial aragonite would be required. This is significant with respect to commonly reported last interglacial age

uncertainties of ca.1 ka. To produce an age offset of 10 ka after 5 ka of deposition would require 5% initial aragonite, within the range of likely values for the sample CC26-14. An initial aragonite content of only 0.03% lost 10 ka after deposition leads to an apparent age increase of 0.1 ka, similar to reported last interglacial uncertainties using high-precision U-Th techniques (e.g. Cheng et al., 2013).

The problem of "invisible" diagenesis revealed in this study demands a more careful approach in speleothem studies in the future. Samples from caves hosted in dolomite bedrock, as well as samples from caves where traces of aragonite are currently present or were present at any time in the past (as shown by other speleothems from the same gallery) and cases where the drip waters hover perilously close to $SI_{aragonite}$ <0 should be used with caution despite their pristine appearance. Careful petrographic observation, including detection of microscopic-scale porosity, and high-resolution geochemical mapping are advisable before U-Th dating in these cases. Micro CT analyses can be of great help in identifying porosity anomalies at very high resolution and as a method to assist in selecting samples for U-Th dating. Wherever possible, the dating of such speleothems should be performed with a high sample density. It is worth noting that, should similar aragonite-to-calcite transitions typically occur during early diagenesis with samples subsequently remaining as a closed system, it is unlikely that these processes will significantly affect the U-Pb chronometer due to its linear dependence on radiogenic U/Pb ratio, and larger absolute uncertainties.

6.5 CONCLUSIONS

1. In CC26, the influence of diagenesis has been tested by a multi-aliquot analysis approach (which reveals that analytical problems can not be the cause of the outliers), trace element mapping and by applying micro-CT scanning. The results of this study suggest that

the coupling of optical microscopy and elemental analysis with high-resolution dating, could be used as a step forward in the production of accurate, speleothem-based palaeoclimate reconstructions.

2. The present study introduces the concept of invisible diagenesis, when petrographic observations fail to detect clear textural changes. It also supports the use of the concept of "significant recrystallization" in relation to a specific chemical property of speleothems which does not represent primary depositional conditions, in this case U concentration. These two concepts may help in highlighting the influence of diagenetic processes on the accuracy of speleothem-based palaeoclimate reconstructions.
3. It has been demonstrated that "invisible" aragonite-to-calcite transformation implies significant recrystallization with respect to the mobility of U. The timing of the diagenetic process has been constrained in this case, and found to occur over a time span from about 340 years after deposition to relatively recently, depending on initial aragonite content (**Figure 6-10**). The relatively early diagenetic stage of the recrystallization suggests that for those speleothems where U-Pb is the applied chronometer, invisible diagenesis is likely to have no impact on dating.
4. In the case of Holocene samples, even when stalagmites appear to be excellent candidates for U-Th geochronology, invisible diagenesis may influence the accuracy of ages. Speleothems may, in fact, behave as relatively open systems, more so than has been previously thought, and even if only very small portions have experienced diagenesis, this can result in misleading ages. CC26 appears to have been open mostly for U, which is the only significantly mobilized element. This suggests that early diagenesis in speleothems characterized by columnar fabric, may not significantly alter palaeoclimate proxies that change at a millennial scale

Chapter 7

7 INTERPRETING CARBON ISOTOPES IN A CORCHIA CAVE SPELEOTHEM BY COMBINING $\delta^{13}C$ AND DEAD CARBON PROPORTION (DCP)

Speleothem $\delta^{13}C$ is usually more challenging to interpret compared to $\delta^{18}O$ and very often unravelling the drivers requires support from other proxies. In this study, the 'dead carbon proportion' (DCP) calculated from combined U-Th and ^{14}C dating was used to develop a more robust interpretation of the carbon isotope systematics in Corchia speleothems, using the example of stalagmite CC26 which grew during the last ~12ka. The DCP values in CC26 are the highest ever recorded in a speleothem, spanning the range 44.8 to 68.8%. It is proposed that combination of closed-system dissolution and sulphuric-acid dissolution, as indicated by drip-water analyses (Piccini et al., 2008), are the two the most likely mechanisms involved in producing such a high DCP in this stalagmite. Additionally, the DCP record shows a long-term decreasing trend during the Holocene, similar to the stalagmite's $\delta^{13}C$ profile (Zanchetta et al., 2007), providing an independent support for the previous interpretation of $\delta^{13}C$ at Corchia site as reflecting long-term soil recovery above the cave while the climate system shifts from glacial to interglacial conditions

(Drysdale et al., 2004). Furthermore, DCP is in agreement with a high-resolution record of Holocene hydrological variability as recorded in the trace element proxies from the same specimen (Regattieri et al., 2014).

7.1 INTRODUCTION

Although the palaeoclimate potential of $\delta^{13}C$ in speleothems was recognised at the same time as that of oxygen isotopes ($\delta^{18}O$) (Hendy, 1971), the presentation and interpretation of $\delta^{13}C$ records are under-represented in the literature (Fairchild and Baker, 2012). This situation is likely the result of the multiple sources and complex processes that may affect speleothem $\delta^{13}C$, and, in particular, the greater susceptibility of $\delta^{13}C$ to local (including 'in-cave') effects, such as variable soil cover and prior calcite precipitation (PCP). This leads to the often-observed tendency for coeval $\delta^{18}O$ profiles from a single cave to be in reasonable agreement, but the $\delta^{13}C$ profiles to differ markedly. This hampers inter-sample consistency in palaeoclimate/palaeo-environmental interpretation of speleothem $\delta^{13}C$.

The vast majority of oxygen in cave $CaCO_3$ minerals is sourced from the parent water, which most commonly reflects the $\delta^{18}O$ of precipitation above the cave. Although the processes that ultimately contribute to rainfall $\delta^{18}O$ are also complex (Lachniet, 2009), global and regional patterns of rainfall $\delta^{18}O$ are relatively well understood (McDermott, 2004; Rozanski et al., 1982), and thus speleothem $\delta^{18}O$ interpretations are, arguably, more firmly anchored to theory. The sources of carbon in speleothem $\delta^{13}C$ include atmospheric CO_2, soil CO_2, C derived from the dissolution of karst rock and, in certain cases, C derived from methane. The classical model for speleothem formation is the addition of carbon dioxide, produced by root respiration and microbial decomposition of soil organic matter, to rainwater (Genty and Massault, 1997) to form carbonic acid, which quickly dissociates into H^+ and HCO_3^- ions. The former provides the low pH conditions necessary to

enhance carbonate bedrock solubility, which ultimately contributes further C to the dissolved inorganic carbon (DIC) pool of the cave percolation waters. The CO_2 partial pressure (pCO_2) difference between the cave atmosphere (relatively low) and the emergent percolation waters results in carbonate precipitation to form speleothems. Typically, such calcium carbonate dissolution and reprecipitation is driven solely by the carbonic acid system, and the proportion of soil-derived CO_2 in speleothem carbonates commonly amounts to 80-90% (Genty et al., 1999; Hoffmann et al., 2010; Noronha et al., 2014; Southon et al., 2012). For each source, the isotopic ratio, $^{13}C/^{12}C$, is different, and the partitioning of C isotopes ratios during the various reactions/phase changes likewise differs (Dulinski and Rozanski, 1990; Hendy, 1971).

An important consideration in speleothem $\delta^{13}C$ studies is the ratio of host-rock C to soil-sourced C to the total DIC pool. This is dependent upon the conditions under which dissolution of bedrock is occurring, i.e. open vs. closed system (Hendy, 1971). Under open-system conditions there is a continuous equilibration between percolation water and soil CO_2 during bedrock dissolution, and the $\delta^{13}C$ in the speleothem reflects the lower carbon isotope ratio of the soil CO_2, with no detectable contribution from the carbon isotope signal from the carbonate host rock; the situation is opposite for closed-system conditions. In nature, a mixture of closed- and open-system conditions usually occurs (Hendy, 1971; McDermott, 2004).

The $\delta^{13}C$ signal in speleothems is also dependent upon factors that act on the soil pCO_2 and soil CO_2 isotopic ratio (Genty et al., 2006; Genty et al., 2003), including temporal changes in the type and density of vegetation above the cave (Dorale et al., 1992; Bar Matthews et al., 1996), and the intensity of biogenic activity independent of vegetation type (Drysdale et al., 2004; Hellstrom et al., 1998), and other in-cave characteristics, such as hydrological pathways and processes (including incongruent dissolution and prior calcite precipitation: Fairchild et al., 2000), and cave microclimate (for example, increased ventilation may

increase degassing and/or evaporation leading to kinetic fractionation: Mattey et al., 2010; Spötl et al., 2005, Frisia et al., 2011).

Speleothems from Corchia Cave (Italy) record hydroclimatic changes on millennial to glacial-interglacial time scales because of the location of the cave relative to air masses sourced from the North Atlantic (Drysdale et al., 2004, 2005, 2007, 2009; Zanchetta et al., 2007). This cave system yields a continuous record for at least the last 12 glacial-interglacial cycles spanning the last million years (Drysdale et al., 2011), with older speleothems suggesting the record is likely to extend back to at least 1.4 Ma (Hellstrom, unpublished data).

Typical speleothem $\delta^{13}C$ values in a temperate climate zone characterised by C3 vegetation are in the range -14‰ to -6‰ (McDermott, 2004). Corchia speleothems are rather unusual in this context with $\delta^{13}C$ values in the range -4‰ to almost +5‰, much higher than expected for this climate zone (McDermott, 2004). Furthermore, Corchia speleothems display a lagged decrease in $\delta^{13}C$ compared to $\delta^{18}O$ during glacial-interglacial transitions (Drysdale et al., 2004; Zanchetta et al., 2007). This pattern has been explained as indicative of very slow soil development above the cave as climate conditions ameliorate during glacial-interglacial transitions (Drysdale et al., 2004, 2005, 2009; Zanchetta et al., 2007). This interpretation has not been verified, however, with data from other proxies. The purpose of this study is to test this interpretation by using ^{14}C results from a stalagmite that covers the last 12 ka. The stalagmite, CC26, has been the subject of previous studies, including of $\delta^{13}C$ variability (Zanchetta et al., 2007; Regattieri et al. 2014).

During their formation, speleothem carbonates incorporate C of different isotopic composition: stable isotopes of ^{12}C and ^{13}C and a minor amount of radiogenic ^{14}C. The latter, under certain conditions, enables speleothems to be dated using the radiocarbon method (Broecker et al., 1960; Hua et al., 2012). The method, however, has

some limitations, which hampers its routine use in dating of speleothems.

One of the major drawbacks of the ^{14}C dating method, which is applicable to all ^{14}C-datable materials, is the relatively short half-life (5730 y) of ^{14}C providing an upper limit to its utility of about 50 000 years (Bard et al., 2004; Hua, 2009), which is a fraction of the limit of the more widely applied U-Th dating method for speleothems (about 600 000 years: Hellstrom, 2003). The ^{14}C method, however, has been proven very useful in the dating of young speleothems characterised by very low U content and low $^{230}Th/^{232}Th$ (Hua et al., 2012).

A significant limitation in the radiocarbon dating method which also affects all radiocarbon datable archives is changes in ^{14}C activity in the atmosphere (resulting from variable production rates and shifting redistribution between different reservoirs of Earth's carbon cycle through time). This problem is circumvented by using calibration curves which describe changes in atmospheric ^{14}C activity based on independently dated archives such as tree rings, macrofossils from for example lacustrine sediments and corals (Hua et al., 2009; Reimer et al., 2013). Speleothems are now recognized as a potentially useful tool in the determination of atmospheric ^{14}C activity variations and thus in ultimately improving calibration curves and extending them beyond the range of available dendrochronology (~14 000 years) (e.g. Hua et al, 2009, Southon et al., 2012); this is because they can be dated independently by U-series methods (Hoffmann et al., 2010; Noronha et al., 2014).

A further limitation in radiocarbon dating of speleothems is the variable dead carbon proportion (DCP) in speleothems. This is carbon formed by dissolution of ancient carbonate bedrock which is free of ^{14}C and/or contains carbon leached from aged soil organic matter. DCP is usually variable during the time of deposition of a speleothem and dependent on hydrological and environmental conditions prevalent above the cave (Griffiths et al., 2012; Noronha et al., 2014). It is also

influenced by the conditions of dissolution, in the same manner as $\delta^{13}C$ where, under open-system conditions, soil CO_2 dominates the signal causing DCP in speleothems to be lower. An opposite trend occurs as the hydrochemical system moves towards the closed-system end-member, when the contribution from bedrock with undectetable ^{14}C activity is more important. A study of a speleothem from China also revealed a case where DCP was stable during the Allerod/Younger Dryas and the Younger Dryas/Holocene transitions, periods likely to have been characterised by significant climate and vegetation changes (Southon et al., 2012). Based on this observation, the authors hypothesised DCP stability throughout their whole record, which spans 10.6 to 26.8 ka, and produced an atmospheric ^{14}C record. The record produced is in good agreement with previously published results, but the mechanism for DCP stability remains unclear. A modelling study by Noronha et al. (2015) proposed that DCP stability occurs when the C incorporated in speleothems is predominantly sourced from the decomposition of old organic matter in deep vadose zones where changes in temperature and moisture conditions from the surface are attenuated. This mechanism was previously used to explain attenuation of the atmospheric bomb ^{14}C signal in speleothems in general (Genty and Massault, 1999). The DCP is furthermore affected by the pCO_2 conditions in the soil where, in general, lower pCO_2 leads to higher DCP and vice versa (Fohlmeister et al., 2011).

In this study, an attempt is made to provide a plausible explanation of the unusual $\delta^{13}C$ characteristics of Corchia speleothems by exploring the potential of using DCP as a proxy for soil evolution above the cave. In the light of recent research (Griffiths et al., 2012; Noronha et al., 2014), the causes of any short-term changes in DCP data that might be related to climatic perturbations of a similar frequency are also explored. In achieving these aims, radiocarbon and U-Th data are combined to determine the DCP in Holocene stalagmite CC26 by using the atmospheric ^{14}C data from the IntCal13 calibration

curve, which is well constrained for the time period covered by the CC26 record. Finally, the DCP record is compared with the $\delta^{13}C$ and trace element results from the same speleothem (Regattieri et al., 2014; Zanchetta et al., 2007) interpreted as a proxy for millenial- scale hydrological changes.

7.2 SITE DESCRIPTION

The CC26 stalagmite grew in Antro del Corchia (Corchia Cave) located in the Alpi Apuane massif (central Italy). The stalagmite was collected as a broken piece from Galleria delle Stalattiti (GdS), a chamber situated at ~840 m a.s.l. and located about 400 m below the surface and 2 km from the closest entrance. The cave developed in steeply inclined Upper Triassic Grezzoni Dolomite, metamorphosed carbonates (marbles) and cherty metalimestone, "Brecce di Seravezza" or dolomitic marble (Piccini et al., 2008). The cave host rocks are partially overlain by impermeable basement rocks (phyllites and metavolcanics). GdS is characterized by stable climatic conditions with a mean annual temperature of 8.4 +/- 0.3 °C and a relative humidity of 100 +/- 0.2% (Piccini et al., 2008). Monitoring studies of drip and pool waters in GdS reveal constant stable isotope and trace element ratios (Piccini et al., 2008; Baneschi et al., 2011) throughout the year. This is in agreement with tritium analyses which show that the water residence time in the aquifer above the cave is about 50 years (Doveri et al., 2005).

7.3 SAMPLE DESCRIPTION AND METHODOLOGY

CC26 is a 25 cm long stalagmite but, for the purpose of this study, only the top 157 mm (**Figure 7-1**) was used. This section grew continuously during the last ~12.4 ka (**Chapter** 6). The Holocene portion of CC26

consists exclusively of columnar calcite, with the exception of the top millimetre, which contains a ~0.5 mm thick layer of aragonite fans only partially transformed into calcite (**Chapter** 6).

Half of the stalagmite was sliced into a ~1 cm-thick slab and cut along its growth axis. Samples for paired U-Th and ^{14}C dating were extracted as solid pieces along the growth axis using a dental air drill fixed to a manually navigated milling machine following the barely visible laminations. In total, 78 samples were extracted. U-Th (**Chapter** 6*)* and ^{14}C analyses for 44 samples were performed on the solid piece recovered from the same depth position (in black on **Figure 7-1**) and an additional 10 ^{14}C samples for which U-Th analyses were not performed (in red on **Figure 7-1**).

The U-Th dating methodology and results are described in **Chapter** 6 and therefore not presented here. The age-depth model was produced using the error-weighted-mean corrected U-Th ages from multiple measurements of the same aliquot and employing a finite positive growth-rate model (Drysdale et al., 2005; Scholz et al., 2012).

Solid pieces were used for ^{14}C analyses to avoid possible contamination with modern atmospheric CO_2 on the outer surface of the samples. For the same reason ~8-10 mg samples were pre-cleaned by acid etching in ~2 mL 85% H_3PO_4 at 90°C for 5 minutes to remove the outer surface (15-20% of sample mass is removed). Clean samples were then completely dissolved in the acid solution to form CO_2 gas. The gas was then converted to graphite using excess H_2 over an Fe catalyst (Hua et al., 2001) and the graphite was rear-pressed into an aluminum cathode for accelerator mass spectrometry (AMS) analyses. All ^{14}C samples were analysed using the STAR facility at the Institute for Environmental Research, ANSTO (Fink et al, 2004). The results are corrected for background and isotopic fractionation using measured $\delta^{13}C$, and normalized to a 95% oxalic acid (HOx-I) standard.

Stable isotope variability in CC26 was the subject of a study by Zanchetta et al. (2007); subsequently, trace element data were

combined with stable isotopes to produce a palaeomoisture time series on the same chronology (Regattieri et al. 2014). To consider the new ^{14}C results in the light of these previous studies, the previous chronology was matched with the one from **Chapter** 6 by measuring $\delta^{13}C$ and $\delta^{18}O$ on leftovers from U-Th and ^{14}C analyses from this study and performed a comparison of the old and new chronology via their respective $\delta^{13}C$ records. Stable isotope analyses were conducted at The University of Melbourne (Australia) on an AP2003 continuous-flow mass spectrometer. The results are expressed in delta notation with respect to the VPDB standard. Long-term analytical precision of an in-house reference standard (Carrara marble), previously calibrated to international reference materials NBS-18 and NBS-19, was better than 0.05 and 0.1‰ (1σ) for $\delta^{13}C$ and $\delta^{18}O$ respectively.

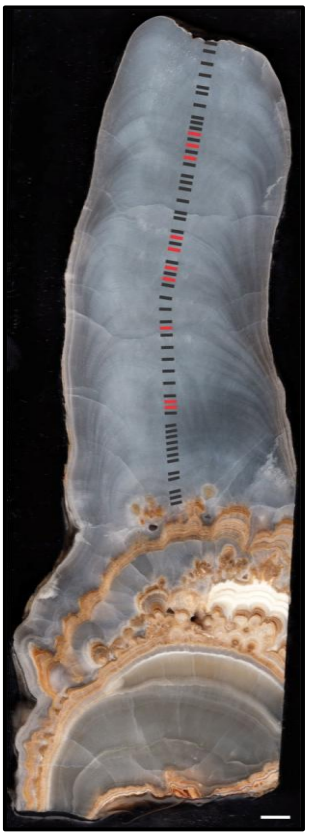

Figure 7-1. A polished slice of the CC26 stalagmite with indicated positions for U-Th (in black) and ^{14}C analyses (in black and red). The white error bar is 1cm in length.

7.4 RESULTS

The age-depth models and $\delta^{13}C$ depth series of data collected in 2007 (Zanchetta et al., 2007) and 2015 (this study) are in agreement for most of the record but there is an offset in chronologies for the bottom 35 mm of the analysed portion of the stalagmite (**Figure 7-2**). This offset is a result of the fact that the 2007 and 2015 sampling campaigns followed slightly different paths, with the 2015 chronology extending the record and improving the chronology for the oldest part of the record. Stable isotope ratios from Zanchetta et al. (2007) and the Mean Anomaly Index (MAI) from Regattieri et al. (2014) were synchronised to the new chronology via adjustment of the depths for age positions from Zanchetta et al. (2007) with the 2015 chronology. The slight shift in the 2007 chronology for the oldest portion (only data older than 8.9 ka are affected by, on average, about 3.5 mm), however, does not affect interpretations from previous publications, which dealt mainly with climate events in the younger, unaffected sections of the stalagmite (Zanchetta et al., 2007; Regattieri et al., 2014).

The DCP for each sample was calculated by combining measured ^{14}C activities and the mean model U-Th age (**Chapter** 6*)* using the approach of Genty and Massault (1997) and the **Equation 7-1**:

Equation 7-1. $$DCP = \left(1 - \frac{a^{14}C_{initial}}{a^{14}C_{atm.\ initial}}\right) * 100\%$$

where initial ^{14}C activity of the speleothem and that of the atmosphere are given by :

Equation 7-2. $$a^{14}C_{initial} = a^{14}C_{measured}/e^{-\lambda t}$$

Equation 7-3. $$a^{14}C_{atm.\ initial} = a^{14}C_{atm.}/e^{-\lambda t}$$

where λ is the ^{14}C decay constant of 1/8267 yr^{-1}, and t is U/Th age of a particular speleothem sample.

From **Equation 7-1**,**Equation 7-2Equation 7-3**:

Equation 7-4. $$DCP = \left(1 - \frac{a^{14}C_{measured}}{a^{14}C_{atm.}}\right) * 100\%$$

where $a^{14}C_{measured}$ is the ^{14}C activity measured in speleothem samples, while $a^{14}C_{atm.}$ is the atmospheric ^{14}C activity derived from the current internationally-ratified radiocarbon calibration, IntCal13 (Reimer et al., 2013). For each sample, the DCP uncertainty was calculated by combining the error on ^{14}C measured in the speleothem, and the uncertainty of past atmospheric ^{14}C activity from IntCal13 associated with the modelled 2σ U-Th age range.

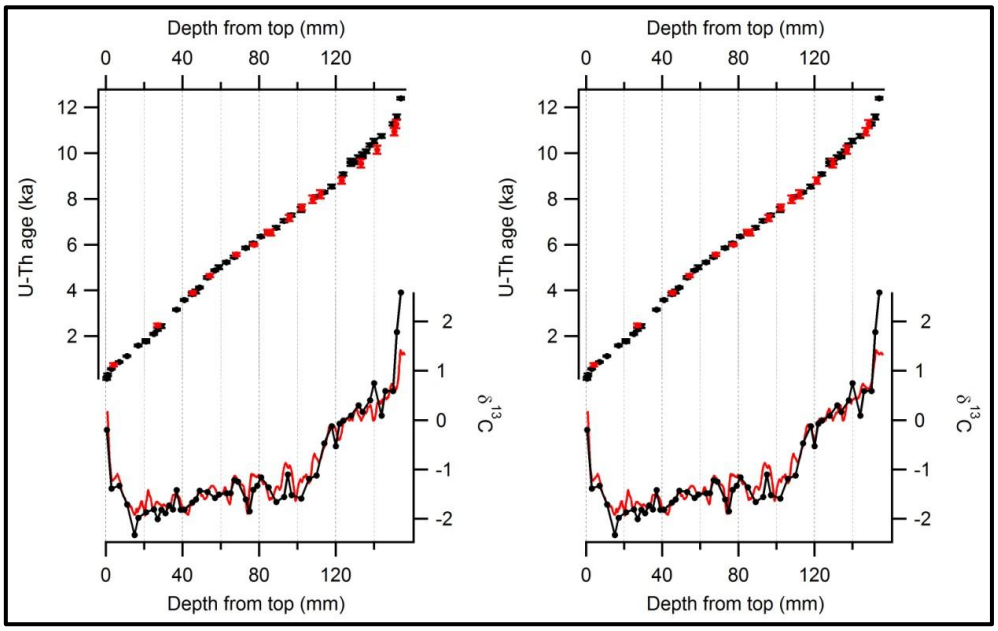

Figure 7-2. Comparison of U-Th and stable isotope results from 2007 (in red) and this study (in black). The sampling in two campaigns followed slightly different transects, resulting in a minor mismatch of chronology (left panel) in the bottom 35 mm. Tuning of old onto the new depth was performed aligning the age-depth positions for the 2007 dataset and aligning two $\delta^{13}C$ depth profiles (right panel).

Table 7-1. Radiocarbon and $\delta^{13}C$ results for 54 CC26 samples. U-Th ages are mean ages of the age-depth model available in **Chapter** 6. All uncertainties are given in brackets. U-Th age uncertainties (2σ) are combined standard uncertainties of the age-depth model. Uncertainties for all radiocarbon data are given as 1σ. $a^{14}C_{atm}$ data are from Reimer et al., 2013.

Sample name	Lab ID	Depth from top (mm) (±100% unc)	$\delta^{13}C$ (‰)	U-Th mean model age vs. 1950 (ka) (2σ)	$a^{14}C_{measured}$ (pMC) (1σ)	$a^{14}C_{atm}$ (pMC) (1σ)	DCP (%) (1σ)
CC26-1	OZP754	0.5 (0.5)	-0.20	0.102 (0.213)	49.46 (0.21)	NA*	N/A*
CC26-2	OZQ361	3.0 (0.5)	-1.39	0.512 (0.096)	41.96 (0.18)	94.32 (0.76)	55.5 (0.4)
CC26-4	OZP755	7.0 (0.5)	-1.33	0.817 (0.075)	39.29 (0.17)	89.57 (0.56)	56.1 (0.3)
CC26-6	OZQ362	11.0 (0.5)	-1.71	1.1077 (0.071)	39.75 (0.17)	86.55 (0.22)	54.1 (0.2)
CC26-8	OZP756	15.0 (0.5)	-2.33	1.382 (0.142)	35.37 (0.17)	83.33 (1.56)	57.6 (0.8)
CC26-9	OZQ363	17.0 (0.5)	-1.98	1.539 (0.071)	30.91 (0.16)	81.53 (0.56)	62.1 (0.3)
CC26-11	OZP757	21.0 (0.5)	-1.87	1.731 (0.101)	32.06 (0.16)	79.93 (0.95)	59.9 (0.5)
CC26-13	OZQ364	25.0 (0.5)	-1.81	2.046 (0.084)	30.29 (0.15)	77.19 (0.58)	60.8 (0.4)
CC26-14a	OZP758	27.0 (0.5)	-2.01	2.235 (0.095)	36.75 (0.17)	75.57 (0.89)	51.4 (0.6)
CC26-15	OZQ365	29.0 (0.5)	-1.82	2.389 (0.118)	35.45 (0.17)	74.68 (0.65)	52.5 (0.5)
CC26-16	OZT118	31.0 (0.5)	-1.89	2.575 (0.206)	30.83 (0.14)	73.12 (1.77)	57.8 (1.0)
CC26-17	OZP759	33.0 (0.5)	-1.73	2.747 (0.238)	31.42 (0.16)	71.90 (1.88)	56.3 (1.2)
CC26-18	OZT119	35.0 (0.5)	-1.81	2.918 (0.195)	33.13 (0.15)	70.79 (1.72)	53.2 (1.2)
CC26-19	OZQ366	37.0 (0.5)	-1.42	3.105 (0.101)	35.21 (0.14)	69.31 (0.56)	49.2 (0.5)
CC26-20	OZT120	39.0 (0.5)	-1.82	3.312 (0.144)	31.14 (0.14)	67.81 (1.01)	54.1 (0.7)
CC26-21	OZP760	41.0 (0.5)	-1.82	3.517 (0.095)	30.80 (0.14)	66.39 (0.66)	53.6 (0.5)

Sample name	Lab ID	Depth from top (mm) (±100% unc)	$\delta^{13}C$ (‰)	U-Th mean model age vs. 1950 (ka) (2σ)	$a^{14}C_{measured}$ (pMC) (1σ)	$a^{14}C_{atm}$ (pMC) (1σ)	DCP (%) (1σ)
CC26-23	OZQ367	45.0 (0.5)	-1.67	3.773 (0.096)	32.64 (0.15)	64.68 (0.64)	49.5 (0.6)
CC26-24a	OZP761	47.0 (0.5)	-1.61	3.893 (0.099)	33.27 (0.15)	63.96 (0.56)	48.0 (0.5)
CC26-25	OZQ368	49.0 (0.5)	-1.43	4.066 (0.095)	34.73 (0.15)	62.97 (0.59)	44.8 (0.6)
CC26-27	OZP762	53.0 (0.5)	-1.46	4.504 (0.112)	31.63 (0.15)	60.66 (0.60)	47.9 (0.6)
CC26-29	OZQ369	57.0 (0.5)	-1.58	4.814 (0.081)	26.98 (0.13)	58.84 (0.51)	54.1 (0.5)
CC26-30	OZP763	59.0 (0.5)	-1.51	4.939 (0.104)	24.65 (0.13)	58.26 (0.62)	57.7 (0.5)
CC26-32	OZQ370	63.0 (0.5)	-1.48	5.167 (0.080)	23.25 (0.12)	57.15 (0.07)	59.3 (0.2)
CC26-33	OZT121	65.0 (0.5)	-1.48	5.285 (0.093)	20.74 (0.12)	56.54 (0.32)	63.3 (0.3)
CC26-34	OZP764	67.0 (0.5)	-1.22	5.404 (0.086)	24.66 (0.12)	55.91 (0.49)	55.9 (0.4)
CC26-35	OZT122	69.0 (0.5)	-1.25	5.536 (0.127)	24.13 (0.13)	54.91 (0.96)	56.1 (0.8)
CC26-37	OZQ371	73.0 (0.5)	-1.61	5.788 (0.081)	21.70 (0.10)	53.46 (0.37)	59.4 (0.3)
CC26-38	OZT123	75.0 (0.5)	-1.85	5.895 (0.085)	16.52 (0.10)	52.93 (0.07)	68.8 (0.2)
CC26-39	OZP765	77.0 (0.5)	-1.41	6.004 (0.087)	23.42 (0.11)	52.12 (0.45)	55.1 (0.4)
CC26-40	OZT124	79.0 (0.5)	-1.33	6.148 (0.107)	21.24 (0.12)	51.31 (0.19)	58.6 (0.3)
CC26-41	OZQ372	81.0 (0.5)	-1.16	6.291 (0.078)	21.55 (0.11)	50.52 (0.31)	57.3 (0.3)
CC26-43	OZP766	85.0 (0.5)	-1.36	6.470 (0.074)	18.68 (0.09)	49.31 (0.43)	62.1 (0.4)
CC26-45	OZQ373	89.0 (0.5)	-1.66	6.677 (0.096)	17.43 (0.09)	49.19 (0.33)	63.8 (0.3)
CC26-47	OZP767	93.0 (0.5)	-1.56	6.976 (0.099)	15.99 (0.08)	46.83 (0.35)	65.9 (0.3)

Sample name	Lab ID	Depth from top (mm) (±100% unc)	$\delta^{13}C$ (‰)	U-Th mean model age vs. 1950 (ka) (2σ)	$a^{14}C_{measured}$ (pMC) (1σ)	$a^{14}C_{atm}$ (pMC) (1σ)	DCP (%) (1σ)
CC26-48	OZT125	95.0 (0.5)	-1.10	7.100 (0.106)	17.69 (0.12)	46.22 (0.55)	61.7 (0.5)
CC26-49a	OZQ374	97.0 (0.5)	-1.28	7.222 (0.100)	18.53 (0.09)	45.67 (0.45)	59.4 (0.4)
CC26-51	OZP768	102.0 (0.5)	-1.59	7.474 (0.143)	15.60 (0.08)	44.05 (0.99)	64.6 (0.8)
CC26-53	OZQ375	106.0 (0.5)	-1.19	7.753 (0.202)	15.98 (0.09)	42.41 (1.21)	62.3 (1.1)
CC26-55	OZP769	110.0 (0.5)	-1.12	8.029 (0.112)	16.88 (0.08)	40.83 (0.64)	58.7 (0.7)
CC26-57	OZQ376	114.0 (0.5)	-0.47	8.230 (0.094)	16.55 (0.09)	39.80 (0.42)	58.4 (0.5)
CC26-59	OZP770	118.0 (0.5)	-0.12	8.485 (0.134)	14.85 (0.07)	38.44 (0.65)	61.4 (0.7)
CC26-60	OZT127	120.0 (0.5)	-0.53	8.666 (0.186)	12.17 (0.08)	37.68 (0.47)	67.7 (0.5)
CC26-61	OZT128	122.0 (0.5)	-0.09	8.836 (0.182)	14.65 (0.10)	37.08 (0.76)	60.5 (0.9)
CC26-62	OZQ377	124.0 (0.5)	-0.01	9.020 (0.135)	14.33 (0.08)	36.51 (0.34)	60.7 (0.4)
CC26-64	OZP771	128.0 (0.5)	0.09	9.503 (0.100)	12.44 (0.07)	34.65 (0.47)	64.1 (0.5)
CC26-66a	OZQ378	132.0 (0.5)	0.30	9.756 (0.106)	11.72 (0.06)	33.63 (0.25)	65.1 (0.3)
CC26-67	OZP772	134.0 (0.5)	0.17	9.882 (0.122)	10.92 (0.07)	33.33 (0.17)	67.2 (0.3)
CC26-69	OZQ379	138.0 (0.5)	0.40	10.283 (0.113)	12.69 (0.07)	32.21 (0.48)	60.6 (0.6)
CC26-70	OZP773	140.0 (0.5)	0.75	10.453 (0.124)	11.01 (0.07)	31.48 (0.27)	65.0 (0.4)
CC26-72	OZQ380	144.0 (0.5)	0.09	10.681 (0.123)	9.78 (0.06)	30.92 (0.35)	68.4 (0.4)
CC26-73	OZP774	146.0 (0.5)	0.55	10.860 (0.184)	10.54 (0.06)	30.57 (0.40)	65.5 (0.5)
CC26-75	OZQ381	150.0 (0.5)	0.59	11.215 (0.146)	9.75 (0.05)	29.52 (0.39)	67.0 (0.5)

Sample name	Lab ID	Depth from top (mm) (±100% unc)	$\delta^{13}C$ (‰)	U-Th mean model age vs. 1950 (ka) (2σ)	$a^{14}C_{measured}$ (pMC) (1σ)	$a^{14}C_{atm}$ (pMC) (1σ)	DCP (%) (1σ)
CC26-76	OZP775	152.0 (0.5)	1.79	11.534 (0.253)	13.34 (0.07)	28.87 (0.63)	53.8 (1.0)
CC26-77	OZQ382	154.0 (0.5)	2.59	12.313 (0.432)	12.19 (0.06)	26.86 (1.07)	54.6 (1.8)

The AMS ^{14}C results together with U-Th dates of CC26 are provided in **Table 7-1**. The DCP record of CC26 is presented in **Figure 7-3** together with the $\delta^{13}C$ data. CC26 is characterised by some of the highest DCP values ever reported for speleothems (in the range 44.8 to 68.8%), with most of the samples having a DCP above 50%. The DCP dataset shows a long-term decreasing trend over the Holocene, over which multi-centennial to millennial scale excursions are superimposed. These short-term excursions in DCP are larger than any reported in the published literature so far (Genty et al., 2001; Rudzka et al., 2011; Griffiths et al., 2012; Noronha et al., 2014). The long-term decreasing trend of DCP during Holocene broadly follows $\delta^{13}C$.

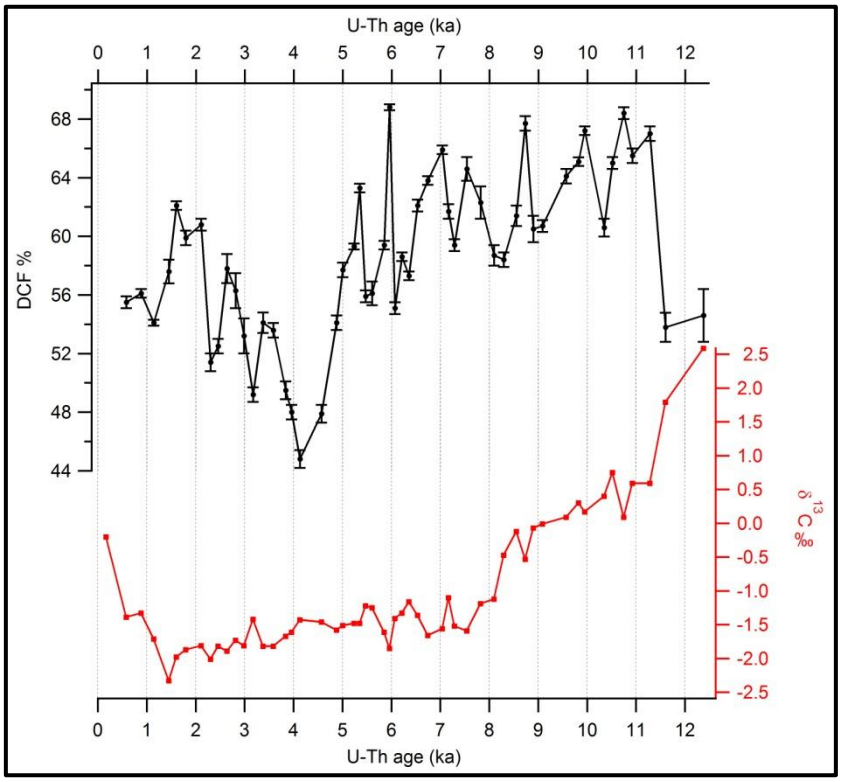

Figure 7-3. DCP vs $\delta^{13}C$ time series in CC26. Both DCP and $\delta^{13}C$ are high, suggesting an important contribution of host-rock sourced C. For more details please refer to the discussion section.

7.5 DISCUSSION

7.5.1 THE EFFECT OF DIAGENETIC ALTERATIONS ON DCP RECORD IN CC26

In **Chapter** 6 it was revealed that stalagmite CC26 experienced partial aragonite-to-calcite transformation, which caused a limited number of samples to yield anomalously old U-Th ages. The replication of another calcite prism from the same stratigraphic position resulted in an age in correct stratigraphic order, confirming that diagenetic alteration is very localised. This was supported by micro-CT results. Based on these results, it was suggested that diagenetic alteration in CC26 did not change significantly the stable isotope ratios of oxygen and carbon and those trace elements with similar partition coefficients in aragonite and calcite (**Chapter** 6). Hence, the DCP data presented in this study are representative of primary depositional conditions.

7.5.2 AN EXPLANATION FOR DCP VALUES HIGHER THAN 50%

DCP in CC26 is higher than 50% almost during the whole growth interval. DCP in speleothems reflects the contribution of CO_2 from ^{14}C-depleted carbon sources (bedrock and/or old soil organic matter (SOM)) compared to the DIC of the incident infiltration water, and is translated into the speleothems (Genty et al., 2001). Previous studies at Corchia Cave have suggested that the main recharge zone of the GdS lies most likely between 1200 and 1400 m.a.s.l. (Drysdale et al., 2004). This area is characterized by a typical alpine landscape where only limited pockets of grass-covered soils occur. Where higher plants occur, the soil is often composed of a thin layer of leaf litter mantling periglacial slope deposits. As a result, the contribution of old soil organic matter (as suggested for other caves; Oster et al., 2010; Noronha et al., 2015) can be considered as minimal for the high DCP values recorded in the stalagmite, unless that source lies trapped at depth in fractures.

Furthermore, the DCP exceeds 50%, even during the Younger Dryas, when climate conditions are likely to have been cold and dry. Continuous, well-developed soil profiles are restricted today only to a submontane depression formed due to differential erosion of low permeability, non-karstifiable Palaeozoic basement rocks (phyllites and metavolcanics). The basement covers a part of the cave including GdS but it is only superficially fractured and it is considered that water does not percolate through these rocks to reach the cave (Piccini et al., 2008). Hence, runoff from this area in unlikely to have direct influences on the carbon isotope composition or the ^{14}C of Corchia speleothems, including CC26.

The high bedrock contribution to the dissolved inorganic carbon (DIC) in CC26 calcite is furthermore supported by high $\delta^{13}C$ values in the speleothem, since soil-derived C would contribute isotopically light biogenic CO_2, resulting in much lower values of speleothem $\delta^{13}C$: typically in the range -14‰ to -6‰ for mid latitude sites characterised by C3 vegetation cover (McDermott, 2004). The CC26 $\delta^{13}C$ values are in the range of -2.33 to +2.59 ‰, close to the isotopic composition of the carbonate bedrock (1.88 +/-1‰ for the Grezzoni unit: Cortecci et al., 1999). Hence, the major contribution to the carbon in the $CaCO_3$ crystal lattice of CC26 is likely to come from host-rock $CaCO_3$ rather than CO_2 evolved from soil organic matter oxidation, which is hypothesised to be main source of C in other published speleothem records (Genty et al., 1999, 2001; Oster et al., 2010).

A number of studies have interpreted DCP variability as a hydrological proxy, where lower DCP is observed during dry climate conditions while the opposite is the case during wet episodes (Griffiths et al, 2012; Noronha et al, 2014). The proposed mechanism involves shifts between open- and closed-system dissolution, which is dependent on water saturation levels in the epikarst. An open system indicates dry conditions when younger carbon is introduced into the DIC pool through the equilibration of soil water with soil air while, during wet

episodes, the system moves towards closed-system conditions and contribution from soil CO_2 is reduced due to the rapid transit time of percolation waters, leading to C that is predominantly sourced from carbonate host rock free of ^{14}C (Genty et al., 2001; Griffiths et al., 2012).

Completely closed-system dissolution by carbonic acid, however, can explain only 50% of DCP (Hendy, 1971) as, for neutralisation of one mole of dissolved CO_2, one mole of carbonate is needed and not a single value approaching 50% has been reported for speleothems in the past. Hence, to explain DCP above 50%, as is the case in CC26, additional processes must be invoked. The contribution of old soil organic matter could theoretically increase the DCP above 50% (Rudzka et al., 2011), but this phenomenon is not supported by the $\delta^{13}C$ values, which would still be negative, even for this source of organic matter.

The reason for high DCP is likely to be bedrock dissolution by processes other than dissolution by carbonic acid derived solely by the combination of rainfall and atmospheric/soil CO_2.

The drip waters in GdS are strongly enriched in SO_4^{2-} compared to the rainfall samples and drip waters collected from other parts of the cave (**Table 7-2**), and it was proposed that the sulphate ions are originating from pyrite oxidation, as pyrite mineral inclusions are present in the Grezzoni unit (Piccini et al., 2008). The high Mg/Ca of CC26 is indicative of the waters having come into contact with dolomitic beds (**Chapter** 6). Oxidation of pyrite would lead to formation of sulphuric acid in the drip water, enhancing its capacity to dissolve the bedrock and hence increasing the DCP in speleothems, possibly above the 50% limit theoretically achievable by the sole dissolution by carbonic acid. The influence of sulphuric-acid dissolution on speleothem formation has been rarely studied, with the exception of high-elevation Spannagel Cave in the Austrian Alps (Spötl et al., 2004). Corchia is another cave site where sulphuric acid dissolution may have an important impact on the formation of speleothems. The combination

of closed-system dissolution and sulphuric-acid dissolution, together, constitute the two most likely mechanisms responsible for high (over 50%) DCP values in stalagmite CC26.

Table 7-2. Hydrochemistry data from CNR1 and CNR2 stations in Corchia Cave (from Piccini et al., 2008). Values in brackets are uncertainties.

Station name	pH	Ca (mmol/L)	Mg (mmol/L)	Na (mmol/L)	K (mmol/L)	Cl (mmol/L)
CNR2	8.14 (0.14)	0.82 (0.02)	0.91 (0.03)	0.17 (0.01)	0.01 (0.00)	0.14 (0.02)
CNR1	7.97 (0.06)	0.93 (0.06)	0.33 (0.04)	0.17 (0.02)	0.00 (0.00)	0.18 (0.02)

Station name	SO_4 (mmol/L)	HCO_3 (mmol/L)	Mg/Ca (mmol/L)	SI Aragonite (mmol/L)	SI Dolomite (mmol/L)	SI Calcite (mmol/L)
CNR2	0.36 (0.02)	2.75 (0.03)	1.11 (0.03)	0.11 (0.14)	0.45 (0.27)	0.27 (0.14)
CNR1	0.06 (0.01)	2.33 (0.11)	0.36 (0.05)	-0.04 (0.06)	-0.34 (0.15)	0.12 (0.06)

7.5.3 LONG-TERM CHANGES IN $\delta^{13}C$ AND DCP

Despite being higher than 50% throughout almost the entire record, the DCP generally decreases during the last ~11.3 ka. The two oldest DCP data do not follow this decreasing trend however and will be discussed in the **section 7.5.4** (**Figure 7-3**). There is a significant positive relationship between $\delta^{13}C$ and DCP in the last ~11.3ka; r = 0.52 (n = 51), p<0.0001 (**Figure 7-4**).

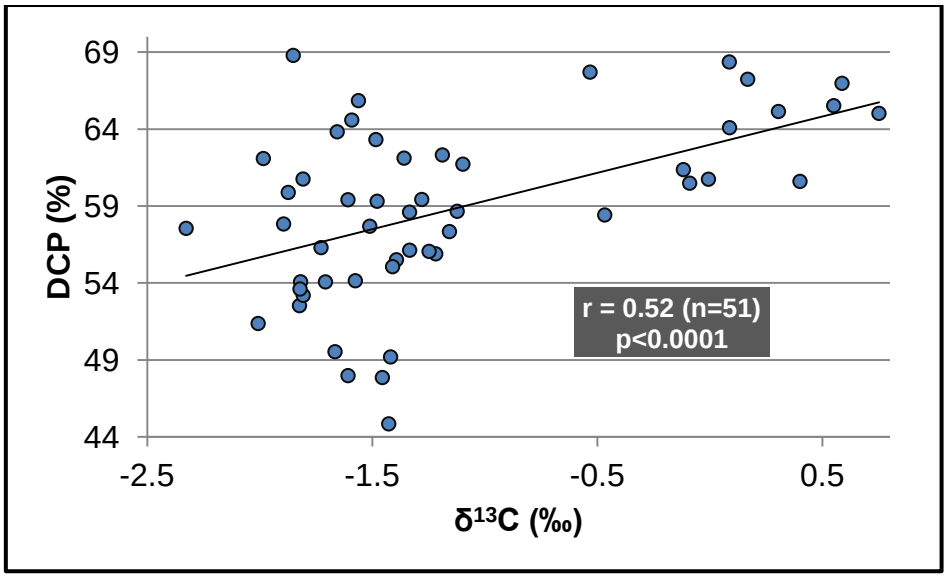

Figure 7-4. Correlation between $\delta^{13}C$ and DCP for the samples corresponding to the last ~11.3ka

The long-term decreasing trend in both proxies implies that both $\delta^{13}C$ and DCP might be responsive to the same long-term environmental and/or climate conditions. Although variability of $\delta^{13}C$ can be caused by multiple processes, as alluded to in the introduction, a parallel decrease in $\delta^{13}C$ and DCP can be caused by a limited number of factors. The decrease in $\delta^{13}C$ in Corchia speleothems, including CC26, was interpreted previously as a result of increased biogenic soil activity above the cave due to amelioration of climate conditions following the glacials, with the climate becoming wetter and warmer, thus promoting revegetation and soil development increasing the soil air pCO_2 (Drysdale et al., 2004; 2009; Zanchetta et al., 2007). This would then increase the availability of soil CO_2 for input of isotopically light biogenic carbon into the percolation water, consequently decreasing the speleothem $\delta^{13}C$. A time lag was also observed between $\delta^{18}O$ and $\delta^{13}C$, which was interpreted in terms of the delayed response in soil development to amelioration of climate conditions related to glacial-interglacial transitions (Drysdale et al., 2009). The development of vegetation and soil would, at the same time, generate the increased proportion of less-^{14}C-depleted carbon into the DIC pool through increased soil pCO_2 from

plant respiration, decreasing the proportion of dead carbon sourced from bedrock, ultimately decreasing the DCP in the speleothem. The hypotheses of soil development above the cave is hence in agreement and supported by the observed decrease in DCP.

The increase in soil development and concurrent increase in soil pCO_2 would enable more carbonic acid to be produced, increasing the Ca^{2+} content in the drip water and finally possibly increasing the growth rate of the stalagmite. CC26 has a relatively uniform growth rate during the Holocene (excluding the decrease in growth rate during the last ~400 years before the stalagmite ceased to grow) and indeed an increase in growth rate during the low DCP periods has not been observed. However, the growth rate of a single stalagmite is not determined only by the soil pCO_2 and Ca^{2+} content in drip water but also by the difference between soil and cave air pCO_2 and drip rate, so it is reasonable to suggest that the absence of an increase in growth rate is not a constraint on the proposed explanation.

Furthermore, a positive correlation between $\delta^{13}C$ and DCP can be a consequence of changes in open/closed-system dissolution conditions (Genty et al., 2001). The long-term shift from more closed- to more open-system dissolution would cause a reduction in the contribution of dead carbon from dissolution of bedrock, which is also characterised by higher $\delta^{13}C$, consequently leading to a decrease in both $\delta^{13}C$ and DCP. Open-system dissolution is favoured by lower water availability (Griffiths et al., 2012; Noronha et al., 2014). However, stable isotopes of O and trace element results from the same speleothem, both sensitive to changes in hydrology, do not show a long-term decrease in water availability in CC26 during the Holocene (Zanchetta et al., 2007; Regattieri et al., 2014), supporting the interpretation of soil development as the key factor driving the observed long-term decrease in $\delta^{13}C$ and DCP.

An additional factor which would cause both $\delta^{13}C$ and DCP to change is kinetic fractionation. CC26 was recovered *in situ* and it was

inactive at the moment of collection. U-Th dating results show that the stalagmite stopped growing ~150 years ago, although the uncertainty of this age is about +/-50 years. The $\delta^{13}C$ results from drip water at CRN-2 station within the Galleria delle Stalatitti are -3.36 +/-0.15 ‰ which is ~3‰ lower compared to the $\delta^{13}C$ measured at the top of the stalagmite CC26. One might propose that CC26 is precipitated under disequilibrium conditions usually related to increased degassing due to ventilation or evaporation conditions in the cave chamber (Hendy, 1971; Spötl et al., 2005; Mattey et al., 2010). However, since the monitored drip water is not the drip water which fed CC26, and it has not been possible to collect recent calcite (Drysdale et al., 2004; Drysdale pers. comm. 13 January 2016), this cannot be confirmed. Good replication for a part of the record with another stalagmite collected from the same chamber (CC27, Drysdale unpublished data) and the fact that there is no correlation between $\delta^{18}O$ and $\delta^{13}C$ in CC26 (Hendy, 1971), argues against kinetic fractionation being a driver of $\delta^{13}C$ and DCP Holocene variability in CC26.

7.5.4 MILLENIAL SCALE DCP VARIABILITY

Superimposed on the long-term decrease during the Holocene are remarkable shifts in DCP at centennial to millennial time scales. Standard (z) scores of DCP and $\delta^{13}C$, both detrended for their long-term Holocene decreases, are plotted together with the Mean anomaly index (MAI) from Regattieri et al. (2014) (**Figure 7-5**).

The similarity of the MAI and DCP records is quite striking although they have opposite trends, i.e. DCP is decreasing when MAI (and $\delta^{13}C$) is increasing, and *vice versa*. The MAI is based on $\delta^{18}O$, $\delta^{13}C$ and Mg/Ca data from CC26 and negative excursions are interpreted by Regatierri et al. (2014) as representing relatively wet climate conditions while positive values are indicative of relatively dry conditions (NB: Corchia Cave lies in a very wet environment, so the patterns reflect

deviations from a mean state, and negative values do not indicate 'aridity' *sensu stricto*). The DCP in CC26 follows almost every wet-dry excursion depicted by MAI, meaning that it is probably responsive to the same centennial- to millennial-scale shifts in hydrological conditions.

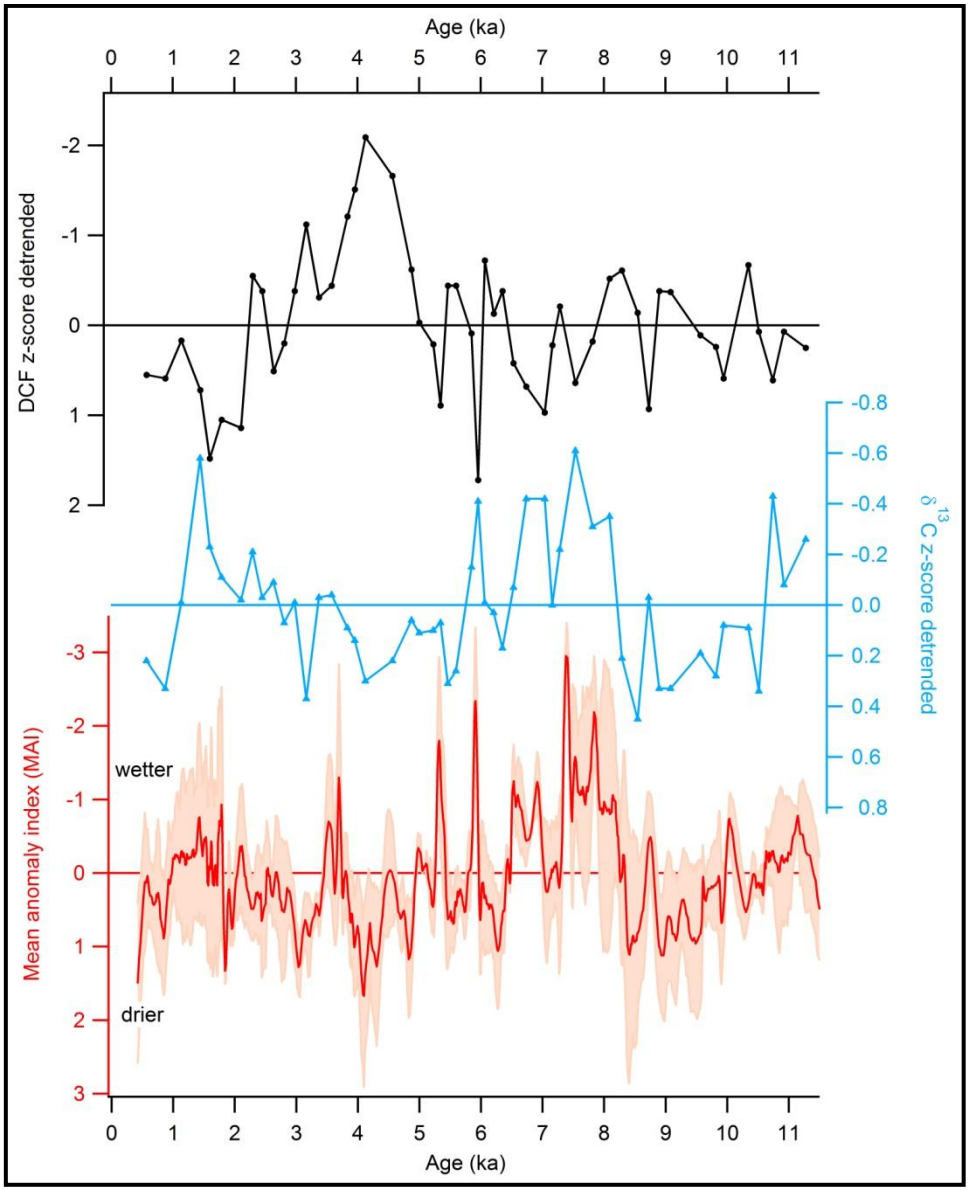

Figure 7-5. Detrended z-scores of DCP and $\delta^{13}C$ compared to Mean anomaly index (MAI) from Regattieri et al. (2014). DCP captures almost every wet-dry excursion as recorded in the MAI. Detrended DCP and $\delta^{13}C$ time series show antipathetic behaviour on millennial time scale. All y-axes are inverted. For interpretation please refer to the main text.

During dry events, when water supply in the aquifer is decreasing, DCP is characterised by a smaller percentage. The decrease in water supply would shift the system to more open-system-dissolution conditions, leading to enhanced exchange between soil water and soil air CO_2 and decreasing the contribution from host-rock sourced C, and culminating in a decrease in speleothem DCP. In contrast, during wet conditions, the situation would be reversed and more closed-system dissolution would increase the contribution from radiocarbon-free host rock. If switching between open- and closed-system dissolution was the major driver of millennial scale $\delta^{13}C$ variability, it would show the same trend as DCP, i.e. $\delta^{13}C$ would decrease during dry (open conditions) and increase during wet (closed) periods. This is, however, not the case in CC26 meaning that, even during the periods of lower discharge, CC26 was formed under predominantly closed-system dissolution conditions and that to explain millennial scale changes in DCP other processes have to be considered.

The GdS is overlain by more than 400 m of host rock. Cave monitoring studies have revealed relatively stable drip-water hydrochemistry, typical of long transit times (about 50 years) as supported by tritium analyses (Doveri et al., 2005; Piccini et al., 2008; Baneschi et al., 2011). The long transit time would allow for degassing and reprecipitation of carbonate *en route* through the processes of prior calcite precipitation (PCP), particularly enhanced during periods of reduced moisture (Fairchild et al., 2006). Occurrence of PCP in CC26 is also supported by a positive correlation of $\delta^{13}C$ and Mg/Ca ratio (Regattieri et al., 2014). Another mechanism with the same consequences would be incongruent dissolution of dolomite (IDD), which might be expected considerating the dolomitic bedrock through which water percolates on its way to the GdS. This mechanism is rejected as important for the Holocene portion of CC26 based on the positive correlation of Mg/Ca and Sr/Ca ratios (Regattieri et al., 2014). The opposite should occur in the case of IDD. PCP is additionally

proposed to have occurred in CC26 during dry episodes in some cases increasing the supersaturation of drip water with respect to aragonite, leading to deposition of this mineral instead of calcite (**Chapter** 6). PCP would cause an increase in $\delta^{13}C$ as well as enrichment in ^{14}C of percolation waters, which would be mirrored in the isotopic composition of the speleothem formed from this solution upon its entrance to the cave (Fairchild et al., 2006; Scholz et al., 2009). Hence, PCP would cause opposite trends in $\delta^{13}C$ and DCP, with $\delta^{13}C$ increasing while DCP is decreasing during drier climate conditions. This is exactly what can be observed in CC26 record, implying that PCP might be the critical process leading to millennial-scale variability of DCP in CC26.

Another interesting feature of this dataset is that DCP is much more variable compared to the $\delta^{13}C$ record. Comparison of detrended *z* scores for these two proxies reveals that the standard deviation for DCP is 0.77% while that for $\delta^{13}C$ is only 0.26‰ (**Figure 7-5**). More variable DCP than $\delta^{13}C$ is indeed expected during preferentially closed-system dissolution, particularly in the case where low initial soil air pCO_2 exists (Fohlmeister et al., 2011). This condition is to be expected at Corchia Cave. As Fohlmeister et al. (2011) demonstrated, ^{14}C in DIC will decrease with decreasing initial soil air pCO_2 but will increase again when initial soil pCO_2 is lower than 50 000-60 000 ppm.

During the Younger Dryas (YD), DCP was still above 50% but 13% lower than at the next sampling point at ~11.3 ka (**Figure 7-3**). At the same time $\delta^{13}C$ shows a sharp decrease of 2‰. This is the time when growth of CC26 was resumed after a break in deposition. CC26 is similar to other speleothems from Corchia Cave in that it is characterised by a very slow growth rate, as indicated by the CC26 age-depth model. During the YD, the growth rate was about five times slower (mean 2.4 mm/ka) compared to the Holocene (mean ~12.5 mm/ka), implying extremely low soil pCO_2. Considering the general characteristics of the Younger Dryas as a dry and cold period judging by patterns registered in other European palaeoclimate archives (Rudzka et

al., 2011; Noronha et al., 2014), one could assume that soil pCO_2 at this time was very low (Fohlmeister et al., 2011), causing the DCP to shift to lower values compared to the following time interval and explaining this mismatch with the overall decreasing trend in the Holocene. Another explanation for the relatively low DCP and high $\delta^{13}C$ would be PCP but, as demonstrated by Regattieri et al., (2014), the oldest portion of the CC26 record is characterised by a negative correlation between Mg/Ca and Sr/Ca making the role of PCP less probable.

Although CC26 DCP appears responsive to changes in hydrological conditions, the increase related to the Sapropel 1 wet event (ca 6600 to 9500 yr cal. BP) (Zanchetta et al., 2007 and references therein) is less pronounced than the decrease in DCP during the 4.2 ka dry event (Regattieri et al., 2014). This is opposite to what has been observed in a Chinese speleothem HS4 (Noronha et al., 2014), where the record was more responsive to wetter conditions. In that study, the authors proposed that speleothems with lower-than-average DCP, i.e. speleothems formed under more open-system dissolution conditions, are less sensitive to dry events, supporting this additionally with examples from other speleothems mostly covering the Younger Dryas in Europe (Noronha et al., 2014). Such sites are characterised by predominantly open-system-dissolution conditions, with DCP in almost all cases being lower than 20% (Rudzka et al., 2011). As CC26 was mostly formed under conditions of closed-system dissolution it might be that the samples which grew under closed-system conditions are more responsive to dry events, as opposed to speleothems formed under open-system conditions, as presented in Noronha et al. (2014). The possible mechanism could be an increased sensitivity of closed-system dissolution to pCO_2 in the soil zone (Fohlmeister et al., 2011), although this might be a limited characteristic of very few settings similar to Corchia.

7.6 CONCLUSIONS

The conclusions of this chapter are:

1. The DCP time-series of CC26 supports the previously proposed hypothesis that the long-term decrease in $\delta^{13}C$ in Corchia speleothems following glacial conditions reflects a slow rate of soil development (albeit limited) above the cave.

2. Speleothem CC26 is characterized by DCP values higher than 50% through almost the entire last ~12 kyr. Such a high DCP cannot be explained simply by closed-system dissolution of ^{14}C-free host rock by carbonic acid and a contribution of aged soil organic matter. Rather, it is likely to be a consequence of the specific geological setting of Corchia Cave, where sulphuric-acid dissolution takes place together with carbonic-acid dissolution.

3. The DCP in this stalagmite is responsive to millennial-scale changes in hydrology, as depicted by trace element and stable isotope results (MAI index) (Regattieri et al., 2014). The proposed mechanism is prior calcite precipitation, which is inferred from the antipathetic behavior of $\delta^{13}C$ and DCP during these millennial scale events.

4. DCP is characterised by much more variability than $\delta^{13}C$ from the same speleothem, which is indicative of closed-system dissolution and consistent with the model proposed by Fohlmeister et al. (2011).

5. The CC26 DCP record is less sensitive to wet climate events compared to dry excursions, a finding which is in disagreement with a similar study on a Chinese stalagmite HS-4 (Noronha et al., 2014) and stalagmites from Europe (Rudzka et al., 2011). This discrepancy may be related to the different dissolution conditions of drip water forming Corchia stalagmites comparing to

speleothems from the previous studies. Unlike those speleothems, which were formed under more open-system conditions, CC26 was formed predominantly under closed-system dissolution. Drip water and hence speleothems formed under closed-system conditions are more sensitive to pCO_2 in the soil zone (Fohlmeister et al., 2011). More data from the sites where stalagmites are formed under predominantly closed-system dissolution would be beneficial in order to test this hypothesis.

Chapter 8

8 CONCLUSIONS AND FUTURE DIRECTIONS

This thesis is constructed around three different themes as presented in the introduction chapter and has been organised in the form of manuscripts. Each of the manuscripts (published or in preparation) was aimed to address particular geochronological and/or palaeoclimate questions. The conclusions of the thesis are presented in accordance to the themes set out in the introduction.

Theme 1. *Developing a precise and accurate radiometric chronology for glacial-interglacial climate transitions during the part of the Middle Pleistocene Transition- MPT (0.98 to 0.86 Ma)*

Speleothems are regarded as one of the most powerful palaeoclimate archives (e.g., Henderson, 2006) due to their suitability for precise and accurate dating with the U-Th dating methods and improved mass spectrometric techniques (Hellstrom, 2003; Zhao et al., 2009), and their propensity to furnish high-resolution proxy records (Baker et al., 2011; Orland et al., 2012; Orland et al., 2014). The palaeoclimate potential of speleothems older than 500 ka has remained largely unexplored

because of the inability to produce accurate and precise internal chronologies for such samples.

Although the use of U-Pb dated speleothems for palaeoclimate study is increasing (e.g. Meyer et al., 2009; Vaks et al., 2013; Sniderman et al., 2016), this research, for the first time, has explored the potential for generating long palaeoclimate records within individual speleothems older than 500 ka by using the U-Pb dating method (Woodhead et al., 2006; 2012). The results are presented in **Chapter** 4 and 5 and they show that resolving speleothem chronologies at suborbital time scales using the U-Pb dating method is well within the realms of possibility. The U-Pb chronology of stalagmite CC8 (**Chapter** 4) was replicated and further improved (**Chapter** 5) by using two additional stalagmites, CC119 and CC122. In total, 20 U-Pb isochrons were constructed to constrain the local initial common Pb composition, based upon which 59 single-aliquot ages were then calculated. For disequilibrium corrections, $^{234}U/^{238}U$ ratios for each age point were measured. All disequilibrium corrected ages were placed on a common depth scale by correlating speleothem $\delta^{18}O$ depth profiles.

A composite age-depth model was then applied to the whole dataset. The results reveal that almost the whole record is dated with a precision better than +/-7 kyr (95% confidence interval) and that the timing of the start of each termination is constrained with a precision better than +/- 4.1 kyr.

Previous research in Corchia Cave has revealed that speleothem $\delta^{18}O$ correlates with sea-surface temperature (SST) changes reconstructed from North Atlantic and Western Mediterranean marine sediments (Drysdale et al., 2004; 2009) through the effect of changes in SST on moisture advection and rainfall amount above the cave. The approach of Drysdale et al. (2009) was followed and $\delta^{18}O$ tuned with available SST records from the North Atlantic. In this way, Corchia radiometric chronology was transposed to the benthic $\delta^{18}O$ record of ice-volume changes and an accurate and precise radiometric chronology

for glacial terminations was achieved. This chronology, independent of astronomical tuning, allowed comparison of the benthic record and orbital parameters in order to test orbital hypotheses.

The results indicate that TXII and TX both started at points of relatively high tilt angle (obliquity) while the phasing with respect to precession is inconsistent. TXII started when Northern Hemisphere summer insolation was approaching maximum intensities, whereas TX started when Southern Hemisphere summer insolation was approaching maximum intensities. This implicates obliquity as the principal driver of both terminations, leaving a more ambiguous role for precession.

Future directions:

This aspect of the study has demonstrated that speleothems have the potential to offer critical perspectives on glacial-interglacial climate variability during the MPT. The extension of the record either side of the studied interval would be an important next step which would offer the possibility of determining if and when exactly the shift from obliquity- to precession-paced glacial-interglacial cycles that is usually linked with the MPT occurred. The success of these studies will ultimately depend on the suitability of the stalagmite samples to U-Pb dating. In this context, U content (minimum a few ppm) and low and stable common Pb composition will be the most limiting factors. Considering the results from this study and previous studies on stalagmites from Corchia Cave (Drysdale et al., 2009; Woodhead et al., 2006) it is reasonable to suggest that this site might offer the appropriate high-quality material, and certainly has the predisposition to play an important role in further advancements of our understanding of glacial-interglacial transitions and the Middle Pleistocene transition (and beyond).

Another possible direction for future research would be development of speleothem-based temperature record using the

clumped isotope method (Daëron et al., 2011). This would enable testing of the proposed assumption that Corchia $\delta^{18}O$ follows sea-surface temperature changes, even during the MPT.

The greatest limitation in this study, however, was a lack of high-resolution marine records which, in a single core, should contain all proxies needed to transpose the Corchia radiometric chronology onto the benthic $\delta^{18}O$ record of ice-volume changes. Compilation of high-resolution marine records covering this time period from the North Atlantic would be useful in testing the tuning procedure and the conclusions about the timing of terminations presented here.

Theme 2: *To explore "invisible" diagenesis and its effects on accuracy of U-Th chronometer for speleothems*

Despite their usual pristine nature and high suitability for U-Th dating, speleothems may experience diagenetic alteration. This will breach the closed-system behaviour assumption essential for producing accurate U-Th chronologies, leaving such samples unsuitable for palaeoclimate research.

By conducting high-resolution U-Th dating while undertaking the research questions in theme 3, it was discovered that a number of U-Th age determinations in stalagmite CC26 departed significantly from the expected age. These results are presented in **Chapter** 6. All suspect ages were older than expected, indicating that U loss possibly occurred. However, unlike most of the published work on diagenetically altered samples, CC26 did not show any visible evidence of diagenesis in hand specimen (Zanchetta et al., 2007).

A multi-aliquot-analysis approach revealed that analytical problems were not the cause of the outliers. The largest outlier was 309% older than its assumed 'true' age and to explain this outlier an

aragonite precursor must had been deposited at this particular location. Trace-element mapping and petrographic examination of thin sections from this stalagmite did not reveal any signs of diagenesis but they did show aragonite zones where U is highly concentrated in very small (micron-sized) buds on the top of the stalagmite. It is proposed that fluid undersaturated with respect to aragonite percolated through the stalagmite and dissolved previously formed aragonite buds. High-resolution micro-CT scanning revealed porous areas in the stalagmite, and it is proposed that these secondary features were very likely pathways for U loss. The restricted number of these porous lenses is in agreement with the very limited number of outliers in this dataset, and furthermore explains the successful replication of another calcite prism from the same depth position. A model for the timing of U-loss events was produced and, in the case of the largest outlier, diagenetic alteration was found to occur over a time span between about 340 years after deposition and relatively recently, depending upon the initial aragonite content.

This study has important implications for high-precision, low-resolution U-Th speleothem geochronologies, and indicates that speleothems may behave as relatively open systems more often than previously thought. Even if only small portions of the sample have experienced diagenesis this can lead to inaccurate U-Th chronologies.

Future directions:

Although it may not be possible to apply high-resolution U-Th dating with replicated measurements systematically in all future speleothem studies, greater caution should be used when interpreting datasets based on low-resolution dating. This is particularly the case when growth rate in a single speleothem shows unexpected changes during relatively short time periods, characterised by relatively stable climate conditions. Replication of the record would be beneficial in these

cases to support the chronology (as well as climate signal interpretations) in each case.

This study, for the first time, employed micro-CT scanning for the purpose of investigating diagenesis in speleothems. The results indicate that micro-CT might be useful in targeting samples for U-Th dating or places to avoid when sampling for dating. Confirmation of these findings on pristine-looking speleothems from other cave sites would also be beneficial.

Theme 3: Using the Holocene as a case study, to decipher the mechanisms driving post-glacial stable carbon isotope ($\delta^{13}C$) changes in Corchia speleothems by combining ^{14}C dating, U-Th dating and $\delta^{13}C$ data

For the purpose of theme 3, radiocarbon and U-Th analyses were combined to determine the DCP in a Holocene speleothem using atmospheric ^{14}C data from the IntCal13 calibration curve. DCP was then used to test the hypothesis of $\delta^{13}C$ post-glacial changes in Corchia speleothems. This proxy has been interpreted as reflective of soil development above the cave during glacial-interglacial transitions (Drysdale et al., 2004; 2009; Zancheta et al., 2007) but until now this hypothesis had not been tested.

54 samples were analysed for ^{14}C and U-Th age-depth model ages were used to constrain the DCP. DCP results are in agreement with the previously proposed hypothesis that the long-term decrease in $\delta^{13}C$ in Corchia speleothems following glacial terminations reflects the slow rate of soil development (albeit limited) above the cave. In CC26, some of the highest DCP values ever found in speleothems are recorded (range: 44.8 to 66.8%). This is interpreted as being a consequence of predominantly closed-system dissolution conditions via carbonic acid dissolution and

the contribution of radioactively dead C from sulphuric acid dissolution – a consequence of the specific geological characteristics of host rock above the Galleria delle Stalattiti. On millennial time-scales, DCP is responsive to hydrological changes as previously described by the mean anomaly index - MAI - (Regattieri et al. 2014) based on trace element and stable isotope data from the same specimen. Since DCP and $\delta^{13}C$ show antipathetic behaviour on this time scale, it is concluded that prior calcite precipitation (PCP) is the major driver for millennial-scale variability in DCP. Furthermore, z scores for DCP and $\delta^{13}C$ was compared. The comparison shows that DCP is much more variable than $\delta^{13}C$, which provides additional support for closed-system dissolution, and is in agreement with the model proposed by Fohlmeister et al. (2011). Additionally, DCP appears to be less sensitive to wet than to dry climate conditions, which is opposite to the observations of Noronha et al. (2014) and Rudzka et al. (2011). While all previously studied sites are characterised by predominantly open-system conditions, Corchia is, as indicated above, a site where closed-system dissolution is predominantly taking place. It might be that closed systems are more responsive to dry events, although the precise mechanisms remain unclear and demand further study.

Future directions:

One of the most intriguing features of the CC26 DCP dataset is the fact that DCP is higher than 50% during almost the entire studied growth interval. The proposed mechanism is a combination of closed-system conditions and sulphuric-acid dissolution. Although drip water analyses from Galleria delle Stalattiti undoubtedly show increased SO_4 content when compared to the waters from other parts of the cave (Piccini, 2008), and support the hypothesis that sulphuric-acid dissolution has a role in the formation of these speleothems, quantifying the contribution the sulphuric-acid dissolution was beyond the scope of

this study. Modelling studies would be advisable here in order to quantify the role of sulphuric-acid dissolution, not only as a mechanism for producing extremely high DCP, but potentially as a factor contributing to the more sensitive response to dry, as opposed to wet, climate conditions. During wet climate conditions, sulphuric-acid dissolution might be promoted, i.e. it might be attenuated during drier conditions due to less water availability. To test this hypothesis future modelling studies are required.

9 REFERENCES

1. Abe-Ouchi, A., Saito, F., Kawamura, K., Raymo, M.E., Okuno, J., Takahashi, K., Blatter, H., 2013. Insolation-driven 100,000-year glacial cycles and hysteresis of ice-sheet volume. Nature 500, 190-193.
2. Ayalon, A., Bar-Matthews, M., Kaufman, A., 1999. Petrography, strontium, barium and uranium concentrations, and strontium and uranium isotope ratios in speleothems as palaeoclimatic proxies: Soreq Cave, Israel. Holocene 9, 715-722.
3. Baker, A., Genty, D., Dreybrodt, W., Barnes, W.L., Mockler, N.J., Grapes, J., 1998. Testing Theoretically Predicted Stalagmite Growth Rate with Recent Annually Laminated Samples: Implications for Past Stalagmite Deposition. Geochimica et Cosmochimica Acta 62, 393-404.
4. Baker, A., Wilson, R., Fairchild, I.J., Franke, J., Spötl, C., Mattey, D., Trouet, V., Fuller, L., 2011. High resolution $\delta^{18}O$ and $\delta^{13}C$ records from an annually laminated Scottish stalagmite and relationship with last millennium climate. Global and Planetary Change 79, 303-311.
5. Baldini, J.U.L., 2010. Cave atmosphere controls on stalagmite growth rate and palaeoclimate records, pp. 283-294.
6. Baneschi, I., Piccini, L., Regattieri, E., Isola, I., Guidi, M., Lotti, L., Mantelli, F., Menichetti, M., Drysdale, R.N., Zanchetta, G., 2011. Hypogean microclimatology and hydrogology of the 800-900 m asl level in the Monte Corchia cave (Tuscany, Italy): Preliminary considerations and implications for paleoclimatological studies. Acta Carsologica 40, 175-187.
7. Bar-Matthews, M., Ayalon, A., Gilmour, M., Matthews, A., Hawkesworth, C.J., 2003. Sea - land oxygen isotopic relationships from planktonic foraminifera and speleothems in the Eastern Mediterranean region and their implication for paleorainfall during interglacial intervals. Geochimica et Cosmochimica Acta 67, 3181-3199.
8. Bar-Matthews, M., Ayalon, A., Kaufman, A., 2000. Timing and hydrological conditions of Sapropel events in the Eastern Mediterranean, as evident from speleothems, Soreq cave, Israel. Chemical Geology 169, 145-156.
9. Bard, E., Antonioli, F., Silenzi, S., 2002a. Sea-level during the penultimate interglacial period

based on a submerged stalagmite from Argentarola Cave (Italy). Earth and Planetary Science Letters 196, 135-146.

10. Bard, E., Delaygue, G., Rostek, F., Antonioli, F., Silenzi, S., Schrag, D.P., 2002b. Hydrological conditions over the western Mediterranean basin during the deposition of the cold Sapropel 6 (ca. 175 Kyr BP). Earth and Planetary Science Letters 202, 481-494.

11. Bard, E., Rostek, F., Hénot-Combes, G., 2004. A Better Radiocarbon Clock. Science 303, 178-179.

12. Beck, J.W., Richards, D.A., Edwards, R.L., Silverman, B.W., Smart, P.L., Donahue, D.J., Hererra-Osterheld, S., Burr, G.S., Calsoyas, L., Jull, A.J.T., Biddulph, D., 2001. Extremely large variations of atmospheric 14C concentration during the last glacial period. Science 292, 2453-2458.

13. Belli, R., Frisia, S., Borsato, A., Drysdale, R., Hellstrom, J., Zhao, J.X., Spötl, C., 2013. Regional climate variability and ecosystem responses to the last deglaciation in the northern hemisphere from stable isotope data and calcite fabrics in two northern Adriatic stalagmites. Quaternary Science Reviews 72, 146-158.

14. Berger, A. and Loutre, M.F., 1991. Insolation values for the climate of the last 10 million years. Quaternary Science Reviews 10, 297-317.

15. Boch, R., Spötl, C., Frisia, S., 2011. Origin and palaeoenvironmental significance of lamination in stalagmites from Katerloch Cave, Austria. Sedimentology 58, 508-531.

16. Borsato, A., Frisia, S., Fairchild, I.J., Somogyi, A., Susini, J., 2007. Trace element distribution in annual stalagmite laminae mapped by micrometer-resolution X-ray fluorescence: Implications for incorporation of environmentally significant species. Geochimica et Cosmochimica Acta 71, 1494-1512.

17. Borsato, A., Johnston, V., Frisia, S., Miorandi, R., & Corradini, F., 2016. Temperature and altitudinal influence on karst dripwater chemistry: implications for regional-scale palaeoclimate reconstructions from speleothem. Geochim. Cosmochim. Acta. (Accepted 22 November 2015).

18. Broecker, W.S., Olson, E.A., Orr, P.C., 1960. Radiocarbon Measurements and Annual Rings in Cave Formations. Nature 185, 93-94.

19. Bruker, 2010. Quantitative Analysis of Geological Samples: Combined XRD-XRF Analysis. Bruker AXS GmbH, Karlsruhe, pp. 1-4.

20. Cabrol P. 1978. Contribution à l'étude du concrétionnement carbonaté des grottes du sud de la France, morphologie, genése et diagenése. Centre d'Etudes et de Recherches Géologiques et Hydrogéologiques, Memoires. Montpellier, France, no. 12; 275.

21. Capozzi, R., Dinelli, E., Negri, A., Picotti, V., 2006. Productivity-generated annual laminae in mid-Pliocene sapropels deposited during precessionally forced periods of warmer Mediterranean climate.

Palaeogeography, Palaeoclimatology, Palaeoecology 235, 208-222.

22. Cheng, H., Edwards, R.L., Broecker, W.S., Denton, G.H., Kong, X., Wang, Y., Zhang, R., Wang, X., 2009. Ice age terminations. Science 326, 248-252.

23. Cheng, H., Lawrence Edwards, R., Shen, C.C., Polyak, V.J., Asmerom, Y., Woodhead, J., Hellstrom, J., Wang, Y., Kong, X., Spötl, C., Wang, X., Calvin Alexander, E., 2013. Improvements in ^{230}Th dating, ^{230}Th and ^{234}U half-life values, and U-Th isotopic measurements by multi-collector inductively coupled plasma mass spectrometry. Earth and Planetary Science Letters 371-372, 82-91.

24. Clark, P.U. and Pollard, D., 1998. Origin of the middle Pleistocene transition by ice sheet erosion of regolith. Paleoceanography 13, 1-9.

25. Clark, P.U., Archer, D., Pollard, D., Blum, J.D., Rial, J.A., Brovkin, V., Mix, A.C., Pisias, N.G., Roy, M., 2006. The middle Pleistocene transition: characteristics, mechanisms, and implications for long-term changes in atmospheric pCO_2. Quaternary Science Reviews 25, 3150-3184.

26. Cliff, R.A., Spötl, C., Mangini, A., 2010. U-Pb dating of speleothems from Spannagel Cave, Austrian Alps: A high resolution comparison with U-series ages. Quaternary Geochronology 5, 452-458.

27. Coplen, T.B., 2007. Calibration of the calcite-water oxygen-isotope geothermometer at Devils Hole, Nevada, a natural laboratory. Geochimica et Cosmochimica Acta 71, 3948-3957.

28. Cortecci, G., Dinelli, E., Indrizzi, M.C., Susini, C., Adorni Braccesi, A., 1999. The Apuane Alps metamorphic complex, northern Tuscany: chemical and isotopic features of Grezzoni and marmi dolomitici. Atti. Soc. tosc. Sci. nat., Mem., Serie A, 106, 78-89

29. Cronin, T.M., 2010. Paleoclimates; Understanding Climate Change Past and Present, New York, Columbia University Press, pp. 113-147.

30. Crucifix, M., 2008. Global change: Climate's astronomical sensors. Nature 456, 47-48.

31. Daëron, M., Guo, W., Eiler, J., Genty, D., Blamart, D., Boch, R., Drysdale, R., Maire, R., Wainer, K., Zanchetta, G., 2011. $^{13}C^{18}O$ clumping in speleothems: Observations from natural caves and precipitation experiments. Geochimica et Cosmochimica Acta 75, 3303-3317.

32. Day, C.C. and Henderson, G.M., 2011. Oxygen isotopes in calcite grown under cave-analogue conditions. Geochimica et Cosmochimica Acta 75, 3956-3972.

33. Day, C.C. and Henderson, G.M., 2013. Controls on trace-element partitioning in cave-analogue calcite. Geochimica et Cosmochimica Acta 120, 612-627.

34. De Choudens-Sánchez and V., Gonzalez, L.A., 2009. Calcite and aragonite precipitation under controlled instantaneous supersaturation: Elucidating the role of $CaCO_3$ saturation state

and Mg/Ca ratio on calcium carbonate polymorphism. Journal of Sedimentary Research 79, 363-376.

35. Deininger, M., Fohlmeister, J., Scholz, D., Mangini, A., 2012. Isotope disequilibrium effects: The influence of evaporation and ventilation effects on the carbon and oxygen isotope composition of speleothems - A model approach. Geochimica et Cosmochimica Acta 96, 57-79.

36. de Ruiter, D.J., Pickering, R., Steininger, C.M., Kramers, J.D., Hancox, P.J., Churchill, S.E., Berger, L.R., Backwell, L., 2009. New Australopithecus robustus fossils and associated U-Pb dates from Cooper's Cave (Gauteng, South Africa). Journal of Human Evolution 56, 497-513.

37. Desmarchelier, J.M., Hellstrom, J.C., McCulloch, M.T., 2006. Rapid trace element analysis of speleothems by ELA-ICP-MS. Chemical Geology 231, 102-117.

38. Diekmann, B. and Kuhn, G., 2002. Sedimentary record of the mid-Pleistocene climate transition in the southeastern South Atlantic (ODP Site 1090). Palaeogeography, Palaeoclimatology, Palaeoecology 182, 241-258.

39. Dodonov, A.E., 2005. The stratigraphic transition and suggested boundary between the Early and Middle Pleistocene in the loess record of northern Eurasia, Geological Society Special Publication, pp. 209-219.

40. Dorale, J. A., González, L. A., Reagan, M. K., Pickett, D. A., Murrell, M. T., and Baker, R. G., 1992. A high resolution record of Holocene climate change in speleothem calcite from Cold Water Cave, northeast Iowa. Science 258, 1626–1630.

41. Dorale, J.A. and Liu, Z., 2009. Limitations of hendy test criteria in judging the paleoclimatic suitability of speleothems and the need for replication. Journal of Cave and Karst Studies 71, 73-80.

42. Doveri M., Leone G., Mussi M. & Zanchetta G., 2005. Composizione isotopica di acque ipogee nell'Antro del Corchia (Alpi Apuane, Toscana nord-occidentale). Memorie Istituto Italiano di Speleologia, S. II, 18: 119-132.

43. Dredge, J., Fairchild, I.J., Harrison, R.M., Fernandez-Cortes, A., Sanchez-Moral, S., Jurado, V., Gunn, J., Smith, A., Spötl, C., Mattey, D., Wynn, P.M., Grassineau, N., 2013. Cave aerosols: Distribution and contribution to speleothem geochemistry. Quaternary Science Reviews 63, 23-41.

44. Drysdale, R.N., Zanchetta, G., Hellstrom, J.C., Fallick, A.E., Zhao, J.X., Isola, I., Bruschi, G., 2004. Palaeoclimatic implications of the growth history and stable isotope ($\delta^{18}O$ and $\delta^{13}C$) geochemistry of a Middle to Late Pleistocene stalagmite from central-western Italy. Earth and Planetary Science Letters 227, 215-229.

45. Drysdale, R.N., Zanchetta, G., Hellstrom, J.C., Fallick, A.E., Zhao, J.X., 2005. Stalagmite evidence for the onset of the Last Interglacial in southern Europe at 129 ± 1 ka. Geophysical Research Letters 32, 1-4.

46. Drysdale, R.N., Zanchetta, G., Hellstrom, J., Maas, R., Fallick, A., Pickett, M., Cartwright, I., Piccini, L., 2006. Late Holocene drought responsible for the collapse of Old World civilizations is recorded in an Italian cave flowstone. Geology 34, 101-104.

47. Drysdale, R.N., Zanchetta, G., Hellstrom, J.C., Fallick, A.E., McDonald, J., Cartwright, I., 2007. Stalagmite evidence for the precise timing of North Atlantic cold events during the early last glacial. Geology 35, 77-80.

48. Drysdale, R.N., Hellstrom, J.C., Zanchetta, G., Fallick, A.E., Sánchez Goñi, M.F., Couchoud, I., McDonald, J., Maas, R., Lohmann, G., Isola, I., 2009. Evidence for Obliquity Forcing of Glacial Termination II. Science 325, 1527-1531.

49. Drysdale, R., Couchoud, I., Zanchetta, G., Hellstrom, J.C., Spötl, C., Woodhead, J.D., Perrette, I., Baneschi, I., Bajo, P., Gagan, M., Isola, I., Greig, A., 2011. The last 11 glacial-interglacial cycles recorded in a single speleothem from Corchia Cave. Climate Change – The Karst Record (KR6), University of Birmingham 26-29th June 2011.

50. Drysdale, R.N., Paul, B.T., Hellstrom, J.C., Couchoud, I., Greig, A., Bajo, P., Zanchetta, G., Isola, I., Spötl, C., Baneschi, I., Regattieri, E., Woodhead, J.D., 2012. Precise microsampling of poorly laminated speleothems for U-series dating. Quaternary Geochronology 14, 38-47.

51. Dulinski, M. and Rozanski, K., 1990. Formation of $^{13}C/^{12}C$ isotope ratios in speleothems: a semi- dynamic model. Radiocarbon 32, 7-16.

52. Elderfield, H., Ferretti, P., Greaves, M., Crowhurst, S., McCave, I.N., Hodell, D., Piotrowski, A.M., 2012. Evolution of ocean temperature and ice volume through the mid-Pleistocene climate transition. Science 337, 704-709.

53. Emeis, K.C., Schulz, H.M., Struck, U., Sakamoto, T., Doose, H., Erlenkeuser, H., Howell, M., Kroon, D., Paterne, M., 1998. Stable isotope and alkenone temperature records of sapropels from Sites 964 and 967: Constraining the physical environment of sapropel formation in the eastern Mediterranean Sea. Proceedings of the Ocean Drilling Program: Scientific Results 160, 309-332.

54. Emiliani, C., 1966. Isotopic paleotemperatures. Science 154, 851-857.

55. Expedition 306 Scientists, Site U1313. In Channell, J.E.T., Kanamatsu, T., Sato, T., Stein, R., Alvarez Zarikian, C.A., Malone, M.J., and the Expedition 303/306 Scientists. Proc. IODP, 303/ 306: College Station TX (Integrated Ocean Drilling Program Management International, Inc.). (2006) doi:10.2204/iodp.proc.303306.112.2006

56. Fairchild, I.J., Borsato, A., Tooth, A.F., Frisia, S., Hawkesworth, C.J., Huang, Y., McDermott, F., Spiro, B., 2000. Controls on trace element (Sr–Mg) compositions of carbonate cave waters: implications for

speleothem climatic records. Chemical Geology 166, 255-269.
57. Fairchild, I.J., Baker, A., Borsato, A., Frisia, S., Hinton, R.W., McDermott, F., Tooth, A.F., 2001. Annual to sub-annual resolution of multiple trace-element trends in speleothems. Journal of the Geological Society 158, 831-841.
58. Fairchild, I.J., Smith, C.L., Baker, A., Fuller, L., Spötl, C., Mattey, D., McDermott, F., 2006. Modification and preservation of environmental signals in speleothems. Earth-Science Reviews 75, 105-153.
59. Fairchild, I.J. and Treble, P.C., 2009. Trace elements in speleothems as recorders of environmental change. Quaternary Science Reviews 28, 449-468.
60. Fairchild, I.J. and Baker, A., 2012. Speleothem Science: From Process to Past Environments.
61. Ferretti, P., Crowhurst, S.J., Hall, M.A., Cacho, I., 2010. North Atlantic millennial-scale climate variability 910 to 790ka and the role of the equatorial insolation forcing. Earth and Planetary Science Letters 293, 28-41.
62. Fink, D., Hotchkis, M., Hua, Q., Jacobson, G., Smith, A.M., Zoppi, U., Child, D., Misfud, C., van der Gaast, H., Williams, A., Williams, M., 2004. The ANTARES AMS facility at ANSTO. Nuclear Instruments and Methods in Physics Research B, 109-115.
63. Fischer, H., Severinghaus, J., Brook, E., Wolff, E., Albert, M., Alemany, O., Arthern, R., Bentley, C., Blankenship, D., Chappellaz, J., Creyts, T., Dahl-Jensen, D., Dinn, M., Frezzotti, M., Fujita, S., Gallee, H., Hindmarsh, R., Hudspeth, D., Jugie, G., Kawamura, K., Lipenkov, V., Miller, H., Mulvaney, R., Parrenin, F., Pattyn, F., Ritz, C., Schwander, J., Steinhage, D., van Ommen, T., Wilhelms, F., 2013. Where to find 1.5 million yr old ice for the IPICS "Oldest-Ice" ice core. Clim. Past 9, 2489-2505.
64. Fleitmann, D., Cheng, H., Badertscher, S., Edwards, R.L., Mudelsee, M., Göktürk, O.M., Fankhauser, A., Pickering, R., Raible, C.C., Matter, A., Kramers, J., Tüysüz, O., 2009. Timing and climatic impact of Greenland interstadials recorded in stalagmites from northern Turkey. Geophys. Res. Lett. 36, L19707.
65. Fohlmeister, J., Scholz, D., Kromer, B., Mangini, A., 2011. Modelling carbon isotopes of carbonates in cave drip water. Geochimica et Cosmochimica Acta 75, 5219-5228.
66. Folk, L.R., 1965. Some aspects of recrystallization in ancient limestones. in Pray, L.C., and Murray, R.C., eds., Dolomitization and Limestone Diagenesis:SEPM, Special Publication 13,14-48.
67. Ford, D. C. and Williams, P. 2007. Karst Geomorphology and Hydrology. John Wiley & Sons.
68. Frisia, S., 1996. Petrographic evidences in speleothems: some examples. Speleochronos 7, 21-30.
69. Frisia, S., Borsato, A., Fairchild, I.J., McDermott, F., 2000. Calcite fabrics, growth mechanisms, and environments of formation in speleothems

from the Italian Alps and Southwestern Ireland. Journal of Sedimentary Research 70, 1183-1196.

70. Frisia, S., Borsato, A., Fairchild, I.J., McDermott, F., Selmo, E.M., 2002. Aragonite-calcite relationships in speleothems (Grotte de Clamouse, France): Environment, fabrics, and carbonate geochemistry. Journal of Sedimentary Research 72, 687-699.

71. Frisia, S., Borsato, A., Spötl, C., Villa, I.M., Cucchi, F., 2005. Climate variability in the SE Alps of Italy over the past 17 000 years reconstructed from a stalagmite record. Boreas 34, 445-455.

72. Frisia, S. and Borsato, A., 2010. Chapter 6 Karst, pp. 269-318.

73. Frisia, S., Fairchild, I.J., Fohlmeister, J., Miorandi, R., Spötl, C., Borsato, A., 2011. Carbon mass-balance modelling and carbon isotope exchange processes in dynamic caves. Geochimica et Cosmochimica Acta 75, 380-400.

74. Frisia, S., 2015. Microstratigraphic logging of calcite fabrics in speleothems as tool for palaeoclimate studies. International Journal of Speleology 44, 1-16.

75. Frumkin, A. and Stein, M., 2004. The Sahara–East Mediterranean dust and climate connection revealed by strontium and uranium isotopes in a Jerusalem speleothem. Earth & Planetary Science Letters 217, 451.

76. Gascoyne, M., 1992. Palaeoclimate determination from cave calcite deposits. Quaternary Science Reviews 11, 609-632.

77. Genty, D. and Massault, M., 1997. Bomb ^{14}C recorded in laminated speleothems: Calculation of dead carbon proportion. Radiocarbon 39, 33-48.

78. Genty, D. and Massault, M., 1999. Carbon transfer dynamics from bomb- ^{14}C and $\delta^{13}C$ time series of a laminated stalagmite from SW France-Modelling and comparison with other stalagmite records. Geochimica et Cosmochimica Acta 63, 1537-1548.

79. Genty, D., Massault, M., Gilmour, M., Baker, A., Verheyden, S., Kepens, E., 1999. Calculation of past dead carbon proportion and variability by the comparison of AMS ^{14}C and TIMS U/Th ages on two Holocene stalagmites. Radiocarbon 41, 251-270.

80. Genty, D., Baker, A., Massault, M., Proctor, C., Gilmour, M., Pons-Branchu, E., Hamelin, B., 2001. Dead carbon in stalagmites: carbonate bedrock paleodissolution vs. ageing of soil organic matter. Implications for ^{13}C variations in speleothems. Geochimica et Cosmochimica Acta 65, 3443-3457.

81. Genty, D., Blamart, D., Ouahdi, R., Gilmour, M., Baker, A., Jouzel, J., Van-Exter, S., 2003. Precise dating of Dansgaard-Oeschger climate oscillations in western Europe from stalagmite data. Nature 421, 833-837.

82. Genty, D., Blamart, D., Ghaleb, B., Plagnes, V., Causse, C., Bakalowicz, M., Zouari, K., Chkir, N., Hellstrom, J., Wainer,

K., Bourges, F., 2006. Timing and dynamics of the last deglaciation from European and North African $\delta^{13}C$ stalagmite profiles—comparison with Chinese and South Hemisphere stalagmites. Quaternary Science Reviews 25, 2118-2142.

83. GeoPIXE software for PIXE and SXRF imaging, http://nmp.csiro.au/GeoPIXE.html

84. Gildor, H. and Tziperman, E., 2001. A sea ice climate switch mechanism for the 100-kyr glacial cycles. Journal of Geophysical Research C: Oceans 106, 9117-9133.

85. Goede, A., McCulloch, M., McDermott, F., Hawkesworth, C., 1998. Aeolian contribution to strontium and strontium isotope variations in a Tasmanian speleothem. Chemical Geology 149, 37-50.

86. Griffiths, M.L., Drysdale, R.N., Gagan, M.K., Frisia, S., Zhao, J.-x., Ayliffe, L.K., Hantoro, W.S., Hellstrom, J.C., Fischer, M.J., Feng, Y.-X., Suwargadi, B.W., 2010a. Evidence for Holocene changes in Australian–Indonesian monsoon rainfall from stalagmite trace element and stable isotope ratios. Earth and Planetary Science Letters 292, 27-38.

87. Griffiths, M.L., Drysdale, R.N., Vonhof, H.B., Gagan, M.K., Zhao, J.-x., Ayliffe, L.K., Hantoro, W.S., Hellstrom, J.C., Cartwright, I., Frisia, S., Suwargadi, B.W., 2010b. Younger Dryas–Holocene temperature and rainfall history of southern Indonesia from δ18O in speleothem calcite and fluid inclusions. Earth and Planetary Science Letters 295, 30-36.

88. Griffiths, M.L., Fohlmeister, J., Drysdale, R.N., Hua, Q., Johnson, K.R., Hellstrom, J.C., Gagan, M.K., Zhao, J.x., 2012. Hydrological control of the dead carbon fraction in a Holocene tropical speleothem. Quaternary Geochronology.

89. Hartland, A., Fairchild, I.J., Lead, J.R., Borsato, A., Baker, A., Frisia, S., Baalousha, M., 2012. From soil to cave: Transport of trace metals by natural organic matter in karst dripwaters. Chemical Geology 304-305, 68-82.

90. Hays, J.D., Imbrie, J., Shackleton, N.J., 1976. Variations in the Earth's Orbit: Pacemaker of the Ice Ages. Science 194, 1121-1132.

91. Hayward, B.W., Kawagata, S., Grenfell, H.R., Sabaa, A.T., O'Neill, T., 2007. Last global extinction in the deep sea during the mid-Pleistocene climate transition. Paleoceanography 22.

92. Head, M.J. and Gibbard, P.L., 2005. Early-Middle Pleistocene transitions: An overview and recommendation for the defining boundary, pp. 1-18.

93. Head, M.J., Pillans, B., Farquhar, S.A., 2008. The Early-Middle Pleistocene Transition: Characterization and proposed guide for the defining boundary. Episodes 31, 255-259.

94. Hellstrom, J., McCulloch, M., Stone, J., 1998. A detailed 31,000-year record of climate and vegetation change, from the isotope geochemistry of two New Zealand speleothems.

Quaternary Research 50, 167-178.

95. Hellstrom, J.C., McCulloch, M.T., 2000. Multi-proxy constraints on the climatic significance of trace element records from a New Zealand speleothem. Earth and Planetary Science Letters 179, 287-297.

96. Hellstrom, J., 2003. Rapid and accurate U/Th dating using parallel ion-counting multi-collector ICP-MS. Journal of Analytical Atomic Spectrometry 18, 1346-1351.

97. Hellstrom, J., 2006. U–Th dating of speleothems with high initial 230Th using stratigraphical constraint. Quaternary Geochronology 1, 289-295.

98. Henderson, G.M., 2006. Caving in to new chronologies. Science 313, 620-622.

99. Hendy, C.H., Wilson, A.T., 1968. Palaeoclimatic data from speleothems. Nature 219, 48-51.

100. Hendy, C.H., 1971. The isotopic geochemistry of speleothems-I. The calculation of the effects of different modes of formation on the isotopic composition of speleothems and their applicability as palaeoclimatic indicators. Geochimica et Cosmochimica Acta 35, 801-824.

101. Hendy, E.J., Tomiak, P.J., Collins, M.J., Hellstrom, J., Tudhope, A.W., Lough, J.M., Penkman, K.E.H., 2012. Assessing amino acid racemization variability in coral intra-crystalline protein for geochronological applications. Geochimica et Cosmochimica Acta 86, 338-353.

102. Hernández-Almeida, I., Sierro, F.J., Cacho, I., Flores, J.A., 2012. Impact of suborbital climate changes in the North Atlantic on ice sheet dynamics at the Mid-Pleistocene Transition. Paleoceanography 27, PA3214.

103. HIill, C. and Forti P., 1997. Cave Minerals of the World, Second Edition. National Speleological Society, Inc., Alabama, pp.61 – 62

104. Hodge, E., McDonald, J., Fischer, M., Redwood, D., Hual, Q., Levchenko, V., Drysdale, R., Waring, C., Fink, D., 2011. Using the ^{14}C bomb pulse to date young speleothems. Radiocarbon 53, 345-357.

105. Hoffmann, D.L., Beck, J.W., Richards, D.A., Smart, P.L., Singarayer, J.S., Ketchmark, T., Hawkesworth, C.J., 2010. Towards radiocarbon calibration beyond 28 ka using speleothems from the Bahamas. Earth and Planetary Science Letters 289, 1-10.

106. Hoffmann, D.L., Spötl, C., Mangini, A., 2009. Micromill and in situ laser ablation sampling techniques for high spatial resolution MC-ICPMS U-Th dating of carbonates. Chemical Geology 259, 253-261.

107. Hönisch, B., Hemming, N.G., Archer, D., Siddall, M., McManus, J.F., 2009. Atmospheric carbon dioxide concentration across the mid-pleistocene transition. Science 324, 1551-1554.

108. Hua, Q., Jacobsen, G.E., Zoppi, U., Lawson, E.M., Williams, A.A., Smith, A.M., McGann, M.J., 2001. Progress in radiocarbon target preparation at the ANTARES

AMS centre. Radiocarbon 43, 275-282.

109. Hua, Q., 2009. Radiocarbon: A chronological tool for the recent past. Quaternary Geochronology 4, 378-390.

110. Hua, Q., M. Barbetti, D. Fink, K.F. Kaiser, M. Friedrich, B. Kromer, V.A. Levchenko, U. Zoppi, A.M. Smith, and F. Bertuch, 2009. Atmospheric 14C variations derived from tree rings during the early Younger Dryas. Quaternary Science Reviews 28, 2982-2990.

111. Hua, Q., McDonald, J., Redwood, D., Drysdale, R., Lee, S., Fallon, S., Hellstrom, J., 2012. Robust chronological reconstruction for young speleothems using radiocarbon. Quaternary Geochronology 14, 67-80.

112. Huang, Y., Fairchild, I.J., 2001. Partitioning of Sr^{2+} and Mg^{2+} into calcite under karst-analogue experimental conditions. Geochimica et Cosmochimica Acta 65, 47-62.

113. Huber, K., Weckström, K., Drescher-Schneider, R., Knoll, J., Schmidt, J., Schmidt, R., 2010. Climate changes during the last glacial termination inferred from diatom-based temperatures and pollen in a sediment core from Längsee (Austria). Journal of Paleolimnology 43, 131-147.

114. Huybers, P. and Wunsch, C., 2005. Obliquity pacing of the late Pleistocene glacial terminations. Nature 434, 491-494.

115. Huybers, P., 2006. Early pleistocene glacial cycles and the integrated summer insolation forcing. Science 313, 508-511.

116. Huybers, P., 2007. Glacial variability over the last two million years: an extended depth-derived agemodel, continuous obliquity pacing, and the Pleistocene progression. Quaternary Science Reviews 26, 37-55.

117. Huybers, P., 2009. Pleistocene glacial variability as a chaotic response to obliquity forcing. Climate of the Past 5, 481-488.

118. Huybers, P., 2011. Combined obliquity and precession pacing of late Pleistocene deglaciations. Nature 480, 229-232.

119. Imbrie. J. And Imbrie, K.P., 1979. Ice Ages: Solving the Mystery. Cambridge, MA:Harvard University Press.

120. Imbrie, J.; Hays, J. D.; Martinson, D. G.; McIntyre, A.; Mix, A. C.; Morley, J. J.; Pisias, N. G.; Prell, W. L.; Shackleton, N. J., 1984. The orbital theory of Pleistocene climate: support from a revised chronology of the marine $\delta^{18}O$ record. In: Milankovitch and Climate: Understanding the Response to Astronomical Forcing, Proceedings of the NATO Advanced Research Workshop held 30 November - 4 December, 1982 in Palisades, NY. Edited by A. Berger, J. Imbrie, H. Hays, G. Kukla, and B. Saltzman. Dordrecht: D. Reidel Publishing, p. 269-305.

121. Imbrie, J.Z., Imbrie-Moore, A., Lisiecki, L.E., 2011. A phase-space model for Pleistocene ice volume. Earth and Planetary Science Letters 307, 94-102.

122. Incarbona, A., Dinarès-Turell, J., Di Stefano, E., Ippolito, G., Pelosi, N., Sprovieri, R., 2013. Orbital variations in planktonic foraminifera assemblages from the Ionian Sea during the Middle Pleistocene Transition. Palaeogeography, Palaeoclimatology, Palaeoecology 369, 303-312.

123. Jin, H., Jian, Z., 2013. Millennial-scale climate variability during the mid-Pleistocene transition period in the northern South China Sea. Quaternary Science Reviews 70, 15-27.

124. Joannin, S., Bassinot, F., Nebout, N.C., Peyron, O., Beaudouin, C., 2011. Vegetation response to obliquity and precession forcing during the Mid-Pleistocene Transition in Western Mediterranean region (ODP site 976). Quaternary Science Reviews 30, 280-297.

125. Jouzel, J.and Masson-Delmotte, V., 2010. Deep ice cores: The need for going back in time. Quaternary Science Reviews 29, 3683-3689.

126. Jouzel, J., Masson-Delmotte, V., Cattani, O., Dreyfus, G., Falourd, S., Hoffmann, G., Minster, B., Nouet, J., Barnola, J.M., Chappellaz, J., Fischer, H., Gallet, J.C., Johnsen, S., Leuenberger, M., Loulergue, L., Luethi, D., Oerter, H., Parrenin, F., Raisbeck, G., Raynaud, D., Schilt, A., Schwander, J., Selmo, E., Souchez, R., Spahni, R., Stauffer, B., Steffensen, J.P., Stenni, B., Stocker, T.F., Tison, J.L., Werner, M., Wolff, E.W., 2007. Orbital and millennial antarctic climate variability over the past 800,000 years. Science 317, 793-796.

127. Kawagata, S., Hayward, B.W., Grenfell, H.R., Sabaa, A., 2005. Mid-Pleistocene extinction of deep-sea foraminifera in the North Atlantic Gateway (ODP sites 980 and 982). Palaeogeography, Palaeoclimatology, Palaeoecology 221, 267-291.

128. Kemp, A.E.S., Grigorov, I., Pearce, R.B., Naveira Garabato, A.C., 2010. Migration of the Antarctic Polar Front through the mid-Pleistocene transition: Evidence and climatic implications. Quaternary Science Reviews 29, 1993-2009.

129. Kim, S.T., O'Neil, J.R., 1997. Equilibrium and nonequilibrium oxygen isotope effects in synthetic carbonates. Geochimica et Cosmochimica Acta 61, 3461-3475.

130. Kleiven, H.F., Jansen, E., Curry, W.B., Hodell, D.A., Venz, K., 2003. Atlantic Ocean thermohaline circulation changes on orbital to suborbital timescales during the mid-Pleistocene. Paleoceanography 18, 8-1.

131. Kroon, D., Alexander, I., Little, M., Lourens, L.J., Matthewson, A., Robertson, A.H.F., Sakamoto, T., 1998. Oxygen isotope and Sapropel stratigraphy in the eastern Mediterranean during the last 3.2 million years. Proceedings of the Ocean Drilling Program: Scientific Results 160, 181-190.

132. Lachniet, M.S., 2009. Climatic and environmental controls on speleothem oxygen-isotope values. Quaternary Science Reviews 28, 412-432.

133. Lachniet, M.S., Bernal, J.P., Asmerom, Y., Polyak, V., 2012. Uranium loss and aragonite-calcite age discordance in a calcitized aragonite stalagmite. Quaternary Geochronology.

134. Li, W.X., Lundberg, J., Dickin, A.P., Ford, D.C., Schwarcz, H.P., McNutt, R., Williams, D., 1989. High-precision mass-spectrometric uranium-series dating of cave deposits and implications for palaeoclimate studies. Nature 339, 534-536.

135. Li, Z.H., Driese, S.G., Cheng, H., 2014. A multiple cave deposit assessment of suitability of speleothem isotopes for reconstructing palaeo-vegetation and palaeo-temperature. Sedimentology 61, 749-766.

136. Lisiecki, L.E. and Raymo, M.E., 2005. A Pliocene-Pleistocene stack of 57 globally distributed benthic $\delta^{18}O$ records. Paleoceanography 20, 1-17.

137. Lisiecki, L.E., 2010. Links between eccentricity forcing and the 100,000-year glacial cycle. Nature Geoscience 3, 349-352.

138. Lourens, L.J., 2004. Revised tuning of Ocean Drilling Program Site 964 and KC01B (Mediterranean) and implications for the $\delta^{18}O$, tephra, calcareous nannofossil, and geomagnetic reversal chronologies of the past 1.1 Myr. Paleoceanography 19, PA3010 3011-3020.

139. Ludwig, K.R., 1977. Effect on initial radioactive-daughter disequilibrium on U-Pb isotope apparent ages of young minerals. J Res US Geol Surv 5, 663-667.

140. Ludwig, K.R., 2001. Isoplot/Ex, rev. 2.49. A Geochronological Toolkit for Microsoft Excel. Berkeley Geochronology Center, Berkley, USA. Special Publication, 1a.

141. Machel, H.G., 1997. Recrystallization versus neomorphism, and the concept of "significant recrystallization" in dolomite research. Sedimentary Geology 113, 161-168.

142. Malaizé, B., Jullien, E., Tisserand, A., Skonieczny, C., Grousset, E.F., Eynaud, F., Kissel, C., Bonnin, J., Karstens, S., Martinez, P., Bory, A., Bout-Roumazeilles, V., Caley, T., Crosta, X., Charlier, K., Rossignol, L., Flores, J.A., Schneider, R., 2012. The impact of African aridity on the isotopic signature of Atlantic deep waters across the Middle Pleistocene Transition. Quaternary Research 77, 182-191.

143. Mangini, A., Schlosser, P., 1986. The formation of Eastern Mediterranean sapropels. Marine Geology 72, 115-124.

144. Marino, M., Maiorano, P., Lirer, F., Pelosi, N., 2009. Response of calcareous nannofossil assemblages to paleoenvironmental changes through the mid-Pleistocene revolution at Site 1090 (Southern Ocean). Palaeogeography, Palaeoclimatology, Palaeoecology 280, 333-349.

145. Martín-García, R., Alonso-Zarza, A.M., Martín-Pérez, A., 2009. Loss of primary texture and geochemical signatures in speleothems due to diagenesis: Evidences from Castañar Cave,

Spain. Sedimentary Geology 221, 141-149.

146. Martínez-Garcia, A., Rosell-Melé, A., Jaccard, S.L., Geibert, W., Sigman, D.M., Haug, G.H., 2011. Southern Ocean dust-climate coupling over the past four million years. Nature 476, 312-315.

147. Maslin, M.A. and Ridgwell, A.J., 2005. Mid-Pleistocene revolution and the 'eccentricity myth', Geological Society Special Publication, pp. 19-34.

148. Mattey, D.P., Fairchild, I.J., Atkinson, T.C., Latin, J.P., Ainsworth, M., Durell, R., 2010. Seasonal microclimate control of calcite fabrics, stable isotopes and trace elements in modern speleothem from St Michaels Cave, Gibraltar, Geological Society Special Publication, pp. 323-344.

149. McClymont, E.L., Sosdian, S.M., Rosell-Melé, A., Rosenthal, Y., 2013. Pleistocene sea-surface temperature evolution: Early cooling, delayed glacial intensification, and implications for the mid-Pleistocene climate transition. Earth-Science Reviews 123, 173-193.

150. McDermott, F., 2004. Palaeo-climate reconstruction from stable isotope variations in speleothems: A review. Quaternary Science Reviews 23, 901-918.

151. McDermott, F., Schwarcz, H.P., Rowe, P.J., 2005. Isotopes in Speleothems. In: Leng, M.J. (Ed.), Isotopes in Palaeoenvironmental Research, Springer, Dordrecht, The Netherlands, 185–225.

152. McDonald, J., Drysdale, R., Hill, D., 2004. The 2002-2003 El Niño recorded in Australian cave drip waters: Implications for reconstructing rainfall histories using stalagmites. Geophysical Research Letters 31, 1-4.

153. McDonald, J. and Drysdale, R., 2007. Hydrology of cave drip waters at varying bedrock depths from a karst system in southeastern Australia. Hydrological Processes 21, 1737-1748.

154. McMillan, E.A., Fairchild, I.J., Frisia, S., Borsato, A., McDermott, F., 2005. Annual trace element cycles in calcite–aragonite speleothems: evidence of drought in the western Mediterranean 1200–1100 yr BP. Journal of Quaternary Science 20, 423-433.

155. Meyer, M.C., Cliff, R.A., Spötl, C., Knipping, M., Mangini, A., 2009. Speleothems from the earliest Quaternary: Snapshots of paleoclimate and landscape evolution at the northern rim of the Alps. Quaternary Science Reviews 28, 1374-1391.

156. Meyer, M.C., Cliff, R.A., Spötl, C., 2011. Speleothems and mountain uplift. Geology 39, 447-450.

157. Mickler, P.J., Banner, J.L., Stern, L., Asmerom, Y., Edwards, R.L., Ito, E., 2004a. Stable isotope variations in modern tropical speleothems: Evaluating equilibrium vs. kinetic isotope effects. Geochimica et Cosmochimica Acta 68, 4381-4393.

158. Mickler, P.J., Ketcham, R.A., Colbert, M.W., Banner, J.L., 2004b. Application of high-resolution X-ray computed tomography in determining the suitability of speleothems for

use in paleoclimatic, paleohydrologic reconstructions. Journal of Cave and Karst Studies 66, 4-8.

159. Morse, J. W., Wang, Q., Tsio M.Y.,1997. Influences of temperature and Mg:Ca ratio on $CaCO_3$ precipitates from seawater. Geology 25, 85-87.

160. Mudelsee, M., Schulz, M., 1997. The mid-pleistocene climate transition: Onset of 100 ka cycle lags ice volume build-up by 280 ka. Earth and Planetary Science Letters 151, 117-123.

161. Naafs, B.D.A., Hefter, J., Ferretti, P., Stein, R., Haug, G.H., 2011. Sea surface temperatures did not control the first occurrence of Hudson Strait Heinrich Events during MIS 16. Paleoceanography 26, PA4201.

162. Naafs, B.D.A., Hefter, J., Acton, G., Haug, G.H., Martínez-Garcia, A., Pancost, R., Stein, R., 2012. Strengthening of North American dust sources during the late Pliocene (2.7Ma). Earth and Planetary Science Letters 317-318, 8-19.

163. Noronha, A.L., Johnson, K.R., Hu, C., Ruan, J., Southon, J.R., Ferguson, J.E., 2014. Assessing influences on speleothem dead carbon variability over the Holocene: Implications for speleothem-based radiocarbon calibration. Earth and Planetary Science Letters 394, 20-29.

164. Noronha, A.L., Johnson, K.R., Southon, J.R., Hu, C., Ruan, J., McCabe-Glynn, S., 2015. Radiocarbon evidence for decomposition of aged organic matter in the vadose zone as the main source of speleothem carbon. Quaternary Science Reviews 127, 37-47.

165. Orland, I.J., Bar-Matthews, M., Ayalon, A., Matthews, A., Kozdon, R., Ushikubo, T., Valley, J.W., 2012. Seasonal resolution of Eastern Mediterranean climate change since 34ka from a Soreq Cave speleothem. Geochimica et Cosmochimica Acta 89, 240-255.

166. Orland, I.J., Burstyn, Y., Bar-Matthews, M., Kozdon, R., Ayalon, A., Matthews, A., Valley, J.W., 2014. Seasonal climate signals (1990-2008) in a modern Soreq Cave stalagmite as revealed by high-resolution geochemical analysis. Chemical Geology 363, 322-333.

167. Ortega, R., Maire, R., Devès, G., Quinif, Y., 2005. High-resolution mapping of uranium and other trace elements in recrystallized aragonite-calcite speleothems from caves in the Pyrenees (France): Implication for U-series dating. Earth and Planetary Science Letters 237, 911-923.

168. Oster, J.L., Montañez, I.P., Guilderson, T.P., Sharp, W.D., Banner, J.L., 2010. Modeling speleothem $\delta^{13}C$ variability in a central Sierra Nevada cave using ^{14}C and $^{87}Sr/^{86}Sr$. Geochimica et Cosmochimica Acta 74, 5228-5242.

169. Paillard, D., 1998. The timing of Pleistocene glaciations from a simple multiple-state climate model. Nature 391, 378-381.

170. Parkhurst, D.L. and Appelo, C.A.J., 1999. User's guide to PHREEQC (version 2)- A computer program for speciation,

batch-reaction, one-dimensional transport, and inverse geochemical calculations: U.S. Geological Survey Water-Resources Investigations Report 99-4259, 312 p.

171. Paton, C., Hellstrom, J., Paul, B., Woodhead, J., Hergt, J., 2011. Iolite: Freeware for the visualisation and processing of mass spectrometric data. Journal of Analytical Atomic Spectrometry 26, 2508-2518.

172. Paul, B., Paton, C., Norris, A., Woodhead, J., Hellstrom, J., Hergt, J., Greig, A., 2012. CellSpace: A module for creating spatially registered laser ablation images within the Iolite freeware environment. Journal of Analytical Atomic Spectrometry 27, 700-706.

173. Pena, L.D., Goldstein, S.L., 2014. Thermohaline circulation crisis and impacts during the mid-Pleistocene transition. Science 345, 318-322.

174. Perrin, C., Prestimonaco, L., Servelle, G., Tilhac, R., Maury, M., Cabrol, P., 2014. Aragonite-calcite speleothems: Identifying original and diagenetic features. Journal of Sedimentary Research 84, 245-269.

175. Piccini, L., Zanchetta, G., Drysdale, R.N., Hellstrom, J., Isola, I., Fallick, A.E., Leone, G., Doveri, M., Mussi, M., Mantelli, F., Molli, G., Lotti, L., Roncioni, A., Regattieri, E., Meccheri, M., Vaselli, L., 2008. The environmental features of the Monte Corchia cave system (Apuan Alps, central Italy) and their effects on speleothem growth. International Journal of Speleology 37, 153-172.

176. Pickering, R. and Kramers, J.D., 2010. Re-appraisal of the stratigraphy and determination of new U-Pb dates for the Sterkfontein hominin site, South Africa. Journal of Human Evolution 59, 70-86.

177. Pickering, R., Kramers, J.D., Partridge, T., Kodolanyi, J., Pettke, T., 2010. U-Pb dating of calcite-aragonite layers in speleothems from hominin sites in South Africa by MC-ICP-MS. Quaternary Geochronology 5, 544-558.

178. Pickering, R., Dirks, P.H.G.M., Jinnah, Z., de Ruiter, D.J., Churchill, S.E., Herries, A.I.R., Woodhead, J.D., Hellstrom, J.C., Berger, L.R., 2011a. Australopithecus sediba at 1.977 Ma and Implications for the Origins of the Genus Homo. Science 333, 1421-1423.

179. Pickering, R., Kramers, J.D., Hancox, P.J., de Ruiter, D.J., Woodhead, J.D., 2011b. Contemporary flowstone development links early hominin bearing cave deposits in South Africa. Earth and Planetary Science Letters 306, 23-32.

180. Pingitore, N.E., Jr. 1982. The role of diffusion during carbonate diagenesis. Journal Sedimentary Petrology 52, 27-39.

181. Pisias, N.G., Moore Jr, T.C., 1981. The evolution of Pleistocene climate: A time series approach. Earth and Planetary Science Letters 52, 450-458.

182. Polyak, L., Best, K.M., Crawford, K.A., Council, E.A., St-Onge, G., 2013. Quaternary history of sea ice in the western Arctic Ocean based on

foraminifera. Quaternary Science Reviews.

183. Polyak, V., Hill, C., Asmerom, Y., 2008. Age and evolution of the grand canyon revealed by U-Pb dating of water table-type speleothems. Science 319, 1377-1380.

184. Railsback, L.B., Brook, G.A., Jian, C., Kalin, R., Fleisher, C.J., 1994. Environmental controls on the petrology of a late Holocene speleothem from Botswana with annual layers of aragonite and calcite. Journal of Sedimentary Research A: Sedimentary Petrology and Processes 64 A, 147-155.

185. Railsback, L.B., Dabous, A.A., Osmond, J.K., Fleisher, C.J., 2002. Petrographic and geochemical screening of speleothems for U-series dating: An example from recrystallized speleothems from Wadi Sannur Cavern, Egypt. Journal of Cave and Karst Studies 64, 108-116.

186. Raymo, M.E., Ruddiman, W.F., Shackleton, N.J., Oppo, D.W., 1990. Evolution of Atlantic–Pacific d13C gradients over the last 2.5 m.y. Earth and Planetary Science Letters 97, 353–368.

187. Raymo, M.E., Oppo, D.W., Curry, W., 1997. The mid-Pleistocene climate transition: A deep sea carbon isotopic perspective. Paleoceanography 12, 546-559.

188. Raymo, M.E. and Nisancioglu, K., 2003. The 41 kyr world: Milankovitch's other unsolved mystery. Paleoceanography 18, 11-11.

189. Raymo, M.E., Oppo, D.W., Flower, B.P., Hodell, D.A., McManus, J.F., Venz, K.A., Kleiven, K.F., McIntyre, K., 2004. Stability of North Atlantic water masses in face of pronounced climate variability during the Pleistocene. Paleoceanography 19, PA2008.

190. Raymo, M.E., Lisiecki, L.E., Nisancioglu, K.H., 2006. Plio-pleistocene ice volume, antarctic climate, and the global δ18O record. Science 313, 492-495.

191. Raymo, M.E. and Huybers, P., 2008. Unlocking the mysteries of the ice ages. Nature 451, 284-285.

192. Regattieri, E., Zanchetta, G., Drysdale, R.N., Isola, I., Hellstrom, J.C., Dallai, L., 2014. Lateglacial to Holocene trace element record (Ba, Mg, Sr) from Corchia Cave (Apuan Alps, central Italy): Paleoenvironmental implications. Journal of Quaternary Science 29, 381-392.

193. Reimer, P.J., Bard, E., Bayliss, A., Beck, J.W., Blackwell, P.G., Bronk Ramsey, C., Buck, C.E., Cheng, H., Edwards, R.L., Friedrich, M., Grootes, P.M., Guilderson, T.P., Haflidason, H., Hajdas, I., Hatté, C., Heaton, T.J., Hoffmann, D.L., Hogg, A.G., Hughen, K.A., Kaiser, K.F., Kromer, B., Manning, S.W., Niu, M., Reimer, R.W., Richards, D.A., Scott, E.M., Southon, J.R., Staff, R.A., Turney, C.S.M., van der Plicht, J., 2013. IntCal13 and Marine13 radiocarbon age calibration curves 0-50,000 years cal BP. Radiocarbon 55, 1869-1887.

194. Richards, D.A., Bottrell, S.H., Cliff, R.A., Ströhle, K., Rowe, P.J., 1998. U-Pb dating of a speleothem of Quaternary age.

Geochimica et Cosmochimica Acta 62, 3683-3688.

195. Richards, D.A., Dorale, J.A., 2003. U-series chronology of speleothems and paleoclimate. Uranium-series geochemistry. Reviews in Mineralogy and Geochemistry 52, 407-460.

196. Riechelmann, D.F.C., Schröder-Ritzrau, A., Scholz, D., Fohlmeister, J., Spötl, C., Richter, D.K., Mangini, A., 2011. Monitoring Bunker Cave (NW Germany): A prerequisite to interpret geochemical proxy data of speleothems from this site. Journal of Hydrology 409, 682-695.

197. Rodríguez-Sanz, L., Graham Mortyn, P., Martínez-Garcia, A., Rosell-Melé, A., Hall, I.R., 2012. Glacial Southern Ocean freshening at the onset of the Middle Pleistocene Climate Transition. Earth and Planetary Science Letters 345-348, 194-202.

198. Rossignol-Strick, M., 1985. Mediterranean Quaternary sapropels, an immediate response of the African monsoon to variation of insolation. Palaeogeography, Palaeoclimatology, Palaeoecology 49, 237-263.

199. Rossignol-Strick, M., Paterne, M., 1999. A synthetic pollen record of the eastern Mediterranean sapropels of the last 1 Ma: Implications for the time-scale and formation of sapropels. Marine Geology 153, 221-237.

200. Rozanski, K., Sonntag, C., Munnich, K.O., 1982. Factors controlling stable isotope composition of European precipitation. Tellus 34, 142-150.

201. Ruddiman, W.F., McIntyre, A., Raymo, M.E., 1986. Paleoenvironmental Results from North Atlantic Sites 607 and 609. In: Ruddiman,W.F., Kidd, R.B., Thomas, E., et al. (Eds.), Initial Reports, DSDP 94. U.S. Govt. Printing Office, Washington, 855–878.

202. Ruddiman, W.F., Raymo, M.E., Martinson, D.G., Clement, B.M., Backman, J., 1989. Pleistocene evolution: Northern Hemisphere ice sheets and North Atlantic Ocean. Paleoceanography 4, 353-412.

203. Rudzka, D., McDermott, F., Baldini, L.M., Fleitmann, D., Moreno, A., Stoll, H., 2011. The coupled δ 13C-radiocarbon systematics of three Late Glacial/early Holocene speleothems; insights into soil and cave processes at climatic transitions. Geochimica et Cosmochimica Acta 75, 4321-4339.

204. Ryan, C., Siddons, D., Kirkham, R., Dunn, P., Kuczewski, A., Moorhead, G., De Geronimo, G., Paterson, D., De Jonge, M., Hough, R., 2010. The new Maia detector system: methods for high definition trace element imaging of natural material, AIP Conference Proceedings, p. 9.

205. Schmitz, M.D., Schoene, B., 2007. Derivation of isotope ratios, errors, and error correlations for U-Pb geochronology using ^{205}Pb-^{235}U-(^{233}U)-spiked isotope dilution thermal ionization mass spectrometric data. Geochem. Geophys. Geosyst. 8, Q08006.

206. Scholz, D., Hoffmann, D.L., 2011. StalAge - An algorithm designed for construction of speleothem age models. Quaternary Geochronology 6, 369-382.

207. Scholz, D., Hoffmann, D.L., Hellstrom, J., Bronk Ramsey, C., 2012. A comparison of different methods for speleothem age modelling. Quaternary Geochronology 14, 94-104.

208. Scholz, D., Tolzmann, J., Hoffmann, D.L., Jochum, K.P., Spötl, C., Riechelmann, D.F.C., 2014. Diagenesis of speleothems and its effect on the accuracy of ^{230}Th/U-ages. Chemical Geology 387, 74-86.

209. Shackleton, N., 1967. Oxygen isotope analyses and pleistocene temperatures re-assessed. Nature 215, 15-17.

210. Shackleton, N.J., Opdyke, N.D., 1976. Oxygen-isotope and paleomagnetic stratigraphy of pacific core V28-239 late Pliocene to latest Pleistocene, Memoir of the Geological Society of America, pp. 449-464.

211. Shackleton, N.J., Berger, A., Peltier, W.R., 1990. An alternative astronomical calibration of the lower Pleistocene timescale based on ODP Site 677. Transactions of the Royal Society of Edinburgh: Earth Sciences 81, 251-261

212.

213. Sharp, Z., 2007. Principles of Stable Isotope Geochemistry. Pearson Prentice Hall, Upper Saddle River, NJ.

214. Sniderman, J.M.K., Woodhead, J.D., Hellstrom, J., Jordan, G.J., Drysdale, R.N., Tyler, J.J., Porch, N. (2016) The Pliocene as a reversal of late Noelene acidification. P.N.A.S. in press.

215. Siddall, M., Hönisch, B., Waelbroeck, C., Huybers, P., 2010a. Changes in deep Pacific temperature during the mid-Pleistocene transition and Quaternary. Quaternary Science Reviews 29, 170-181.

216. Siddall, M., Rohling, E.J., Blunier, T., Spahni, R., 2010b. Patterns of millennial variability over the last 500 ka. Climate of the Past 6, 295-303.

217. Skinner, L.C., Shackleton, N.J., 2005. An Atlantic lead over Pacific deep-water change across Termination I: Implications for the application of the marine isotope stage stratigraphy. Quaternary Science Reviews 24, 571-580.

218. Sosdian, S., Rosenthal, Y., 2009. Deep-sea temperature and ice volume changes across the pliocene-pleistocene climate transitions. Science 325, 306-310.

219. Southon, J., Noronha, A.L., Cheng, H., Edwards, R.L., Wang, Y., 2012. A high-resolution record of atmospheric 14C based on Hulu Cave speleothem H82. Quaternary Science Reviews 33, 32-41.

220. Spötl, C. and Mangini, A., 2002. Stalagmite from the Austrian Alps reveals Dansgaard–Oeschger events during isotope stage 3:: Implications for the absolute chronology of Greenland ice cores. Earth and Planetary Science Letters 203, 507-518.

221. Spötl, C., Vennemann, T.W., 2003. Continuous-flow isotope ratio mass spectrometric

analysis of carbonate minerals. Rapid Communications in Mass Spectrometry 17, 1004-1006.

222. Spötl C., Mangini A., Burns S.J., Frank N., Pavuza N., 2004. Speleothems from the high-Alpine Spannagel Cave, Zillertal Alps (Austria). In: I.D. Sasowsky, J. Mylroie (Eds.), Studies of Cave Sediments: Physical and Chemical Records of Paleoclimate, Kluwer, Dortrecht, 243– 256.

223. Spötl, C., Fairchild, I.J., Tooth, A.F., 2005. Cave air control on dripwater geochemistry, Obir Caves (Austria): Implications for speleothem deposition in dynamically ventilated caves. Geochimica et Cosmochimica Acta 69, 2451-2468.

224. Spötl, C., 2011. Long-term performance of the Gasbench isotope ratio mass spectrometry system for the stable isotope analysis of carbonate microsamples. Rapid Communications in Mass Spectrometry 25, 1683-1685.

225. Stirling C.H., Esat, T.M., Lambeck, K., McCulloch, M,T., Blake, S.G., Lee, D-C., Halliday, A.N., 2001. Orbital forcing of the marine isotope stage 9 interglacial. Science 291, 290–293.

226. Sun, Y., Clemens, S.C., An, Z., Yu, Z., 2006. Astronomical timescale and palaeoclimatic implication of stacked 3.6-Myr monsoon records from the Chinese Loess Plateau. Quaternary Science Reviews 25, 33-48.

227. Tera, F. and Wasserburg, G.J., 1972. U–Th–Pb systematics in three Apollo 14 basalts and the problem of initial Pb in lunar rocks. Earth and Planetary Science Letters 14, 281–304.

228. Treble, P., Shelley, J.M.G., Chappell, J., 2003. Comparison of high resolution sub-annual records of trace elements in a modern (1911-1992) speleothem with instrumental climate data from southwest Australia. Earth and Planetary Science Letters 216, 141-153.

229. Treble, P.C., Chappell, J., Shelley, J.M.G., 2005. Complex speleothem growth processes revealed by trace element mapping and scanning electron microscopy of annual layers. Geochimica et Cosmochimica Acta 69, 4855-4863.

230. Tremaine, D.M., Froelich, P.N., Wang, Y., 2011. Speleothem calcite farmed in situ: Modern calibration of δ18O and δ13C paleoclimate proxies in a continuously-monitored natural cave system. Geochimica et Cosmochimica Acta 75, 4929-4950.

231. Tzedakis, P.C., Hooghiemstra, H., Pälike, H., 2006. The last 1.35 million years at Tenaghi Philippon: revised chronostratigraphy and long-term vegetation trends. Quaternary Science Reviews 25, 3416-3430.

232. Tziperman, E., Gildor, H., 2003. On the mid-Pleistocene transition to 100-kyr glacial cycles and the asymmetry between glaciation and deglaciation times. Paleoceanography 18, 1-1.

233. Vaks, A., Woodhead, J., Bar-Matthews, M., Ayalon, A., Cliff, R.A., Zilberman, T., Matthews,

A., Frumkin, A., 2013. Pliocene-Pleistocene climate of the northern margin of Saharan-Arabian Desert recorded in speleothems from the Negev Desert, Israel. Earth and Planetary Science Letters 368, 88-100.

234. van Breukelen, M.R., Vonhof, H.B., Hellstrom, J.C., Wester, W.C.G., Kroon, D., 2008. Fossil dripwater in stalagmites reveals Holocene temperature and rainfall variation in Amazonia. Earth and Planetary Science Letters 275, 54-60.

235. Vanghi V., Iriarte, E., Aranburu, A., 2015. High resolution X-ray computed tomography for petrological characterization of speleothems. Journal of Cave and Karst Studies 77, no. 1, 75–82.

236. Venz, K.A., Hodell, D.A., Stanton, C., Warnke, D.A., 1999. A 1.0 Myr record of Glacial North Atlantic Intermediate Water variability from ODP site 982 in the northeast Atlantic. Paleoceanography 14, 42-52.

237. Walczak, I.W., Baldini, J.U.L., Baldini, L.M., McDermott, F., Marsden, S., Standish, C.D., Richards, D.A., Andreo, B., Slater, J., 2015. Reconstructing high-resolution climate using CT scanning of unsectioned stalagmites: A case study identifying the mid-Holocene onset of the Mediterranean climate in southern Iberia. Quaternary Science Reviews 127, 117-128.

238. Walker, J., Cliff, R.A., Latham, A.G., 2006. U-Pb isotopic age of the StW 573 hominid from Sterkfontein, South Africa. Science 314, 1592-1594.

239. Wang, Y.J., Cheng, H., Edwards, R.L., An, Z.S., Wu, J.Y., Shen, C.C., Dorale, J.A., 2001. A high-resolution absolute-dated late pleistocene monsoon record from Hulu Cave, China. Science 294, 2345-2348.

240. Wassenburg, J.A., Immenhauser, A., Richter, D.K., Jochum, K.P., Fietzke, J., Deininger, M., Goos, M., Scholz, D., Sabaoui, A., 2012. Climate and cave control on Pleistocene/Holocene calcite-to-aragonite transitions in speleothems from Morocco: Elemental and isotopic evidence. Geochimica et Cosmochimica Acta 92, 23-47.

241. Weirauch, D., Billups, K., Martin, P., 2008. Evolution of millennial-scale climate variability during the mid-Pleistocene. Paleoceanography 23(3), PA3216.

242. Winograd, I.J., Coplen, T.B., Landwehr, J.M., Riggs, A.C., Ludwig, K.R., Szabo, B.J., Kolesar, P.T., Revesz, K.M., 1992. Continuous 500,000-Year Climate Record from Vein Calcite in Devils Hole, Nevada. Science 258, 255-260.

243. Woodhead, J., Hellstrom, J., Maas, R., Drysdale, R., Zanchetta, G., Devine, P., Taylor, E., 2006. U-Pb geochronology of speleothems by MC-ICPMS. Quaternary Geochronology 1, 208-221.

244. Woodhead, J., Hellstrom, J., Pickering, R., Drysdale, R., Paul, B., Bajo, P., 2012. U and Pb variability in older speleothems and strategies for their

chronology. Quaternary Geochronology 14, 105-113.

245. Woodhead, J.and Pickering, R., 2012. Beyond 500 ka: Progress and prospects in the U-Pb chronology of speleothems, and their application to studies in palaeoclimate, human evolution, biodiversity and tectonics. Chemical Geology 322-323, 290-299.

246. Woodhead, J., Reisz, R., Fox, D., Drysdale, R., Hellstrom, J., Maas, R., Cheng, H., Edwards, R.L., 2010. Speleothem climate records from deep time? Exploring the potential with an example from the Permian. Geology 38, 455-458.

247. Zanchetta, G., Drysdale, R.N., Hellstrom, J.C., Fallick, A.E., Isola, I., Gagan, M.K., Pareschi, M.T., 2007. Enhanced rainfall in the Western Mediterranean during deposition of sapropel S1: stalagmite evidence from Corchia cave (Central Italy). Quaternary Science Reviews 26, 279-286.

248. Zanchetta, G., Bar-Matthews, M., Drysdale, R.N., Lionello, P., Ayalon, A., Hellstrom, J.C., Isola, I., Regattieri, E., 2014. Coeval dry events in the central and eastern Mediterranean basin at 5.2 and 5.6ka recorded in Corchia (Italy) and Soreq caves (Israel) speleothems. Global and Planetary Change 122, 130-139.

249. Zhang, H., Cai, Y., Tan, L., Qin, S., An, Z., 2014. Stable isotope composition alteration produced by the aragonite-to-calcite transformation in speleothems and implications for paleoclimate reconstructions. Sedimentary Geology 309, 1-14.

250. Zhao, J.x., Yu, K.f., Feng, Y.x., 2009. High-precision 238U-234U-230Th disequilibrium dating of the recent past: a review. Quaternary Geochronology 4, 423-433.

251. Zhou, H., Feng, Y.x., Zhao, J.x., Shen, C.C., You, C.F., Lin, Y., 2009. Deglacial variations of Sr and 87Sr/86Sr ratio recorded by a stalagmite from Central China and their association with past climate and environment. Chemical Geology 268, 233-247.

252. Zisu, N.S., Schwarcz, H.P., Konyer, N., Chow, T., Noseworthy, M.D., 2012. Macroholes in stalagmites and the search for lost water. Journal of Geophysical Research: Earth Surface 11

Author/s:
Bajo, Petra

Title:
Geochemical investigations of Corchia speleothems: implications for past climate change

Date:
2016